DISS. ETH NO. 24547

CMBL - A High-intensity Muon Beam Line & Scintillation Target with Monitoring System for Next-generation Charged Lepton Flavour Violation Experiments

A thesis submitted to attain the degree of

DOCTOR OF SCIENCES of ETH ZURICH

(Dr. sc. ETH Zurich)

presented by

Felix Anton Berg

Dipl.-Phys., Ruprecht-Karls-Universität Heidelberg

born on 28.09.1983

citizen of Germany

accepted on the recommendation of

Prof. Klaus Stefan Kirch

Prof. Christoph Grab

2017

Abstract

One of the main driving forces of Particle Physics at the Intensity Frontier is the search for Rare Decays. The detection of a "forbidden" decay mediated by an as yet undiscovered boson or through flavour mixing would be a clear sign of "New Physics" beyond the Standard Model (SM). Good access with a clear signature is provided in the charged Lepton Flavor Violation (cLFV) sector. High production rates and more convenient lifetimes make the muon the most promising candidate [1], whereby the main focus lies on the so-called Golden Channels [2]. Nowadays searches such as the upcoming Mu3e [3] experiment or the upgraded MEG II [4] experiment aim at sensitivities of the order $\mathcal{O}\left(10^{-16}\right)$ for the decay $\mu^+ \to e^+ + e^- + e^+$ and $\mathcal{O}\left(10^{-14}\right)$ for the reaction channel $\mu^+ \to e^+ + \gamma$ respectively. With the MEG II detector performance upgrade a factor two increase in the stopping rate can be handled leading to $7 \cdot 10^7$ μ^+-stops/s on target, whilst Mu3e with its novel detector and triggerless DAQ design can accept stopping rates an order of magnitude higher than the world's most intense DC muon beams at the Paul Scherrer Institute (PSI). However, the first part of the staged detector design is planned to run at $\mathcal{O}\left(10^8\right)$ μ^+-stops/s. The πE5 muon channel at the Paul Scherrer Institute, as the only available experiment location able to provide such high rates must therefore share both experiments. Challenged by the severe spatial constraints in the experimental area, a new Beam Line, the Compact Muon Beam Line (CMBL), has been designed, simulated in detail, constructed and extensively studied with the aim of achieving intensity frontier rates for Mu3e without compromising the physics goals of each experiment and enabling a minimum switch-over period between experiments. Initial commissioning of the beam line showed a transmission of $\sim$58% from the intermediate collimator system. Profile and rate measurements at the final focus and intermediate positions provided full information about the transverse phase space of the beam. Using this information a detailed G4Beamline [5] simulation validated by the measurements was used to identify limiting apertures, which motviated an upgrade of the last two dipole magnets. A commissiong run in 2016 showed that with these improvements a rate of $\sim$8$\cdot$10^7 μ^+/s at 2.2 mA proton current can be achieved at the injection to the Mu3e spectrometer. Simulations show that $\mathcal{O}\left(10^8\right)$ μ^+/s at the centre of the Mu3e solenoid can be achieved when using the 60 mm muon production target and a nominal operation at 2.4 mA proton current.

Up to now the πE5 beam line provides no continuous non-invasive online beam diagnostics tools. Profile monitoring by means of a scintillation stopping target, in the case of MEG II, was studied tested and has proven to be extremely beneficial. A continuous beam monitoring during the 2016 MEG Pre-Engineering Run was evaluated based on beam position, beam size and relative intensity changes, which includes effects induced by radiation damage. A parallel measurement of the proton beam position on the muon production target TgE and the muon beam position at the MEG II stopping target showed a linear correlation between the proton beam centring, the muon beam intensity and the muon beam centroid shift at the target position. The high precision and fast acquisition of the

full beam spot allows to reduce the time for beam commissioning for MEG II and provides a direct measure of the actual muon distribution and intensity during the run.

The design and comissioning of a novel compact muon beam line together with a scintillation target capable of continuous monitoring the muon stopping distribution and intensity will enable the MEG II and Mue3 experiments to search for two of the three muon "Golden Channels" at the intensity frontier.

Zusammenfassung

Die experimentelle Suche nach seltenen Zerfällen dominiert die heutige Teilchenphysik an der Intensitätsfront. Der Nachweis eines "verbotenen" Zerfalls, der nur durch bislang unentdeckte Austauchteilchen möglich wird, bedeutete einen eindeutigen Nachweis "neuer Physik" jenseits des Standard Modells. Leptonenzahlverletzung im geladenen Sektor bietet einen guten experimentellen Zugang, wobei hohe Produktionsraten und die vergleichsweise lange Lebensdauer den Myonzerfall prädestinieren [1]. Die sogenannten "Goldenen Kanäle" $\mu^+ \rightarrow e^+ + e^- + e^+$, $\mu^+ \rightarrow e^+ + \gamma$, $\mu^- + N \rightarrow e^- + N$ sind durch ihre klare Signatur besonders geeignet [2]. Die aktuellsten Limite wurden am PSI bestimmt [6, 7, 8] und kommende Experimente für die beiden erstgenannten Kanäle werden am PSI ausgeführt. MEG II ($\mu^+ \rightarrow e^+ + \gamma$) [4] zielt hierbei auf eine Verbesserung der Sensitivität um mehr als eine Grössenordnung auf $\mathcal{O}\left(10^{-14}\right)$ und das neuartige Mu3e Experiment [3] wird in einem stufenweisen Ansatz eine Sensitivität $\mathcal{O}\left(10^{-16}\right)$ erreichen, vier Grössenordnungen unter dem aktuellen Limit. MEG II stellt eine umfassende Neukonstruktion des MEG-Detektors dar, die es erlaubt mit einer Rate von $7 \cdot 10^7$ μ^+/s die bisherige Stopprate im Target mehr als zu verdoppeln. Das neuartige Detektordesign und die triggerlose Datenaufnahme in Mu3e wird in der finalen Stufe Raten von 10^9 μ^+/s akzeptieren, was die derzeit weltweit höchstmöglichen Raten am PSI um eine Grössenordnung übertrifft. Die erste Stufe des Mu3e Experiments mit einer anvisierten Sensitivität von $\mathcal{O}\left(10^{-15}\right)$ sieht Raten von 10^8 μ^+/s vor, was das πE5-Areal am PSI als die weltweit leistungsfähigste für die Teilchenphysik zur Verfügung stehende Quelle prädestiniert.

Gleichzeitig wird das MEG II-Experiment an dieser Strahllinie aufgebaut, was eine wechselseitige Nutzung erfordert. Angesichts der räumlichen Beschränkungen auf den vorderen Teil des Areals führte dies zur Entwicklung einer neuen kompakten Erweiterung der bestehenden Strahllinie, der Compact Muon Beam Line (CMBL), die im Zuge dieser Arbeit geplant, simuliert, aufgebaut und in Teststrahlzeiten charakterisiert wurde. Die ersten Ergebnisse der Strahlzeiten lieferten eine Transmission vom Übergabepunkt zum Ende der CMBL von $\sim$ 58 %. Weiterentwickelte Simulationen, basierend auf den Resultaten der ersten Strahlzeit, zeigten weitere Optimierungsmöglichkeiten auf und führten zur Neukonstruktion zweier Vakuumkammern und der Überarbeitung eines Ablenkmagneten, was in der finalen Strahlzeit eine Rate von $\sim$8·10^7 μ^+/s an der Injektion zu dem zu entwickelndem Mu3e Spektrometer ermöglichte.

Die hohen Raten der πE5-Strahllinie, die auch von MEG II nahezu ausgeschöpft werden, erfordern eine verbesserte Überwachung der Strahlzentrierung und des Profils am Zentrum des MEG II-Detektors. Der Einsatz eines 150 μm dünnen Szintillators als Stopptarget und eines Kamerasystems zur Monitorierung, wurde im Rahmen dieser Arbeit in 2 Teststrahlzeiten vorbereitet. Die Langzeitmonitorierung des Szintillationstargets erlaubte die optischen Strahlenschäden des Targets zu charakterisieren und ergab, dass eine effektive Nutzbarkeitsdauer über eine Messperiode von MEG II möglich ist. Die hohe Präzision dieser Technik impliziert eine Messgenauigkeit besser als 100 μm für die Strahlzentrierung

und Profile für einen späteren Einsatz in MEG II. In weiteren Messungen konnte erstmals an den Sekundärstrahllinien des PSI die Abhängigkeit der Zentrierung des Myonstrahls von der Lage des Protonstrahls am Produktionstarget nachgewiesen werden.

Die neue Strahlführungslinie CMBL und das Szintillationstarget befördern die nun am PSI fortgesetzte Suche nach leptonenzahlverletzenden Zerfällen im geladenen Sektor.

To my daughter Hanna Florina

Contents

1. Introduction

This thesis was carried out in the context of the upcoming Mu3e [3] and the MEG II [4] experiments, which will search, at the intensity frontier, for the cLFV decay channels $\mu^+ \rightarrow e^+ + e^- + e^+$ and $\mu^+ \rightarrow e^+ + \gamma$ respectively. For Mu3e a new compact beam line (CMBL) was designed and commissioned, which is capable of providing the highest rates to the Mu3e experiment while matching the spatial constraints imposed by the shared use of the πE5 area at PSI with MEG II. The most recently measured, yet not final rates, yielded $\sim$8·10^7 μ^+/s at 2.2 mA proton current at the injection point to the Mu3e spectrometer solenoid, still to be built.

The upgraded detector of MEG II is planned to run at more than twice the rate of the former MEG experiment, which will be close to the maximum beam intensity that can be achieved. This demands for accurate monitoring of the muon beam properties at the centre of the MEG II experiment. To this purpose a scintillation stopping target, viewed by a Charge-Coupled Device (CCD) camera system, was introduced and tested. In a long-term beam monitoring test the high precision capabilities of this setup could be shown and the influence of radiation damage on the target's optical properties could be characterized, proving that the use of such a beam monitoring system in MEG II, over a full beam period, should be possible. The high precision of this technique with its online beam monitoring capabilities was for the first time at the PSI secondary beam lines used to measure the direct dependence of the muon beam centering on the proton beam position at the production target.

The thesis is structured as outlined below:

- In the remainder of this chapter a brief introduction to the theoretical framework of current particle physics, the SM, is depicted. The most important aspects as well as the model limitations are discussed, motivating the search for continuative theories. A qualitative outlook on Beyond the Standard Model (BSM) theories is accompanied by an overview of the different experimental approaches, for which the cLFV muon decays are discussed in more detail. Following this, a description of muon production and in particular surface muons and their generation is given together with an overview of the PSI secondary beam lines. The last part of this chapter is dedicated to an overview of two of the major cLFV muon experiments specific to PSI, Mu3e and MEG II.

- The second chapter describes the design, setup and commissioning of the CMBL. An introduction to the main theoretical aspects of accelerator physics and the simulation tools, that were used, is followed by an overview of the beam line layout and the required elements. Following this, the simulation studies that follow different approaches are explained. Matrix code simulations of the full beam line are presented, as well as fieldmap based simulation models, which investigate either the first part of the beam line or the latter CMBL only component part. First test beam results are

shown together with the beam characterization. Based on the these results critical components in the beam line were identified, which led to an improved setup. The final test beam results are discussed together with conclusions and an outlook on accomplished and further aspects of the CMBL to be studied.

- Chapter 3 is dedicated to the scintillation target studies undertaken for the MEG II experiment. A brief introduction to the working principles of organic scintillators is given. First test beam results gave the proof-of-principle for such a muon beam monitoring technique using a mirror and CCD camera system, while the main analysis techniques used to analyze the data are described. The subsequent long-term beam test at the centre of the MEG II spectrometer magnet suffered from the camera sensitivity to the magnetic field and the temperature. However, the data analysis outlined, shows that these problems could be overcome. The acquired information from several thousand beam profile and background images is shown and illustrates the high precision achievable, already implying the influence of radiation damage on the profile. The dependence of the muon beam intensity and the centroid on the proton beam position at the production target was measured for the first time and is shown here. The final part of the chapter uses the combined information from the previous analysis steps, to present the light yield degradation of the scintillator over the test beam period. Fitting these data proves that the beam monitoring over a full run period should be possible. Finally, in the conclusions to this chapter several ways to improve the setup are outlined.

- The appendix chapter lists additional information on aspects that arose during the work on the beam line. Improvements that were made to the beam scanner systems are explained. An optimization software for G4BL, that was developed in the context of this thesis is presented and a way to enhance the overall beam intensity in the experimental area of MEG II and Mu3e is depicted.

1.1. Muons in the context of the Standard Model of particle physics

The Standard Model (SM) of particle physics is the state-of-the-art description of the most fundamental particles and processes that exist, though excluding gravity from its mediating interactions, which at the subatomic scale is however negligible. Figure 1.1 lists all the fundamental particles that are known up to now and that are implemented in the SM. Matter is formed by particles, that carry spin $\frac{1}{2}$ (fermions), while interactions are
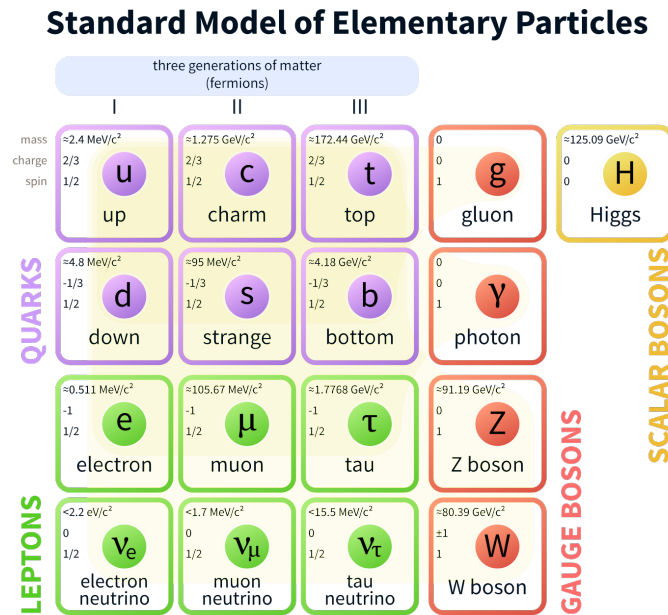
Figure 1.1.: *Overview of the fundamental particles in the SM [9]*

described by mediating gauge bosons that have integer spin. The discovery of the Higgs boson in 2012 [10, 11] added the final missing piece to the SM by proving the existence of the Higgs field, which yields an explanation for the fundamental particle masses. The fermions split into quarks and leptons, each formed into three generations or flavours. In the case of the six leptons these are the charged electron, muon and tauon and their associated neutral partners the neutrinos. The interaction between these spin $\frac{1}{2}$ particles is mediated in the case of the electromagnetic force by its gauge boson the photon, while in the case of a weak interaction the mediation is performed by the charged $W^{+/-}$ bosons or the neutral Z^0 boson. The strong interaction between quarks is via the eight gauge bosons known as gluons.

The masses of the charged leptons are well known whereas the neutrino masses have not yet been determined but are now known to be finite. The Homestake experiment [12] was the first to measure a deficiency in the rate of solar electron neutrinos ν_e reaching the Earth from the sun, which is explained by mixing of the neutrino flavour states on their way to the Earth. The mixing angles are closely related to the neutrino masses whereby the

relationship between the mass eigenstates $\nu_{1,2,3}$ and flavour eigenstates $\nu_{e,\mu,\tau}$ is described by the Pontecorvo-Maki-Nakagawa-Sakata (PMNS) matrix U [13, 14]:

$$\begin{pmatrix} \nu_e \\ \nu_\mu \\ \nu_\tau \end{pmatrix} = \begin{pmatrix} U_{e1} & U_{e2} & U_{e3} \\ U_{\mu 1} & U_{\mu 2} & U_{\mu 3} \\ U_{\tau 1} & U_{\tau 2} & U_{\tau 3} \end{pmatrix} = \begin{pmatrix} \nu_1 \\ \nu_2 \\ \nu_3 \end{pmatrix} \tag{1.1}$$

The SM is not only a very succesful predictive theory but also one of the most tested models, confirming predictions not only in the case of the top and charm quarks, but also with the gauge bosons, such as the W, Z and most recently the Higgs boson and no serious deviations of the fundamental constants/model parameters have yet been observed [15].
However, despite the big success of the SM in various fields of particle physics there are still several open questions which cannot be answered by the current theory:

- The observation of the matter-antimatter asymmetry in the universe
- Unification of forces including the strong interaction
- ... and even gravitation?
- Source of the number of particle families
- Dark matter
- Hierarchy problem

These issues suggest that the SM does not provide a full picture but rather represents a low-energy approximation of a more fundamental theory. Various new models, so-called BSM theories, exist and are subject to extensive research from both the theoretical and the experimental side.
BSM theories, introduce new kinds of fields and new particles that mediate the associated forces. Conversely this allows to either validate, exclude, or constrain the parameter space of BSM theories by searching for new types of particles. The experimental approaches can be summarized in three points:

- Energy frontier : Experiments at the energy frontier search for new particles that are generated in high energy collisions at particle colliders. This allows one to scan different energy ranges for new resonances and new particles. The Large Hadron Collider (LHC) operates at a maximum centre-of-mass energy of $\sqrt{s}$ =13 TeV, which is essentially the production limit that can be accessed at the moment.

- Cosmic frontier : In this approach particles from space or their products from interaction with the earth's atmosphere are detected. Important aspects are the search for dark matter candidates and for matter-antimatter asymmetry in the universe.

- Intensity frontier: Intensity frontier experiments aim for an indirect detection of BSM physics. The basic idea is that new particles are not produced directly but mediate additional reaction channels, which leads to enhanced cross-sections for certain reactions. Precision experiments aim at measuring particle properties, such as e.g. the electric dipole moment of the neutron [16], the g-factor of the muon [17], or the proton radius [18], in order to find deviations from the SM predictions. A clean signature of new physics, free from SM backgrounds, could be found in the search for "forbidden" decays that have a vanishing cross section in the SM. So-called cLFV experiments search for decay channels in which the lepton number is not conserved as

in the case of the low-energy regime $\mu \to 3e$ or $\mu \to e + \gamma$ or at the collider scale such as e.g. $Z \to e\mu$ or $H \to \mu\tau$ [19]. Experiments at the intensity frontier mainly focus on the decays of muons, where the comparatively long life time and easy production make the muon a most promising candidate in the search for cLFV decays.

The different approaches are not seen as competitive first hand but rather regarded as complementary to each other. The advantage of the direct production of new particles in high-energy collisions is that new particles are not only detected but direct measurements of the particles' properties, such as their mass, are possible. The indirect approaches however provides no direct access to BSM particle properties as this information depends on the theoretical models. Conversely, the mediating mass range that can be probed by this method can be orders of magnitude higher than the highest energies produced by particle accelerators and depends on the energy scale of BSM physics of the model.

1.1.1. cLFV searches with muons

As described above neutrino flavour mixing has been observed and so proves a non-zero mass for the neutrinos. However in the charged sector no lepton flavour violation has ever been observed. SM decays of charged leptons involve neutrinos, so that the lepton number is conserved. For example in the case of the Michel decay $\mu^- \to e^- + \bar{\nu}_e + \nu_\mu$ the lepton number in the initial state equals the lepton number of the final state $L_\mu = +1$. However, also in the SM neutrino oscillations can give rise to a finite probability of lepton number violation in the charged sector, which is shown in an exemplary manner for the reaction $\mu^+ \to e^+ + \gamma$ in figure 1.2. However the expected cross-section scales with the fourth power
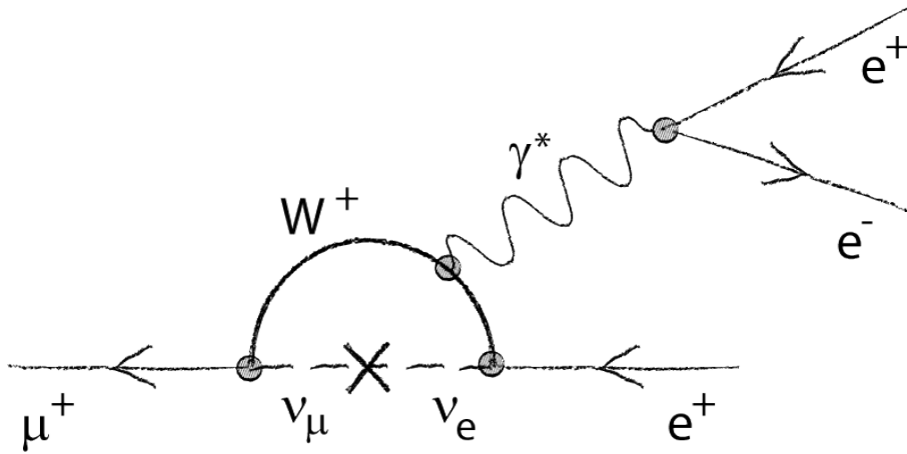
Figure 1.2.: *[20] The Feynman diagram illustrates the contribution to the cLFV decay $\mu^+ \to e^+ + \gamma$ by the SM, which involves the internal flavour transition of the muon neutrino into an electron neutrino.*

of the mass differences between the neutrino families and is therefore strongly supressed, leading to an immeasurably small branching ratio [21]:

$$\mathcal{B}\left(\mu^+ \to e^+ + \gamma\right) \simeq \frac{3\alpha}{32\pi} \left| \sum_{i=2,3} U_{\mu i}^* U_{ei} \frac{\Delta m_{\nu_{i1}}^2}{m_W^2} \right|^2 < 10^{-54} \tag{1.2}$$

where α is the fine structure constant, U the PMNS matrix, $\Delta m^2_{\nu_{ij}}$ the mass-squared differences of the neutrino eigenstates and m_W the mass of the W-boson.

Due to the tiny cross section a detection of such a decay would be a clear sign for new physics.

There are three so-called "Golden Channels" [2] in the cLFV muon decay that have been investigated in the past and are subject to intense searches by upcoming experiments.

- $\mu^- + N \to e^- + N$: In this approach an intense beam of negative muons is stopped in a target. A pure conversion $\mu^- \to e^-$ in the presence of a nucleus would be followed by the emission of the mono-energetic decay electron, which has to be detected. The energy equals the muon mass with a small correction from the nuclear recoil. The present best result on this decay mode was set by the SINDRUM II experiment at PSI and published in 2006 [8] with an upper limit on the branching ratio of 7.0·10⁻¹³ at 90 % confidence level using a gold target. New experiments at J-PARC [22] and Fermilab [23] aim at reducing this limit by four orders of magnitude if no signal is found.

- $\mu^+ \to e^+ + e^+ + e^-$: The current upper limit on the branching ratio for this channel was published in 1988 [7] and was set by the SINDRUM experiment at PSI to be lower than 1.0·10⁻¹² at 90 % confidence level. A new experiment at PSI, Mu3e, is aiming for a final sensitivity of $\mathcal{O}\left(10^{-16}\right)$, which will be achieved in a staged approach. The experimental setup and the signal signature is described in a dedicated subsection 1.4.

- $\mu^+ \to e^+ + \gamma$: In 2016 the MEG collaboration published the most stringent upper limit on the $\mu^+ \to e^+ + \gamma$ decay [6] 4.2·10⁻¹³ at 90 % confidence level. The MEG detector is currently being upgraded and the MEG II experiment plans to start data-taking in 2018, thereby aiming for an improved sensitivity by an order of magnitude.

Figure 1.3 shows the history of upper limits set by cLFV experiments in the golden channels.

No signal has been found so far, but the experimental results constrain the parameter space of various BSM models. Equation 1.3 shows the simplified effective Lagrangian [25] that can be used to judge in a model-independent way the sensitivity to the energy scale of BSM physics in the decay modes $\mu^+ \to e^+ + e^+ + e^-$ and $\mu^+ \to e^+ + \gamma$ for interactions only at tree level or photon penguin diagrams, that are shown in figure 1.4.

$$\mathcal{L}_{cLFV} = \frac{m_\mu}{(\kappa + 1)\,\Lambda^2}\bar{\mu}_R \sigma_{\mu\nu} e_L F^{\mu\nu} + \frac{\kappa}{(\kappa + 1)\,\Lambda^2}\bar{\mu}_L \gamma_\mu e_L (\bar{e}\gamma^\mu e) \qquad (1.3)$$

Here m_μ is the muon mass, Λ the energy scale of the effective field theory, $F^{\mu\nu}$ the photon field strength and γ the Dirac matrix. The indices L/R indicate the chirality of the fermion fields. The dimensionless parameter κ expresses the relative strength of the dipole interaction (first term) with respect to the four-fermion contact (second) term. Figure 1.5 [25] illustrates the energy scale Λ plotted against κ and illustrates the energy ranges, accounting for the masses of new bosons and the coupling parameters, that can be tested in the $\mu^+ \to e^+ + e^+ + e^-$ and $\mu^+ \to e^+ + \gamma$ channels. It can be seen, that the search for both transitions is complementary, showing different sensitivities to the shown dipole and four-fermion interactions. In order to cover the full range of possible new physics, following both approaches is essential. Furthermore the accesible high energy scales emphasize the need
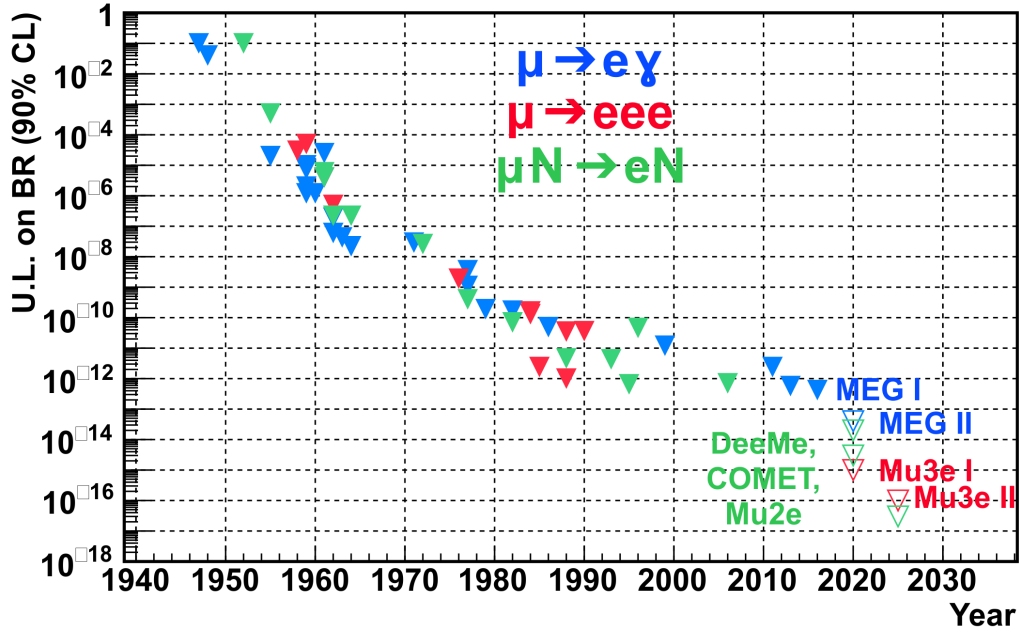
Figure 1.3.: *History of cLFV upper limits on the golden channels. The plot is adapted from [24]*

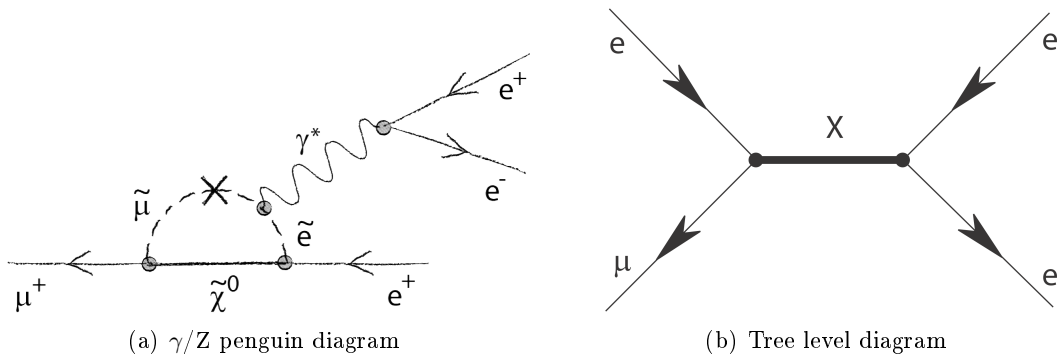
(a) γ/Z penguin diagram

(b) Tree level diagram

Figure 1.4.: *[20] Shown are the Feynman diagrams of dipole and contact term interactions involving BSM particles that are taken into account in figure 1.5*
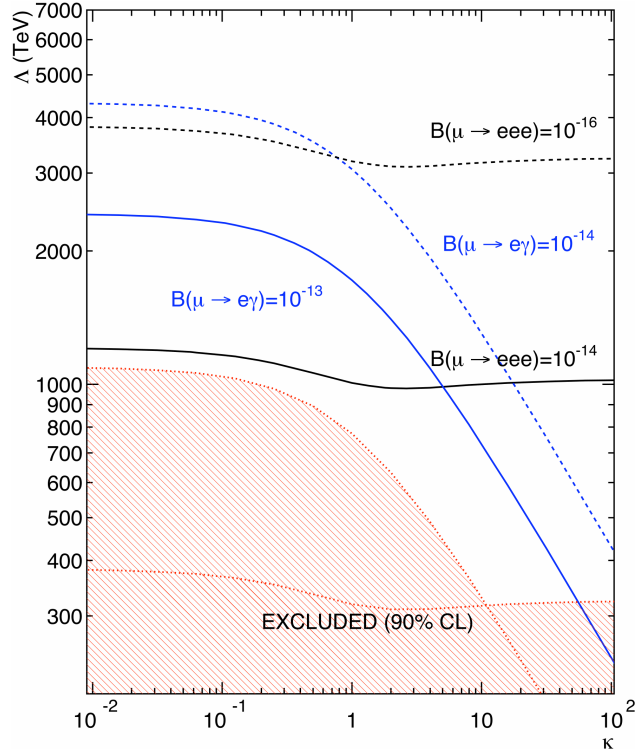
Figure 1.5.: *[25] The plot illustrates the high energy scales which can be tested in a model independent way by searching for the cLFV decays $\mu^+ \to e^+ + e^+ + e^-$ and $\mu^+ \to e^+ + \gamma$ using an effective field theory approach. For smaller κ values (dipole interactions) $\mu^+ \to e^+ + \gamma$ measurements are sensitive to much higher energies than $\mu^+ \to e^+ + e^+ + e^-$. Conversely new physics that is dominated by four-fermion interactions (higher κ values) is much more likely to be discovered by $\mu^+ \to e^+ + e^+ + e^-$ experiments.*

for new experiments, either by clearly detecting a signal or by setting new more restrictive limits, which deal as benchmarks for BSM theories. More comprehensive effective field theory approaches are followed by the PSI Laboratory for Particle Physics (LTP) theory group which include all contact terms [26] up to one-loop contributions and also emphasize the complementarity of the mentioned decay searches of the muon.

All of the current best upper limits were measured at PSI and a new generation of cLFV experiments, searching for $\mu^+ \to e^+ + e^+ + e^-$ and $\mu^+ \to e^+ + \gamma$, is underway, namely Mu3e and MEG II.

1.2. Muon production & properties

In the former cLFV experiments SINDRUM and MEG as well as in the future Mu3e and MEG II experiments a positively charged stopped muon beam is used to search for the sought after decay signature. In order to keep the multiple scattering (MSC) of the decay products small, which limits the detector resolution, thin stopping targets made of low nuclear charge materials are preferred. This necessiates a small range straggling of the stopped muon beam, which is determined partially by the muon beam momentum spread but predominantly by the central momentum [27].

The backward extracted under 165° πE5 muon beam is generated by a high-intensity 2.2 mA[1] and 590 MeV proton beam that interacts with a pion production target made of polycrystalline graphite. Subsequently, charged pions that are produced in the target predominantly decay into muons via the following reactions:

$$\pi^+ \to \mu^+ + \nu_\mu$$
$$\pi^- \to \mu^- + \bar{\nu}_\mu$$

The production target TgE which provides secondary beams to πE5 and four other beam lines is a radiation-cooled rotating wheel, which has a width of 6 mm and a length of either 40 mm or 60 mm [28]. A Computer Aided Design (CAD) view of the muon production target is shown in figure 3.44.

Positively charged pions are produced above a threshold energy $\sim$ 280 MeV via the following reactions (single pion production):

$$p + p \to p + n + \pi^+ \tag{1.4}$$
$$p + p \to d + \pi^+ \tag{1.5}$$
$$p + n \to n + n + \pi^+ \tag{1.6}$$

or as in the case of double pion production reactions, which require threshold energies above 600 MeV:

$$p + p \to p + p + \pi^+ + \pi- \tag{1.7}$$
$$p + p \to n + n + \pi^+ + \pi^+ \tag{1.8}$$
$$p + p \to n + p + \pi^+ + \pi^0 \tag{1.9}$$
$$p + p \to d + \pi^+ + \pi^0 \tag{1.10}$$
$$p + n \to p + n + \pi^+ + \pi^- \tag{1.11}$$
$$p + n \to n + n + \pi^+ + \pi^0 \tag{1.12}$$
$$p + n \to d + \pi^- + \pi^+ \tag{1.13}$$

The threshold energies E_{thr} for the different production channels are given by:

$$E_{thr} = \frac{1}{2m_p} \left(\left(\sum_i m_i \right)^2 - \left(\sum_j m_j \right)^2 \right) \tag{1.14}$$
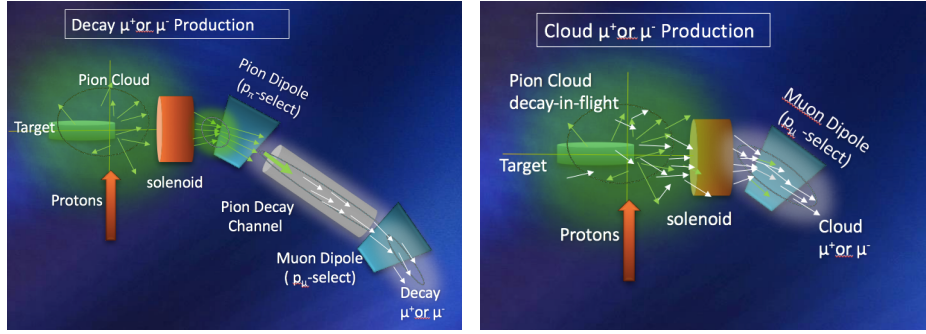
---

[1]In 2016 the High Intensity Proton Accelerator (HIPA) facility started to operate at 2.4 mA as nominal current, though proton beam related issues reduced the current for the 2016 test beam

where m_p is the proton mass, $\sum_i m_i$ is the summed mass of the final products and $\sum_j m_j$ the summed mass of the incoming reaction partners.

There are mainly three types of muon beams used by experiments that are schematically shown in figure 1.6. These are based either on muons stemming directly from the production target, as is the case of surface or sub-surface muons or from the decay of pions-in-flight either in the vicinity of the target leading to cloud muons or in a dedicated decay-channel as in the case of decay muons. Whereas surface muons have a fixed momentum at birth due to the 2-body kinematics, the cloud and decay muons have a box-spectrum ranging between the limits:

$$P_\mu^{Fwd} = \left(\beta_\pi + \beta_\mu^{CM}\right) \frac{P_\pi}{\beta_\pi \left(1 + \beta_\mu^{CM}\right)} \tag{1.15}$$

$$P_\mu^{Bkw} = \left(\beta_\pi - \beta_\mu^{CM}\right) \frac{P_\pi}{\beta_\pi \left(1 + \beta_\mu^{CM}\right)} \tag{1.16}$$

(a) Production of decay muons

(b) Production of cloud muons
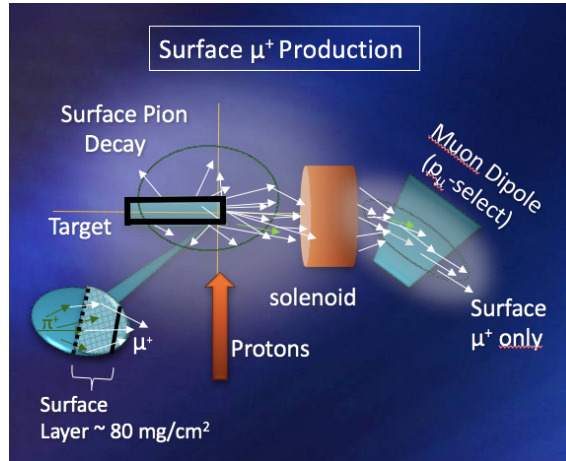
(c) Production of surface muons

Figure 1.6.: *Shown are the different types of muon beams. The figures were taken from [29].*

Decay muon channel : In order to reach high muon beam intensities, the produced pions are extracted and decay along a dedicated channel. Decay muons that are directed backwards in the pion rest frame can be well separated by the different momentum from the other beam components (π, μ in forward direction and e), which minimizes the background. A drawback of this method is that high energies are needed to have competitive rates and a long decay solenoidal channel is required to match the pion decay length $L_\pi = c\beta\gamma\tau_\pi$. By using this method muons from pions of either charge signs can be produced and typically show a high polarization $\sim$80 %. However, due to the higher momenta involved, thicker targets or degraders are required to cope with the larger range-straggling.

Cloud muon channel : Cloud muons are produced from pion decay-in-flight in the vincinity of the production target and therefore have a low polarization due to the wide angular acceptance of the channel. Competitive production rates necessiate high muon momenta. By selecting cloud muons, as in the case of πE5 e.g. for μ^- beams, a high beam correlated background is produced, especially at low momenta. However cloud muons, due to their generation, reflect the timing structure of the proton beam, which can be used for Time-Of-Flight (TOF) coincidence, or a Wien-filter is used to supress the background. The extended muon production volume leads to a larger phase space, which has to be challenged by a large acceptance beam line and as in the case of a decay channel, either by the use of a degrader or a thicker stopping target, due to the inherent higher momenta.

Surface muon channel : So-called "surface muons" are an optimal trade-off between a low momentum with a small range straggling and high muon beam intensities. Some of the pions stop ($p_{\pi^+} = 0$) near the target surface and decay at rest generating monochromatic and 100 % polarized surface muons with a momentum given by the two-body decay kinematics:

$$m_{\pi^+}c^2 = \sqrt{p_{\mu^+}^2 c^2 + m_{\mu^+}^2 c^4} + \sqrt{p_{\nu_\mu}^2 c^2 + m_{\nu^+}^2 c^4} \tag{1.17}$$

The neutrino mass is approximated to zero and together with momentum conservation

$$p_{\nu_\mu} + p_{\mu^+} = 0 \tag{1.18}$$

the muon momentum from a pion decay at rest is given by:

$$\rightarrow p_{\mu^+} = \frac{c}{2m_{\pi^+}} \left(m_{\pi^+}^2 - m_{\mu^+}^2 \right) = 29.79 \ MeV/c \tag{1.19}$$

The corresponding momenta of the muon and the neutrino are given by p_{μ^+/ν_μ} and the pion and muon masses by m_{π^+/μ^+}. Below the kinematic edge at 29.79 MeV/c the muon beam intensity scales with $p_{\mu^+}^{3.5}$ [27]. The muon momentum spectrum is given by the range spread of pion stops below the target surface and is superimposed by a contribution from cloud muons, that stem from pion decay outside the target volume [27]. The momentum distribution at the experimental setup is determined by the convolution of the initial momentum distribution and the momentum acceptance of the beam line. The surface muons show an isotropic angular distribution at production and therefore only the horizontal and vertical acceptance defines the transverse phase space volume at the end of the beam line.

1.3. High intensity muon beam lines at PSI

PSI provides an outstanding infrastructure for experiments that require low energy muon and pion beams. PSI hosts in total 7 secondary beam lines which transport daughter particles from 2 graphite production targets, that are hit by 590 MeV protons, to the experimental areas. An overview of the experimental areas is shown in figure 1.7. The proton
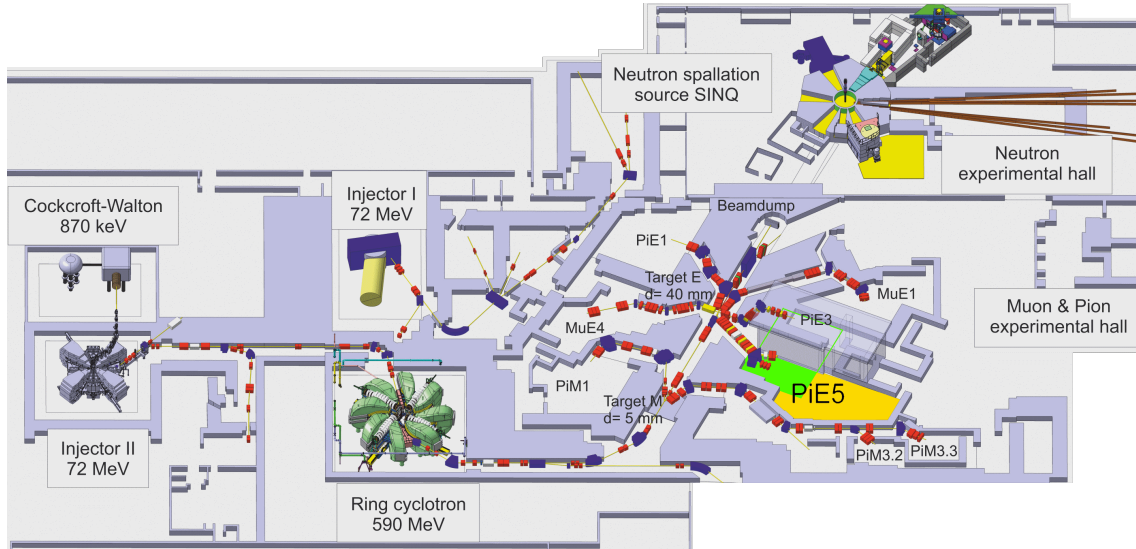

Figure 1.7.: *Overview of the PSI HIPA experimental hall and beam lines: The proton beam source is located on a platform on top of a Cockroft-Walton structure at 870 kV. From here the beam is transfered to the injector 2 sector cyclotron, where it is accelerated to 72 MeV. The protons are then transfered to the ring cyclotron which accelerates the protons to their final 590 MeV energy. After that the proton beam is deflected to the first muon production target M followed by TgE which provides the generated daughter particles to 5 different beam lines. Out of these, the πE5 beam line transports the produced particles to the experimental area that is used by MEG and will be the location for the MEG II and the Mu3e experiments. The residual ∼70 % of the proton beam is dumped in the "Swiss Neutron Source" SINQ [30].*

beam is provided by the HIPA [31] facility operating at currents up to 2.4 mA meaning 1.4 MW beam power. This outstanding beam intensity generates high rate secondary beams when passing the two production targets and provides surface muon rates exceeding 10^8 μ^+/s. Two different production targets, namely target M (thin target) and TgE (thick target), having different shapes and thicknesses, are in use. The different target shapes yield different production rates while the transmission and beam properties, such as momentum spread or transverse phase space, are given by the secondary beam lines, which view the targets under different angles. The users of the PSI secondary beam lines roughly subdivide into two groups. The Muon Spin Resonance (μSR) experiments use highly polarized positively charged muon beams to probe magnetic material properties under well-defined temperature and magnetic field conditions, while the particle physics community hosts a variety of experiments that make use of pion and muon beams of either charge sign.

There are two beam lines that provide surface muon rates higher than 10^8 μ^+/s, namely μE4 and πE5. The first one is dedicated to ultra-slow muon μSR, which makes πE5 to the most suitable beam line in the world for high rate particle physics experiments with muons.

There are plans by other projects [32, 33] to increase the maximum muon rates by orders of magnitude, though there is a qualitative difference as these are at pulsed accelerator facilities. As synchrotrons are used at these facilities to accelerate protons to energies of multiple GeV, the pulse repetition rates are much smaller than at the HIPA ring cyclotron and hence emphasis is placed on pulsed negative muon beams for $\mu \to e$ conversion experiments such as COMET [22] and Mu2e [23] since these are not rate limited as in the case of the coincidence experiments MEG II or Mu3e. The lifetimes in the laboratory rest frame of those pions, that decay at the production target surface, smear out the surface muon production. The 50 MHz beam structure of the HIPA ring cyclotron therefore generates a surface muon beam with an approximately flat time distribution, keeping the instantanous rate low, which is desired for coincidence experiments such as MEG II or Mu3e.

Currently πE5 is the only location that can provide sufficient beam intensity for MEG II and the first phase of Mu3e to reach the physics goals, hence necessiating the shared use of the πE5 experimental area by both experiments.

1.4. The Mu3e experiment

Mu3e, searching for the cLFV decay $\mu^+ \to e^+ + e^- + e^+$ with a final sensitivity of $\mathcal{O}\left(10^{-16}\right)$, was approved by the PSI committee in 2013 [3]. The collaboration consists of $\sim$30 phycisists from different institutes in Germany and Switzerland. Mu3e is expected to start with an engineering run in 2019.

1.4.1. The $\mu^+ \to e^+ + e^- + e^+$ signature and background contributions

In Mu3e surface muons are stopped in a hollow double-cone target and decay at rest at the centre of the Mu3e detector. Although the BSM physics mechanism, that could lead to signal detection, is not known the cLFV decay of a positively charged muon into 2 positrons and one electron puts several constraints on the signal:

- Momentum conservation requires the momenta of the outgoing positrons and the electron to sum up to zero: $0 = \sum_i p_i = p_{e_1^+} + p_{e^-} + p_{e_2^+}$

- As a further consequence of momentum conservation the tracks of the emitted $e^{+/-}$ have to be coplanar

- Stemming from the same reaction, the positrons and the electron have to be coincident in time and must have a common vertex

- The total energy has to sum up to the muon rest mass: $M_\mu c^2 = E_{e_1^+} + E_{e^-} + E_{e_2^+}$

There are two main kinds of background, that Mu3e has to deal with:

- Accidental background can be caused by the coincident detection of two positrons and an electron that stem from different decays but show similar characteristics in the detector to those mentioned above. The main source of background-like electrons is Bhabha scattering of decay positrons with electrons of the target material. A smaller contribution has to be expected from photon conversion and Compton scattering. In order to keep the number of produced electrons low, the stopping target material

Table 1.1.: *Envisaged properties of the final MuPIX chip for Mu3e*

Pixel dimensions	$80{\times}80~\mu\mathrm{m}^2$
Active area	$20{\times}20~\mathrm{mm}^2$
Cooling	He gas flow
Radiation length X/X_0	0.115 %
Data bandwith	1.25 Gbit/s

budget has to be minimized and a material with a low nuclear charge Z has to be chosen.

- Radiative muon decay with internal conversion $\mu^+ \rightarrow e^+ + e^- + e^+ + \bar{\nu}_\mu + \nu_e$ where the neutrinos have a very low momentum can mimic a clear signal and needs to be supressed by a good momentum resolution of the detector.

The background sources can be supressed by good vertex, timing and momentum resolution in the case of accidental background, whereas a false signal from radiatve muon decay with internal conversion can only be averted by a good momentum resolution. These limitations are to a great extent alleviated by means of the sophisticated design of the Mu3e setup.

1.4.2. The Mu3e detector

The search for $\mu^+ \rightarrow e^+ + e^- + e^+$ in Mu3e will be undertaken in a staged approach, which foresees an early commissioning phase Ia, data-taking in the πE5 area at PSI to reach an intermediate sensitivity of $\mathcal{O}\left(10^{-15}\right)$ called phase Ib and a phase II at a novel beam line not built yet, to further push the final sensitivity down by an additional order of magnitude. Figure 1.8 shows the different experiment configurations for the various phases. The setup is located at the centre of a superconducting solenoid with a warm bore diameter of 1 m and a total length of $\sim$3 m, which allows the momenta of the decay $e^{+/-}$ to be measured as well as providing focussing of the incoming muon beam. The inner diameter of the detector puts constraints on the muon beam which will be described in the next chapter. The individual subdetectors of Mu3e are summarized in the following.

1.4.2.1. The Mu3e pixel tracker

The key element of the Mu3e detector is the pixel detector, which consists of cylindrical arrangements of pixel modules, that are mounted on polyimide composite support structures, showing an overall minimum thickness. Each module consists of so-called High Voltage Monolithic Active Pixel Sensors (HV-MAPSs) [34] that are based on HV-CMOS technology, which allows Mu3e to implement the readout electronics directly on the chip. The version for Mu3e, called MuPIX [35], is thinned down to 50 micron, corresponding to an equivalent thickness $\sim$0.1 % X/X_0 radiation lengths. Figure 1.9 shows the MuPIX7 chip, that fullfils already most of the requirements for the Mu3e experiment. The MuPIX7 showed in test beams an efficiency $>$99 % and a timing resolution of 14.2 ns [35]. The final chips will be mounted on thin polyimide support structures and the specifiactions are shown in table 1.1. The MuPIX development is well underway and probably MuPIX10 will be the final version for the phase Ib of the Mu3e experiment.
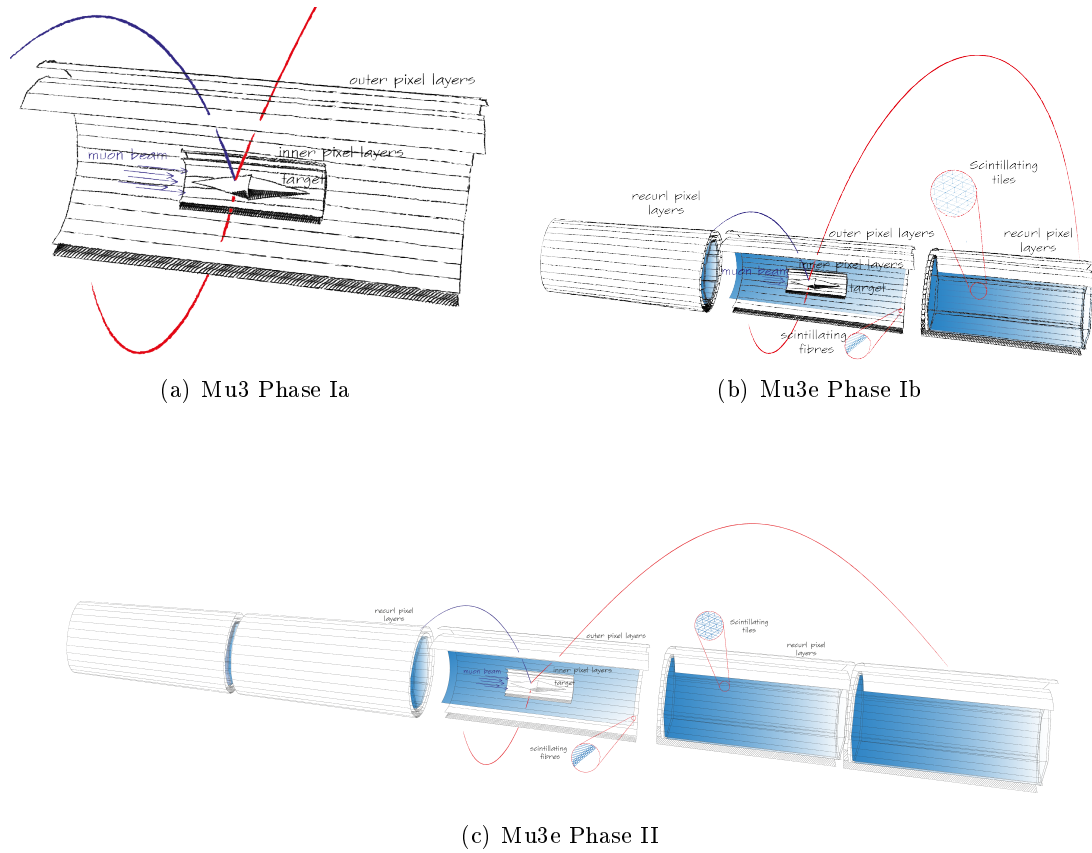
(a) Mu3 Phase Ia

(b) Mu3e Phase Ib

(c) Mu3e Phase II

Figure 1.8.: *[20] Shown are different stages of the Mu3e experiment. The commissioning phase Ia comprises only of the inner and outer central pixel layers and the hollow double cone target. Phase Ib has additional pixel modules on both sides in order to detect recurling $e^{+/-}$ and two subdetectors that provide precise timing information, namely the central thin scintillating fibres and the outer scintillating tiles on the inside of the outer pixel modules. For phase II the acceptance of the detector is further enhanced by adding two further recurl stations.*
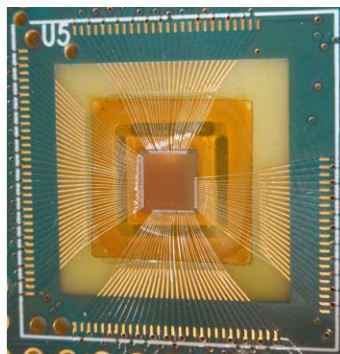

Figure 1.9.: *[20] Shown is the MuPIX7 chip with a thickness of 50 micron, a pixel size of 100×80 μm^2 and a total size of 0.3×0.3 cm^2.*

1.4.2.2. The Mu3e timing detectors

The timing information in Mu3e is taken from two different types of detector, that are based on organic scintialltors with a Silicon Photomultiplier (SiPM) readout.

Thin scintillating fibres between the inner and the outer pixel layers of the central pixel detector are expected to give timing information to better than 1 ns. On the inner side of the recurl station pixel layers thicker scintillating tiles provide timing information to better than 100 ps. The scintillating fibre detector has been studied in detail [36, 24] and prototype measurements with different fibres and claddings showed, that these goals can well be achieved. The fibre detector will be composed of ribbons made of three or four layers of 250 μm cladded scintillating fibres with a length of 30 cm. The fibres are read out from both ends with SiPM from Hamamatsu and the signals are processed with the MuTRIG chip based on the SiPM Timing Chip (STiC) [37] design. The fibre detector layout is shown in figure 1.10
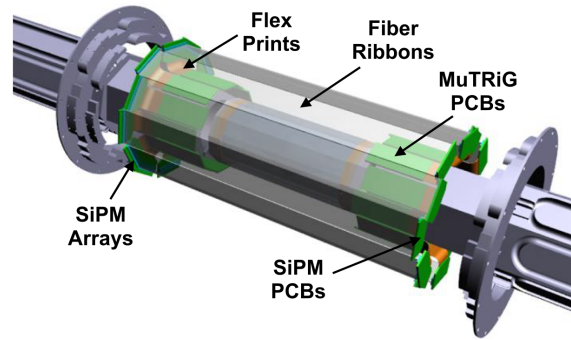

Figure 1.10.: *Shown is the layout of the fibre detector. The figure was taken from [24].*

The scintillating tiles placed in the recurl stations at both ends of the Mu3e detector are planned to have a timing resolution of less than 100 ps and tests with a prototype have shown, that a resolution of 56 ps could be achieved in the best case [38]. The tiles are made of 6.5×6.5×5 mm^3 BC418 scintillator and are arranged in submodules of 4×4 individual tiles that are again grouped in 14 to a module, shown in figure 1.11. The tile detector has an efficiency close to 100 %.

1.4.2.3. The Mu3e Data Acquisition (DAQ) system

Mu3e DAQ is made in a triggerless way, in which the individual detectors continuously send zero-supressed hit information to the DAQ system. The overall readout scheme is shown in figure 1.12, whereby the number of channels still may vary in the final version of the detector. All hits in the detector are assigned with a timestamp and are sent to the front-end Field Programmable Gate Arrays (FPGAs), where they are collected and ordered into readout frames of 50 ns length. The following switching boards merge the recieved information and forward it to a PC filter farm for further processing, such as event-building, application of cuts and fitting algorithms. The processed data is finally stored by the Maximally Integrated Data Acquisition System (MIDAS) [39] system, where it is combined with additional information from the slow-control system online database.
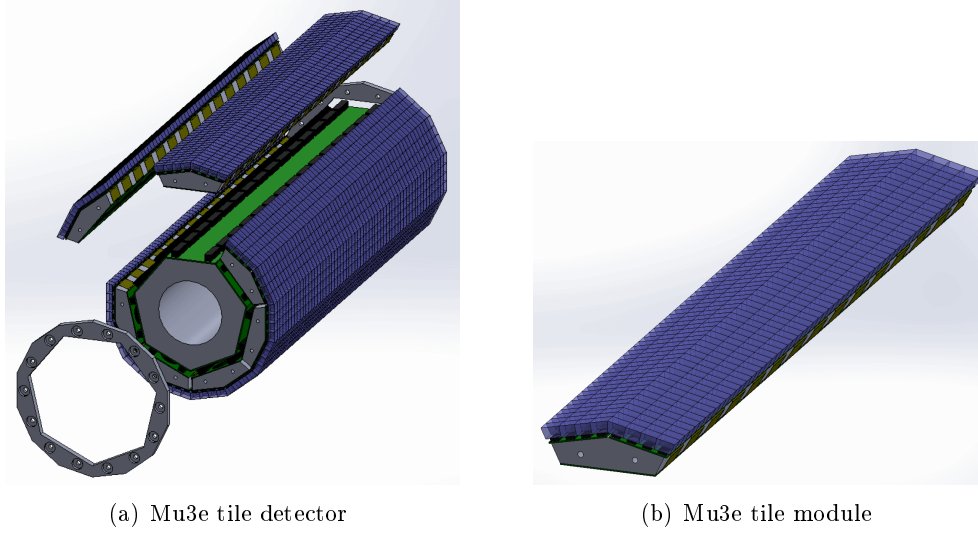
(a) Mu3e tile detector

(b) Mu3e tile module

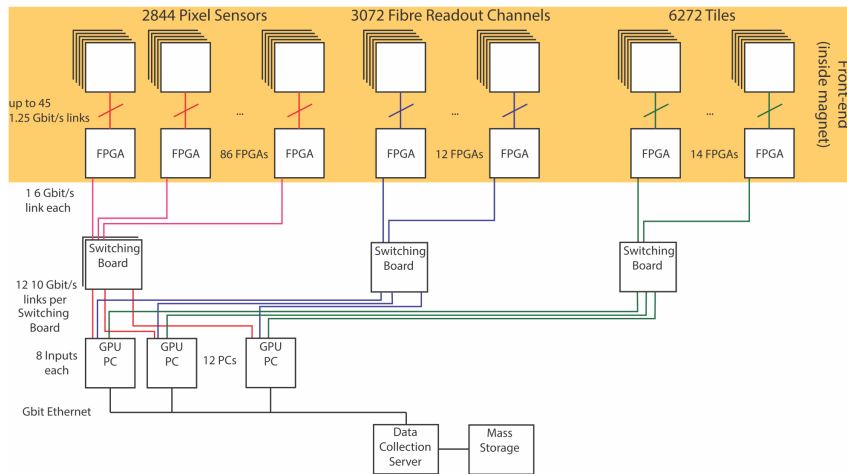**Figure 1.11.:** *[20] Shown is the Mu3e tile detector and one of its modules.*

Figure 1.12.: *[20] The Mu3e DAQ system works without a hardware trigger.*

1.4.2.4. The Mu3e Target and Magnet

The current target design consists of thin Mylar foils, that are glued together to form a hollow double cone with a radius at the centre of 19 mm and an overall length of 100 mm. The Mylar thickness on the upstream (US) side is 75 μm and 85 μm on the downstream (DS) side. This shape gives an optimal spreading of decay vertices and the difference in US and DS thickness ensures a homogeneous occupancy of the inner tracking detectors.

The magnet, that will be used to derive the momentum information of the decay products is a 1 m warm bore diameter superconducting solenoid with a length of approximately 3 m and a central magnetic field of 1 T. The outer dimensions of the solenoid are governed by the physics case of the experiment and are just sufficient to fit into the experimental area given by the specially designed short CMBL. Unfortunately the initial design by a first company led to a canceled contract but a new tendering process has been started and the magnet is expected to be available for Mu3e in 2019.

The phase II setup of Mu3e necessiates a completely new beam with an intensity of $\mathcal{O}\left(10^9\right)$ $\mu^+/$s, which is envisaged to be achieved with the High Intensity Muon Beam (HiMB) project [40, 41] at PSI. For the initial commissioning and phase I data-taking only the πE5 area at PSI is capable of delivering the required muon rates. The beam line for Mu3e is the topic of the next chapter.

1.5. The MEG II experiment

In 2016 the currently most stringent upper limit on the branching ratio $BR\left(\mu^+ \rightarrow e^+ + \gamma\right)$ $\leq$4.2·10^{-13} was set by the MEG experiment at 90 % confidence level [6]. As the data analysis of MEG is finished the old setup is not explained here, but a detailed description of the MEG setup can be found in [42].

In 2013 the proposal of the MEG II experiment was accepted by the PSI commitee [4]. Compared to MEG all subdetectors have either been completely replaced or upgraded which together with a new Radiative Decay Counter (RDC) subdetector allows for a ~10 times improved sensitivity aiming at $\sim 4 \cdot 10^{-14}$.

In MEG II, as formerly in MEG, an incoming beam of surface muons is stopped in a thin slab target located at the centre of the COnstant Bending RAdius solenoid (COBRA) magnet.

1.5.1. The experimental signature of $\mu^+ \rightarrow e^+ + \gamma$ and background contributions

The $\mu^+ \rightarrow e^+ + \gamma$ decay at rest has a clear experimental signature which is characterized by the two-body decay kinematics:

- Momentum conservation leads to a back-to-back emission of the outgoing γ and e^+

- The energy of both, the positron and the γ, amount to half the muon rest mass $m_{\mu^+}/2$=52.83 MeV

- Common vertex of the positron and photon on the stopping target

- Coincidence in time

The main physics background in the search for this decay mode stems from radiative muon decay $\mu^+ \rightarrow e^+ + \gamma + \nu_e + \bar{\nu}_\mu$, which can mimic a signal in the case of small neutrino momenta, this is linearly dependent on the muon rate. To overcome this kind of background an accurate measurement of the energies of the positron and the photon is essential. However, the main limitation of the experiment in terms of background is due to random coincidences from high energy Michel positrons and photons mainly from annihilation-in-flight (AIF), Bremsstrahlung and radiative muon decay, this background is quadratically dependent on the muon rate. The contribution from AIF will be kept low, compared to MEG, due to a minimized material budget introduced by the new drift chamber system. In order to identify high energy γs from radiative muon decay a new RDC detector is introduced that detects low energy positrons that accompany this decay mode.

1.5.2. The MEG II detector

Figure 1.13 illustrates the main features of COBRA and the subdetectors that are essential for the tracking of the positrons. The muon beam in this figure enters from the right and is stopped in the target at the centre of COBRA. The Liquid Xenon (LXe) calorimeter to detect the γs is shown in figure 1.14 together with a visualization of a $\mu^+ \rightarrow e^+ + \gamma$ event. The main aspects of the individual subdetector componenets are outlined below.
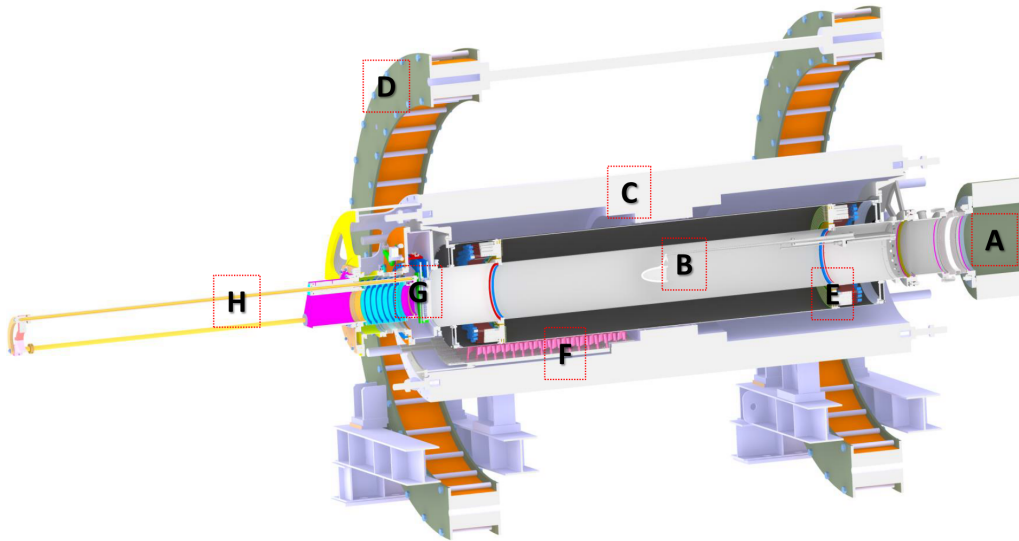
Figure 1.13.: *Shown is a cut view of the MEG II detector without the γ-calorimeter.*
A: The BTS is the last part of the MEG beamline US of the detector
B: The stopping target is mounted on a pneumatic movable arm
C: The cryostat of the COBRA spectrometer magnet (inner parts not visible here)
D: Compensation coils to reduce the magnetic field outside of COBRA, in the vincinity of the calorimeter
E: 1.8 m long drift chamber - right at the marker the endplate can be seen on which the wires are fixed
F: The DS TC tiles are shown in pink (the US part is not visible in the model)
G: DS part of the RDC counter that can be moved out of the beam during C-W calibration runs
H: Insertion system that can be moved inside COBRA for dedicated calibration runs
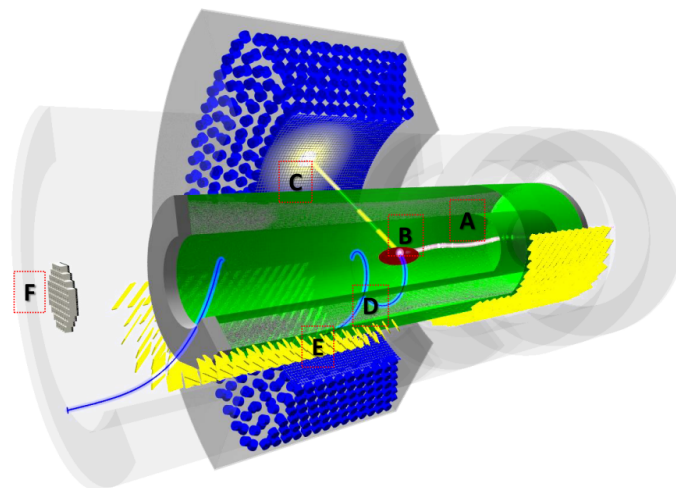*(The CAD Model was provided by Dieter Fahrni)*

Figure 1.14.: *[43] A muon (depicted as A) coming in from the right is stopped in the target (B). The decay γ is emitted in the direction of and produces scintillation light in the LXe calorimeter (C). The decay positron that is emitted back-to-back with respect to the photon follows a helical path in the solenoidal field and passes the CDC (D) and TC (E). The DS RDC counter recieves no hit.*

1.5.2.1. The MEG II cylindrical drift chamber

The positron momentum, angle and vertex reconstruction relies on a new highly sophisticated single volume cylindrical drift chamber consisting of ~1200 20 μm thick gold-plated tungsten sense wires and ~6400 40 μm thick silver-plated aluminum field wires. The wires are fixed on the endplates attached to a 1.8 m long carbon fibre cylinder at the centre of the COBRA magnet. The wires are mounted with alternating stereo angles which provides high resolution track information by employing information from adjacent planes. The single-volume design of the CDC together with a low-Z gas mixture (90 % He & 10 % iso-butane) reduces the material budget below $1.7 \cdot 10^{-3} X_0$, thereby minimizing the multiple scattering which has a positive effect on the envisaged detector resolution. The inner radius of the CDC amounts to 18 cm which restricts the number of positron hits to higher momenta. The wiring of the drift chamber is done in an automated way and figure 1.15 shows an intermediate status of the drift chamber production. The envisaged
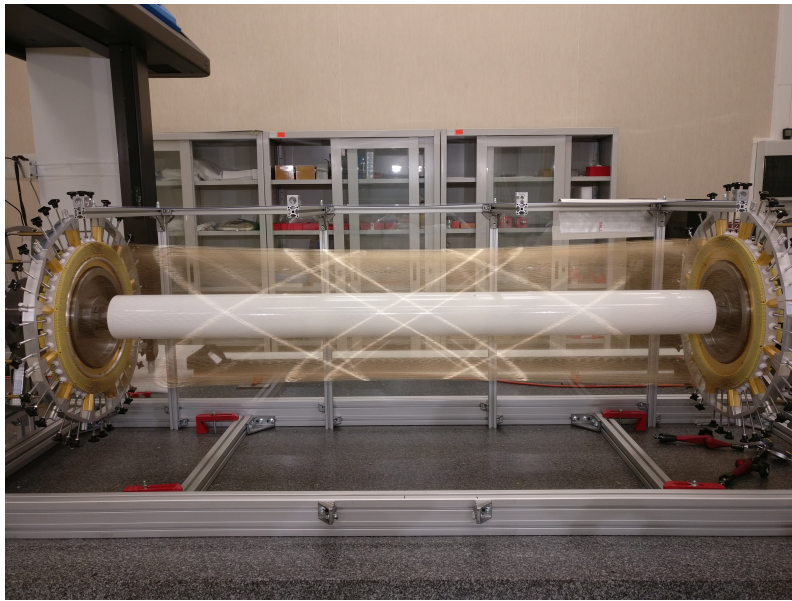

Figure 1.15.: *[43] Shown is the production status of the MEG II CDC with approximately 50 % of the final ~1200 sense wires and ~6400 field wires being installed. The picture was provided by Marco Chiappini.*

resolution for the MEG II CDC is 130 keV/c for the positron momentum and 5.3/3.7 mrad in the polar/azimuthal angle. The envisaged overall efficiency should be ~70 %.

1.5.2.2. The MEG II Timing Counter

The positron timing information to match with the photon timing is provided by the new tile TC subdetector. The timing counter consists of two half barrel shaped support structures, one on the US and one on the DS side of COBRA, both together holding 512 scintillating tiles with attached MPPCs as shown in figure 1.16(a). The TC tiles, shown in figure 1.16(b), consist of $H : 40/50mm \times W : 120mm \times T : 5mm$ BC422 plastic scintillators that are read out from both sides by SiPMs from Hamamatsu. Together with a dedicated
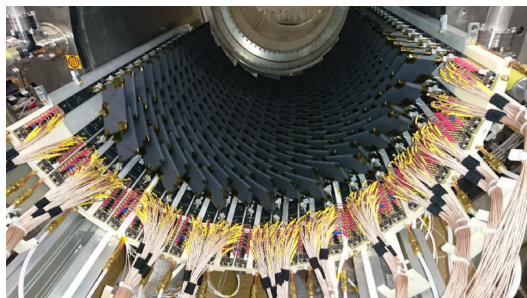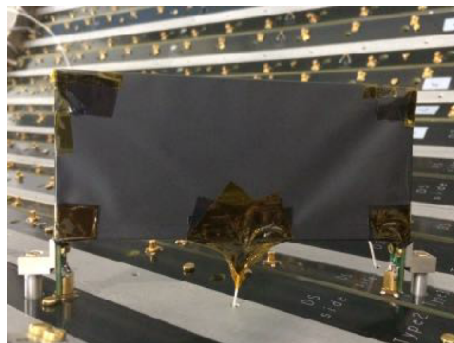
(a) The MEG II timing counter (b) Single scintillating tile

Figure 1.16.: *[43] Shown is the pixelated Timing Counter of MEG II. The left picture shows the installed DS half of the full detector. The right picture shows one of the tiles.*

laser calibration system, coupled with fibres to the bottom of each tile a timing resolution of ~31.5 ps has been confirmed in the 2015 and 2016 MEG II Pre-engineering runs [44], compatible with the design value of 30 ps. The improved time resolution allows for a better pile-up rejection and a reduction of the coincidence window.

1.5.2.3. The COBRA magnet

The COBRA magnet, shown in figure 1.17, is a thin walled superconducting magnet made up of one central coil and symmetrically arranged gradient coils and endcoils in a helium-free cryostat, that has already been used for MEG. The diffferent inner coil types generate a gradient field, shown in figure 1.18. The gradient field has maily two effects: The bending radius of the decay positrons depends on their momentum and only slightly on the emission angles, which led to the naming of the magnet, this has the effect that the e^+ radius is essentially dependent on p_{tot} rather than p_T allowing a radius cut to select p. Furthermore, positrons emitted at angles close to 90° are swept out of the COBRA volume quicker than in an equivalent homogenous field. This results in a reduction of pile-up events. The thin cryostat walls and the cryogen-free design together with the thin coils ensure a minimum material budget of 0.197 X_0 within the acceptance of the photon calorimeter, which minimizes the interaction of decay γs before reaching the LXe calorimeter outside the COBRA volume.

1.5.2.4. The MEG II LXe calorimeter

The photon calorimeter is a C-shaped, single volume γ-detector placed close to the centre of the COBRA magnet. The inner cryostat volume is filled with ~900 l LXe. Photons stop in the LXe and the scintillation light is detected by the surrounding photo detectors, which allows the γ-energy, -position, -direction and precise timing information to be extracted. For the upgrade of the calorimeter the PMTs that were mounted on the entrance face, were replaced with newly developed SiPMs from Hamamatsu that are capable of detecting the scintillation light from LXe in the UV-range. The LXe volume itself has been increased by
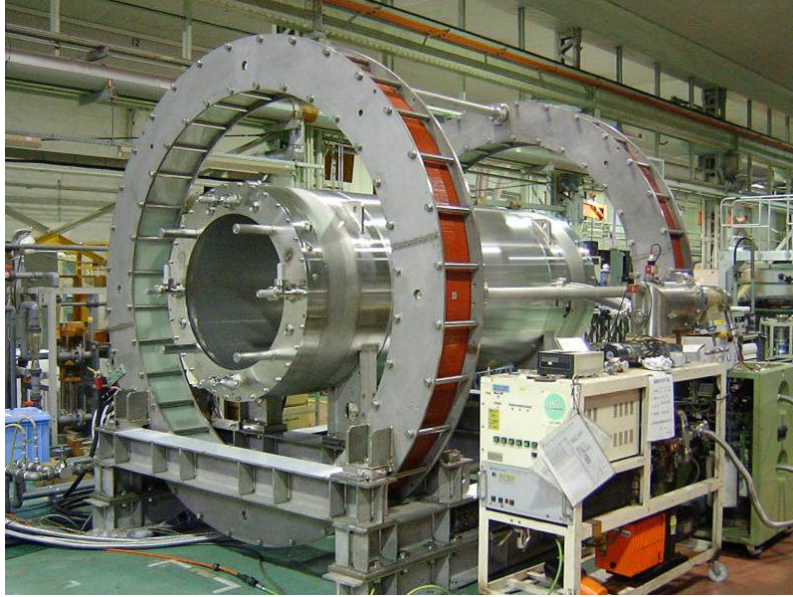
Figure 1.17.: *Shown is the COBRA magnet. The thin-wall cryostat contains the superconducting coils, that generate a gradient field along the axis, ranging from 1.27 T at the centre to 0.49 T at both ends of the cryostat. The normal-conducting compensation coils on both ends suppress the fringe fields outside of the COBRA volume for a proper operation of the LXe calorimeter PMTs.*
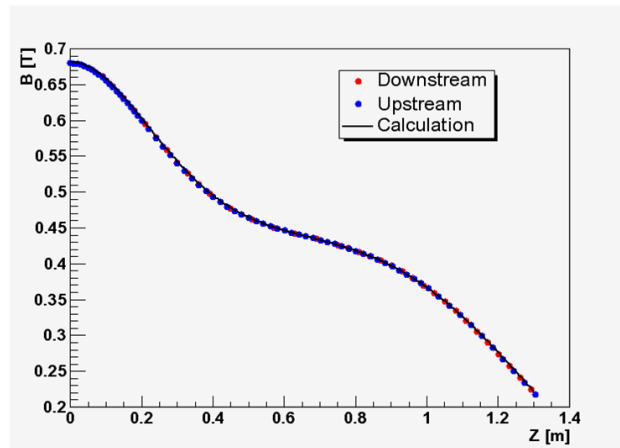

Figure 1.18.: *[43] COBRA field distribution*

redesigned side walls of the PMT and SiPM support structure. The higher granularity and larger fraction of the active area leads to improved time and spatial resolutions especially for events with shallow conversion depths [45]. The upgrade of the LXe calorimeter is almost completed, see figure 1.19, and liquefication of the Xenon has been started to prepare for the first tests.
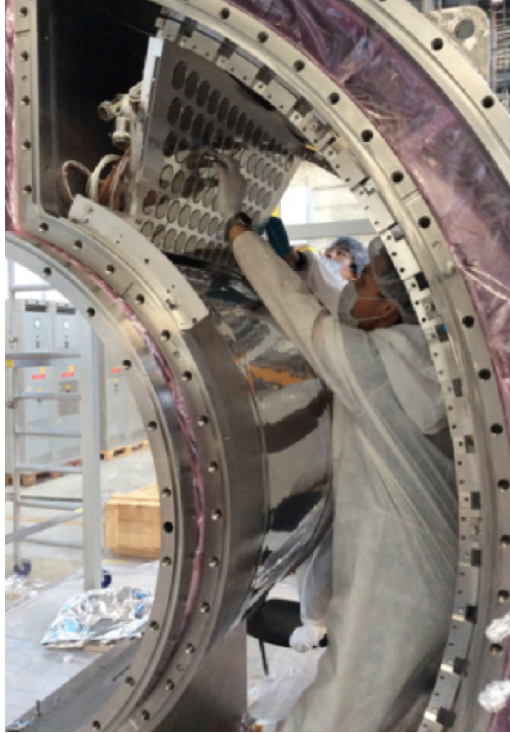

Figure 1.19.: *[43] Shown is the replacement of the inner layer PMTs with dedicated SiPMs from Hamamatsu, which has already been finished.*

1.5.2.5. The MEG II Radiative Decay Counter detector

As outlined above accidental background can arise from photons, that are close to the signal energy and detected in the LXe calorimeter. Figure 1.20 (taken from [42]) summarizes the background contribution from AIF, cosmic muons and radiative muon decay for the MEG version of the LXe calorimeter. It can be seen, that the contribution from RMD is dominant in the signal region. Therefore a new RDC counter has been developed that counts low-energy positrons close to the beam axis on the US and the DS side of COBRA.
High energy γs from RMD restrict the energy of the outgoing positrons to be low (typical between 1-5 MeV). These low energy e^+ [46] cannot be detected by the CDC due to their small bending radius in the solenoidal field. In case of an event detected by the RDC counters a possible associated γ seen in the LXe calorimeter is tagged for the MEG II analysis. A possible US RDC counter is under investigation, as a thin 1 layer ribbon of BCF-12 scintillating fibres read out by SiPMs. Literature (see section 3.1.2) and the results of the 2016 Pre-Engineering run imply significant signal degradation for such a fibre counter that cannot be compensated for during the run. Therefore a radiation damage
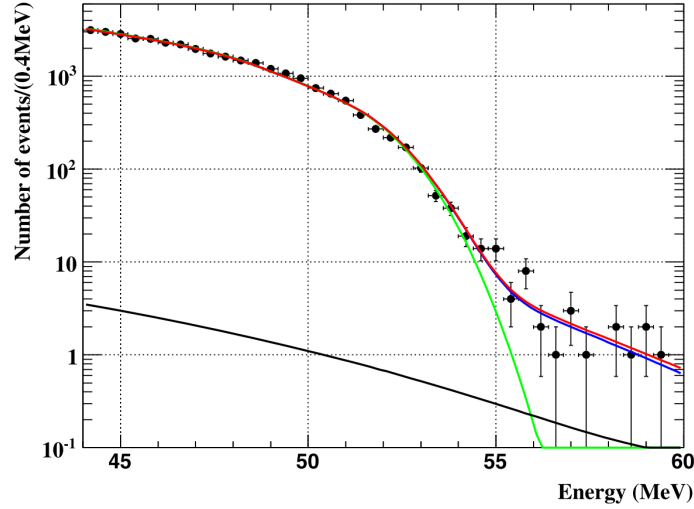
Figure 1.20.: *Shown is the background in the LXe calorimeter that was determined for the MEG setup: Green: RMD only*
Blue: AIF + RMD
Black: Cosmics
Red: Combination of all previous

test is scheduled for 2017 and new designs based on thin diamond detectors are being investigated. However, the design of the DS detector, which is exposed to much lower radiaition dose rates, is finished and a working detector prototype was also tested in 2016.

1.5.2.6. MEG II electronics and DAQ

The MEG II electronics and DAQ concept is mainly based on the novel Waveform DRS4 based Readout Module (WaveDREAM) [47] board. The WaveDREAM crates provide Multi-Pixel Photon Counter (MPPC) high-voltage, variable gain signal amplification and waveform read-out with the Domino Ring Sampler version 4 (DRS4) [48]. A Trigger Concentrator Board (TCB) combines the trigger information from up to 16 WaveDREAM boards each with 16 channels and provides output to a global trigger. The so-called Data Concentrator Board (DCB) enables a pre-processing of the waveforms and outputs the data via GBit ethernet therefore allowing for high DAQ rates. The number of channels in the MEG II experiment increases from ∼3000 (MEG) to 8544 channels which reflects the higher granularity and additional detector components.
The slow-control system is mainly based on SCS2000 [49] and newly developed SCS3000 which can be equipped with dedicated analog-to-digital converter (ADC) and digital-to-analog converter (DAC) boards, which fulfill the requirements of having many channels, stable operation and can be directly adressed by the MIDAS software package that is used for MEG II.

1.5.2.7. The MEG II beam line and stopping target

The enhanced detector resolutions and the higher granularity of the subdetectors lead to a significantly improved pile-up rejection. This enables MEG II to accept a design stopping

rate of $7 \cdot 10^7$ μ^+/s. Due to the finite fraction of muons that are stopped in the target this means, that MEG II will run close to the intensity maximum that can be provided by the beam line, that is shown in figure 1.21. More detailed information on the πE5 beam line
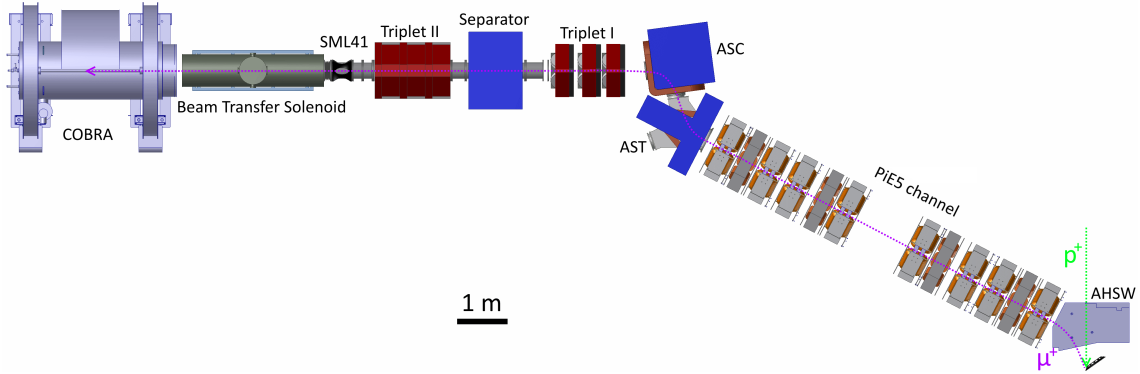

Figure 1.21.: *The beam for MEG is generated at the production target TgE in the proton beam channel. From here it is transported through the πE5 channel, which consists of quadrupole and sextupole magnets. A double bend at the end of the channel deflects the beam towards the reference axis of MEG II. Two quadrupole triplets ensure a good transmission and separation in the Wien filter type particle separator. After passing a collimator system the beam is transported with an air-core solenoid, called BTS, to the MEG II stopping target in the centre of the COBRA magnet.*

is given in the next chapter.

A part of the challenging upgrade also inlcudes the new version of the stopping target, which is foreseen as a thin organic scintillator on a Polyvinyltoluene (PVT) basis. This provides online beam monitoring capabilities allowing careful cross-checks of the MEG II beam properties and speeds up the beam setup period, leaving more time for data-taking in MEG II. The studies that were undertaken for the scintillation target are presented in chapter 3.

In summary almost all subdetectors of MEG II have finished their design phase and are in the state of being assembled. Only the US RDC might necessiate a redesign for radiation damage considerations. MEG II is about to have a fully equipped Engineering Run beginning in 2018 followed by performance data-taking for the remaining part of the year.

2. The Compact Muon Beam Line CMBL

2.1. Mu3e beam line requirements

The continuous high intensity surface muon beam provided by the πE5 channel at PSI can deliver rates of the order of $\mathcal{O}\left(10^8\right)$ μ^+/s and higher rates can be expected from upgrade plans for the High Intensity Proton Accelerator (HIPA) facility in the future. This pre-destines πE5 as the only place in the world to optimally carry out the cLFV experiments MEG II and Mu3e, which both require high muon statistics as well as a continuous muon beam, which ensures a lower instantaneous muon rate compared to a pulsed beam, extremely important for a coincidence experiment where the accidental background can scale as the square of the beam intensity.

The sensitivity requirements for both MEG II and Mu3e demand similar beam properties:

- A continuous surface muon beam with a central momentum of 28 $\frac{MeV}{c}$, yielding the maximum surface muon rate

- A high transmission optics, minimizing the beam losses in the beam line elements and a high rate at the experiment

- A small momentum byte, which keeps the range straggling at the stopping target to a minimum (although the major contribution comes from the central momentum) and reduces the beam size contribution from dispersion

- A small and achromatic beam spot on the stopping target, to allow for a small target as in Mu3e and to ensure a maxmimum acceptance of the detector

- Minimization of beam related background, such as e^+, π^+ from the production target with equal momentum as the muons

- Selection of different particle types and momenta for calibration purposes, such as 53 MeV/c positrons to perform a Mott scattering alignment analysis, or a π^- beam for Charge Exchange (CEX) calibrations in MEG II

The realization of the Mu3e beam line in πE5 is made more diffcult by the fact that the MEG experiment with its large and fixed infrastructure will continue data-taking in πE5 after its upgrade programme to MEG II is completed. This restricts the available space for the Mu3e setup to the front area of πE5, which is partially covered by the floor of the above πE3 area (see figure 1.7). The Mu3e main components include the $\approx$ 3 m(length)×2m(width)×2.5m(height) spectrometer solenoid, housing the target and the detectors, infrastructure components and the beam line elements of the CMBL that couple Mu3e to the existing πE5 beam line. In addition, a concrete wall placed between the front and the rear side of the experimental area further limits the available space. The concrete wall provides the means to carry out work on MEG II that does not require the muon beam, such as setup work, calibrations, or independent physics data taking with the MEG

C-W accelerator, e.g. searching for a fifth force signal [50], while Mu3e is running. The limited space and access puts stringent constraints on the beam line layout and the choice of magnets and requires a challenging beam line design to cope with these restrictions. This leads to the following further requirements:

- Match the spatial constraints imposed by the front area walls and installed equipment
- Feasibility to setup the beam line, which mostly affects the elements that are positioned below πE3
- Minimum switch-over time between the MEG II and the Mu3e setup
- Use of spare existing elements in order to a) keep the beam line costs low b) make use of existing well-proven technology without time-consuming magnet design. Here, either direct usage of beam elements placed in storage or their modification was first considered before the design of a new element.

A careful alignment is of utmost importance and an accurate CAD model of the area was generated at the beginning, based on drawings and refined by measurements with a laser distance measurement device. Further high precision alignment data was provided in 2016 by the PSI survey group. Each step of the beam optics design process had been checked against the CAD model to garantuee a matching of the spatial constraints.

A solution consistent with the above mentioned requirements was found in the CMBL design and figure 2.1 shows a CAD model of the Mu3e beam line and the experimental area. The elements close to the MEG II detector hut and partially covered by the concrete
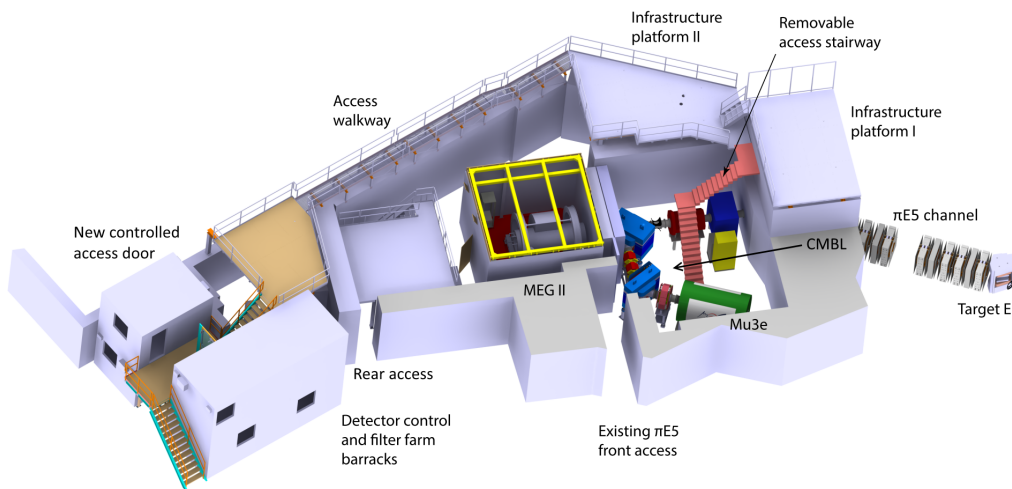

Figure 2.1.: *Shown is a CAD view of the $\pi E5$ area.*

shielding overhang of the walls, have to be positioned as close as only a few centimetres to the wall. Furthermore, the Mu3e spectrometer solenoid, shown in green, leaves not more than a gap of $\approx$ 40 cm to the wall, which necessiated a new area access that is shown in the same model. The minimum invasive switch-over between the MEG II and the Mu3e setup is illustrated in figure 2.2.

The beam line design process, test beam comissioning and optimization of the beam line setup is described in the remainder of this chapter.
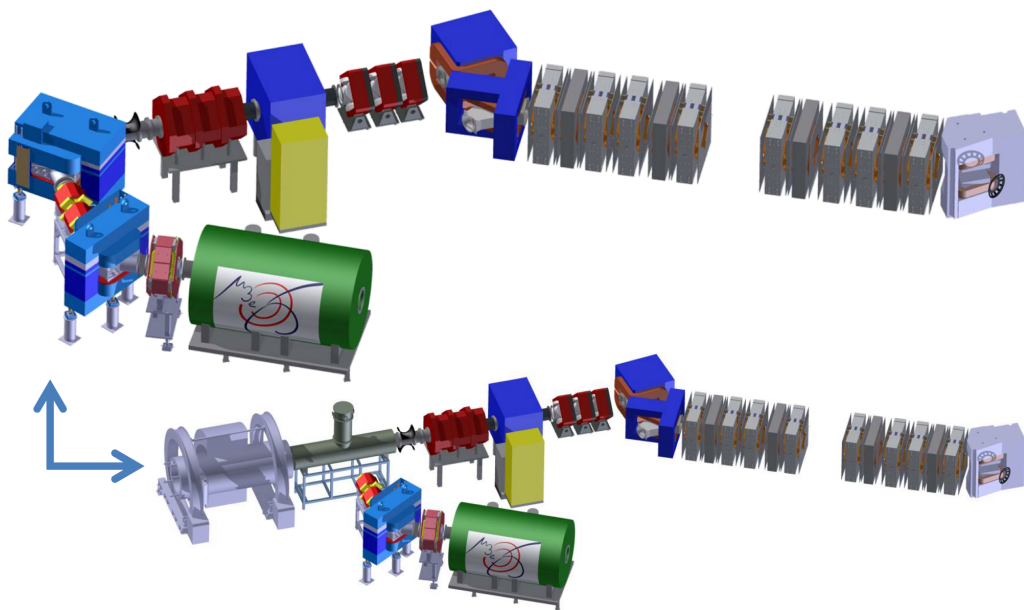
Figure 2.2.: *Switch-over between the Mu3e and the MEG II setups can be done by removing a concrete shielding wall and replacement of a bending magnet of the CMBL with the BTS of MEG II.*

2.2. Beam line design tools

There are two main approaches to carry out beam optical calculations, transport matrix formalism, which splits into single particle tracking or beam envelope propagation and fieldmap based particle tracking that propagates particles stepwise through continuous field distributions. The software codes that are used for the design of the CMBL are:

- TRANSPORT (A computer program for designing charged particle beam transport systems) [51], based on transport matrices, calculates the propagation of the beam matrix σ and provides graphical and ascii form output of the beam envelopes and the phase space ellipses after each element. Fast fitting routines to match first- and second-order constraints are implemented.

- TURTLE (Trace Unlimited Rays Through Lumped Elements) [52] is a transport matrix based tracking algorithm. A built-in Monte-Carlo (MC) generator produces particles that are individually propagated through the beam line. The implementation of apertures reflects the beam constraints introduced by real beam line elements. TURTLE also provides a simple implementation of physics processes such as particle decay and scattering. TURTLE uses the same syntax as TRANSPORT which simplifies the complementary use of both codes, making use of the fitting algorithms and envelope outputs from TRANSPORT with subsequent tracking to investigate aperture losses using TURTLE.

- G4BL [5] is a modern particle tracking software based on Geant4 [53]. Although versatile applications, that make use of the sophisticated Geant4 physics packages, are possible, the well accessible syntax for the in- and output focusses mainly on beam line design. Initial particles can either be generated with a built-in MC generator as in TURTLE or read from a file. The particle tracking is done stepwise through fieldmaps that define B-fields and E-fields at each step.

- Mathematica [54] based first-order transport matrix calculations were implemented for the phase space reconstruction based on profile measurements

2.2.1. Transport Matrix formalism

In particle accelerator modeling locations and velocities are conveniently given in the Frenet-Serret coordinate system which is based on right-handed orthonormal unit vectors, whereby the origin is moved with the reference particle along the reference orbit - see figure 2.3. Therefore the state vector $\vec{r}$ of a particle is given by:
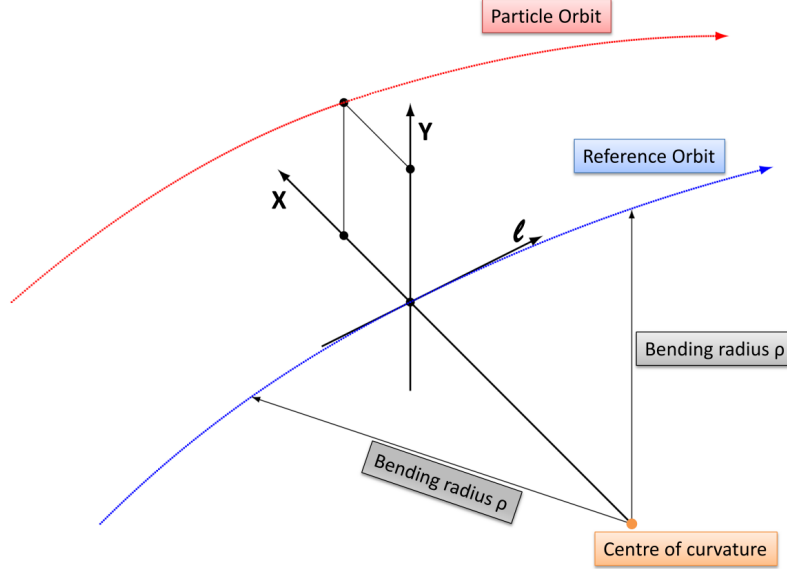

Figure 2.3.: *Shown is the Frenet-Serret coordinate system. The figure has been adapted from [55].*

$$\vec{r} = \begin{pmatrix} x \\ \theta \\ y \\ \phi \\ l \\ \delta \end{pmatrix} \quad \text{with:} \quad \begin{aligned} &x : \text{horizontal offset from the reference orbit (cm)} \\ &\theta : \text{horizontal angular deviation from reference orbit (mrad)} \\ &y : \text{vertical offset from the reference orbit (cm)} \\ &\phi : \text{vertical angular deviation from reference orbit (mrad)} \\ &l : \text{longitudinal offset from the reference particle (cm)} \\ &\delta : \text{momentum deviation } \delta = \frac{p - p_0}{p_0} \ (\%) \end{aligned} \qquad (2.1)$$

A variety of input definitions is used in common literature and software codes. The units above are used in the transport matrix codes TRANSPORT [51] and TURTLE [52] by default. The reference momentum is given by p_0 and the individual particle momentum in the longitudinal direction by p, which equals the total particle momentum in the paraxial approximation. The angles θ and ϕ are also defined in paraxial approximation, for small transverse velocities compared to the longitudinal velocity. This allows the equations of motion to be rewritten in the presence of magnetic and electric fields without time dependence. The example of a magnetic quadrupole and a particle with mass m and charge q is given below:

$$\gamma m \ddot{\vec{r}}(t) = q \cdot \vec{E} + q \cdot \vec{v} \times \vec{B} \qquad (2.2)$$

$$= q \begin{pmatrix} v_y B_l - v_l B_y \\ v_l B_x - v_x B_l \\ v_x B_y - v_y B_x \end{pmatrix} \quad , v_y B_l \ll v_l B_y \text{ and } v_l \approx v_0 \gg v_x, v_y \qquad (2.3)$$

$$\rightarrow \gamma m \ddot{x}\left(t\right) = -q \cdot v_0 \cdot B_y \quad , B_y = g \cdot x \text{ with the constant field gradient } g = \frac{\partial B_y}{\partial x} \quad (2.4)$$

$$\rightarrow \ddot{x}\left(t\right) + \frac{q v_0 g}{\gamma m} x\left(t\right) = 0 \tag{2.5}$$

$$\rightarrow \ddot{x}\left(t\right) + \frac{g q v_0^2}{p} x\left(t\right) = 0 \tag{2.6}$$

For small transverse velocities the pathlength s of a particle after time t is given by:
$s\left(t\right) = v_0 \cdot t$

$$\rightarrow \dot{x}\left(t\right) = \frac{dx}{dt} = \frac{dx}{ds}\frac{ds}{dt} = x'\frac{d(v_0 \cdot t)}{dt} = v_0 \cdot x'\left(s\right) \text{ and } \ddot{x} = v_0^2 x'' \tag{2.7}$$

$$\rightarrow x''\left(s\right) + \frac{g}{\frac{p_0}{q}} x\left(s\right) \tag{2.8}$$

$\frac{p}{q} = B\rho$ is called the magnetic rigidity of the beam. The strength for a horizontal focussing quadrupole is therefore defined with the B-field at the pole tip $|B_0|$ and the pole tip radius a as $K = \frac{|B_0|}{a}\frac{1}{p_0}$. This yields:

$$x\left(s\right) = \cos\left(\sqrt{K}s\right) \cdot x\left(0\right) + \frac{1}{\sqrt{K}} \sin\left(\sqrt{K}s\right) \cdot x'\left(0\right) \tag{2.9}$$

$$x'\left(s\right) = -\sqrt{K} \sin\left(\sqrt{K}s\right) \cdot x\left(0\right) + \cos\left(\sqrt{K}s\right) \cdot x'\left(0\right) \tag{2.10}$$

$$\text{Analogue calculation for the vertical direction yields:} \tag{2.11}$$

$$y\left(s\right) = \cosh\left(\sqrt{K}s\right) \cdot y\left(0\right) + \frac{1}{\sqrt{K}} \sinh\left(\sqrt{K}s\right) \cdot y'\left(0\right) \tag{2.12}$$

$$y'\left(s\right) = \sqrt{K} \sinh\left(\sqrt{K}s\right) \cdot y\left(0\right) + \cosh\left(\sqrt{K}s\right) \cdot y'\left(0\right) \tag{2.13}$$

The propagation of a single particle from its initial state $\vec{r}(0)$ to the final state after a pathlength s is then given by $\vec{r}(s)$:

$$\vec{r}(s) = R \cdot \vec{r}(0) \tag{2.14}$$

with R being in this particular example the transport matrix of the quadrupole.

$$\begin{pmatrix} \cos\left(\sqrt{K}s\right) & \frac{1}{\sqrt{K}}\sin\left(\sqrt{K}s\right) & 0 & 0 & 0 & 0 \\ -\sqrt{K}\sin\left(\sqrt{K}s\right) & \cos\left(\sqrt{K}s\right) & 0 & 0 & 0 & 0 \\ 0 & 0 & \cosh\left(\sqrt{K}s\right) & \frac{1}{\sqrt{K}}\sinh\left(\sqrt{K}s\right) & 0 & 0 \\ 0 & 0 & \sqrt{K}\sinh\left(\sqrt{K}s\right) & \cosh\left(\sqrt{K}s\right) & 0 & 0 \\ 0 & 0 & 0 & 0 & 1 & \frac{s}{\gamma^2} \\ 0 & 0 & 0 & 0 & 0 & 1 \end{pmatrix}$$
$$\tag{2.15}$$

The propagation through other elements is calculated in a similar way, but with different transport matrices for the different elements. An arrangement of successive optical elements in a beam line, the so-called lattice, can therefore be described by:

$$R_{lattice} = R_n \cdot R_{n-1} \cdot ... \cdot R_1 \tag{2.16}$$

where the R_k are the transport matrices of the successive elements in reverse order. The matrices for other elements can be derived as shown above or found in literature e.g. [56, 57]. The length of elements in matrix code is defined by their so-called effective length l_{eff}:

$$l_{eff} = \frac{1}{B_0} \int_{-\infty}^{\infty} \vec{B} \vec{dl} \tag{2.17}$$

where B_0 is the maximum field at the centre and $\int \vec{B} \vec{dl}$ is the integrated B-field along the magnet axis starting and ending at the maximum extent of the fringe fields. If the maximum field is not at the centre both values are quoted and are indicated as such. The length of electrostatic fields is treated in an analogue way.

The MC based matrix tracking code TURTLE [52] generates a given sample of particles with initial phase space coordinates in a specified range as either Gaussian or flatly distributed. TURTLE provides the transport matrices for common elements, and therefore only requires input information on type, length, gap/pole tip radius and strength of the individual elements. Furthermore apertures can be specified that cut the particle tracks, when reaching aperture regions. The main output method of TURTLE has the form of histograms.

In order to describe the full ensemble of particles in a beam, another approach was used e.g. in TRANSPORT [51] as a second tool for the CMBL design, that makes use of the symmetric 6×6 beam matrix σ:

$$\begin{pmatrix} \sigma_{x,x} & \sigma_{x,\theta} & \sigma_{x,y} & \sigma_{x,\phi} & \sigma_{x,l} & \sigma_{x,\delta} \\ \sigma_{\theta,x}=\sigma_{x,\theta} & \sigma_{\theta,\theta} & \sigma_{\theta,y} & \sigma_{\theta,\phi} & \sigma_{\theta,l} & \sigma_{\theta,\delta} \\ \sigma_{y,x}=\sigma{x,y} & \sigma_{y,\theta}=\sigma_{\theta,y} & \sigma_{y,y} & \sigma_{y,\phi} & \sigma_{y,l} & \sigma_{y,\delta} \\ \sigma_{\phi,x}=\sigma_{x,\phi} & \sigma_{\phi,\theta}=\sigma_{\theta,\phi} & \sigma_{\phi,y}=\sigma_{y,\phi} & \sigma_{\phi,\phi} & \sigma_{\phi,l} & \sigma_{\phi,\delta} \\ \sigma_{l,x}=\sigma_{x,l} & \sigma_{l,\theta}=\sigma_{\theta,l} & \sigma_{l,y}=\sigma_{y,l} & \sigma_{l,\phi}=\sigma_{\phi,l} & \sigma_{l,l} & \sigma_{l,\delta} \\ \sigma_{\delta,x}=\sigma_{x,\delta} & \sigma_{\delta,\theta}=\sigma_{\theta,\delta} & \sigma_{\delta,y}=\sigma_{y,\delta} & \sigma_{\delta,\phi}=\sigma_{\phi,\delta} & \sigma_{\delta,l}=\sigma_{l,\delta} & \sigma_{\delta,\delta} \end{pmatrix} \tag{2.18}$$

where the diagonal terms are the projection of the 6-dimensional phase space on a 1-dimensional sub-space:

- $\sqrt{\sigma_{x,x}} = x_m$ is the half extent of the particle distribution in the horizontal direction
- $\sqrt{\sigma_{\theta,\theta}} = \theta_m$ is the half extent of the particle angular distribution in the horizontal direction
- $\sqrt{\sigma_{y,y}} = y_m$ is the half extent of the particle distribution in the vertical direction
- $\sqrt{\sigma_{\phi,\phi}} = \phi_m$ is the half extent of the particle angular distribution in the vertical direction
- $\sqrt{\sigma_{l,l}} = l_m$ is the half extent of the particle distribution in the longitudinal direction

- $\sqrt{\sigma_{\delta,\delta}} = \delta_m$ is the half extent of the particle momentum distribution

The off diagonal elements are given by the linear correlation coefficients between the phase space coordinate parameters $\sigma_{ij} = \arcsin(\rho_{ij})$.

The beam matrix σ spans a six-dimensional phase space ellipsoid which fully characterizes the beam in first order. A common approach to illustrate the phase space covered by a beam is given by the projection on the 2-dimensional sub-spaces corresponding to the horizontal, vertical and the longitudinal direction. The horizontal phase space ellipse for a Gaussian beam is shown in figure 2.4. The size of the ellipse is defined to contain 2 standard
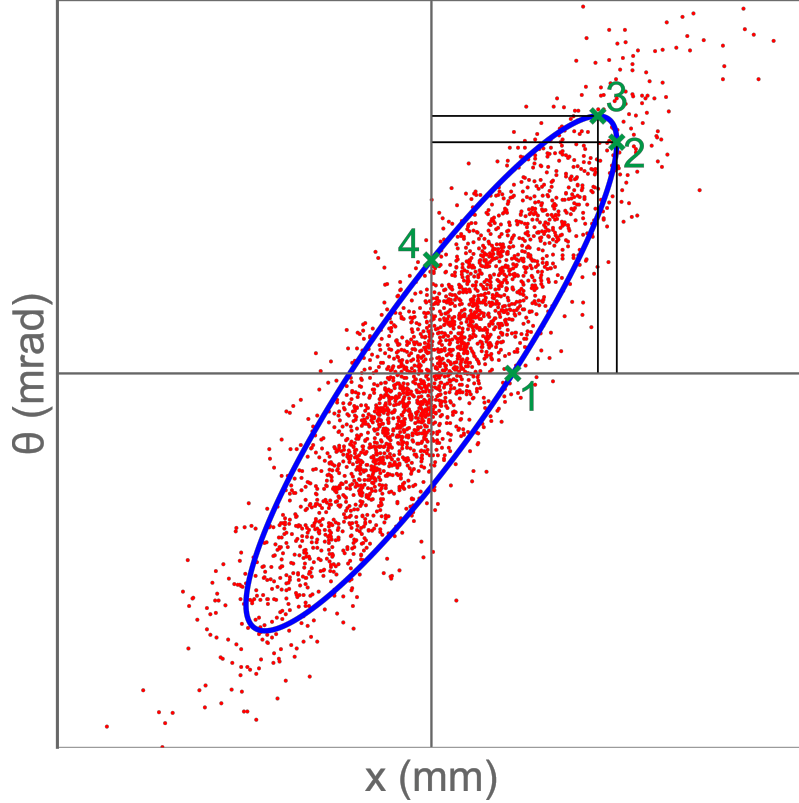
Figure 2.4.: *Shown is the horizontal phase ellipse of a Gaussian distributed beam. The red dots represent individual particles. The blue line illustrates for example the 2-σ ellipse, which is fully determined by 3 parameters of the beam matrix. The characteristic points of the phase ellipse are indicated by green crosses (all values have to be divided by 2 in order to get the corresponding points of the 1-σ ellipse):*

1. *x-coordinate: $2 \cdot x_m \cdot \cos(\arcsin(\rho_{x\theta}))$ θ-coordinate: 0*

2. *x-coordinate: $2 \cdot x_m$ θ-coordinate: $2 \cdot \theta_m \cdot \rho_{x\theta}$*

3. *x-coordinate: $2 \cdot x_m \cdot \rho_{x\theta}$ θ-coordinate: $2 \cdot \theta_m$*

4. *x-coordinate: 0 θ-coordinate: $2 \cdot \theta_m \cdot \cos(\arcsin(\rho_{x\theta}))$*

The area of the ellipse is a first order conserved quantity defined by $\pi \cdot \epsilon_x$, with the horizontal emittance $\epsilon_x = x_m \cdot \theta_m \cdot \cos(\arcsin(\rho_{x\theta}))$.

deviations of the particle distributions x and θ. The definition of the distribution extents x_m and θ_m is arbitrary as long as it is used in a consistent way for the first order matrix

code description. There are different conventions used in the literature, e.g. FWHM, RMS, 2 RMS and 90% containment. In the case of muon beams the standard deviation is a natural definition for the beam size since these beams can be well approximated by a Gaussian distribution. The beam size $x_m(s)$ and $y_m(s)$ along the beam line is called "envelope", since it encloses the specified fraction of particle tracks at each point along the beam line.

The propagation of the beam matrix σ is given by:

$$\sigma(s) = R \cdot \sigma(0) R^T \tag{2.19}$$

The transport matrix R and its transpose R^T, acting on the moments of the 6-dimensional particle distribution that is described by the beam matrix σ, are the same as for the single particle propagation in equation 2.14.

The 6×6 transport matrices R with a determinant equal to 1 represent beam line elements that mediate only conservative first order actions on the beam, which is the case for common linear elements, such as quadrupoles, dipoles and drift spaces. As a consequence of Liouville's theorem in these cases, the size of the area covered by the 6-dimensional phase space ellipsoid is a conserved quantity given by the emittance ϵ. However the action of beam optical elements changes the ellipsoid orientation / inclination angle ($\hat{=}$correlation) and length of the main axes ($\hat{=}$extent of the distribution in its 6 phase space directions). Usually beam lines are designed to avoid couplings between the sub-spaces of the horizontal, vertical and where applicable the longitudinal direction by introducing appropriate elements. For example in the 6×6 transport matrix of the quadrupole 2.15 non-zero terms appear only on the horizontal, the vertical and the longitudinal 2×2 submatrices along the diagonal. Off-diagonal coupling terms can lead to an overall increase of the phase space covered by the ellipsoid / emittance and are therefore avoided in common beam line designs. The coupling between the momentum spread and the horizontal coordinates x or its derivative θ is called dispersion.

The coupling between the horizontal and the vertical phase space is of minor concern in πE5, since all elements up to the Mu3e spectrometer solenoid show no xy-coupling terms in first order. However quadrupole fringe fields and sextupole magnets introduce a slight coupling in second order. The TRANSPORT as well as the TURTLE code provide approximations to quadruple fringe fields as well as 2nd-order terms for all the used elements. In this case 6×6×6 matrices T are introduced and the single particle propagation is given by the first order matrix and the higher order contribution acting on the intitial state of a particle:

$$\vec{r}_i(s) = \sum_j R_{ij}\vec{r}_j(0) + \sum_{jk} T_{ijk}\vec{r}_j(0)\vec{r}_k(0) \tag{2.20}$$

Beside standard element input TRANSPORT and TURTLE also accept input of matrices with arbitrary coefficients. These can be adjusted to match the underlying field geometry [58].

For the design of the CMBL the longitudinal extent of the beam l can be neglected, as there are no time dependent fields through which l could affect the other beam quantities and for a continuous muon beam $l \to \infty$. The matrix calculations for the CMBL are done in a stepwise approach. First an appropriate optical solution is determined with the TRANSPORT fitting capabilities that matches the beam line and the experiment's needs,

such as small beam diameters at distinct apertures in order to enhance transmission, or achromatic beam spots at the experiment location. Secondly, the solution found with TRANSPORT is adapted with TURTLE, particles are tracked through the beam line with implemented apertures. In case of a poor transmission due to aperture cuts an improved optical tune has to be determined by implementing new constraints in the TRANSPORT simulation, leading to an iterative beam line simulation.

The intention of the above introduction of transport matrix formalism and the associated phase space concepts are sufficient for the scope of this thesis. For a more comprehensive view on beam physics the interested reader is referred to [59, 60, 57], that trace back the matrix formalism to the solutions of the so-called Hill's equation. Beside the quantities for characterizing the beam phase space, that were used here, other approaches exist, making use of the so-called TWISS parameters [61], that can be related to the parameters x_m, θ_m, $\rho_{x\theta}$.

2.2.2. Fieldmap based tracking using G4BL

Despite the big successes of matrix code based software in the design of most previous and present-day particle accelerators there are various codes available that are not based on matrix formalism. The use of fieldmaps, comprising of the spatial information of the magnetic $\vec{B}$ and electric $\vec{E}$ fields, provides a more accurate description of a beam line as would be possible with elements described in transport matrix code. The fieldmaps reflect realistic continuous field distributions and allow not only a more accurate representation of standard elements, such as dipoles, quadrupoles etc., but also give the flexibility to introduce arbitrary field geometries associated with non-standard elements.

G4BL is a fieldmap based particle tracking code that further includes sophisticated physics packages. The simulated particles are tracked by solving the equations of motions given by the Lorentz force step by step in the beam line elements. A variety of standard elements, such as quadrupoles, dipoles, solenoids and higher order elements, is available. Fringe fields are approximated with so-called Enge functions as used also in COSY IN-FINITY [62]. Although in general, the default Enge parameters lead to good agreement with a wide range of elements, deviations in the case of large apertures are seen (in the case of the Mu3e beam line: 250 mm - 330 mm pole tip diameter / dipole magnet gap). Figure 2.5 shows the comparison of an on-axis vertical B_y-field of a 240 mm gap dipole magnet, using a generic dipole with default parameters, an accurate fieldmap calculated with the OPERA3D TOSCA [63] Finite Element Method (FEM) code and a generic dipole with manually adjusted Enge parameters. In this case the default setting can not
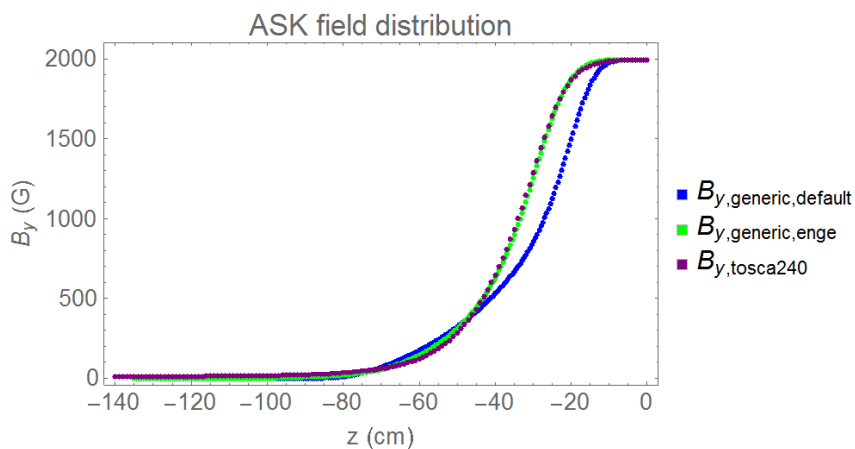
Figure 2.5.: *Shown is the longitudinal field distribution starting in the centre of a 240 mm gap dipole in the magnetic midplane. The default setting for the standard element (blue curve) is obviously not sufficient but the Enge function parameter can be adapted (green curve) to reasonably agree with the distribution of an accurate fieldmap (purple curve).*

properly reproduce the longitudinal field distribution and either an accurate FEM calculation or a measured fieldmap is required to adjust the Enge function parameters in order to achieve a reasonable agreement. Furthermore there are no means to adjust the lateral field distribution. Figure 2.6 shows a 3D plots of the vertical flux density B_y of a standard element dipole in the magnetic midplane. The observed lateral 'flatness' of the fringe field approximation is also applicable for G4BL standard element quadrupoles and is only of
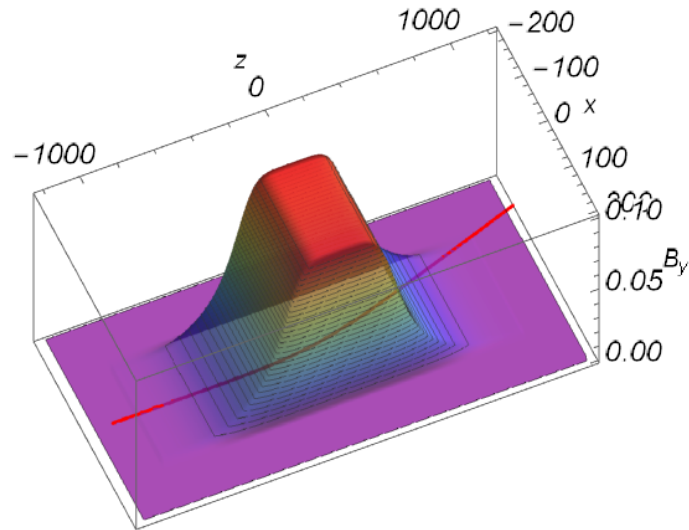
Figure 2.6.: *Shown is a 3D plot of the B_y component of a G4BL standard dipole in the magnetic midplane and an arbitrary trajectory that starts on axis and is deflected in the dipole field. The lateral "flatness" of the fringe field is appropriate for small deflection angles and on-axis injection, in other cases fieldmaps are required for a proper representation of the element.*

minor concern for small deflection angles. However, if the reference trajectory does not coincide with the magnet axis for a significant fraction of the effective length, off-axis field deviations become important. This is the case for bending magnets with large deflection angles, but also for off-axis injection or any overlapping fringe fields. A calculated field-map of the 330 mm aperture ASL dipole together with the reference trajectory is shown in figure 2.83(a)

Higher order elements, such as sextupoles, have no fringe field description in G4BL. Although the higher order fields fall off faster, a fully appropriate representation necessiates fieldmaps.

A large database of materials can be implemented with arbitrary geometries that either lead to cuts of the beam or particle-matter interaction, that can be studied as well.

Various input and output methods provide a large flexibility and detailed information, but also make the input rather complex.

2.2.3. Comparison of TRANSPORT/TURTLE transport matrix descriptions and fieldmap based tracking in G4BL

Despite the above mentioned advantages of using continuous field distributions for tracking rather than transport matrices, transport matrix formalism is still the first choice for initial beam line design, as it is comparatively quick and provides well separated information on the underlying accelerator physics phenomena, such as dispersion and chromaticity.

The strength of a fieldmap based simulation lies in the complexity of field distributions that can be implemented. The simulation accuracy is only limited by the accuracy of the fieldmaps for the individual elements and the chosen stepsize, which limits the computation speed.

One of the major deviations of the matrix code and the fieldmap tracking approach lies in the treatment of the fringe fields. Transport matrices as 2.15 describe homogenous field regions and fringe fields have to be approximated by introducing zero-length (thin lens) matrices that provide 'kicks' at the entrance and exit to the elements' effective lengths. The matrix coefficients of dipole and quadrupole fringe field approximations are determined from fringe field integrals [64] and therefore require fieldmaps as well. Although the thin lens fringe field approximation is valid for small aperture beam line elements with short range fringe fields, muon beam line components are usually designed for maximum transmission, requiring large aperture magnets and vacuum chambers. The large apertures lead to extended fringe fields implying significant deviations of the matrix code description and hence the need for fieldmap based codes such as G4BL.

A comparison between the 1σ beam envelopes calculated with TRANSPORT and G4BL for a 1 m long air-core solenoid with a 20 cm diameter aperture and 0.35 T central magnetic field is shown in figure 2.7. The deviations between G4BL and the matrix code description
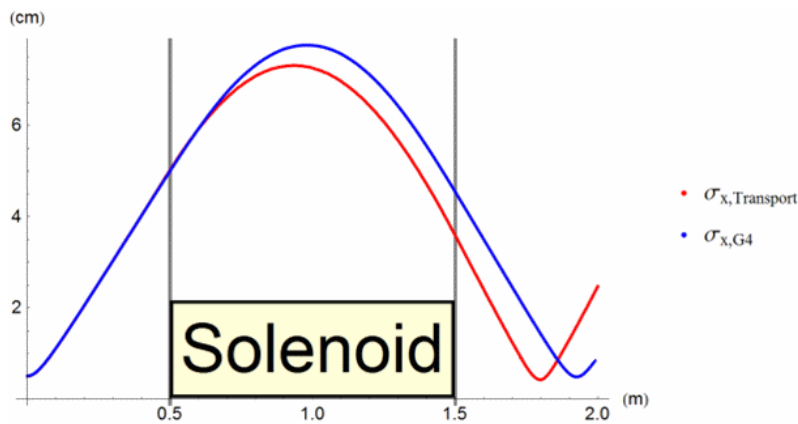
Figure 2.7.: *Shown are the TRANSPORT and the G4BL beam envelopes for the standard implementation of a solenoid in both codes. Deviations between the two codes are observed.*

are obvious, the beam focus is different and the maximum beam size at the antinode in the solenoid is also smaller in TRANSPORT compared to G4BL. As the solenoidal magnetic field is well described with the G4BL standard implementation, in agreement with TOSCA FEM calculations (see figure 2.8), the deviations between the envelopes can be traced back to the description in TRANSPORT.

The fringe field of a solenoid with homogeneous longitudinal field $B_z = B_0$ in matrix code
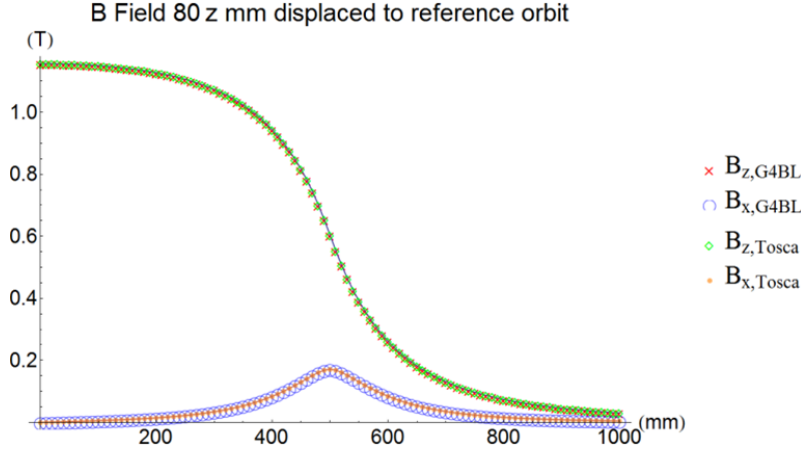
Figure 2.8.: *Shown is a comparison of an off-axis field parallel to the centreline for a solenoid calculated in TOSCA and a G4BL standard element solenoid.*

is usually approximated by a purely radial field at the end of the homogeneous field region:

$$B_r = -\frac{r}{2}B_0\left(\delta\left(z\right) - \delta\left(z - L\right)\right) \tag{2.21}$$

where r is the radial distance from the centreline, z is the longitudinal coordinate along the solenoid axis and L is the solenoid length. The field shape can be implemented in G4BL with a field parametrization. The graphical output is shown in figure 2.9. The envelopes
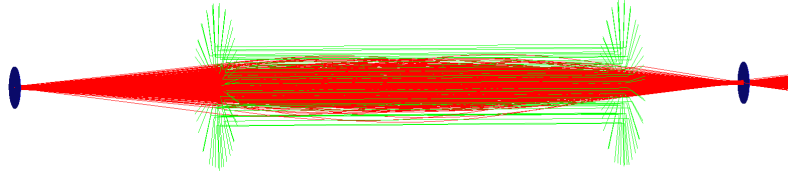
Figure 2.9.: *Shown is a visualization of the fieldlines of a solenoid in matrix code description.*

of TRANSPORT and the corresponding field parametrization in G4BL is shown in figure 2.10 and a good agreement with the 2$^{\text{nd}}$-order matrix code envelope can be observed. As a conclusion, the thin lens approximation for fringe fields in matrix code is useful but is limited and has to be investigated in the case of extended fringe fields. The πE5 beam line elements have comparably large apertures and therefore extended fringe fields as can be seen e.g. in figure 2.33. The fringe field extent of adjacent elements can even overlap and lead to a variety of effects, such as e.g. undesired steering. G4BL can partially account for overlapping fringe fields (see figure 2.20) by the superposition of adjacent fieldmaps, however measured and calculated fieldmaps are mostly evaluated for individual elements and the influence of adjacent iron is therefore neglected.

Some of the elements used in πE5 show deviations from 'pure' fields and can therefore not be fully described in TRANSPORT/TURTLE. For example the QSB type quadrupole that is used in Triplet I shows a significant octupole component (see figure 2.11) due to a simplified pole-shoe design. These effects are not included in TRANSPORT/TURTLE and can therefore lead to deviations.
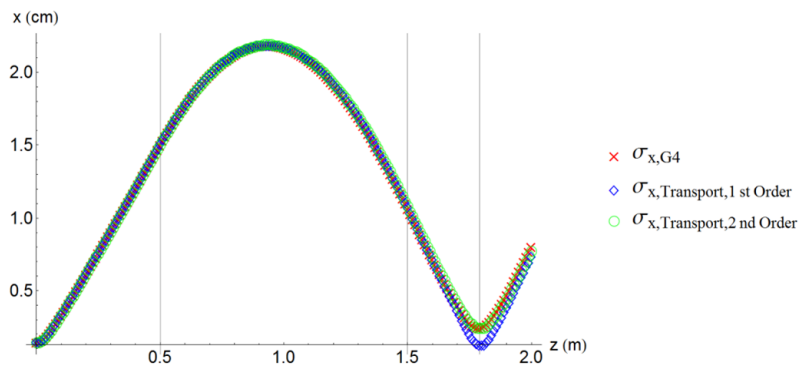
Figure 2.10.: *Shown is the agreement between the envelopes in a matrix code solenoid and a G4BL field parametrization of the matrix code field description.*
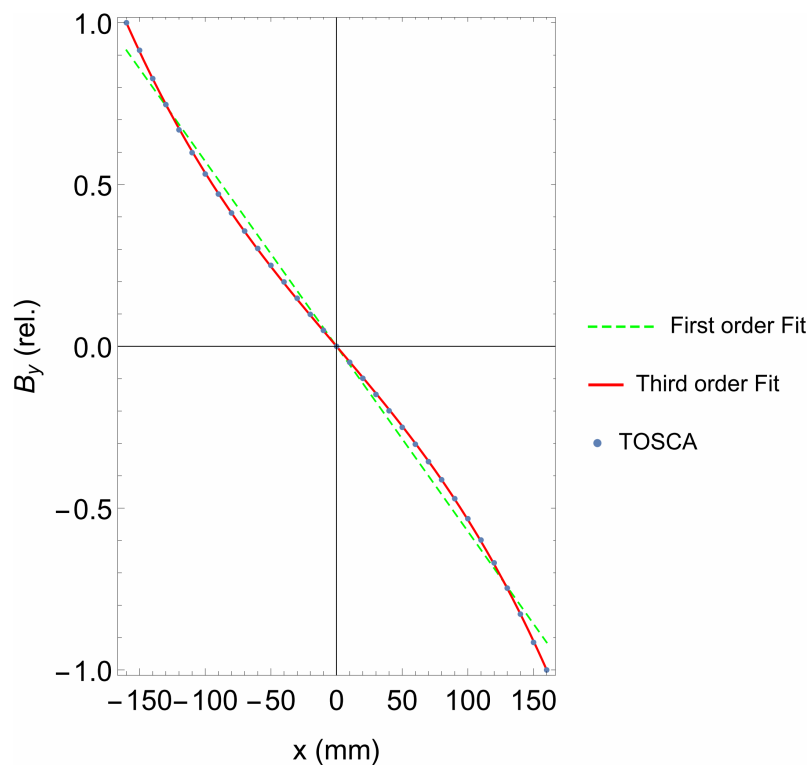
Figure 2.11.: *Shown is the normalized vertical field B_y along a horizontal line at the longitudinal centre of a QSB quadrupole as implemented in the $\pi E5$ beam line. The field is not only given by a constant gradient but also shows a significant octupole component.*

The accuracy given by G4BL on the one hand is a big advantage, whereas it can also complicate the design process in practical terms. For example small changes in the coil currents or the positioning of a dipole magnet, which are fully unconstrained in the G4BL input can cause large deviations from the central orbit and therefore have a large effect on the beam, even giving different effective lengths, which reflects realistically the behaviour of a beam line but makes the simulation more challenging. Another important effect is the observed (mostly undesired) steering capabilities introduced by quadrupole magnets that are traversed off-axis. Therefore, alignment of all elements in the simulation has the same significant implications on the simulated beam as in the real beam line setup. Compared to this severe sensitivity to the input parameters in G4BL, TRANSPORT and TURTLE simulations are usually more stable. Elements (by their matrix representation) are intrinsically aligned and misalignment must be introduced by intention. Hence a small deviation of a dipole bending angle in matrix code description would usually only cause a small change of the dipole focussing properties and therefore only has a small effect on the beam and quadrupole steering is not observed in first order.

All the effects that were summarized above emphasize the superior accuracy of the G4BL code. However, the quantitative difference between the different approaches varies and strongly depends on the choice of beam optics elements and their arrangement. Figure 2.12 illustrates this by comparing a TRANSPORT 1-σ beam envelope for an arbitrary beam and the same envelope generated from a G4BL output both for the same straight section of the πE5 multipole channel right after extraction. The fieldmap calculation in
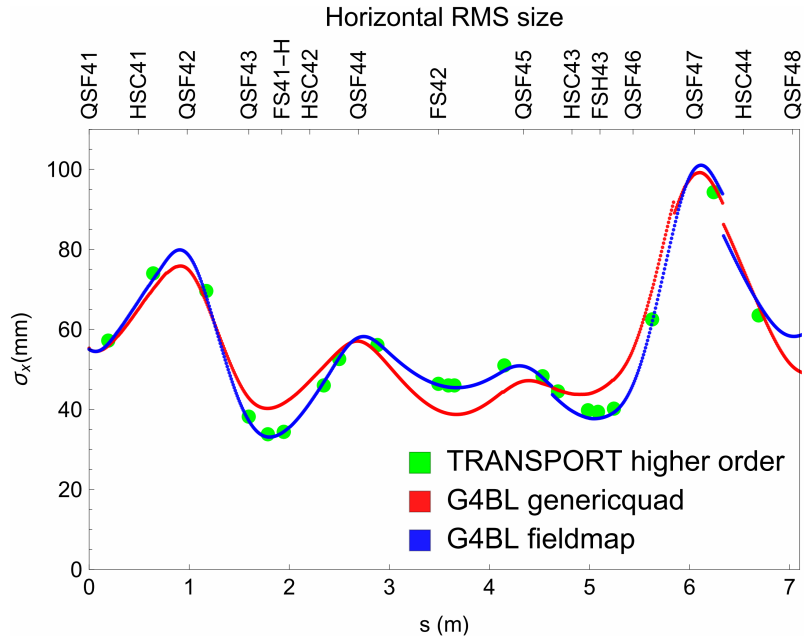
Figure 2.12.: *Shown is a comparison between TRANSPORT and G4BL 1-σ envelopes for the first straight section of the πE5 beam line for an arbitrary beam. The elements and the beam line arrangement are explained in section 2.3.*

G4BL is in good agreement with the second order TRANSPORT envelope for this section,

Table 2.1.: *Shown is a summary of the main characteristic features of TRANSPORT/TURTLE and G4BL*

	TRANSPORT	TURTLE	G4BL
Accuracy limitations	matrix order, field complexity, fringe field implementation, beam losses	as TRANSPORT but without beam loss limitation	stepsize, fieldmap accuracy
Input complexity	Small for standard elements, difficult for complex fields	same as TRANSPORT	requires fieldmaps for non-standard elements, alignment sensitvity
Output	Envelopes (graphical and ascii), phase space ellipses (graphical and ascii)	1D & 2D histograms, beam file output at arbitrary pathlengths or locations	graphical output (3D), various ascii outputs (envelopes, losses, beam at arbitrary pathlengths or impacting specific geometry regions)
Physics	none	scattering, particle decay	full Geant4 physics
Fit routines	Fast, comprehensive	none (but quick implementation of TRANSPORT fit results)	*Optima G4BL* (see appendix 4.4)
Computation time (CMBL)	< 1 sec	$\mathcal{O}$ (seconds)	$\mathcal{O}$ (minutes) for CMBL only $\mathcal{O}$ (10 minutes) for πE5

though in disagreement with the generic quadrupole of G4BL.

As a conclusion to this subsection, the two different approaches do not exclude but rather complement each other. Beam line design using TRANSPORT and TURTLE is much faster compared to G4BL which accounts for the higher computation time and complexity of the input. TRANSPORT/TURTLE turn out to be less sensitive to small deviations from misalignment or field contributions. Furthermore, TRANSPORT provides intrinsically direct access to important and individual beam information, such as dispersion or phase space ellipses, and quickly gives a good qualitative understanding of the underlying beam physics and the relevance of the different parameters. Sophisticated fit algorithms in TRANSPORT allow for quick multiparamter optimization and finally the compatibility between TRANSPORT and TURTLE input formats allows for a fast access to tracking information, such as the beam line transmission.

Given the benefits of both approaches and applying these to the different steps of the design process, the matrix code description with TRANSPORT/TURTLE as well as the more accurate G4BL code are used for the beam optical calculations of the CMBL. Table 2.1 summarizes the advantages and disadvantages of the different codes.

2.3. PiE5 and CMBL beam line overview

πE5 is a high-rate secondary beam channel that is mainly used for experiments with surface muons but can also provide muons, pions and electrons of either charge-sign at a momentum range between $\sim$ 10-120 MeV/c. Large element apertures and vacuum beam pipes ensure a high beam phase space / rate acceptance with a momentum acceptance of $\sim$3% σ. The high rate and flexibility makes it the favourite choice for the intensity frontier experiments such as MEG and Mu3e. Figure 2.13 shows a CAD model overview of the entire secondary beam line from production TgE to the Mu3e spectrometer solenoid. The beam line for Mu3e mainly comprises of three parts: the πE5 channel ending with the ASC dipole; the shared MEG section of the beam line ending at the intermediate focus collimator system; a dedicated Mu3e part ending with the Mu3e solenoid.
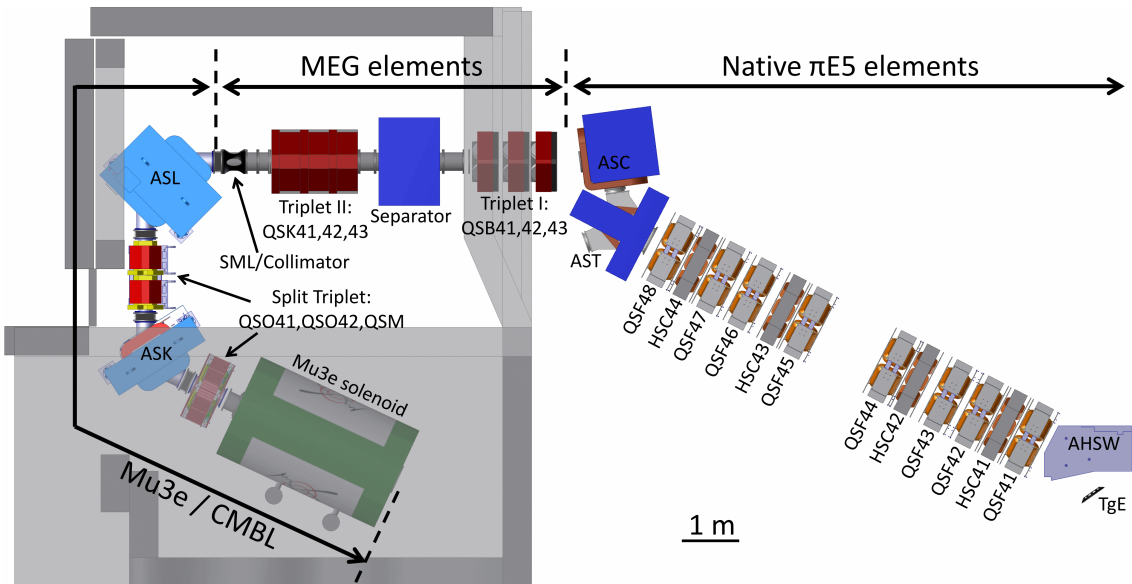
Figure 2.13.: *The CAD model plan view shows the entire Mu3e beam line, starting from the muon production TgE (bottom right) to the Mu3e spectrometer (bottom left). The beam line uses the so-called Z-branch of πE5, which is selected by deflecting the beam to the right in the AST dipole magnet.*

- The first part [65] starting with the extraction dipole AHSW up to the ASC dipole was set up in the 90's. It can serve either of two different branches which can be switched by the AST magnet. For beam optical reasons and the compatibility with the MEG beam line setup, the so-called Z-branch is used for the setup of the CMBL. The Z-branch requires an additional bending magnet ASC that is directly attached to the AST and deflects the beam at a 75° angle to the area. All the πE5 elements are covered by concrete shielding for radiation safety reasons and are mounted on wagons in the shielding.

- The second part comprises of the MEG beam line elements Triplet I to the collimator system prior to injection into the BTS and COBRA that were set up in 2005. For some experiments carried out in the πE5 area these elements had to be removed,

except for Triplet I that is installed behind a Polyethylene (PE) shielding wall and covered by concrete shielding. Marks on the area floor ensure a proper alignment after re-installation of these elements. Mu3e makes use of this well-proven setup, especially the separator, which is necessary to eliminate unwanted beam correlated background.

- The dedicated Mu3e components follow the MEG collimator system. Due to spatial limitations a 90° bending dipole is attached as close as possible to the MEG SML / collimator system, which is partially covered by a concrete shielding overhang and leaves only a few cm gap to the rear shielding wall of the πE5 area. It is followed by the so-called "split triplet", that comprises of a split combination around the last dipole magnet ASK, of a QSO doublet with small lateral extent and a large aperture QSM singlet. Finally, the Mu3e spectrometer solenoid as the end part of the beam line hosts the Mu3e experiment.
  As can be seen the limited space leaves only little freedom for the individual alignment of the elements and therefore also puts severe constraints on the beam optics.

The beam line elements positioning initially relied on the available technical drawings for the front area elements as well as careful measurement and alignment of the accessible elements during the first two test beams using a laser measurement device, spirit-levels and tape measures. For the final beam line setup measurements a laser tracker system was used by the PSI survey group. Based on the various inputs an accurate CAD model was derived, which was used as the basis for the position information in the different simulations and the data analysis of the test beam periods. Changes in the beam line setup or the simulation could immediately be applied to the CAD model.

The matrix code simulation is based on existing scripts of πE5 that were extended to include the CMBL components while the G4BL simulations were set up from the beginning, which motivitated different comparison studies, that were partially presented in the previous section.

The proper alignment in the G4BL simulation was cross-checked by a dedicated coordinate output command of G4BL that contains all elements coordinates, which were converted and overlayed in the CAD model.

In the following subsection the elements are briefly characterized and their implementation in the simulation is described.

2.3.1. Beam line elements

This subsection summarizes the important features of the πE5/CMBL beam line elements. More elements than the ones presented here, together with different optical solutions were studied at the beginning of the CMBL study but were ruled out during the design process. In order to keep the costs for the beam line low and the design time to a minimum, available spare magnets were preferentially considered for the design, which does not mean a severe drawback, since a variety of spare elements was available and a well-suited selection was made. Below, only those elements that were used for the experimental setup are summarized.

Due to considerable fringe field contributions, all elements used in the simulation required a dedicated characterization. For most of the used elements an appropriate matrix code description was already available and had been implemented. The fieldmaps for G4BL are partially based on measurements, that were done by the PSI magnet group, partially on simulations with the OPERA3D TOSCA [63] FEM code, that were provided either by the PSI magnet group or calculated as a part of this thesis. One steering magnet (SML41) was approximated by a constant field expression and one quadrupole type (QSK) was set as a standard element with an appropriate adjustment of the Enge function parameters. The TOSCA calculations made rely on the available technical drawings, whereby attention had to be paid and cross-check measurements were made, which led to adjustments of the model. The TOSCA calculations make use of different B-H curves that reflect the permeability μ of the 'high quality' iron that is mostly used for the pole shoes and yokes and the 'low quality' iron of the magnetic mirror plates. All relevant apertures were intially introduced approximately and later on in an accurate way based on the technical drawings.

2.3.1.1. TgE and the AHSW extraction dipole

Surface muons that originate from the outer layers of the production target TgE, or e^+ and π^+ with the same momentum and angular acceptance are extracted with the AHSW dipole magnet. This magnet, shown in a plan view in figure 3.45, is also part of the proton beam line and has a gap of 240 mm. Tuning the AHSW, as described in section 3.5.4, selects the central particle momentum that is transmitted down the πE5 channel. Muons emitted from the side and the backward faces of the nearby TgE at a backwards angle of $\sim$165° with respect to the proton beam are deflected into the πE5 multipole channel. The field distribution B_y in the magnetic midplane around the AHSW is shown in figure 2.14. Due to the horizontal inclination of the AHSW pole-shoe face (pole face rotation) to the
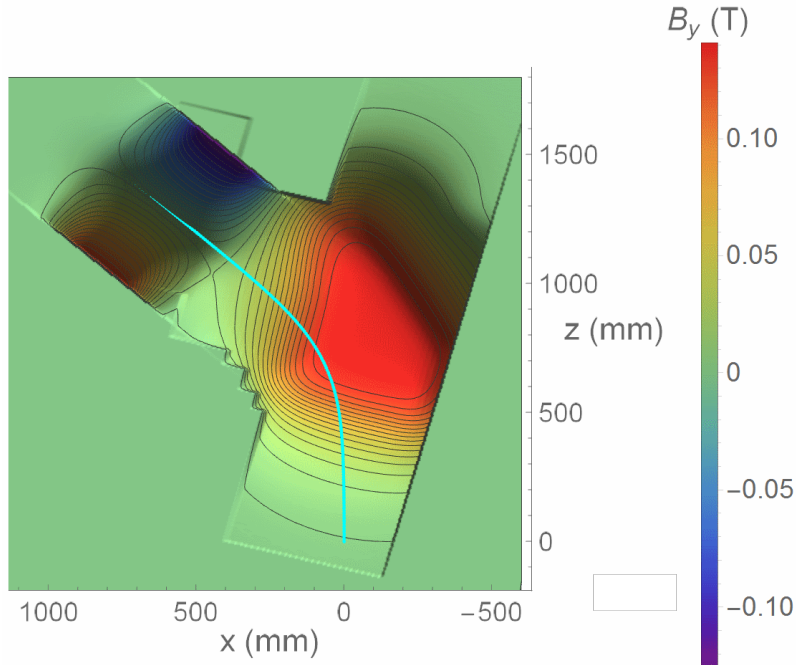
Figure 2.14.: *Shown is the B_y component in the midplane at the target region. The roughly triangular shape of the magnetic field of the AHSW extends weakly to the target region. On the πE5 side of the AHSW the overlap with the field of the first quadrupole QSF41 can be seen. The cyan curve illustrates the trajectory of a 28 MeV/c μ^+ starting at the centre of TgE. The trajectory and the field values were extracted from a G4BL simulation.*

muon reference orbit, the AHSW provides horizontal edge focussing of the beam on either side.

In TRANSPORT/TURTLE the AHSW is modelled with a parametrized second order transfer matrix that reflects the properties of the fieldmap. In G4BL a measured fieldmap was first used then later a TOSCA calculation that also includes the vincinity of the iron parts of the nearby QSF41 was used, which can lead to slightly different fields. Furthermore an accurate model of the AHSW apertures was included.

2.3.1.2. QSF quadrupoles

The QSF is a radiation hard large aperture quadrupole. It has a pole tip radius of 20 cm and a plus-shaped vacuum chamber, which garantuees a high transmission, especially important at the beginning of the beam line where the beam can be off-centre as outlined in the appendix 4.3. The QSF was designed to include also small higher order multipole components in order to improve the πE5 beam optics. Magnetic mirror plates at the injection and extraction side slightly shorten the effective length to $\sim$382 mm, which still exceeds the actual iron length of 300 mm. The central field of the QSF is implemented in TRANSPORT/TURTLE as a standard quadrupole and the fringe fields are parametrized according to the fringe field integrals based on old measurements. The implementation in G4BL with a standard element and default settings fails, since the gradient along the centreline of the magnet shows an unphysical non-differentiable distribution at the centre. In order to approximate the QSF, the fieldmap of the very similar QSM quadrupole magnet was used, whereby the field strengths are scaled by the ratio of their effective lengths $\frac{l_{eff,QSF}}{l_{eff,QSM}}$ and their field factors (G/A, Gauss per Ampere) due to the different number of coil windings. This is a valid approach, since the QSM is a non-radiation hard replica of the QSF magnet, although with more supressed multipole-components.

2.3.1.3. HSC sextupoles

Sextupoles in general are pure second order elements and therefore only have an effect in the higher order mode calculation in TRANSPORT/TURTLE. Their main purpose is twofold: (a) Correction for higher order geometric aberrations and (b) to compensate for chromatic aberrations. The second order chromatic aberrations mainly arise from a dependency of the quadrupole focussing power / the quadrupole strength K (simplification $K(p) \rightarrow K(p_0)$ was introduced in 2.3) on the momentum, which causes the first order focal length of a quadrupole to be smeared out for a non-vanishing momentum byte. The parabolic field of the sextupole is given by:

$$B_x = \frac{\partial^2 B_y}{\partial^2 x} xy \tag{2.22}$$

$$B_y = \frac{1}{2} \frac{\partial^2 B_y}{\partial^2 x} (x^2 - y^2) \tag{2.23}$$

,where $\frac{\partial^2 B_y}{\partial^2 x}$ is a constant for a pure sextupole. This can be seen from the TOSCA simulation for the G4BL field map. Figure 2.15 shows the vertical field component B_y in the longitudinal centre plane of the HSC, perpendicular to the magnetic axis. The HSC provides a pure sextupole field at its longitudinal centre and figure 2.16(c) illustrates the azimuthal symmetry for the absolute field value $B_{tot} = \sqrt{B_x^2 + B_y^2 + B_z^2}$. The iron length is 250 mm and the effective length determined from the vertical B_y component on a line parallel to centreline at a vertical displacement y=50 mm is $\sim$ 355 mm. Figure 2.17 shows the B_y component starting from the centre of the magnet for different displacements in y. The larger 250 mm pole tip radius of the HSC, compared to the QSF, allows both elements to share the same plus-shaped vacuum pipe allowing optimal transmission. The aperture
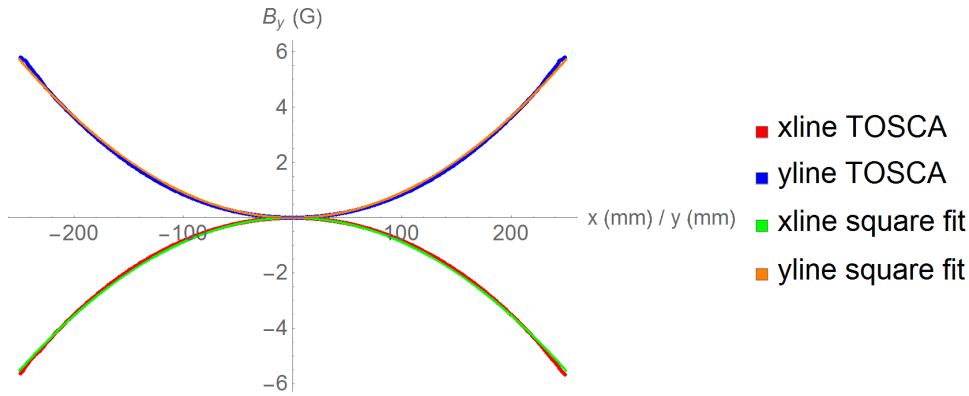
Figure 2.15.: *The B_y component of the magnetic field of the HSC sextupole magnet is plotted along a vertical (pole to pole) and a horizontal line each going through the HSC centre. The corresponding fits indicate the purity of the sextupole field.*
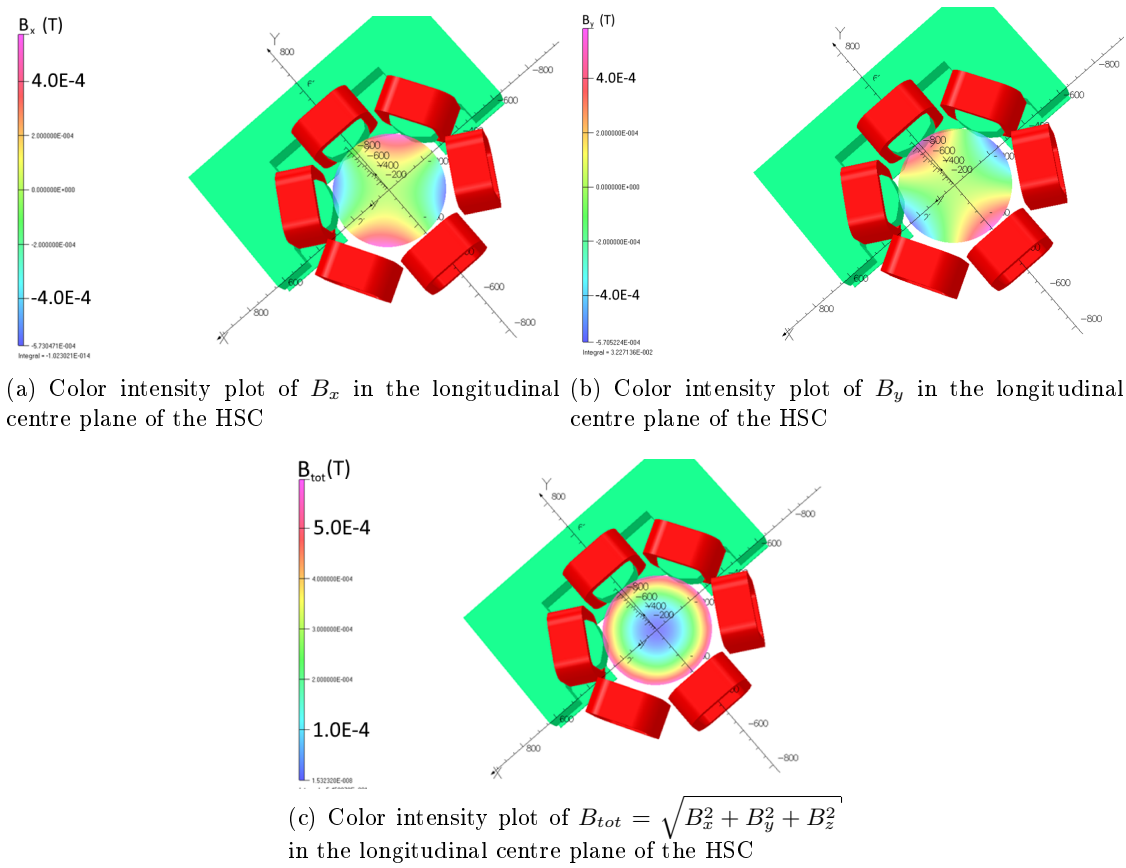
(a) Color intensity plot of B_x in the longitudinal centre plane of the HSC

(b) Color intensity plot of B_y in the longitudinal centre plane of the HSC

(c) Color intensity plot of $B_{tot} = \sqrt{B_x^2 + B_y^2 + B_z^2}$ in the longitudinal centre plane of the HSC

Figure 2.16.: *The color intensity plots of B_x, B_y and B_{tot} at the longitudinal centre plane of the HSC indicate the symmetry of the magnetic fields. Only a quarter of the yoke and mirror plate iron is shown for a better visualization.*
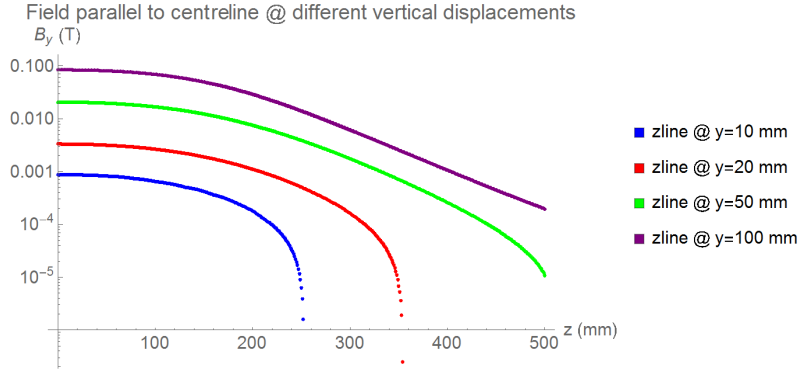
Figure 2.17.: *Shown are the B_y distribution parallel to the centreline starting at the centre of the HSC for different vertical displacements in a logarithmic scale.*

constraints imposed by the vacuum chamber are taken into account in the simulations. The beam optical implementation in TRANSPORT/TURTLE is done with the transport matrix of an ideal sextupole without fringe fields.

2.3.1.4. Slit systems, vacuum valves and beam blocker in the πE5 channel

Apart from magnets, the πE5 multipole channel also comprises of a series of slit systems and vacuum valves that are operated in parallel to the Beam Blocker (BB). The slits, shown in figure 2.18 restrict the beam in either the horizontal (FSH41, FS42, FSH43) or the vertical (FS42) direction, in order to limit the beam intensity and the momentum byte. The BB denoted in figure 2.18 as KSF41 is a massive copper block, that is moved
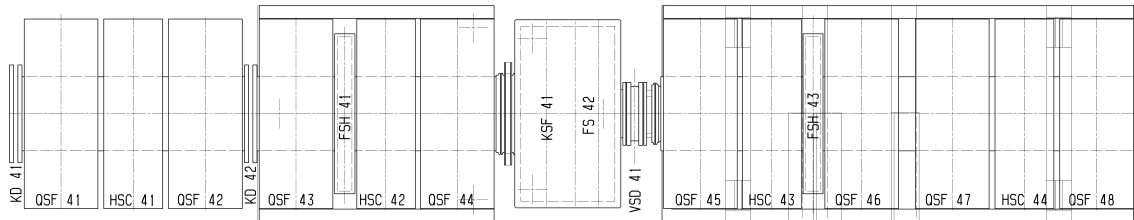
Figure 2.18.: *Shown is an overview on the components in the first straight section of πE5. The beam is injected from the left with the AHSW dipole (not shown).*

into the beam line, when wanting to enter the area and completely stops the beam from the production target. The vacuum valve VSD41 is operated in parallel with the beam blocker. The beam line part housing the VSD41 is the narrowest part (ø320 mm) of the straight section after extraction. This aperture as well as the slits are implemented in the simulations although the slits are usually set to be fully open as Mu3e requires the maximum rate that can be achieved.

2.3.1.5. The AST and ASC dipoles

The AST is a 240 mm gap dipole magnet at the end of the πE5 multipole channel that deflects the beam either via the U- or the Z-branch to the experimental area. As can be seen

in figure 2.19 the sophisticated pole shoe design provides edge focussing on the extraction side due to a pole face rotation different from the 47.5° design bending angle. In addition an approximated pole face curvature on both sides introduces a sextupole moment. The AST implementation in matrix code uses appropriate fringe field integrals and the
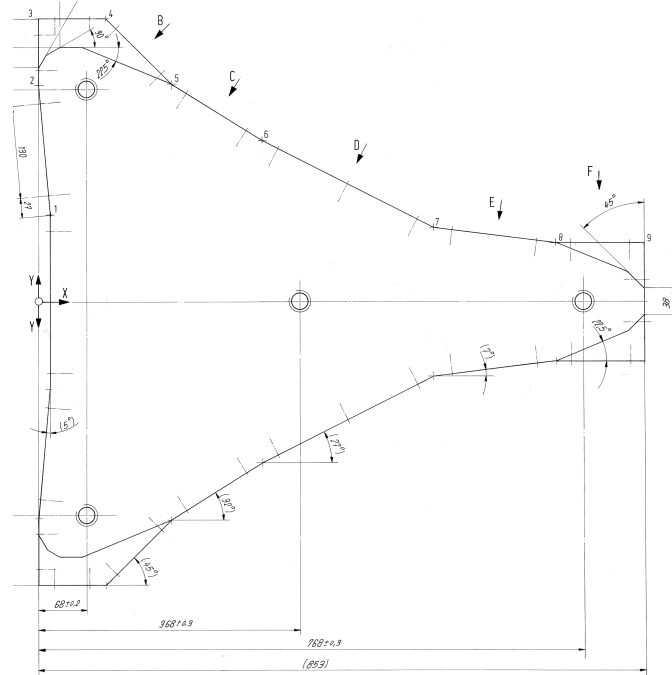
Figure 2.19.: *Shown is the pole-shoe of the AST dipole magnet at the end of the πE5 multipole channel. For the Mu3e and the MEG II experiment the muon beam, coming in from the left, is deflected by a design angle of 47.5° to the bottom right. The approximated pole face curvature introduces a sextupole component and the pole face rotation on the extraction side provides linear edge focussing.*

corresponding pole face rotation. The fieldmap used in G4BL is based on measurements provided by the magnet group.

In the Z-branch, that is used for MEG II and Mu3e, the 240 mm gap C-type ASC magnet deflects the beam by 75° to the experimental area. The pole face rotation at the entrance and exit side provides a slight vertical defocussing. The matrix code implementation accounts for that with fringe field integral values and the corresponding pole face rotation angles. For G4BL a simulated fieldmap of the ASC was provided.

Figure 2.20 shows the vertical field component B_y in the magnetic midplane of the AST-ASC region. As can be seen the fringe fields of the two dipoles overlap. A variety of current combinations for the AST and ASC exist, that provide a good transmission, however only one solution has the correct deflection angle and exactly coincides with the centreline of the DS lattice. Figure 2.21 illustrates two possible settings simulated in G4BL together with the design orbit that is used in the matrix code. The blue markers indicate the trajectory for the AST magnet being tuned to the design angle of 47.5° that is given by the drawing. However the solution that is given by former MEG settings (red empty circles), that was determined by optimization in the experimental area, has a smaller deflection angle in the
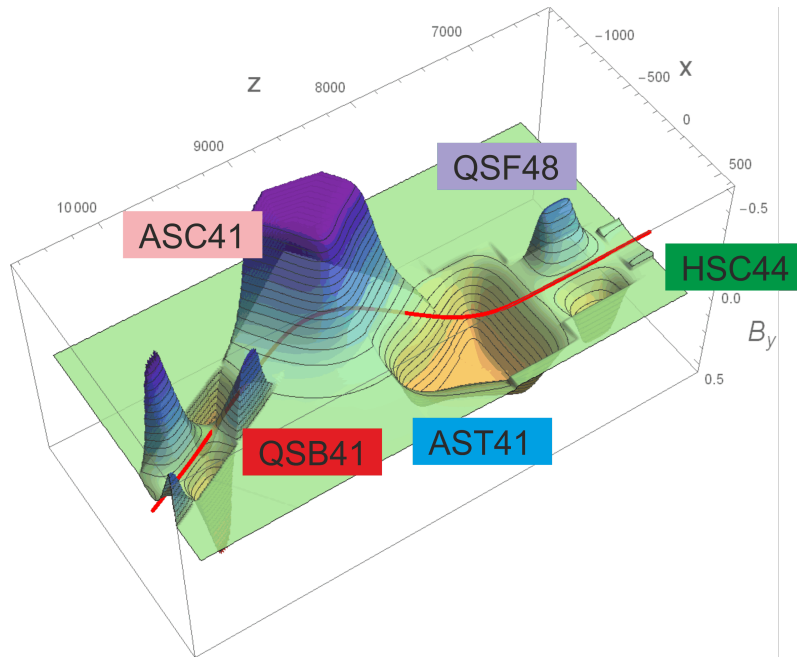
Figure 2.20.: *Shown is the B_y distribution in the magnetic midplane at the region around the AST-ASC chicane together with a reference trajectory. The fields of the QSB and QSF also slightly overlap with the adjacent dipole fields.*

simulation but passes the flange aperture at the connection between both dipoles centred. The central red arcs and orange straight lines indicate the design values that are used in TRANSPORT/TURTLE. The deviation from pure arcs and straight lines as emphasized by the central trajectory again shows the advantage of appropriate fringe field treatment in the fieldmap based tracking approach.
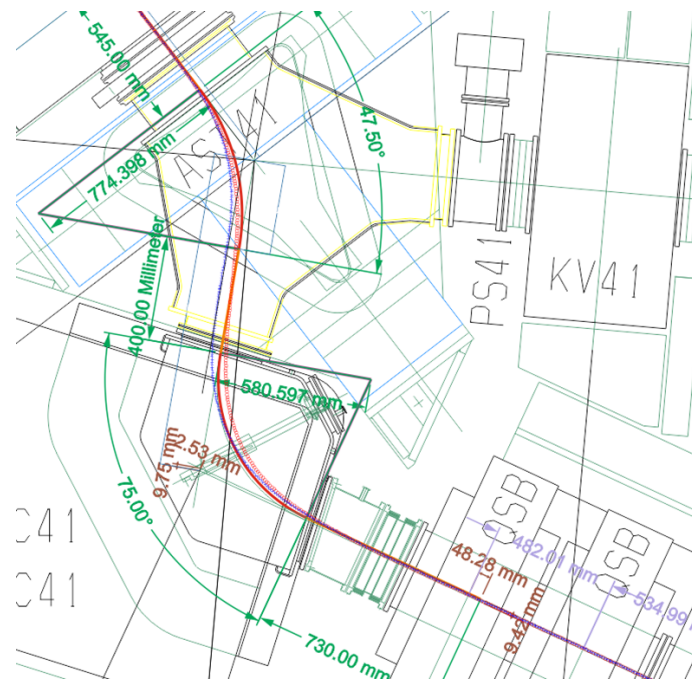
Figure 2.21.: *According to the drawings the beam line design originally foresees a 47.5° bending angle for the AST and 75° bending angle in the opposite direction for the ASC. The design trajectory is overlayed to the drawing and illustrated by orange straight lines and red arcs with 47.5°/75° bending angles and radii defined by the effective length of the magnets. However, tuning the AST fieldmap in the G4BL simulation to a 47.5° deflection angle results in an off-axis reference trajectory (blue markers). The MEG settings for this region yield a reference trajectory (red empty circles) that has a slightly different bending angle but passes the flange aperture between the AST and the ASC centred.*

2.3.1.6. The QSB quadrupole Triplet I

The QSB41-QSB43 are termed as Triplet I. The importance of this part of the beam line is mainly given by the need to properly adjust the beam properties for a good separation and transmission through the following particle separator (Wien filter). Color intensity plots from the TOSCA calculations of the field distributions at the centre of the QSB are shown in figure 2.22. The field decomposition at the longitudinal centre of the QSB shows an

(a) Color intensity plot of B_x in the longitudinal centre plane of the QSB

(b) Color intensity plot of $B_{tot} = \sqrt{B_x^2 + B_y^2 + B_z^2}$ in the longitudinal centre plane of the QSB
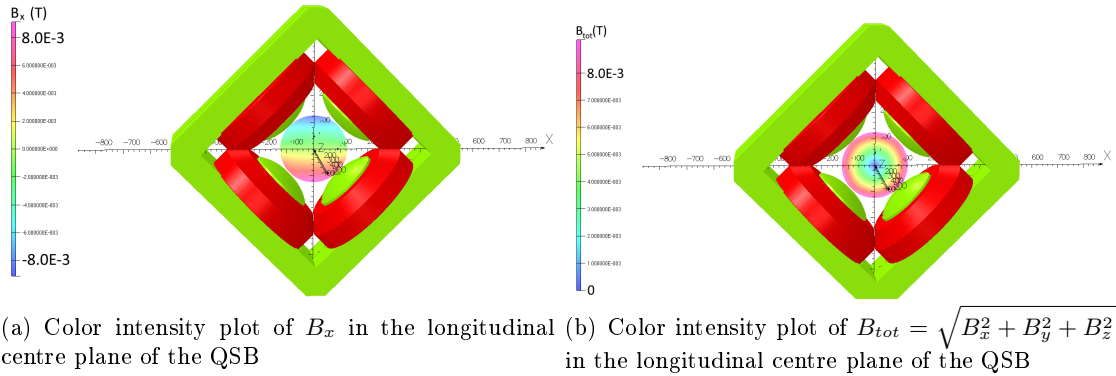
Figure 2.22.: *The TOSCA calculation takes into account the rotational symmetric pole shoes the iron yoke and the coil shape. The rotational symmetry of B_{tot} is shown on the right.*

octupole component (see figure 2.11). Figure 2.23 illustrates the longitudinal distribution of the vertical magnetic field component B_y at a horizontal displacement $x = 10$ mm. The fieldmap is calculated with TOSCA and the matrix representation is based on available information from the fringe field integrals.
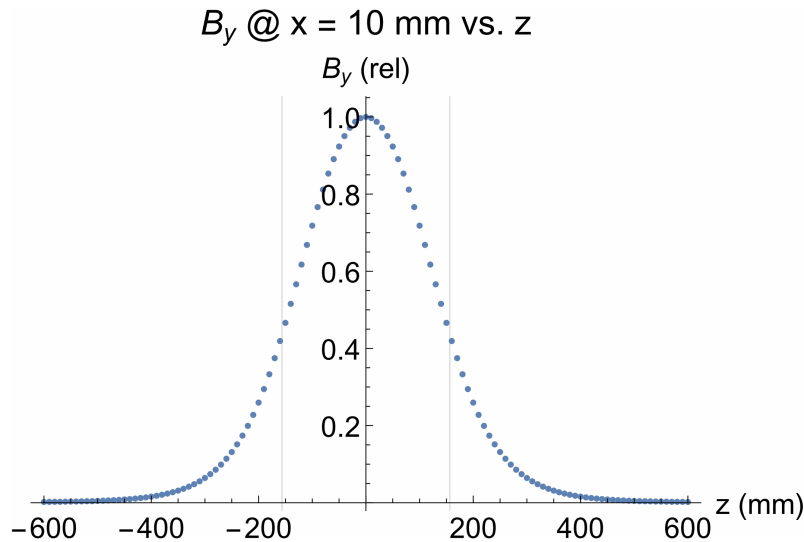
Figure 2.23.: *The normalized gradient shown in the plot corresponds to an effective length of $\sim$313 mm and is indicated with the light-gray lines on either side.*

2.3.1.7. The particle separator SEP41

For a good background suppression the MEG beam line utilizes a Wien-filter type particle separator DS the Triplet I. The central momentum of the beam is defined by the AHSW extraction magnet and subsequently velocities/energies are selected in the combined orthogonal E×B field of the separator. The separation power between muons and positrons of 28 MeV/c is shown in figure 2.24. The positron peak and the Gaussian muon peak are
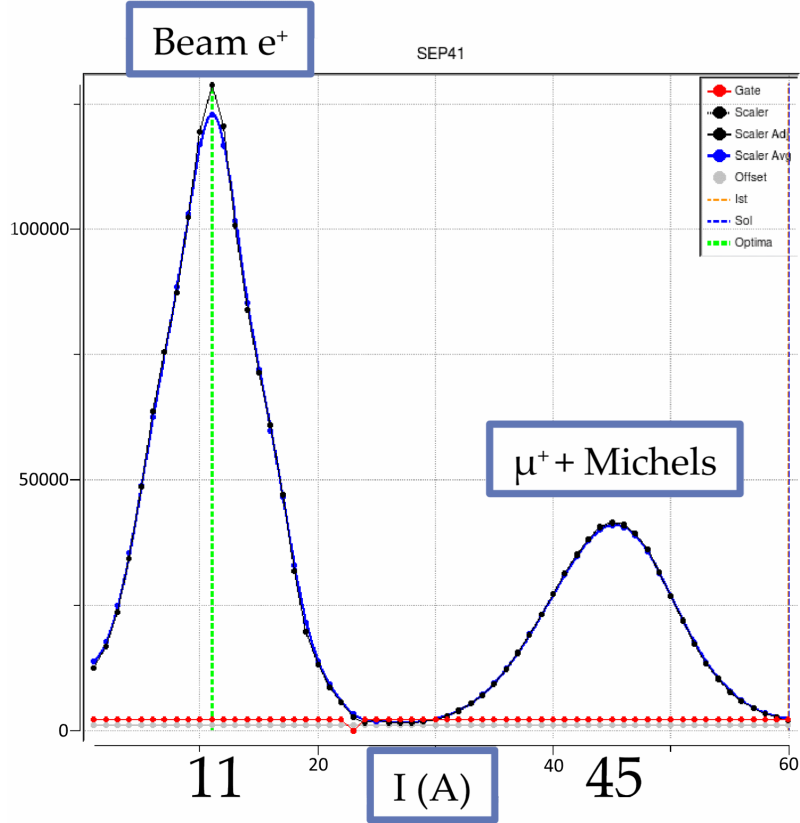
Figure 2.24.: *Separation power of the Wien-filter type separator measured at 28 MeV/c using a small pill scintillator on the DS centreline with a constant electric field of $\sim \frac{195 \ kV}{19 \ cm \ electrode \ gap}$ and scanning the coil currents of the separator magnet. The separation between the e^+ at $\sim$11 A and the muon peak at 45 A depends slightly on the beam line optics and usually amounts to $\gtrsim 5.7$ σ_{μ^+}.*

separated by $\sim 5.7\sigma_{\mu^+} \approx 85$ mm. Separate TOSCA calculations were made for the electrostatic and the magnetostatic fields. The electrostatic simulation only takes into account the deflector plates and the vacuum chamber with apertures. The magnetostatic simulation comprises of the coils and the iron yoke. The B-field distribution in the midplane is shown in figure 2.25. Both fieldmaps can be used in superposition in G4BL and can be tuned independetly. The longitudinal distributions of both fields are shown in figure 2.26. The effective lengths are $l_{eff,E} = 794$ mm for the electric field and $l_{eff,B} = 808/816$ mm for the magnetic field when normalized to the maximum field/the field value at the centre. The maximum high voltage that can be applied is -200 kV (nominal operation at
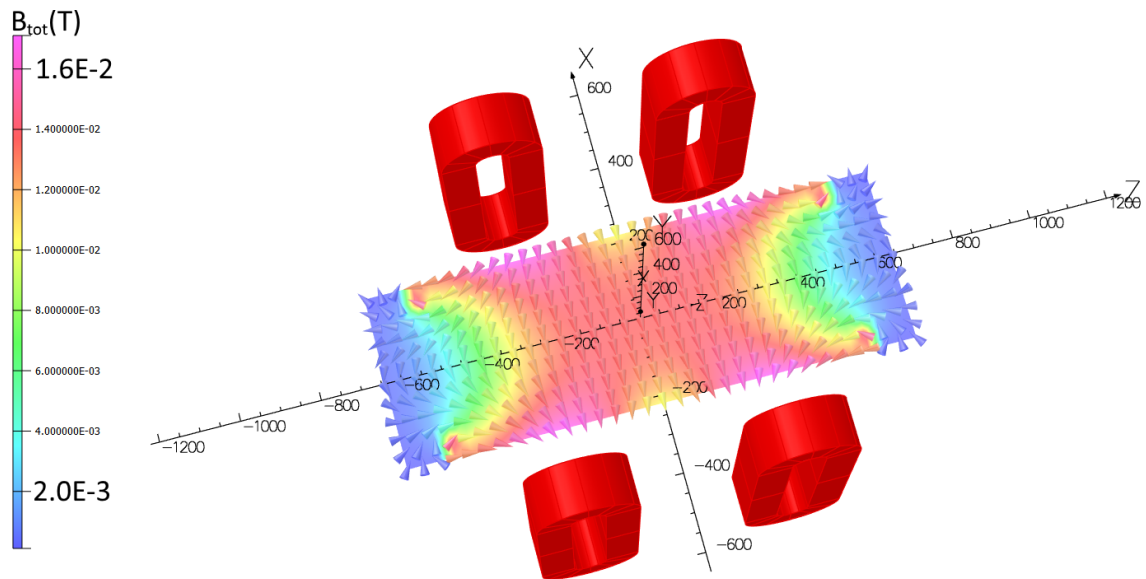
Figure 2.25.: *Shown is the B-field in the magnetic midplane of the separator. The iron yoke used in the TOSCA calculation is hidden for a better visibility.*

(a) Separator B_x distribution along the centreline

(b) Separator E_y distribution along the centreline
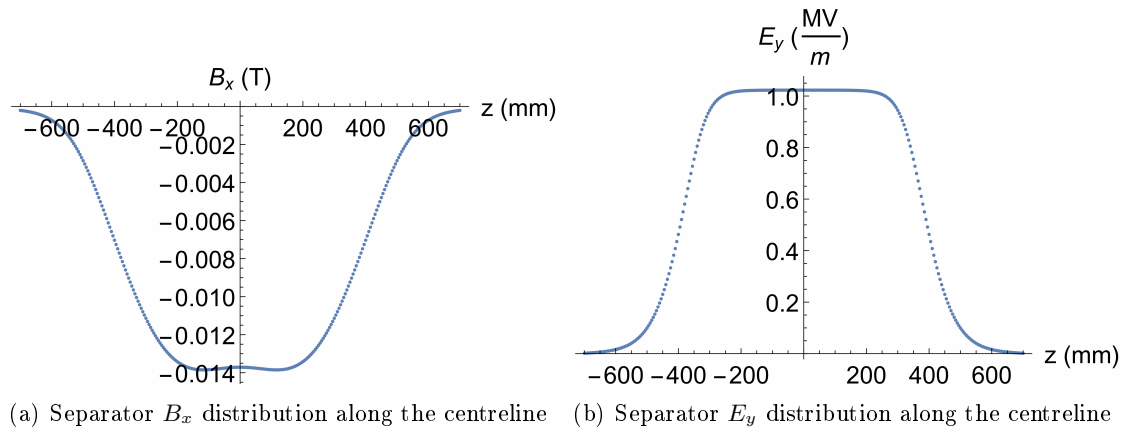
Figure 2.26.: *Shown are the field distributions for the separator E_y- and B_x-field for a corresponding voltage of 195 kV and 45 A coil current. The effective lengths are $l_{eff,E}=798$ mm , $l_{eff,B}=816/808$ mm (normalizing to $B_x(0)/Min(B_x)$)*

p=28 MeV/c: -195 kV) on the upper deflector plate with a 190 mm gap to the grounded lower plate. The fieldline distribution is shown in figure 2.27. The non-zero potential on
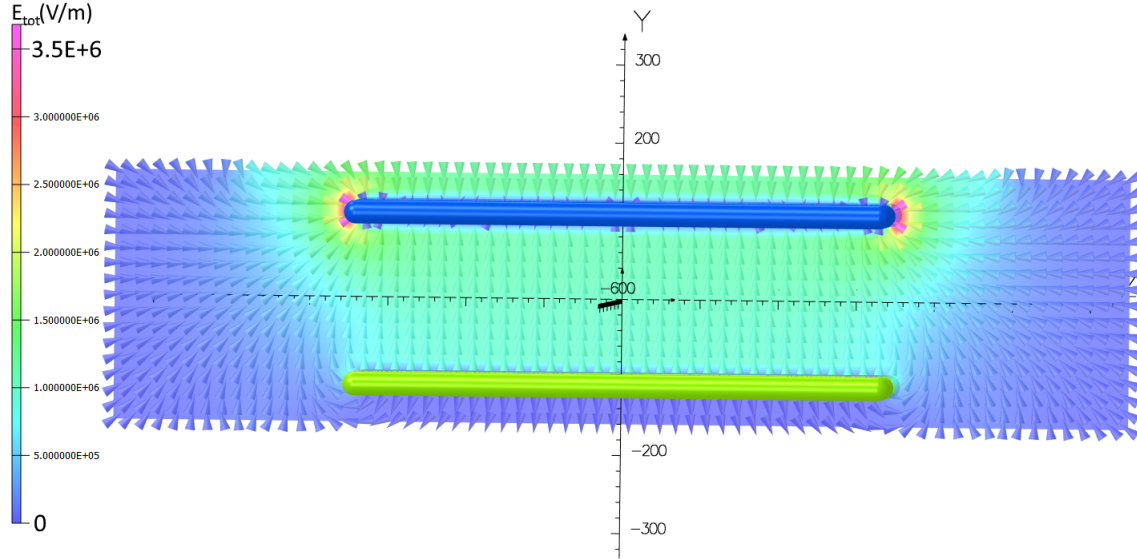
Figure 2.27.: *The electric field of the separator is generated by applying negative high-voltage to the upper electrode while leaving the bottom electrode grounded. The fieldlines shown in the plot imply an accelerating/deccelerating force for particles entering/leaving the separator. The major ticks on the z-axis of the plot are separated by 100 mm.*

the centreline causes positively charged particles to be accelerated on the US side and deccelerated on the DS side and vice versa for negative beams. Hence the reference orbit is slightly distorted, as shown in figure 2.28. However, a displaced central orbit is not
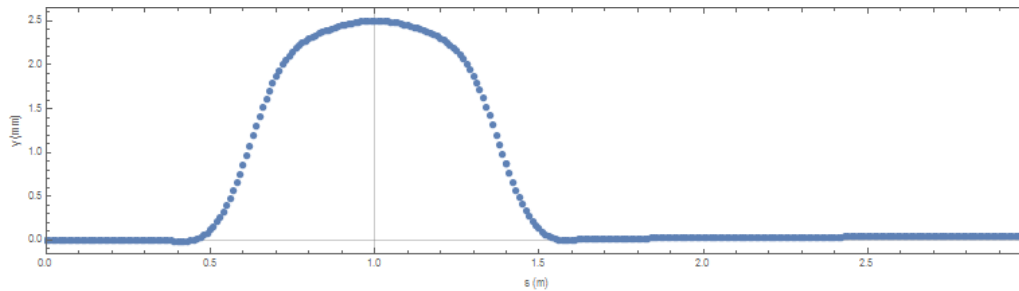
Figure 2.28.: *Example of a 10 MeV/c μ^- starting at s=0 is tracked through the superposition of the separator E-field tuned to 100 kV and the B-field equivalent to 63.2 A coil current, centred at s=1 m. The decceleration on-axis by $\sim \frac{100\ kV}{2}$ causes the reference particle to leave the central orbit at the injection and come back to the central orbit at the exit.*

the only effect of the separator field distributions but the beam profiles are affected as well. Figure 2.29 shows an example for a low momentum negative muon beam tracked through the separator. The effect is smaller for higher energies, but can still be observed. The actual particle separation happens at the downstream collimator system, following the triplet II, where the unwanted beam component is stopped.
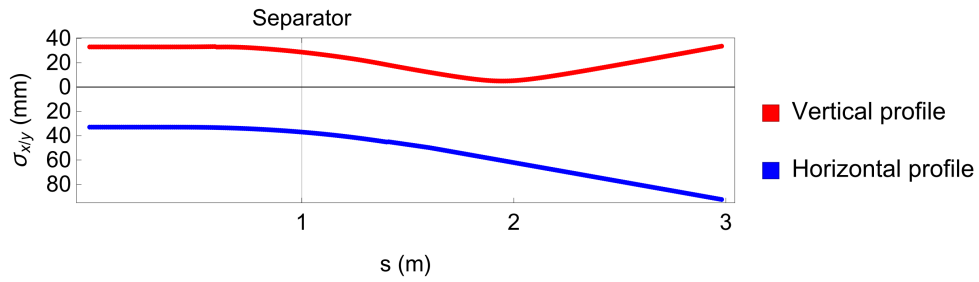
(a) The horizontal and vertical envelopes are plotted for a negative 10 MeV/c muon beam with the separator centred at s=1m
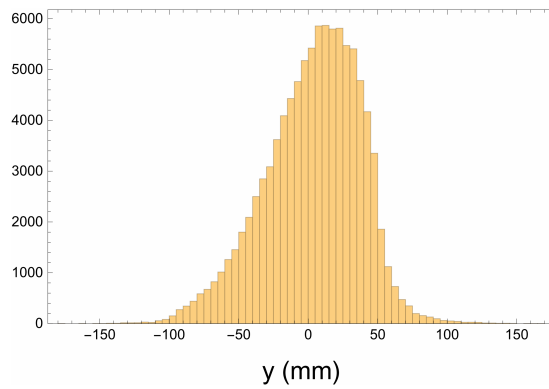
(b) Vertical particle distribution after passage through the separator

Figure 2.29.: *A Gaussian, zero-emittance, parallel 10 MeV/c μ^- beam with $\sigma_x = \sigma_y = 33$ mm is tracked in G4BL through the separator fieldmaps corresponding to 100 kV voltage and 63.1 A coil current.*

2.3.1.8. The QSK Triplet II

The triplet II that consists of QSK type quadrupoles was set up to give an intermediate focus at the DS collimator system yielding separation of the beam positron contamination as well as providing an optimal injection into the BTS for the MEG experiment. For the QSK type quadrupole no fieldmap was available, although the full description in matrix code, including fringe field integrals, is known. Together with the known field strength/current calibration this allowed to properly adjust the fringe field parameters for best agreement between the TRANSPORT higher order description and a G4BL standard element - see figure 2.30. The deviations due to the lateral flatness of the fringe field description in
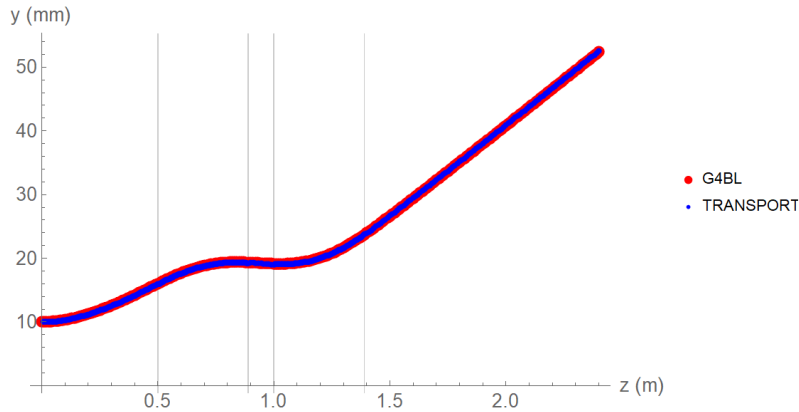
Figure 2.30.: *Shown is a QSK envelope comparison between TRANSPORT and G4BL with adjusted fringe field parameters to the G4BL standard element.*

G4BL are expected to be low, since the triplet II is in the central part of a straight section.

2.3.1.9. The intermediate collimator system & the SML horizontal steering magnet

Particles with a velocity different from the reference velocity, that is set by the Wien filter, are deflected in the vertical direction. A 6 cm thick lead collimator DS of triplet II having a 120 mm diameter aperture stops all residual beam contamination particles, that are sufficiently deflected in the separator. The aperture is introduced in TURTLE and G4BL. On the top and bottom of the vacuum tube, housing the collimator, there are $\cos\theta$-shaped coils, that introduce a horizontal steering. The deflection angle is limited to $\sim$20 mrad with focussing properties being negligable. The SML steerer is therefore only implemented in G4BL with a contant vertical field B_y that matches the effective length.
A 2 mm PE screen is mounted on a frame, that can be either moved in to cover fully the collimator aperture, or moved out of the beam. This screen was used in the past to either stop muons or produce a Michel positron beam from muon decay. During the 2016 CMBL test beam, the PE foil was replaced with a thin Luminophor screen that could be viewed through a window flange with a CCD camera to measure the beam characteristics [66].

2.3.1.10. The ASL and ASK dipoles

The similar ASL and ASK dipoles are PSI standard magnets with an H-type yoke, whereby the ASL has an iron length of 1 m and the ASK only 0.5 m. The ASL, that was used

during the 2014/2015 beam times, had a so-called open yoke, where one side of the yoke had a strongly reduced cross-section. For both magnets fringe field integral values are available. The fieldmaps had to be calculated with TOSCA. The vertical envelopes for a 180 mm gap ASL are compared in figure 2.31 for different fringe field implementations in TRANSPORT and a calculated fieldmap in G4BL. With the result of the first beam time
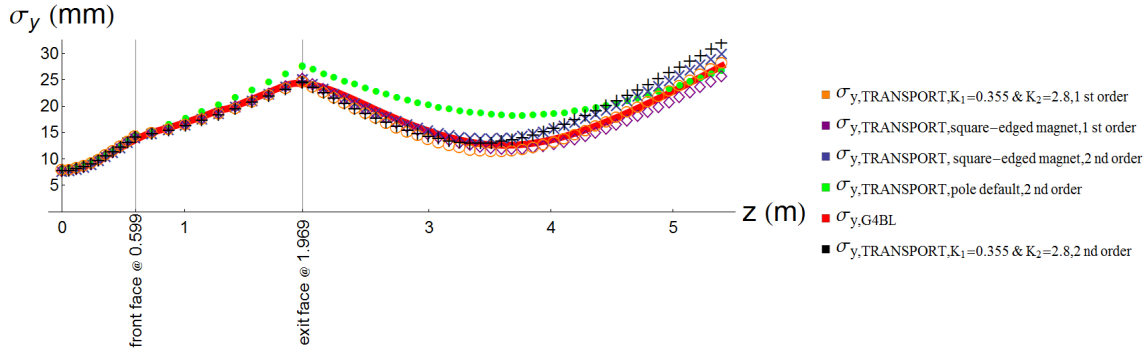
Figure 2.31.: *Shown is a comparison of the fringe field implementations of the ASL for different settings in TRANSPORT and a fieldmap based G4BL simulation.*

Dec. 2014/May 2015 the G4BL simulation showed that the ASL and ASK apertures had to be increased to achieve an optimum transmission (see section 2.6). Therefore the fieldmaps had to be recalculated with the corresponding gaps and a proper vacuum chamber design was determined. This iterative procedure is described in subsection 2.7. Furthermore the deflection angle of the ASK was changed from 60° to 65° to ensure enough space between the Mu3e solenoid and the concrete shielding wall at the end of the beam line.

2.3.1.11. The QSO quadrupoles (first part of the split triplet)

The QSO type quadrupoles that were obtained in 2013 from Conseil Européen pour la Recherche Nucléaire (CERN) and have a 125 mm pole tip radius and an iron length of 400 mm. During the design (see section 2.4) it turned out that the QSO quadrupoles are the only available quadrupoles, that were "slim" enough to allow for a concrete shielding wall between the front and the rear part of πE5, which was one of the important criteria for the CMBL. In the CMBL a doublet of 2 QSO quadrupoles share a common 250 mm diameter round vacuum tube making it the smallest aperture, apart from the collimator focus.
In the matrix code the QSO is approximated with the fringe field of a QSN (a newer PSI design standard magnet) due to their equal pole tip radius. New field measurements were carried out in 2013 at PSI and a fieldmap was provided and implemented in the simulation.

2.3.1.12. The QSM (third quadrupole of the split triplet)

The QSM is a large 20 cm pole tip radius replica of the radiation hard QSF quadrupole and is the last element of the "split triplet" and also of the CMBL. A 320 mm vacuum tube used in the QSM, that could be further increased if needed, yields a good beam transmission at the end of the beam line and partially compensates for beam optical compromises that are necessary due to spatial and element constraints in the CMBL.

The proper matrix code description of the fringe field is used in TRANSPORT/TURTLE and a measured fieldmap of the QSM has been slightly extrapolated for use in G4BL. The horizontal field distribution at the longitudinal centre is shown in figure 2.32. The effective
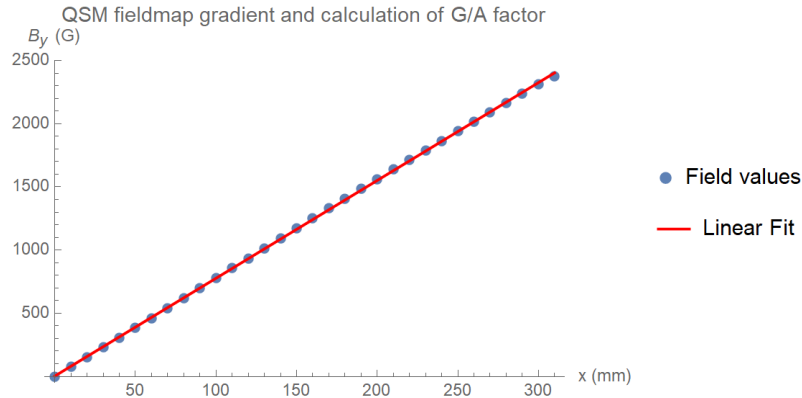
Figure 2.32.: *Shown is the QSM field decomposition in the longitudinal centre plane.*

length is ~395 mm and the gradient distribution along the longitudinal direction is shown in figure 2.33.
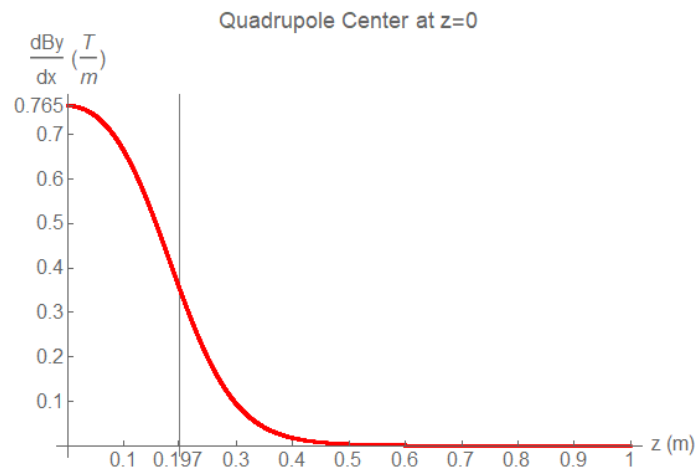
Figure 2.33.: *Shown is the longitudinal distribution of the transverse field gradient close to the centreline starting in the middle of the QSM. The vertical line indicates the extent of the effective length.*

2.3.1.13. The Mu3e solenoid

The main requirement of the entire CMBL setup is to provide a good transmission of the muon beam to the Mu3e target in the centre of the spectrometer solenoid. The Mu3e solenoid is a ~3 m long, ~2 m wide and ~2.5 m high solenoid, whereby the maximum height is constrained by the concrete ceiling (floor of πE3) to 3.5 m height. The solenoid houses the Mu3e experiment and provides a B-field of 1 T at normal operation. This component has not yet been built. The main requirements of the Mu3e solenoid are:

- Match the spatial constraints in the experimental area
- A central field of >1T with a good homogeneity
- A 1 m diameter warm bore for the installation of the Mu3e experiment components
- Iron shielding with an injection opening for a 320 mm vacuum connection

After the cancellation of the contract with Danfysik a new tendering process for the magnet started at the beginning of 2017. The implementation in TRANSPORT/TURTLE is done with a 3 m long solenoid with fringe fields that were described in subsection 2.2.3. A fieldmap of a possible Mu3e solenoid configuration was provided by Sig Martin [67]. The iron shielding significantly reduces the fringe field of the magnet(see figure 2.34), so that the matrix code description yields a reasonable agreement with the fieldmap based tracking - see figure 2.35
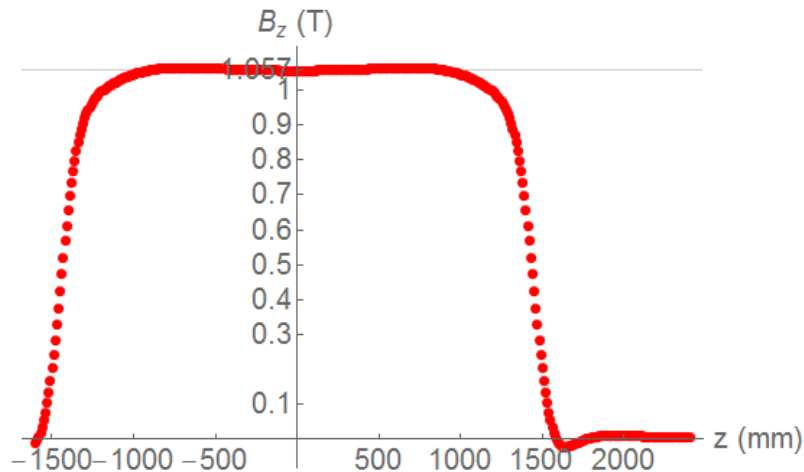
Figure 2.34.: *The effective length of the Mu3e solenoid fieldmap based on field calculations [67] for a realistic configuration is given by $l_{eff} =\sim$ 2828 mm / 2806 mm (normalizing to the field at the centre/maximum field)*
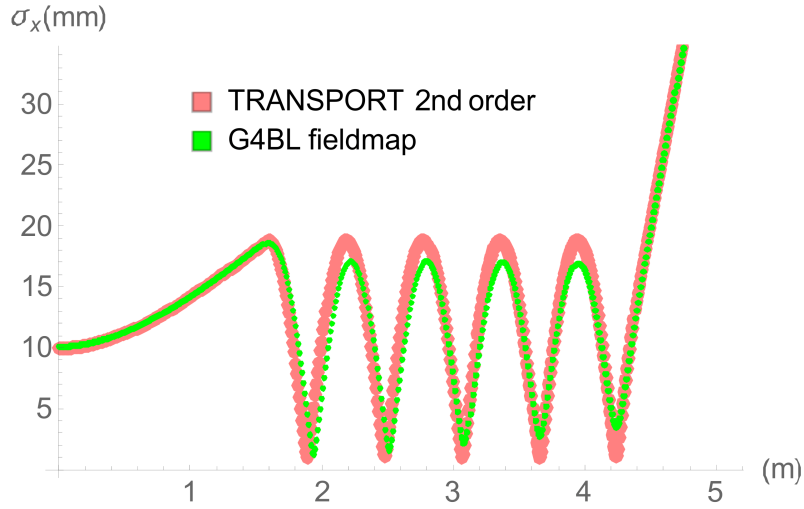
Figure 2.35.: *Shown is a comparison of the Mu3e solenoid implementation in TRANSPORT and G4BL. The iron shielding and segmented coils with properly adjusted currents provide a short fringe field extent with an almost constant central field. Therefore both approaches show reasonable agreement.*

2.4. Initial design of the CMBL

The CMBL was designed in an iterative process with the following separate stages:

- Acquisition of available elements
- TRANSPORT optimizations for different model arrangements using different elements to find an optimal solution
- TURTLE tracking for the optimal optical solution found by TRANSPORT
- Element positioning and cross-checks using the CAD model
- Two-fold modelling with G4BL: A long version starting from TgE and a short version starting close to the intermediate focus collimator system after triplet II, that is based on a modelled transverse phase space distribution obtained from measurements at that location
- Comissioning preparations

Although in the final setup QSO type quadrupoles were used, being the only available quadrupoles that allow for a shielding wall between the front and the rear parts of the πE5 area, these quadrupoles were however not used in the initial calculations. The initial simulations used similar quadrupoles with a slightly larger vacuum chamber for which the ion optical information was available at that time.

2.4.1. Acquisition of elements

For the CMBL test setup only spare elements that were already available at PSI have been used, which minimizes the beam line costs and reduces the development time. This however does not compromise the physics goals but a) means that only well-proven magnet

technology is used b) time for design and production of new magnets is saved c) with a wide-spread variety of elements available an optimum choice could be made.

The elements selected are mostly documented in the form of drawings and/or field measurements. The magnet connections partially had to be renewed. Finally only two vacuum chamber end plates and one vacuum chamber itself had to be produced as well as increasing the pole gap of the ASK dipole magnet, in order to optimize the transmission and change the final deflection angle.

2.4.2. TRANSPORT CMBL studies and TURTLE tracking

Different optical solutions with other elements and alternate positioning have been studied. Iterative modifications on the TRANSPORT script were cross-checked using the CAD model. For best optical properties in combination with the spatial constraints the split-triplet solution, as it was shown in figure 2.13, proved to be the most suitable one. The TRANSPORT result for the intial design is presented in figure 2.36. The main optical
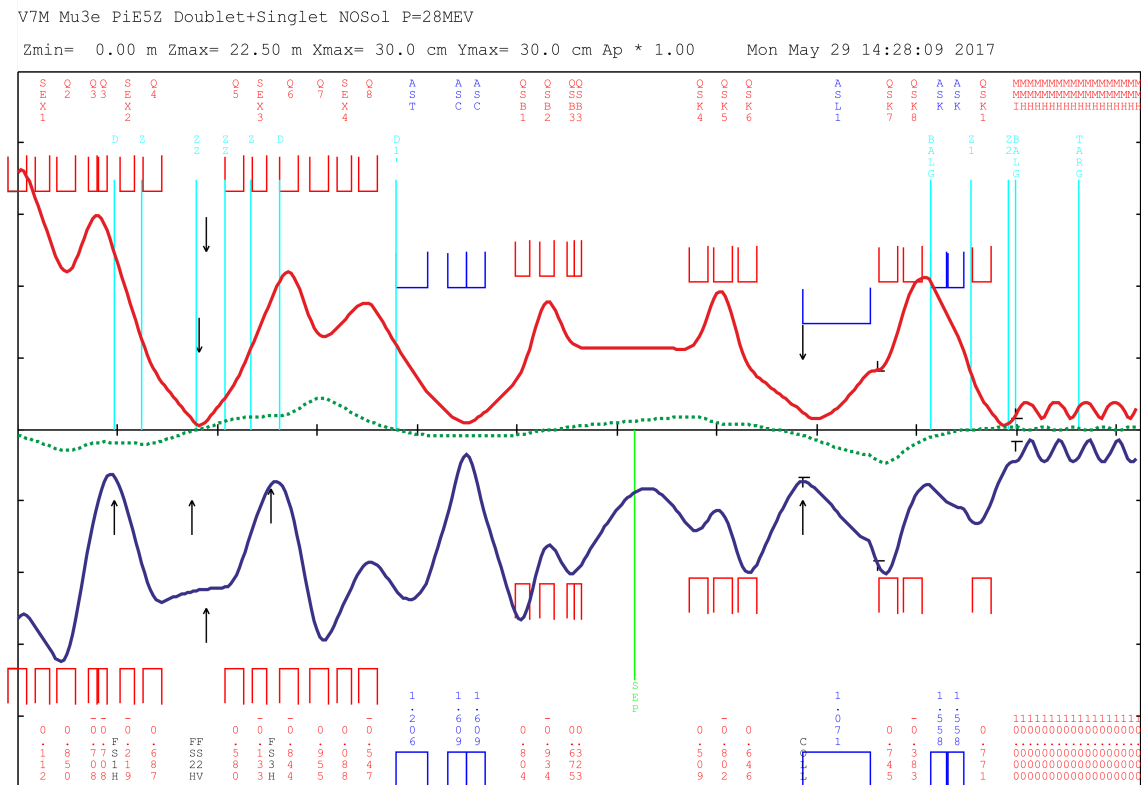
Figure 2.36.: *Shown is the 1st order TRANSPORT envelope calculation for the initial CMBL design starting at the centre of the QSF41. The red line indicates the vertical and the blue line the horizontal 1σ beam width. The green dashed line represents the calculated beam size contribution from dispersion.*

features are the following:

- Achromatic focus optimization constraints

- Vertically parallel beam in separator, with a horizontal waist for maximum separation power

- An intermediate focus between Triplet II and the ASL magnet to place a collimator system

- The smallest beam spot size at the Mu3e target

Using this input for the TURTLE calculation yields an achievable transmission rate of $\sim 70\%$ to the centre of the Mu3e solenoid with the beam spot characteristics at the Mu3e target shown in figure 2.37. The beam spot requires further tuning, however the

Lego Plot No 69 (lin) at z= 21.242 m (TAR)

Mean1 = -0.587
RMS1 = 2.034
Mean2 = 0.032
RMS2 = 3.253
Corr = 0.595
Area/pi = 5.316
Sum = 64778
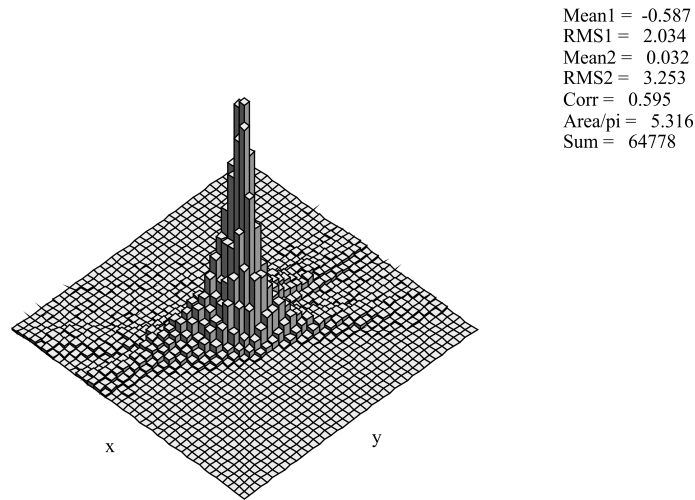
(a) Beam Profile at the target location

Histogram No 65 (lin) at z= 21.242 m (TAR)

Mean = -0.505
RMS = 2.442
Sum = 70286

Histogram No 66 (lin) at z= 21.242 m (TAR)

Mean = -0.002
RMS = 3.290
Sum = 65163
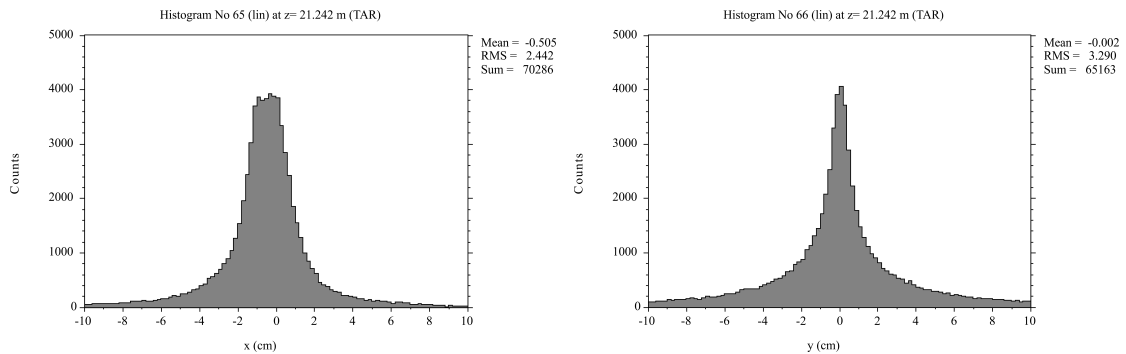
(b) Horizontal beam distribution at the target location

(c) Vertical beam distribution at the target location

Figure 2.37.: *The lego plot and its 1-dimensional projections correspond to the expected beam profile at the centre of the Mu3e solenoid based on a 2nd-order TURTLE tracking calculation. A transmission of ~ 70 % is observed and further optimization promise a smaller footprint on the target. The dimensions are quoted in cm.*

transmission rate confirms this solution and optimization of the experimental setup is regarded to further increase the final rate and achieve the desired beam properties at the target. Therefore the beam line arrangement shown above with the optimized settings represents the baseline solution of the matrix code simulation of the CMBL.

2.4.3. Initial G4BL simulations

As outlined in the previous section 2.2.3 the G4BL simulation can be quite sensitive to the input settings and the scripts quickly become complex with reasonable accuracy required for fieldmaps, power supply current values and the alignment parameters, as the simulation reaches a more refined state. Therefore the simulation scripts used have been split into parts with a framework of Mathematica [54] and Python [68] notebooks set up for input, such as positions or currents, further processing, analysis, cross-checks and optimization. An overview is shown in figure 2.38. The main script comprises of the global parameters,
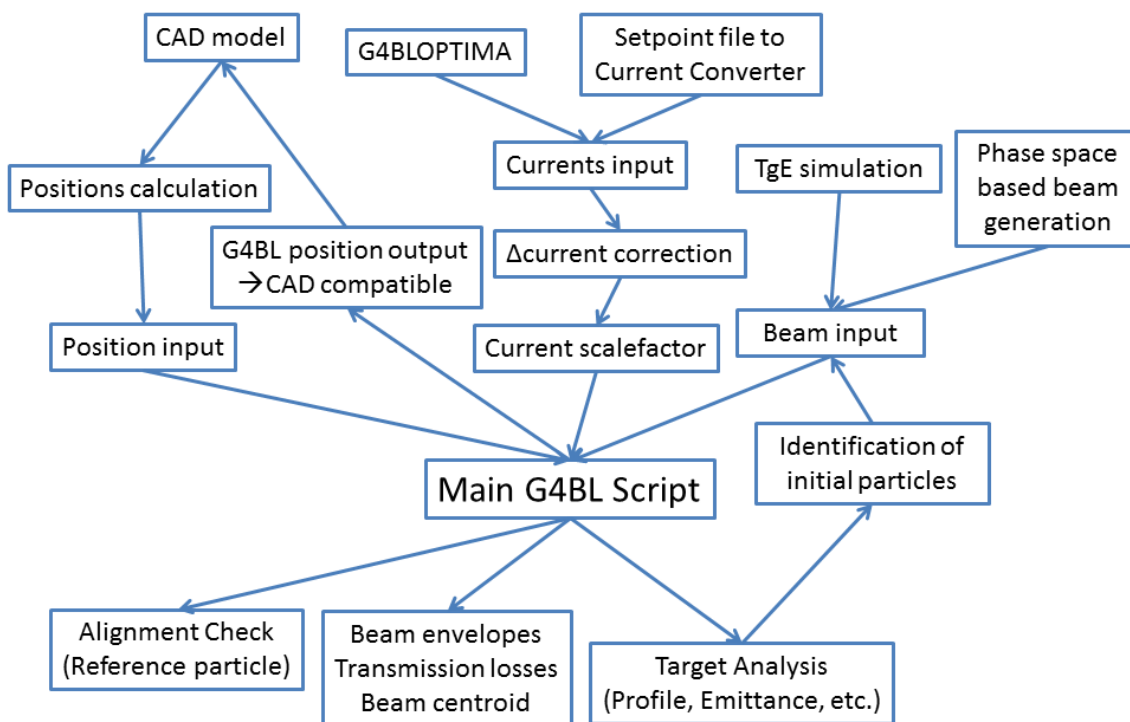
Figure 2.38.: *Shown is an overview of the G4BL simulation and auxiliary scripts that were used for the CMBL design. The steps and capabilities of this framework are explained in the text.*

such as the used physics package or the simulation stepsize, it then loads the beam file and defines all elements and apertures and arranges the beam line. Positions can be easily adapted from the CAD model and are quickly prepared with a separate notebook in an additional file, that is loaded from the main file. A position output command in the main

file produces a survey of all the element positions in the beam line. This output can be converted and overlayed on the CAD model as a cross-check.

Magnet current input via a separate file can be made in 3 ways:

- Manually in the dedicated file

- Automatically via the *Optima G4BL* cross-platform Python optimization code (see appendix 4.4)

- So-called setpoint files from the control software that is used in the experimental area, these can be converted with a separate notebook and the current file overwritten with the values that were actually used during the beam time

Following this the currents are corrected by the observed ∼constant current offsets between "IST" and "SOLL" value that is determined for each element individually. The corrected currents are then scaled in a separate script by the current values for which the fieldmaps have been generated or the known G/A (field/current) factors in the case of the QSKs. The derived strengths are then passed to the main script and applied to the single elements.

The beam files used for the simulations are taken either from a simulation of TgE [66], or are generated with TURTLE and converted with a notebook to BLTrackFile format that is used in G4BL. The TURTLE beam is either used for the initial simulations starting from TgE with the same beam parameters as used in TRANSPORT/TURTLE or are used to generate new beams that are distributed according to the reconstructed phase space in the latter part of the beam line. The phase space reconstructions are determined and adapted for the different beam line settings and setups. A separate Python script has been prepared that identifies those particles out of the initial beam file that are transmitted to a certain point of the beam line and outputs a corresponding BLTrackFile for further use. Separate notebooks have been set up to analyze a) the G4BL output for the reference particle, which is important for the determination of a proper element alignment and time-of-flight analysis during other beam times b) the beam propagation, comprising of RMS envelopes, centroid and particle losses throughout the beam line c) beam properties on detectors, in order to determine the beam profiles and phase space distributions.

The G4BL calculations follow a two-pronged approach: a) A simulation that starts at the production target TgE which is based on either the initial muon phase space mimicking the TRANSPORT starting values or a muon distribution from a production target simulation based on a low-energy parametrization of the pion production cross section [69, 66] b) a G4BL simulation of only the last part of the CMBL that uses a beam, corresponding to the fitted phase space distributions, based on previous measurements or more refined by newer measurements.

2.4.3.1. A G4BL beam line model starting from TgE - "Long Version"

The G4BL model of the full beam line was developed over a longer period during which standard elements in the simulation were replaced by appropriate fieldmaps, elements were changed and new fieldmaps determined as well as more accurate descriptions of beam line apertures implemented. Furthermore, the structure of the input and the analysis scripts changed and improved to the status shown in figure 2.38. In the beginning a beam generated based on the TRANSPORT/TURTLE scripts was used, however this did not allow absolute rates to be quoted but only transmission factors. In the most recent version a

target optimization study has been carried out [66] providing a realistic beam input from a separate simulation of the proton beam impinging on the muon production target and based on a low-energy cross-section parametrization for pion production [69]. The beam that is used in the following simulation corresponds to $2.5 \cdot 10^{12}$ protons on TgE and cuts restrict the beam file to only muons with momenta between 0-40 MeV/c. The beam line settings equal the experimentally determined beam line settings that were used in the CMBL 2016 test beam.

The graphical simulation output of the full beam line starting from TgE up to the SML/collimator system is shown in figure 2.39. The beam shown in the figure represents a subset of 100 μ^+ that make it to the end of the beam line. Due to the isotropic muon generation and the
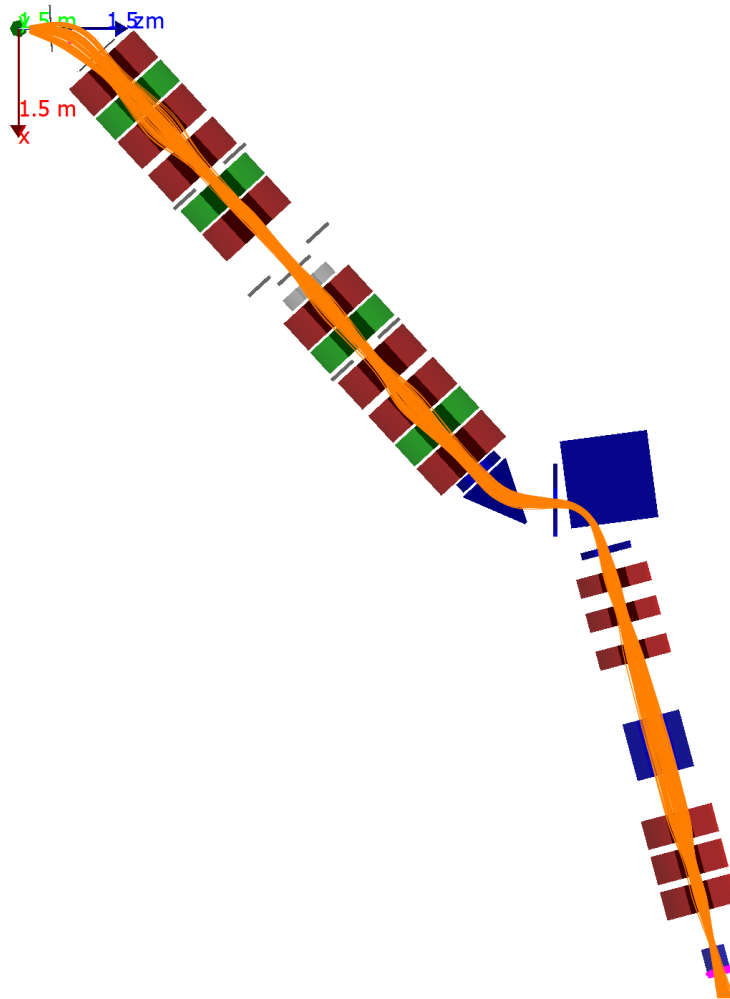
Figure 2.39.: *The graphical output of the G4BL simulation starting from TgE to the SML/collimator system shows the bottom half of the beam line elements, additional apertures and the trajectory of 100 μ^+ reaching the end of the beam line that were selected from the beam file.*

loose momentum cut, that takes into account muons with momenta between 0-40 MeV/c, only a small fraction $\sim 1\permil$ of the started $\sim 2.3 \cdot 10^7$ muons reach the SML/collimator system. The decreasing rate of muons, that propagate along the beam line and are partially

lost at the apertures, is determined by normalizing the number of muons in the simulation to the ratio of protons used for the production target simulation and the nominal proton beam current of 2.2 mA. The rates/losses along the beam line are shown in figure 2.40.
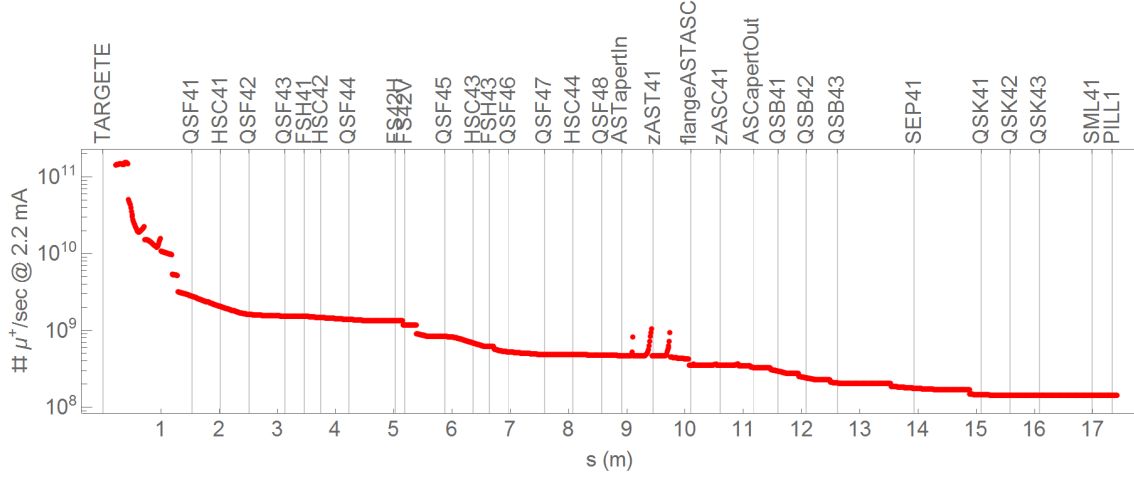
Figure 2.40.: *Shown are the beam rates along the beam line starting from TgE up to the SML/collimator system. The spikes in the AHSW dipole field between the production target and the QSF41 and at the AST ASC dipoles are artefacts from counting the number of muons near a centreline vertex. The transmission to the usual measurement position DS of the SML is $1.43 \cdot 10^8$ μ^+/s at 2.2 mA proton current equivalent. However, for this simulation the Pb collimator in the SML/collimator system was removed to enable enhanced statistics the simulation was done without muon decay. Therefore the transmission rates have to be scaled by their survival probability, that is shown in figure 2.41. The simulated rate at the measurement position then equals $1.30 \cdot 10^8$ μ^+/s.*

All G4BL simulations are done with muon decay set to disabled for a higher statistics. Therefore all particle rates have to be scaled by the survival probabilities according to velocity $\beta = \frac{v}{c}$ / Lorentz factor γ, life time τ and travelled pathlength s.

$$F\left(s, \beta, \gamma, \tau\right) = \mathrm{e}^{-\frac{s}{\beta \gamma c \tau}} \tag{2.24}$$

The survival probabilities for different particle types are shown in figure 2.41. As can be seen, 28 MeV/c pions essentially decay before reaching the experimental area which naturally reduces the beam contamination from pions to a negligible fraction. The rate that follows from the G4BL simulation and the survival probability for the measurement position DS of the collimator is $1.30 \cdot 10^8$ μ^+/s, which is slightly higher than what was measured during the beam times (compare with the results in section 2.8).

The beam envelopes and centroid of all muons with momentum $0 \leq p \leq 40$ MeV/c as well as for only those muons that reach the end of the beam line are shown in figure 2.42. As can be seen the horizontal mean $\bar{x}$ is partially off centre by several centimetres, which is caused by a misalignment at the very beginning of the beam line. The beam comes in off centre at the QSF41 and is therefore deflected back and forth in the B-field of the subsequent elements. The alignment of the elements near TgE was checked again and found to agree with the drawings. Furthermore, as the calculated fieldmap of the AHSW has been used, which includes the iron of the adjacent QSF41 this fieldmap is regarded as being reliable to the accuracy of the TOSCA calculation. The apertures used for the
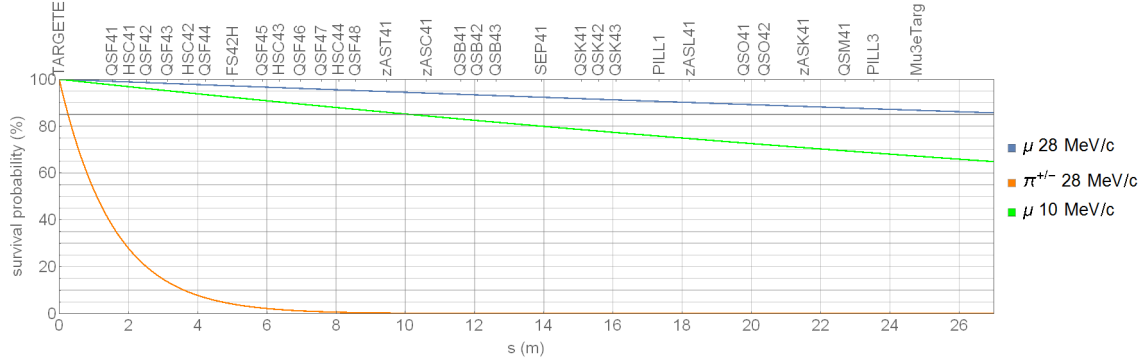
Figure 2.41.: *The survival probabilities are shown for 28 MeV/c muons and pions as well as for 10 MeV/c muons. Due to their shorter lifetime, there is only a negligible pion beam contamination left in the experimental area for surface muon momenta or below. The nominal measurement position DS of the SML is denoted by "PILL1".*

AHSW are located at the narrowest points at the entrance and exit flange and have sizes according to the drawings. The injection into the QSF41 in the simulation may suffer a little as the QSF fieldmap was replaced with a QSM fieldmap which should have almost the same charcteristics. In addition beam measurements show a strong dependence of the beam rate on the injection quadrupoles QSF41 and QSF42, which might give a hint, that these elements not only introduce focussing power but also steering.

The conclusion from this is that a slight misalignment in the beam line setup is likely. Thoughts on how one could overcome this issue and increase rates for all different particle types are explained in appendix section 4.3.

The beam profile at the measurement position DS the SML/collimator system is shown in figure 2.43. The beam at the measurement position is off-centre in both directions. The momentum distribution of the muon beam in the G4BL simulation is compared at the centre of the QSF41 and the measurement position DS the SML/collimator system in figure 2.44. As can be seen the momentum distribution in the centre of the QSF41 shows the expected kinematic edge (equation 1.17) and is still mainly determined by the kinematics at source although the expected $\sim p^{3.5}$ behaviour for momenta below the kinematic edge is already cut. At the DS measurement position the kinematic edge is still visible but the full distribution is convoluted with the momentum acceptance of the beam line. All relevant beam parameters at the centre of the QSF41 (looking either at the full beam or only at the subset of muons that make it to the end of the beam line) and the DS measurement location are listed in table 2.2.

The G4BL simulation starting with the realistic beam generated via pion production at TgE reproduces some of the important features of the beam line very well. Especially, the transverse emittances ϵ_x and ϵ_y are in good agreement with the measurements made during the commissioning runs of the CMBL as well as the rate at the Pill1 position, which is in good agreement with the measurement.

However the simulation shows some significant deviations to the measurements, such as the focus position DS of Triplet II, which is shifted US somewhat. This could be a hint, that the beam either enters the Triplet II with different properties or the implentation of the QSK quadrupoles does not properly reflect the real field distribution and introduces
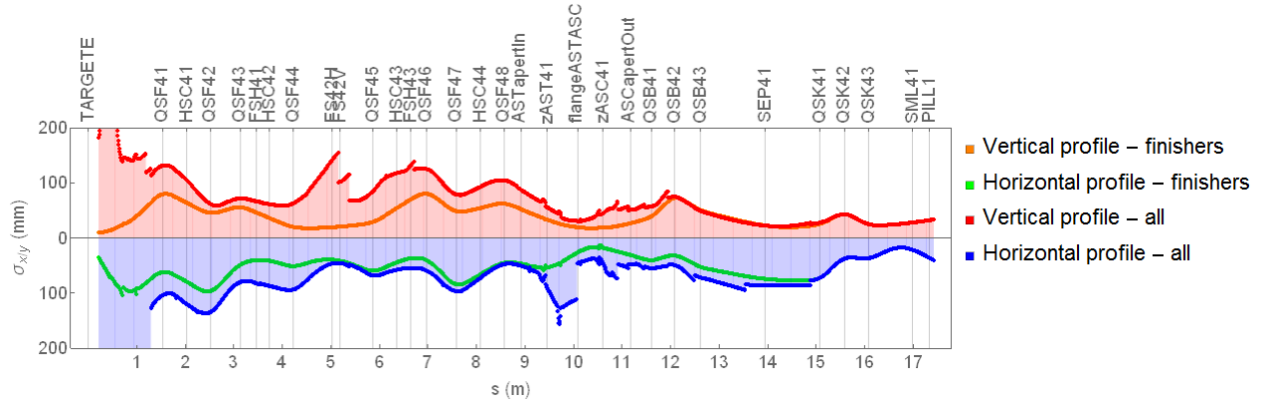
(a) Horizontal and vertical envelopes
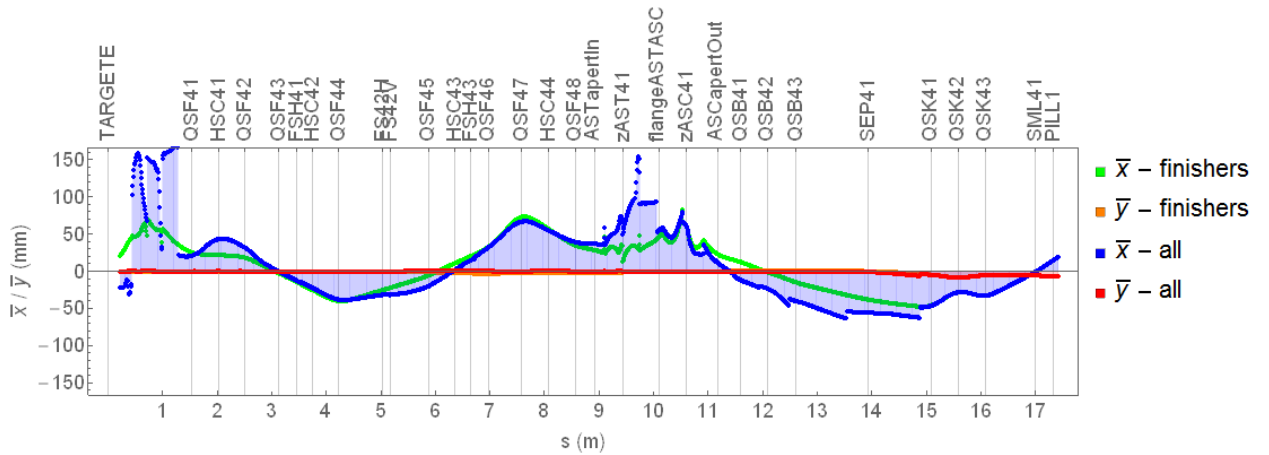
(b) Horizontal and vertical beam centroid

Figure 2.42.: *Shown are (a) the horizontal and vertical RMS beam envelopes and (b) the centroid of all muons in the momentum range 0-40 MeV/c (blue and red lines) and only the subset of muons that is transmitted to the end (green and orange lines). The usual measurement position DS the SML/collimator system is denoted by "PILL1". Discontinuities can be identified associated with aperture cuts that are also visible in the rate plot 2.40 and also artefacts stemming from the wrong assignment, when the centreline changes the direction.*
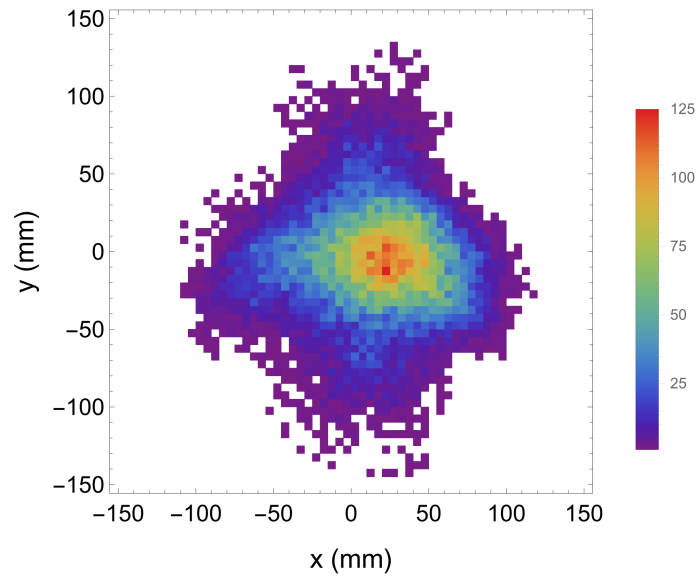
(a) Surface muon beam profile at the measurement position DS the SML/collimator system
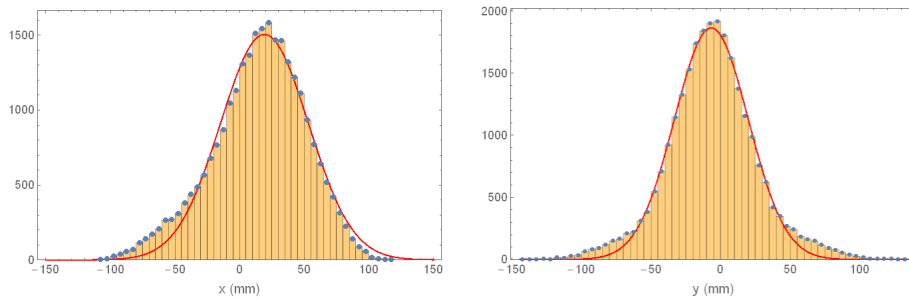
(b) Horizontal surface muon distribution DS the SML/collimator system

(c) Vertical surface muon distribution DS the SML/collimator system

Figure 2.43.: *Shown are the surface muon beam profiles at the measurement position DS the SML/collimator system. The beam parameters are listed in table 2.2.*

(a) Surface muon beam momentum distribution at the centre of the QSF41

(b) Surface muon beam momentum distribution at the measurement position DS the SML/collimator system
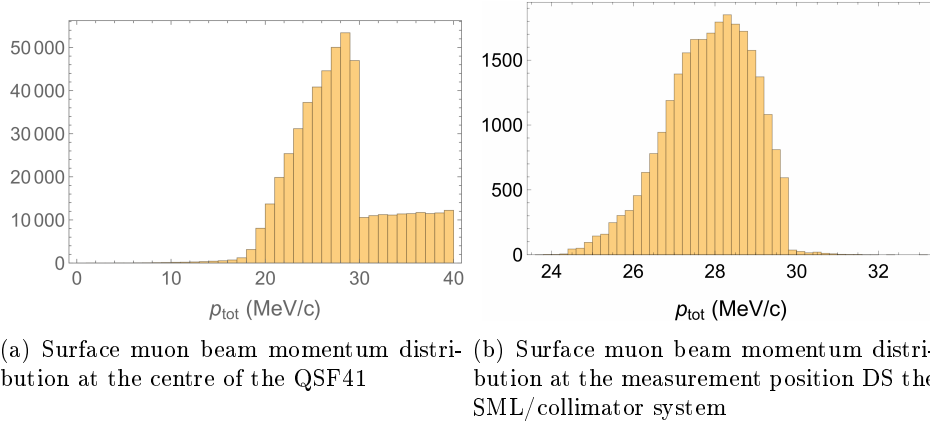
Figure 2.44.: *Shown are the momentum distributions, derived from simulation, at the centre of the QSF41 and the Pill1 position.*

Table 2.2.: *Summary of beam profile parameters at a standard pill measurement position DS the SML/collimator system and at the centre of the QSF41 either taking into account only a subset of muons that make it to the pill measurement position or looking at all muons for the G4BL simulation starting from TgE.*

Location/subset	pill DS collimator	QSF41 centre (all)	QSF41 (finishers)
$\bar{x}$ (mm)	14.9	25.3	25.4
$\bar{y}$ (mm)	-6.3	0.0	-0.4
RMS_x (mm)	35.7	98.3	62.2
RMS_y (mm)	32.2	119.7	79.3
σ_x (mm)	34.0	69.7	78.2
σ_y (mm)	26.5	145.5	83.97
$\rho_{x,x'}$	0.87	0.21	-0.34
$\rho_{y,y'}$	0.71	0.52	0.99
$\epsilon_{x,rms}$ (mm·mrad)	935	22040	2357
$\epsilon_{y,rms}$ (mm·mrad)	421	4529	301
$\bar{p_z}$ (MeV/c)	27.79	27.10	27.83
$\bar{p_{tot}}$ (MeV/c)	27.87	27.82	27.87
RMS_{p_z} (MeV/c)	1.07	5.11	1.07
$RMS_{p_{tot}}$ (MeV/c)	1.07	5.01	1.07
Rate ($\frac{\mu^+}{sec}$ @ 2.2 mA proton current)	$1.30 \cdot 10^8$	$2.68 \cdot 10^9$	$1.30 \cdot 10^8$

too much focussing power. Furthermore, the beam centroid is offset from the centreline throughout the major part of the beam line and also at the Pill1 position. It has to be emphasized that the simulation parameters were directly taken from the empirically determined magnet values in the real setup, which are sensitive to known effects such as misalignment, hysteresis, current fluctuations or drifts, leading to a range of possible values for each parameter. Therefore, as in the real case of the experimental tuning of the beam to maximize the rate, shown to be necessary even for the same setup but for different measurement periods, this approach should also be adopted for the simulation. Thus allowing the initial values to be varied within their uncertainties to maximize the rate. Therefore the beam profiles of the G4BL tune that provides maximum transmission must be compared with the measurements made in the experimental area as a validation test. The optimized G4BL validation will be presented in [66] in the context of background studies for the Mu3e experiment.

In conclusion the full beam line simulation starting from protons on TgE, shows that an advanced level has now been reached. The simulation results achieved using parameters strictly taken as raw input from the available sources show good agreement for important parameters such as the central momentum, transverse phase space and the rates and can be regarded as a success and motivation to continue this approach for a final most realistic description of the Mu3e beam line in the future.

The optics is not fully validated yet, therefore the simulation has only been presented up to the first stage measurement position DS the SML/collimator system for which comparative measurements from the CMBL beam campaigns are available. However, the main simualtion model used for the CMBL was based only on the latter-part of the beam line post Triplet II. This was initially more refined than the long version and used measured phase-space data to define the beam input. This is described in the next subsection.

2.4.3.2. Initial G4BL model of the last part of the beam line based on phase space reconstruction - "Short version"

The main G4BL simulation program used also for the CMBL optimization procedures on the Mu3e target is based on a subset of the full beam line, in which the beam starts right after Triplet II and is transmitted to the end of the beam line.

As for the initial stages of the CMBL layout with the optimal element positions not yet determined and the magnet strengths still requiring optimization, the most urgent task was the beam input definition. Therefore the phase space distribution had to be determined. Profile measurements with fixed magnet values that were formerly made at different distances on the DS side of the SML/collimator system were analyzed and the transverse phase space distributions determined. The formalism based on transfer matrices is described below.

$$\rightarrow \sigma_{hor}\left(s=l\right) = R_{Drift,l} \times \sigma_{hor}\left(0\right) \times R_{Drift,l}^{T} \tag{2.25}$$

where $\sigma_{hor}\left(0/s=l\right)$ is the beam matrix of the horizontal sub-phase space at the starting point / after a drift of length l. $R_{Drift,l}$ is the transport matrix of a drift with length l. With the drift matrix given as:

$$R_{Drift,l} = \begin{pmatrix} 1 & l \\ 0 & 1 \end{pmatrix} \tag{2.26}$$

and the beam matrices $\sigma_{hor}\left(0/s=l\right)$ given as:

$$\begin{pmatrix} x_m^2\left(0/s=l\right) & x_m\left(0/s=l\right)\theta_m\left(0/s=l\right)\rho_{x\theta}\left(0/s=l\right) \\ x_m\left(0/s=l\right)\theta_m\left(0/s=l\right)\rho_{x\theta}\left(0/s=l\right) & \theta_m^2\left(0/s=l\right) \end{pmatrix} \tag{2.27}$$

the beam matrix $\sigma_{hor}\left(s=l\right)$ can then be expressed in terms of the coefficients of the initial beam matrix:

$$= \begin{pmatrix} x_m^2\left(0\right) + 2l\theta_m\left(0\right)\rho_{x\theta}\left(0\right)x_m\left(0\right) + l^2\theta_m^2\left(0\right) & l\theta_m^2\left(0\right) + x_m\left(0\right)\rho_{x\theta}\left(0\right)\theta_m\left(0\right) \\ l\theta_m^2\left(0\right) + x_m\left(0\right)\rho_{x\theta}\left(0\right)\theta_m\left(0\right) & \theta_m^2\left(0\right) \end{pmatrix} \tag{2.28}$$

The information that is accesible by measurement is the beam profile. Therefore at least three measurements are required to derive the full first-order horizontal phase space information $(x_m\left(0\right), \theta_m\left(0\right), \rho_{x\theta}\left(0\right))$, which in this case are provided by different drift lengths l_k:

$$x_m\left(s=l_k, x_m\left(0\right), \theta_m\left(0\right), \rho_{x\theta}\left(0\right)\right) = \sqrt{x_m^2\left(0\right) + 2l_k\theta_m\left(0\right)\rho_{x\theta}\left(0\right)x_m\left(0\right) + l_k^2\theta_m^2\left(0\right)} \tag{2.29}$$

By fitting the phase space parameters $x_m\left(0\right)$, $\theta_m\left(0\right)$ and $\rho_{x\theta}\left(0\right)$ to the measurements $x_m\left(s=l_k, x_m\left(0\right), \theta_m\left(0\right), \rho_{x\theta}\left(0\right)\right)$ the initial phase space is fully determined.

The initial geometrical layout of the G4BL simulation of the last part of the beam line (so-called "short version") is mainly determined by the spatial constraints imposed by the area walls and the already installed beam line components. The alignment of the dipole magnets is described in 2.5.1.1. Once the simulation was set up, magnet currents derived from the TRANSPORT solution were used as a starting point to optimize the beam line for a maximum transmission to the Mu3e target at the centre of the Mu3e
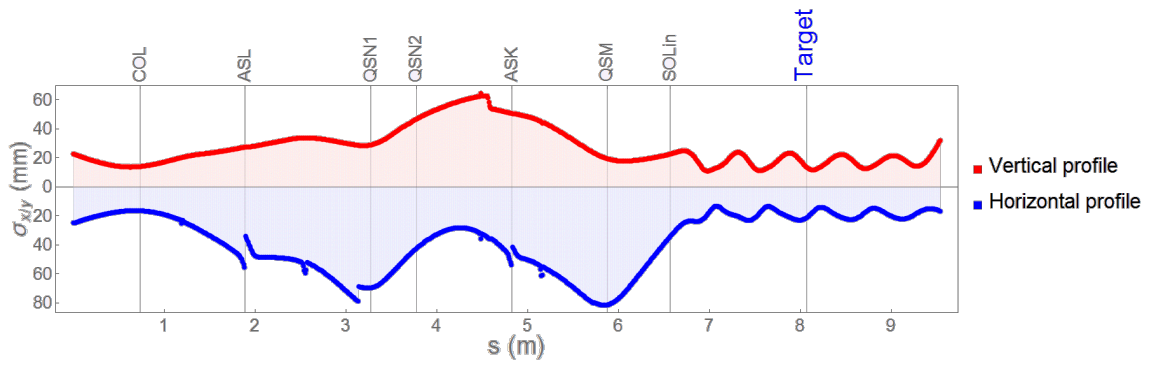
(a) Initial G4BL simulation (short) : beam envelopes
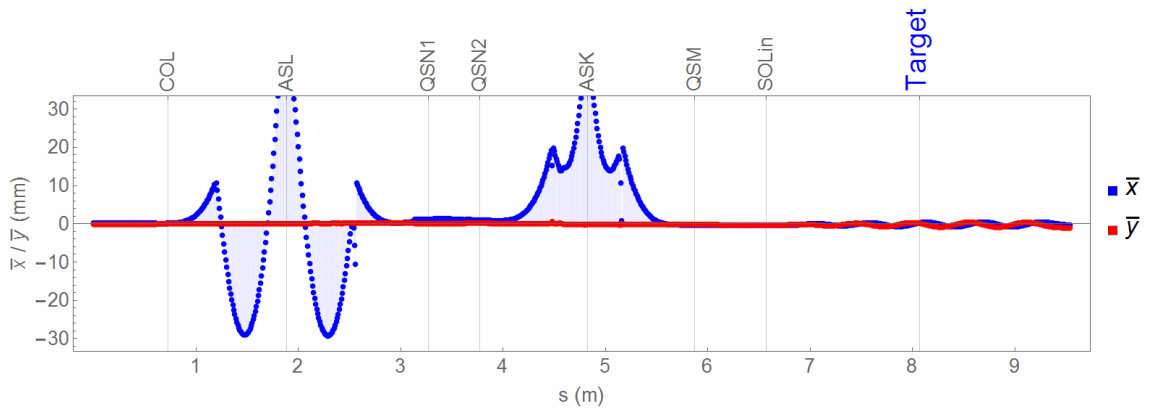
(b) Initial G4BL simulation (short) : beam centroid

Figure 2.45.: *Initial G4BL simulation : Envelopes and beam centroid from the measurement position DS the collimator to the Mu3e target.*
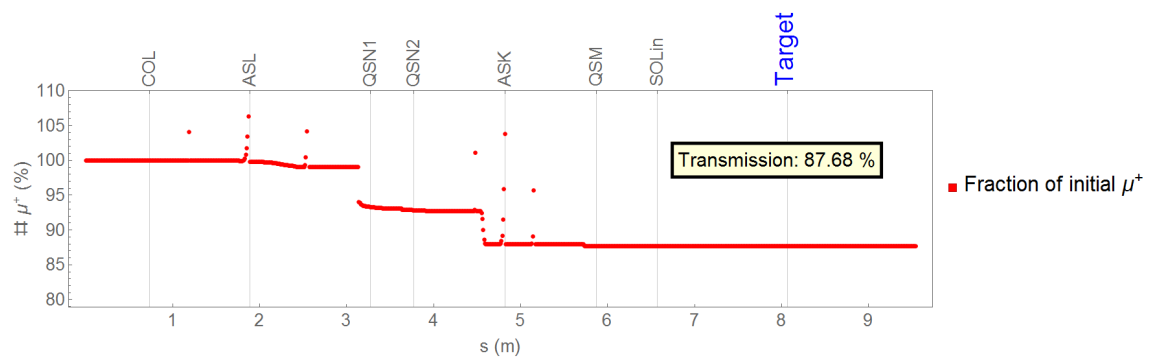
Figure 2.46.: *Shown is the transmission efficiency from the measurement position DS the collimator to the Mu3e target resulting from the initial G4BL simulations.*

solenoid. This optimization was done with the *Optima G4BL* code, that is described in the appendix section 4.4. The beam envelopes and centroid are shown in figure 2.45 and the corresponding transmission plot is shown in figure 2.46. The G4BL simulation shows a good transmsission to the centre of the solenoid, although carried out using loose aperture constraints in the quadrupoles and in the solenoid since the inner structure of the detector and the target size was not clear at that time. The validity of the initial calculations for the "short version" is mainly based on the validity of the aperture implementation and the phase space of the initial beam. Since the beam has to pass the same collimator system as in the case of the measurements, that are the basis of the phase space reconstruction at the collimator focus (see figure 2.36), the beam properties are regarded as similar and justify this approach. However as later measurements show (see next sections) the horizontal phase space is underestimated. The reason being the initial optics used for the phase-space measurements, which stemmed from a MEG optimization whereas the optics used for Mu3e at this location is somewhat different. New phase-space measurements at the collimator using the Mu3e optics are presented in the next section.

2.5. CMBL test beam campaign 2014/2015

The first two 4 week beam test periods of the CMBL setup started at the end of 2014 and continued at the beginning of the 2015 beam period. The preparations that were done in advance and also during the staged setup involved several people and groups from PSI and comprised of:

- Upgrade of infrastructure (cooling water and electrical connections) for the additional elements
- Application of floormarks for the alignment based on the simulation / CAD model
- Preparations of the magnets such as vacuum tests
- Local arrangement of the πE5 shielding wall at the entrance
- Acquisition of further vacuum equipment for the larger beam line
- Evaluation of a positioning procedure for the ASK and QSM elements to be placed under the concrete ceiling

The setup procedure and results of the first combined 2014/2015 test beam campaign are presented in the remainder of this section.

2.5.1. Setup for the CMBL test beam 2014/2015

For the setup of the CMBL a staged approach was chosen that comprised of measurements at three distinct positions that are denoted as "Pill1..3" in figure 2.47. The stage
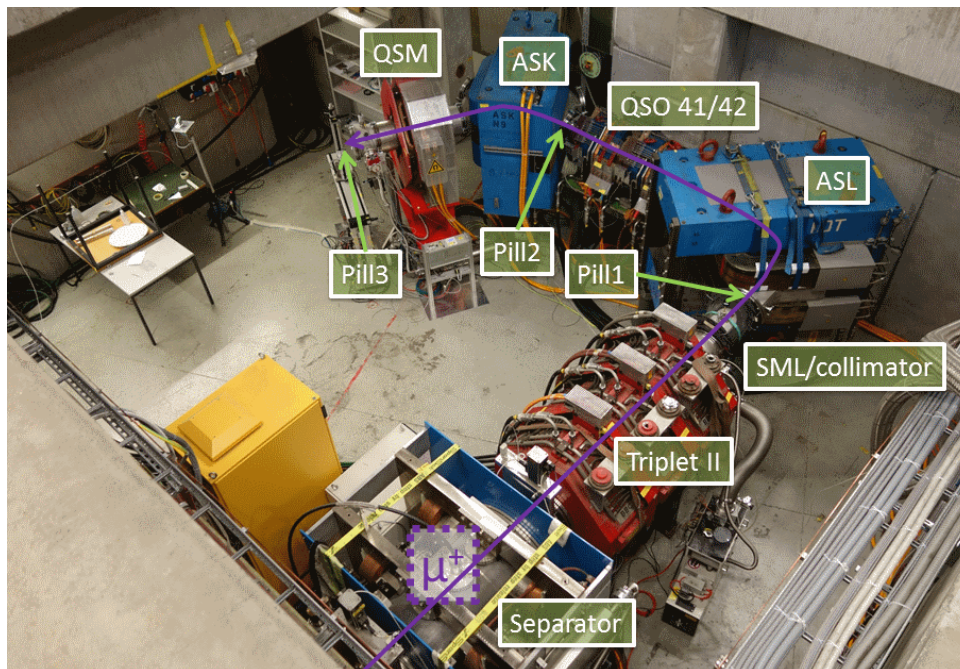
Figure 2.47.: *Shown is the full setup of the CMBL for the 2014/2015 test beam. The measurements were carried out at 3 different positions which are indicated as "Pill1..3" in the picture. The Pill1 position is a measurement position that was also used for the beam tuning of previous MEG beam times. The Pill3 location coincides with the injection point to the planned Mu3e solenoid.*

1 measurement position was at the intermediate focus, also used as a normalization location for MEG data-taking periods. After the completion of the stage 1 beam tuning and data-taking the ASL and the QSO doublet were positioned according to the floor marks and measurements were continued at stage 2. Finally the ASK and the QSM quadrupole were set up, whereby both elements had to be positioned underneath the concrete floor of the πE3 area. The QSM could be positioned simply whereas the ASK needed more effort as shown in figure 2.48, reqiring a counter-balanced beam and the temporary removal of Triplet II to position it.

Figure 2.48.: *By attaching the ASK dipole magnet to a steel beam with a 10 ton concrete block as a counterweight, the ASK could be accurately placed below the πE3 area floor.*

The careful alignment of the magnets was done with plumb lines on the floor marks, spirit-levels and various distance measurement devices, the optimum dipole magnet and vacuum chamber positions having been determined from the G4BL simulations using the calculated fieldmaps. An additional vaccum pump stand and connections were required to maintain the extended beam line vacuum at the few 10^{-6} mbar level.

2.5.1.1. Dipole alignment

The dipole alignment in the G4BL simulation is not only important in obtaining the proper simulation optics, but with a realistic fieldmap implementation allows the coordinates for the CAD model, as well as the floormarks for the experimental setup in the area to be determined. The simulation alignment procedure involves shifting the position of the dipole and tracking a 28 MeV/c reference particle through the most homogeneous part of the fieldmap until the it matches the reference trajectory for the corresponding bending angle and exits on the centreline. Figure 2.49 illustrates the alignment procedure for the ASL dipole and makes use of the calculated fieldmap in TOSCA. The optimum dipole positions were implemented in the CAD model and accordingly the floormarks were applied in the experimental area. The relative alignment of the vacuum chambers were also determined and the chamber positions were adjusted after the magnets were placed in the area.
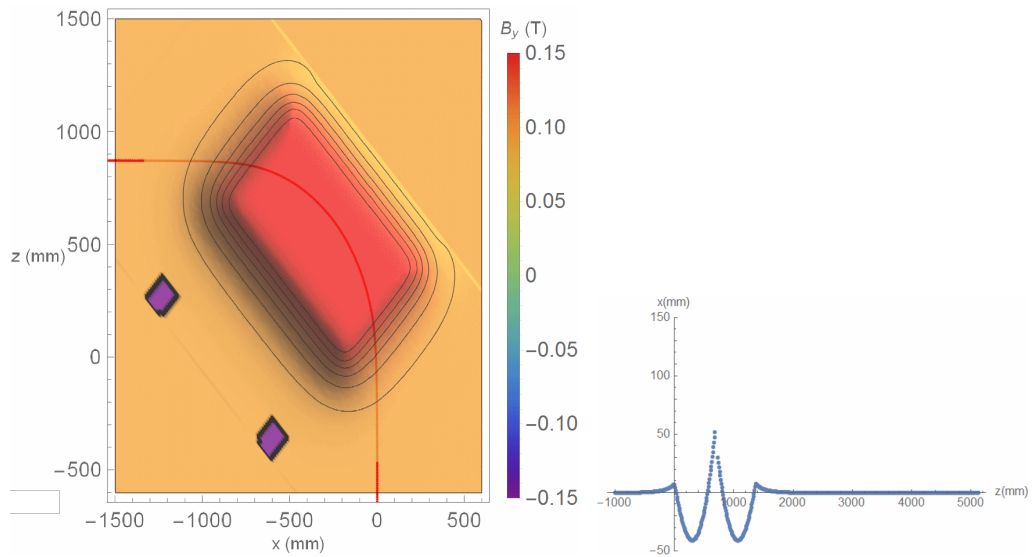
(a) B_y and reference trajectory in the magnetic mid-plane of the ASL

(b) Horizontal deviations between the reference trajectory and the design orbit (The spikes in the middle are artefacts due to the treatment of bent centrelines in G4BL)
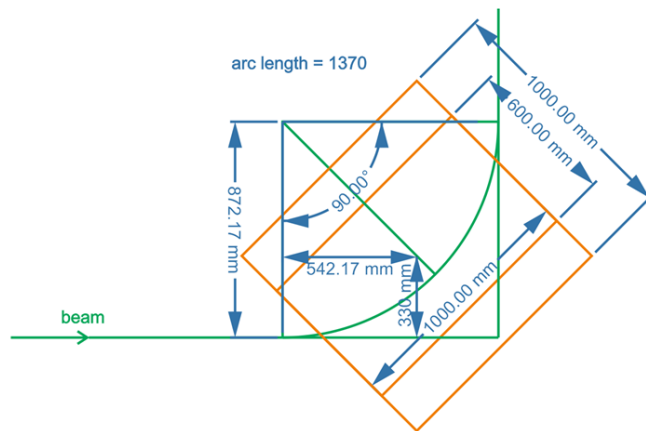
(c) Final alignment of the ASL with respect to the design orbit given by straight lines and an arc.

Figure 2.49.: *Shown is the alignment procedure for the ASL dipole as it was determined for the first comissioning run. a) The 28 MeV/c reference trajectory (red curve) is tracked through the innermost homogeneous field of the open yoke ASL (The violet (negative values) squares correspond to the location of the reduced yoke, where the flux has the opposite direction with respect to the large rectangle area of the pole shoe gap). b) The horizontal alignment of the magnet is checked after each run and the displacement for the next run determined. c) The final coordinate displacements with respect to an arc defined by the effective length is given by $z_{off} = 542$ mm and $x_{off} = 330$ mm.*

2.5.2. Muon beam measurement techniques

The staged installation of beam line elements described allows an initial point→point optics to check the transmission and requires a flange with a 190 micron Mylar window and a small Ne102 scintillator "pill" attached to a PMT, which is mounted on an XY-scanner (see figure 2.50). Using this technique the muon beam is measured in air for which multiple scattering MSC has to be taken into account for the profile analysis. The scanner allows
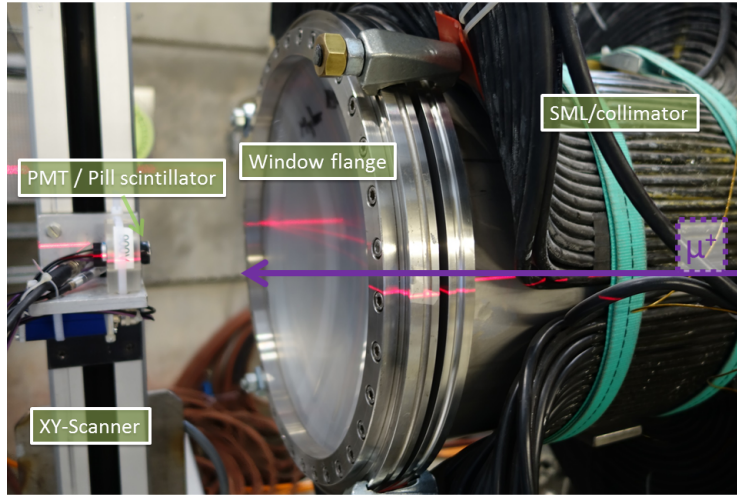
Figure 2.50.: *Profile measurement setup, the picture shows the window flange through which the beam exits the vacuum and the PMT mounted in a plexiglas holder that is attached to the movable arm of the scanner system. The small diameter scintillator at the front side of the PMT is covered with 20 μm thick light-tight aluminum foil and is not visible in the picture.*

for precise movements in the horizontal and vertical direction and comprises of a DAQ system with a LabVIEW [70] interface on a dedicated computer. More information on the scanner system and improvements to the LabVIEW software and alignment are presented in the appendix section 4.5.

Although other beam monitoring methods such as the newly introduced Luminophor beam monitoring [66] or the SciFi tracker [24] technique provide immediate beam measurements of the entire profile the pill counter is still regarded as the standard device. The pill counter has good timing and pulse-height resolution allowing clear discrimination of different particle types (e^+,μ^+,π^+), while having a low background so providing full information on the beam spot when mounted on an XY-scanner. Two different precisely measured pills were used, a ~2 mm diameter round one with a length of ~2 mm and a rectangular one with ~6 mm^2 cross section and a length of ~2 mm, both capable of stopping surface muons. The small cross sections of the pill reduce pile-up, so that surface muon beam rates up to $\mathcal{O}\left(10^9\right)$ μ^+/s still scale linearly to within 2 % with the beam intensity. Therefore the absolute rates can be extracted by scanning the beam profile and counting the number of discriminated events. Oscilloscope screenshots in figure 2.51 show the different signal signatures for beam positrons and surface muons obtained by adjusting the magnetic field of the separator. The beam positrons that are instantanously produced from π^0-decay
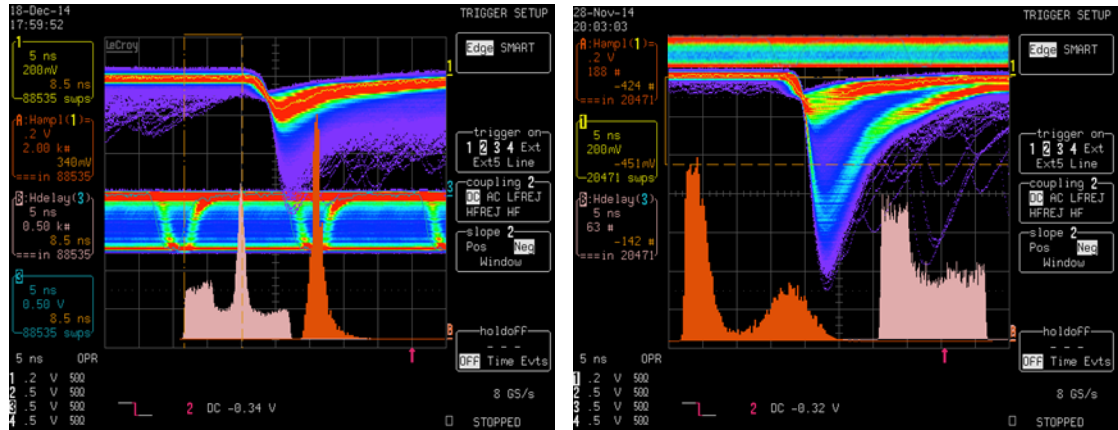
(a) Oscilloscope screenshot (separator set to e^+)   (b) Oscilloscope screenshot (separator set to μ^+)

Figure 2.51.: *The oscilloscope screenshots show the signature of the pill counter signal for different settings of the particle separator. Channel 1 shows the analogue waveform of the PMT. Channel 3 shows the RF pulse when triggering on discriminated positron pulses (channel 2). The orange histograms illustrate the pulse-height spectrum and shows a Landau distribution for the positron beam (left) and a Gaussian distribution for the muons together with the low pulse-heights from Michel positrons (right). The pink histogram contains the time difference between the trigger (e^+/μ^+) and the RF timing signal of the proton beam. Apart from a wrap-around artefact on the left side the pink histogram shows a clear peak in case of the beam positrons and an approximately flat distribution for the muons and their associated Michel positrons.*

show a clear correlation with the RF-signal of the accelerator which has a period of ∼20 nsec. The surface muons that come from the decay of stopped π^+ in the surface layer of the production target show no timing structure due to the pion lifetime. At 28 MeV/c virtually no pions can reach the pill scintillator (see figure 2.41).

The analogue waveform in the muon case shows two distinct distributions, the higher Gaussian distribution corresponds to the muons whereas the lower distribution is mainly due to Michel positrons. For the muon beam optimization the trigger threshold was adjusted to count only muons. For separator scans (as shown in figure 2.24) and tests with positron beams a second threshold was set to count both beam positrons and muons, which are above the noise level coming from thermal noise of the photo cathode or Cherenkov pulses in the glas of the PMT.

The major part of the Michel positron contribution can be attributed to muons that stop inside or in the vincinity of the scintillator pill as confirmed during the meausrements by triggering either on a high threshold to detect only muons or a low threshold in order to detect muons and positrons.

Figure 2.52 shows the graphical output of a G4BL simulation that reproduces the measurement setup. The pure muon beam in the simulation stays constant while the detector assembly is shifted for each simulation run so as to mimic a raster scan as in the actual measurements. The simulation counts the number of muons and the number of decay positrons that hit the scintillator volume at the front face of the pill counter. A comparison of both values yields a ratio $\frac{\#e^+ + \#\mu^+}{\#\mu^+} = 2.4$, whereby this ratio depends on the geometry
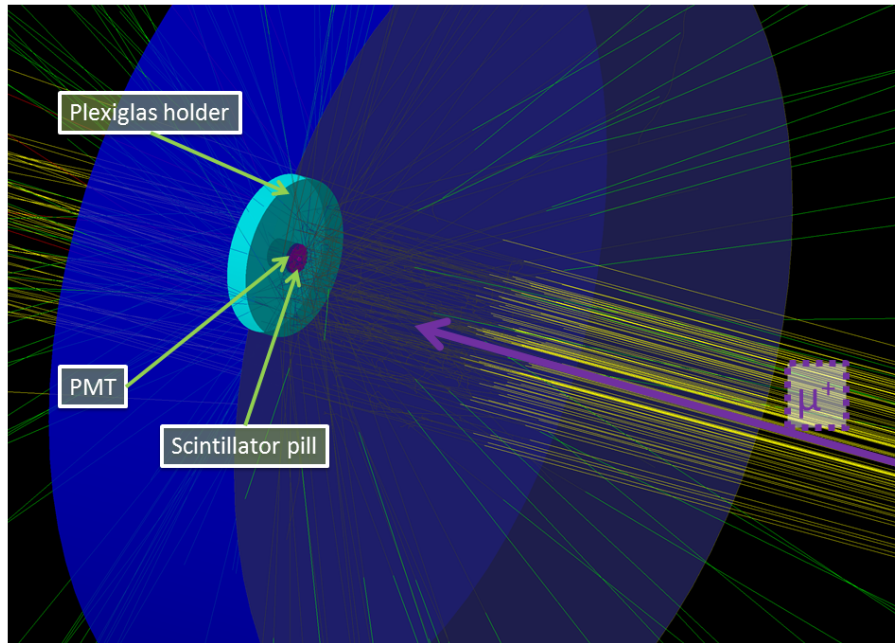
Figure 2.52.: *Shown is the graphical G4BL simulation output of the pill counter setup to determine the muon and Michel positron ratio during a raster scan. The muon trajectories are yellow and the positron trajectories are green. The blue disk represents the air column between the vacuum window and the pill counter.*

and materials as well as on influences stemming from different configurations. The evaluation of the simulated raster scan also yields a slightly larger beam size, when taking into account the Michel positrons, which also agrees with the measurements.

The electronics scheme used for the data acquisition with a DRS4 evaluation board [48] and LabVIEW software is shown in figure 2.53, based on standard NIM & TTL technology. Three main signal inputs are used:

- Pill analogue signal - split into two discriminated chains, low and high threshold to distinguish positrons from muons
- RF-signal - used for TOF information of particles between TgE and pill
- proton signal - normalization signal derived from the MHC4 proton current monitor used to give the number of particles per proton beam current

A clock signal is input to the scaler to cross-check whether the measured rate was derived with a continuous beam, or interruptions occured. From the four discriminated signals three readout-chains are constructed:

- XY-scanner DAQ - using the discriminated high and low threshold pill counter signals for particle counts and the proton signal for normalization
- Beam element optimization OPTIMA - requiring the discriminated pill counter signals for counting and the proton signal for normalization
- Oscilloscope chain - The analogue and discriminated pill counter signals as well as the RF and proton signals are used for monitoring and setting of the thresholds and timing as well as collecting TOF and pulse-height spectrum measurements
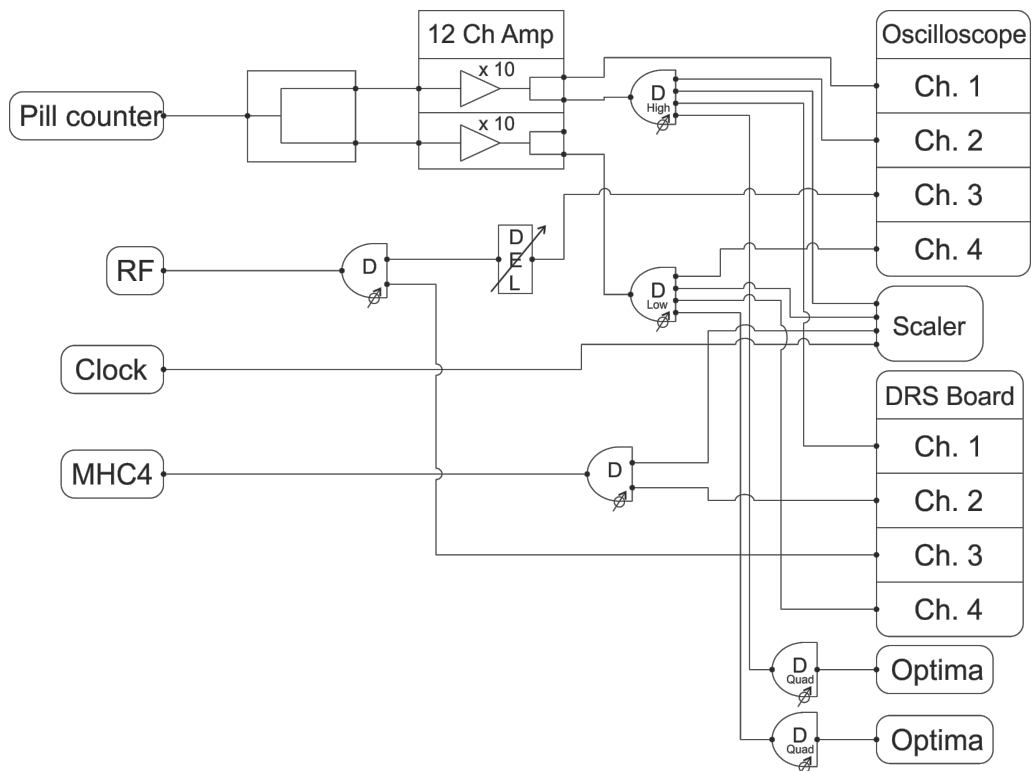
Figure 2.53.: *Shown is the electronics scheme as it was set up for the CMBL beam times. The explanation is given in the text.*

The muon beam optimization method is based on three techniques:

- Beam element optimization using the OPTIMA program - the pill counter is placed at the required position, on axis, along the beam line and the element / elements automatically tuned in user-defined steps to maximize the measured rate. Multiple elements can also be tuned as a group, so preserving the optics, in the case of a quadrupole triplet, effectively changing the focal length of the triplet and shifting the focus US or DS. A screen shot of the Graphical user interface (GUI) in the case of a separator magnet scan is shown in figure 2.24.

- "Cross-scan" - a 2D scan of the beam spot using the pill counter and a LabVIEW program. This method scans in the form of a cross, based on an automated initial low resolution scan to find the peak of the distribution and followed by a high resolution scan through the maximum (see appendix section 4.5). The total normalized beam spot rate and fitted profile parameters are shown in the program output.

- "Raster scan" - this also involves a 2D measurement but of the whole beam spot, which is scanned with a grid spacing of normally 5 mm. A 2D Gaussian fit with correlation is then applied to obtain the spot sizes and centroid and the rate is extracted from scaled summation of the measurement points.

The first two techniques are applied iteratively during an optimization scan, while the raster scan technique is usually used to obtain the final results, since such a grid can result in hundreds of single measurements. Care is also taken when changing dipole magnets by following the hysteresis curve, so ensuring reproducible results.

For a better characterization of the πE5 beam line and also as input for the G4BL simulation phase space reconstructions based on quadrupole tuning was introduced to the existing beam measurement techniques. The method is described in the next subsection.

2.5.3. Results of the 2014/2015 CMBL test beam

At the start of the beam tuning for stage 1 previous MEG standard values were set and the beam line magnets were optimized by use of the available optimization code. At the end of the optimization procedure a raster scan was made with the XY-scanner. The results are shown in figure 2.54. The result of the raster scan was then fitted with a 2D-Gaussian:
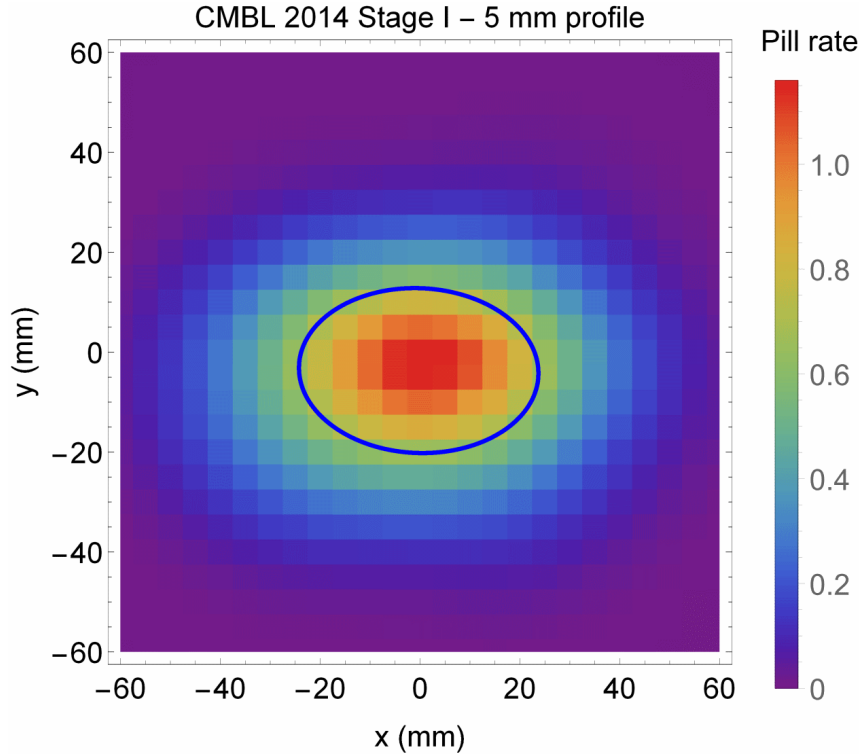
Figure 2.54.: *Shown is the result of the raster scan that was taken at the end of the beam optimization procedure for the stage 1 measurement position. The measurement was made with a high discriminator level to count only muons. Each point was measured for a few seconds and normalized to the correspoding MHC4 signal. The full scan took ∼1 h. The results from a 2D Gauss fit are: $\bar{x}$=-0.26 mm, $\bar{y}$=-3.70 mm, σ_x=23.98 mm, σ_y=16.50 mm, ρ_{xy}=0.03. The total muon beam flux can be extracted from the sum of all points of the raster scan: $1.05 \cdot 10^8$ μ^+/s at 2.2 mA proton current.*

$$f\left(x,y\right) = \hat{A} \cdot e^{-\frac{1}{2 \cdot (1-\rho_{xy}^2)} \left(\frac{(x-\bar{x})^2}{\sigma_x^2} + \frac{(y-\bar{y})^2}{\sigma_y^2} - \frac{2 \cdot \rho_{xy}(x-\bar{x}) \cdot (y-\bar{y})}{\sigma_x \cdot \sigma_y} \right)} \quad (2.30)$$

with the total rate determined from the sum of all individual measurement points of the raster scan according equation 4.7 and gave $1.05 \cdot 10^8$ μ^+/s at a reference proton beam current of 2.2 mA.

A corresponding cross scan taken with the same magnet values yielded a rate of $9.7 \cdot 10\hat{\ }7\mu^+/s$ and showed slightly different beam widths σ_x=25.12 mm and σ_y=15.02 mm. This can be explained by the fact that the muon beam deviates from a pure 2D Gaussian profile and becomes broader towards the edges of the distribution, as confirmed by the evaluation of the individual rows and columns of the raster scan. Figure 2.55 shows the data and

Table 2.3.: *1D Gauss fit results for certain rows & columns of a raster scan*

y-offset (mm)	σ_x (mm)	x-offset (mm)	σ_y (mm)
0	23.27	0	15.90
5	23.51	5	15.93
10	23.86	10	16.14
20	25.26	20	16.60
30	27.08	30	17.26

1D-Gauss fits corresponding to subsets of the raster scan that only use certain rows or columns of the complete scan. Table 2.3 lists the fit results together with their specific

(a) Data subset of the raster scan (figure 2.54) for rows with constant y-offset = 0,5,10,20,30 mm

(b) Data subset of the raster scan (figure 2.54) for columns with constant x-offset = 0,5,10,20,30 mm
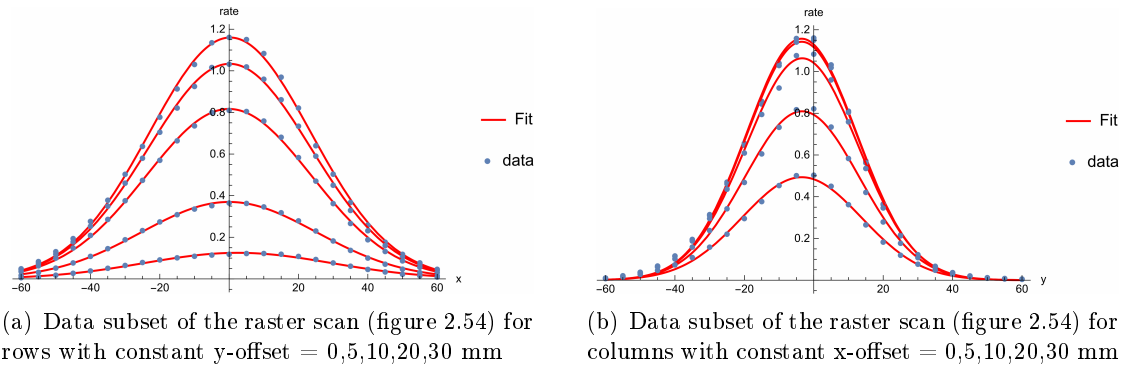
Figure 2.55.: *The left plot shows the different horizontal profiles by chosing distinct rows with constant y-offsets and vice versa for the vertical profiles that are shown on the right. The fit results are shown in table 2.3.*

offsets from the centreline.

In a next step the transverse phase space was characterized. Instead of measuring the beam profile at different positions with fixed magnet values a quicker approach was chosen. By replacing the transport matrix $R_{Drift,l}$ in equation 2.25 with a transport matrix of a quadrupole (equation 2.15) and a subsequent drift space $R_{Drift\&QP(I)}$ the beam matrix $\sigma_{\left(s=l_{QP}+l_{Drift}\right)}$ at the end depends on the beam matrix of the quadrupole and therefore also on the applied current.

$$\rightarrow R_{Drift\&QP(I)} = R_{Drift,const} \times R_{QP}\left(K\left(I\right)\right) \tag{2.31}$$

where K is the quadrupole strength and I is the applied current. The current dependence of the quadrupole strength $K\left(I\right)$ that is determined by the field $B_0\left(I\right)$ at the pole tip is known for all of the used quadrupoles. This allows the transverse phase space at the entrance of the effective length of a quadrupole to be determined using a fixed drift length to the measurement position in a similar way as was done in equations 2.25, 2.27, 2.28. In order to extract the phase space information at the pill1 position the current of the last quadrupole of triplet II, QSK43, was changed and for each magnet setting the beam profile widths were determined with cross scans. In order to obtain the beam sizes in vacuum the measured values had to be corrected for multiple scattering, using a small G4BL simulation

program of the setup. The true beam size in vacuum as well as the correction factor are extracted from equation 2.32.

$$\sigma^2_{air} = \sigma^2_{vac} + \sigma^2_{scat} \qquad (2.32)$$

where σ_{air} is the total beam size with scattering in the window and the air included, σ_{vac} is the beam size in vacuum and σ_{scat} is the contribution to the total beam size from scattering. The resulting reconstruction of the horizontal and the vertical phase space at the entrance of the effective length of the QSK43 is shown in figure 2.56. As a cross check
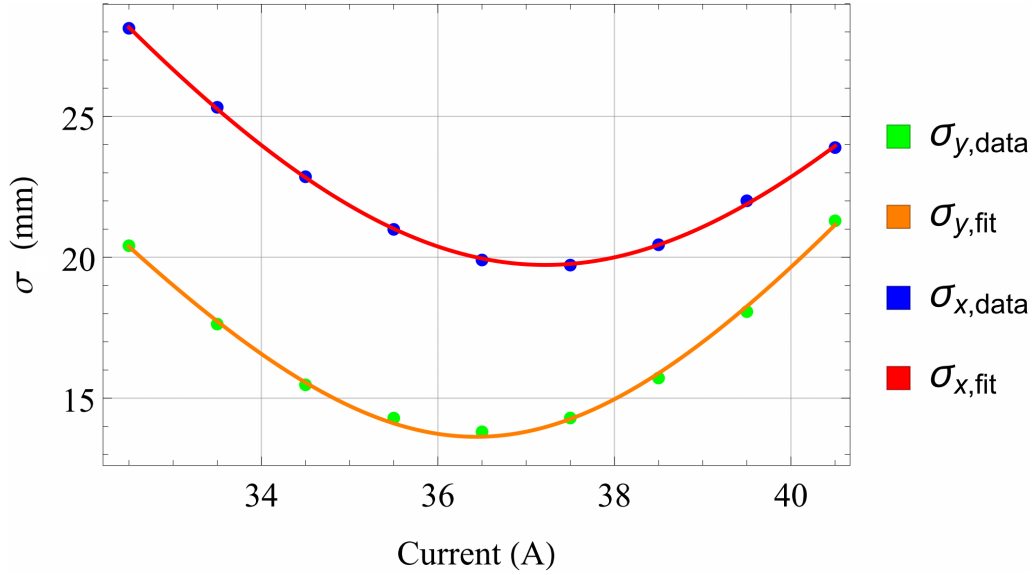
Figure 2.56.: *By changing the quadrupole currents of the QSK43 the size of the beam spot changes. The lines in the plot represent the expectations from the fitted phase space and a good agreement can be observed. The reonstructed phase space parametres are: α_x=-4.06354, β_x=2.7613 m, ϵ_x=1163 mm·mrad, x_m=56.7 mm, θ_m=85.9 mrad, $\rho_{x\theta}$=0.9710 $-$ α_y=18.7133, β_y=9.01 m, ϵ_y=426 mm·mrad, y_m=62.0, ϕ_m=128.8 mrad, $\rho_{y\phi}$=-0.9986*

the phase space was also determined in TRANSPORT with a stochastic multi-envelope fit method, which leads to consistent results and is shown together with the TURTLE results for the same parameters in figure 2.57. The corresponding phase space ellipses are shown in figure 2.58. Despite the succesful determination of the phase space it was observed that the beam is not accurately centred by the fact that different tunes of the QSK43 not only change the beam size but also lead to a shift of the centroids. Figure 2.59 illustrates the dependency of the beam centroid on the applied quadrupole current. Figure 2.60 schematically explains the observed beam centroid shift. In a final measurement the separation quality of the muon beam spot compared to the beam positron spot at the intermediate focus collimator position was made by measuring the centre of the vertical distribution $\bar{y}$ for different magnet settings of the particle separator. Figure 2.61 shows the separation calibration for the stage I beam line tune. The fit yields a separation of $\sim$2.5 mm/A. A low threshold scan of the separator magnet (see figure 2.67) yields a separation of 33 A for the separator coils, which corresponds to a 84 mm separation of the muon and the positron beam centroid.

In the following stage II measurements the ASL dipole and the QSO doublet were installed.
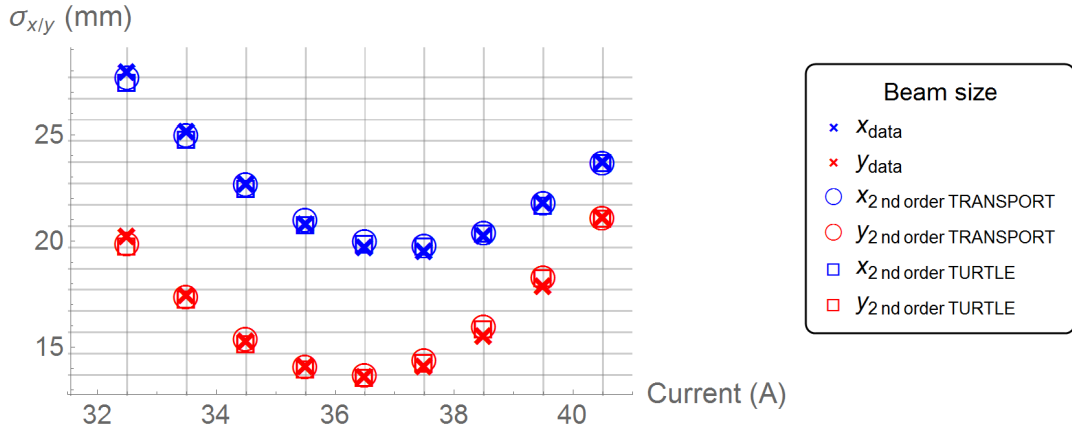
Figure 2.57.: *Shown is the phase space reconstruction based on the TRANSPORT multi-envelope fit method which yields consistent results with the above method. Furthermore the agreement with the TURTLE beam tracking is shown that can be used to generate a corresponding beam file for simulations.*

(a) Reconstructed horizontal phase space ellipse

(b) Reconstructed vertical phase space ellipse
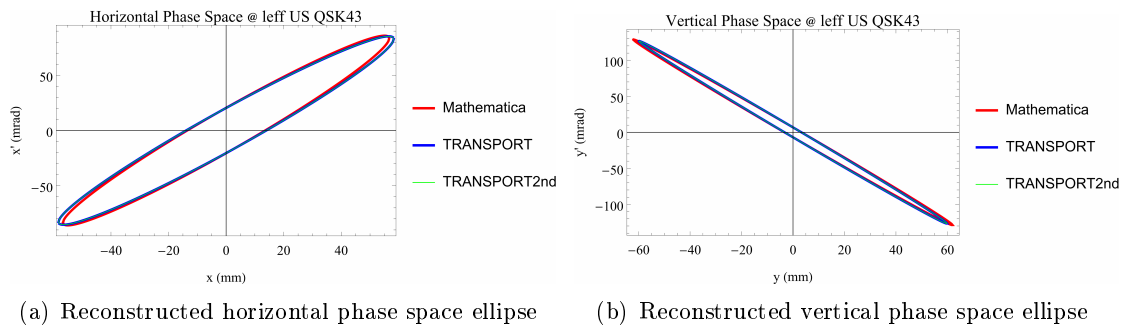
Figure 2.58.: *Shown are the horizontal and the vertical phase space ellipses based on the reconstruction at the Pill1 position and the applied tune.*
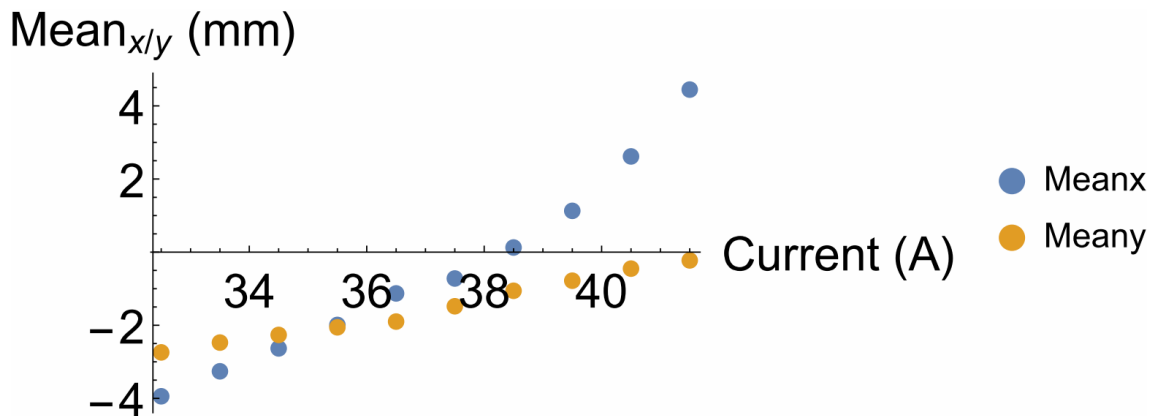
Figure 2.59.: *The beam centroid measured at the Pill1 position is shifted for different quadrupole currents of the QSK43. This implies that the beam is off centre in both transverse directions at the QSK43.*

103

(a) Horizontal centroid shift for different QSK43 currents

(b) Vertical centroid shift for different QSK43 currents
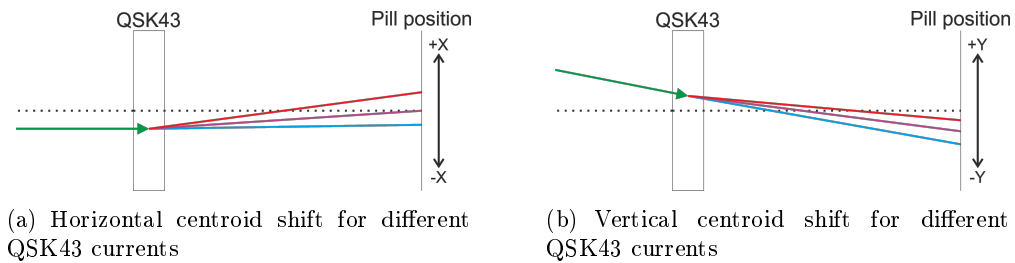
Figure 2.60.: *Since positive currents on the QSK43 correspond to horizontal focussing / vertical defocussing for positive particles the beam centroid at the QSK43 can be estimated to be off from the centreline in negative x- and positive y-direction with a negative vertical angle. The blue lines correspond to a low QSK43 excitation, violet lines to intermediate excitation and the red lines shows the deflection of the incoming (green) beam for high currents.*
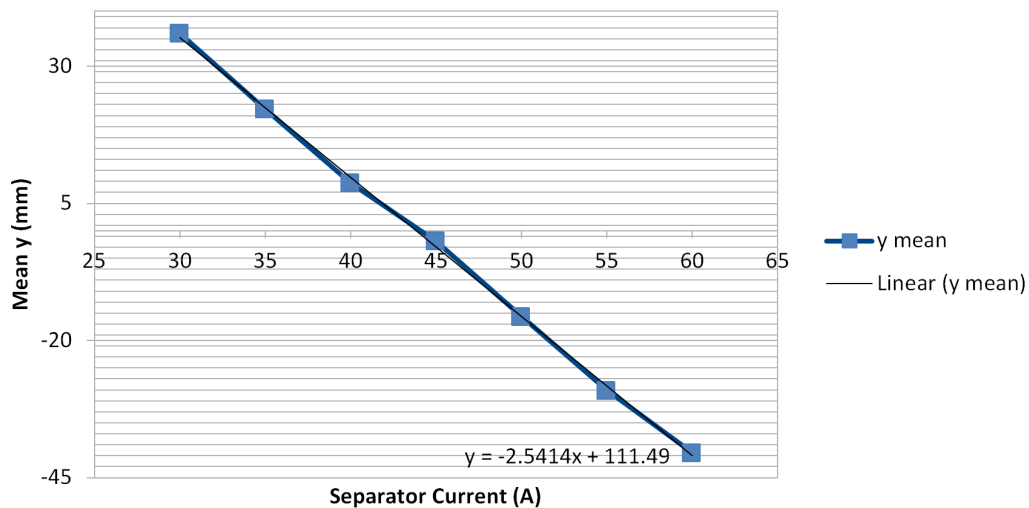
Figure 2.61.: *Shown is the vertical centre $\bar{y}$ of the muon beam spot distribution for different applied separator currents. The linear fit yields a ~2.54 mm/A calibration.*

The ASL vacuum chamber was aligned and the XY-scanner was moved and aligned to the focus position post QSOs. The magnet optimization at this stage turned out to be more challenging than before. The final tune yields a beam profile that is shown in figure 2.62. The raster scan shows significant deviations from a Gaussian shape which is attributed to
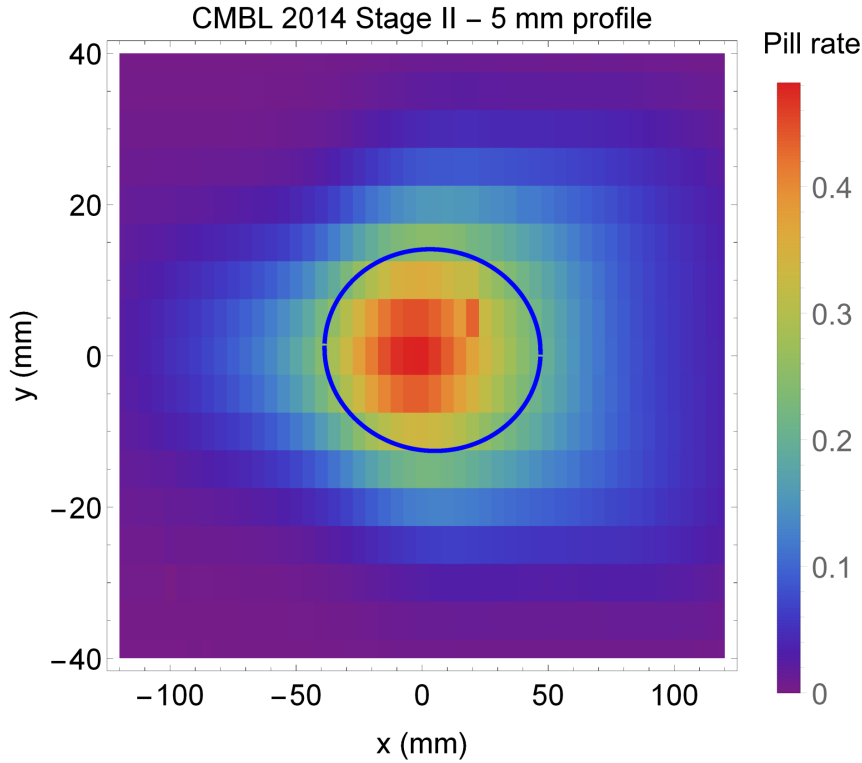
Figure 2.62.: *A 2D Gauss fit of the raster scan, that was taken at the end of the stage II beam tuning in the 2014 CMBL beam time yields: $\bar{x}$=4.11 mm, $\bar{y}$=0.76 mm, σ_x=42.84 mm, σ_y=13.33 mm, ρ_{xy}=0.023 and a rate of 6.03·10^7 μ^+/s at 2.2 mA proton current.*

aperture cuts and dispersion of the beam profile. This can be better seen by the horizontal scan that was taken with the QSO42 set to 70 A and shown in figure 2.63. Beam tuning at the final stage implies that the magnet tune for stage II was not optimal, as the magnet values from stage II to stage III changed significantly and a higher rate was observed at the final focus of the CMBL.

The installation of stage III proved to be the most difficult with the ASK magnet requiring a counter-weight for installation as shown in figure 2.48. Measurements were made at the final injection focus to the solenoid post QSM. As before, the vaccum was closed with the 190 micron Mylar window flange and the beam scanner was set up right behind. At this last stage considerable effort and time was spent to determine the optimal tune for highest transmission. Figure 2.64 shows a raster scan at the final focus yielding a rate of 6.7·10^7 μ^+/s at 2.2 mA. This includes a loss of ∼3.5 % due to decays according to equation 2.24, which gives a survival probability of 96.5 %.

Phase space measurements were also undertaken for stage III using the QSM. With the optical solution that led to figure 2.64 set, the phase space at the entrance of the QSM
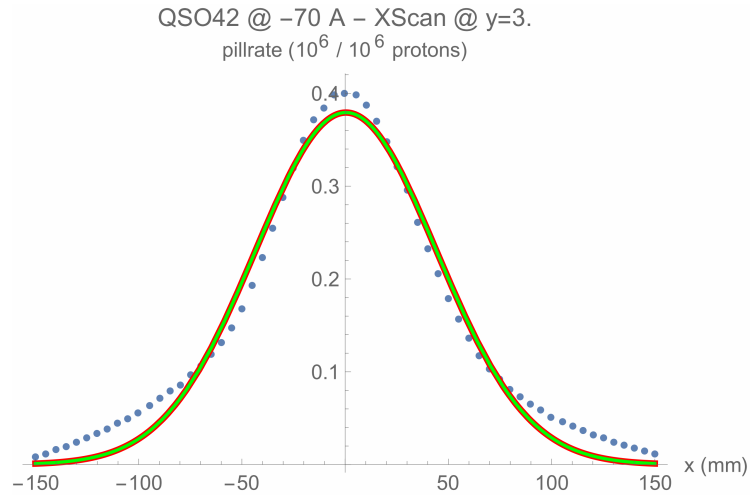
Figure 2.63.: *Shown is the horizontal distribution through the vertical centre of the beam at the Pill2 position. A Gauss fit yields:* $\bar{x}=0.40$ *mm,* $\sigma_x=43.90$ *mm*
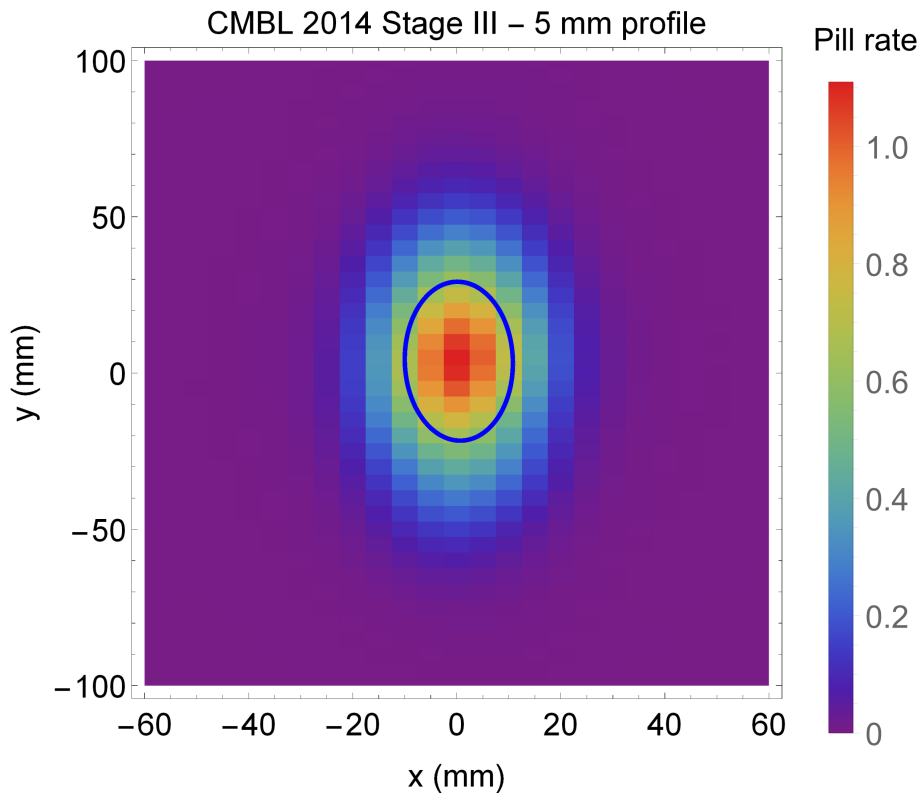
Figure 2.64.: *Shown is the raster scan for an optimized beam tune at the final focus position. A 2D Gauss fit yields:* $\bar{x}=0.39$ *mm,* $\bar{y}=3.80$ *mm,* $\sigma_x=10.39$ *mm,* $\sigma_y=25.42$ *mm,* $\rho_{xy}=0.026$ *and the sum of the individual points give the total rate* $6.68*10e7$ $\mu+/s$ *at 2.2 mA proton current.*

effective length was determined in the same way as described above for the stage I measurement. The phase space fit for different applied QSM currents is shown in figure 2.65. The dependence of the centroid on the QSM current is shown in figure 2.66. At the end of
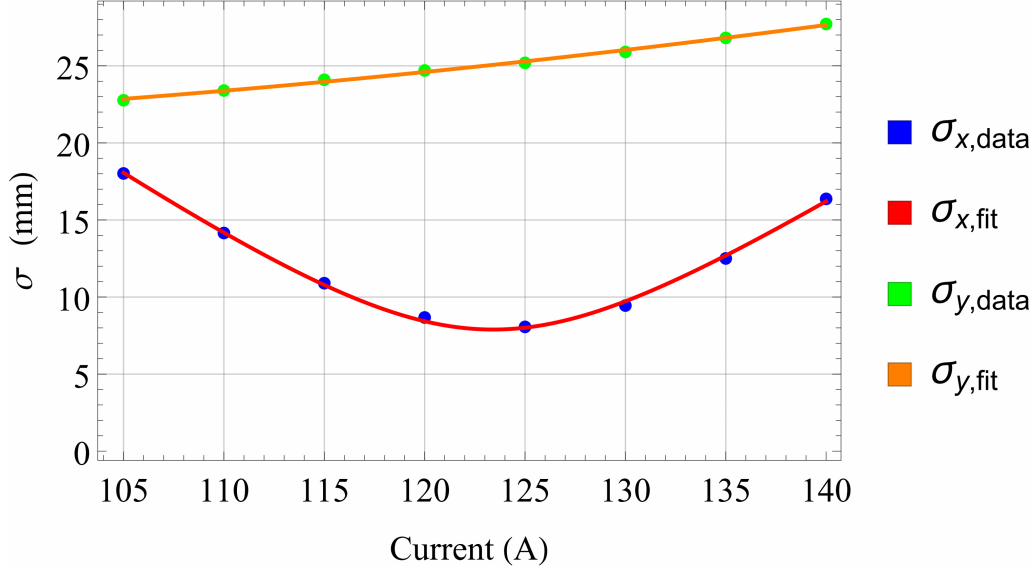
Figure 2.65.: *Quadrupole tuning of the QSM around the central tune allowed the horizontal and vertical phase space to be determined similar to the QSK43 measurement (see figure 2.57). The phase space parametres are: α_x=-3.40, β_x=5.54 m, ϵ_x=809 mm·mrad, x_m=66.95 mm, θ_m=42.88 mrad, $\rho_{x\theta}$=0.9594 − α_y=3.45, β_y=2.73 m, ϵ_y=390 mm·mrad, y_m=32.64 mm, ϕ_m=42.88 mrad, $\rho_{y\phi}$=-0.9604.*

the 2014 beam period an additional low threshold (μ^+ and e^+) separator scan was made and the result is shown in figure 2.67. The beam time 2014 ended on the 23rd December and remaining measurements at the final focus and at stage I with the final focus optics had to be shifted to the beginning of the beam period in 2015. For the 2015 run beam tuning was continued and led to consistent results compared to the 2014 setting.

A measure of the influence of the horizontal slit opening at FSH41 on the beam rate, a so-called slit curve was measured by opening the FSH41 slit apertures symmetrically while measuring the rates on the centreline. The corresponding slit curve is shown in figure 2.68.

In order to improve the total rate at the final focus position a deeper analysis of the beam losses between triplet II and the final QSM focus neccessiated a further phase space measurement at the stage I position with the final QSM optics. Therefore the current values of all preceeding magnets were set according to the beam line tune that was determined during the optimization at the final focus position. The phase space reconstruction is shown in figure 2.69. The centroid shift for different applied QSK43 quadrupole currents is shown in figure 2.70. Not all of the beam profiles that were measured for the phase space reconstruction with the beam line set to "final focus" optics are usable for the phase space reconstruction since the profile distributions differ from a Gaussian shape for a certain range of magnet values. In the horizontal direction the beam profiles shows cut tails at lower currents as in the case for the acutal final focus setting at ∼30 A for the QSK43, as is shown in figure 2.79(b). The vertical distribution shows slightly enhanced tails for
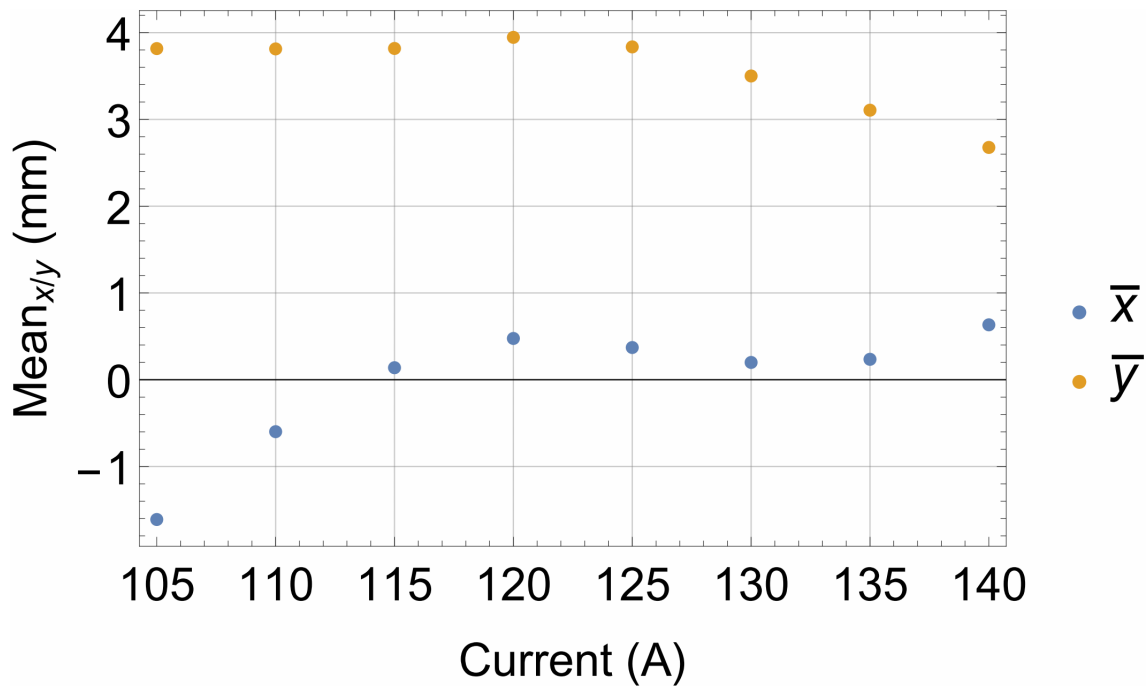
Figure 2.66.: *Shown is the beam centroid at the Pill3 position plotted against the applied QSM current.*

lower currents. However the extraction of the phase space US the QSK43 is still possible by using only valid profiles. Later in figure 2.79(a) it can be shown that this can also reproduce the observed cuts.

Finally a raster scan was taken with "final focus" optics. The result is shown in figure 2.71. After finishing the various measurements for the CMBL setup a steel frame mock-up with the outer dimensions of the then possible Mu3e spectrometer solenoid was set up in the area and aligned. A picture of the mock-up at the end of the CMBL is shown in figure 2.72.
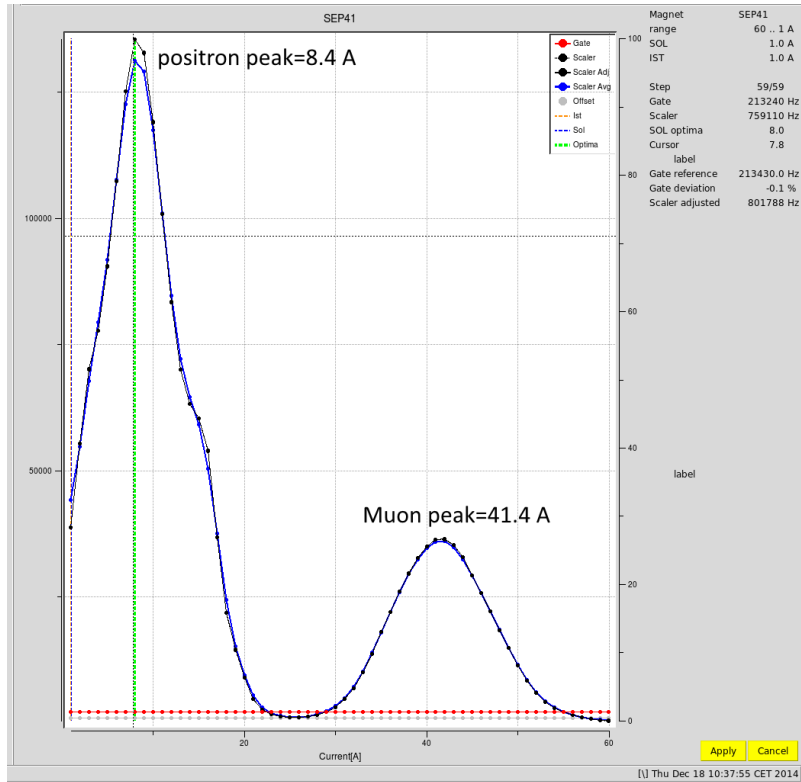
Figure 2.67.: *Shown is a low threshold separator scan at the final focus position. The separator magnet currents are varied and the combined rates of both μ^+ and e^+ are measured on the centreline.*
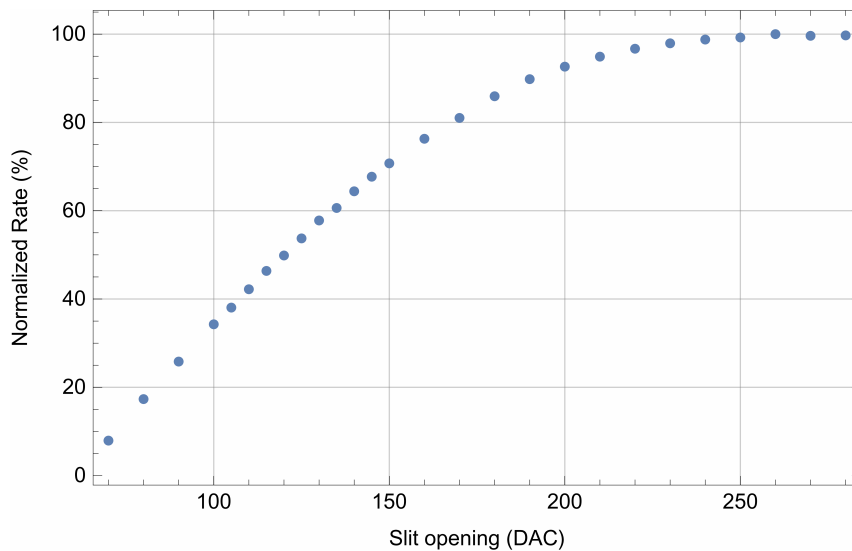
Figure 2.68.: *The plot shows the rates, that were measured on the centreline at the final focus for different slit openings of the FSH41 horizontal slits.*
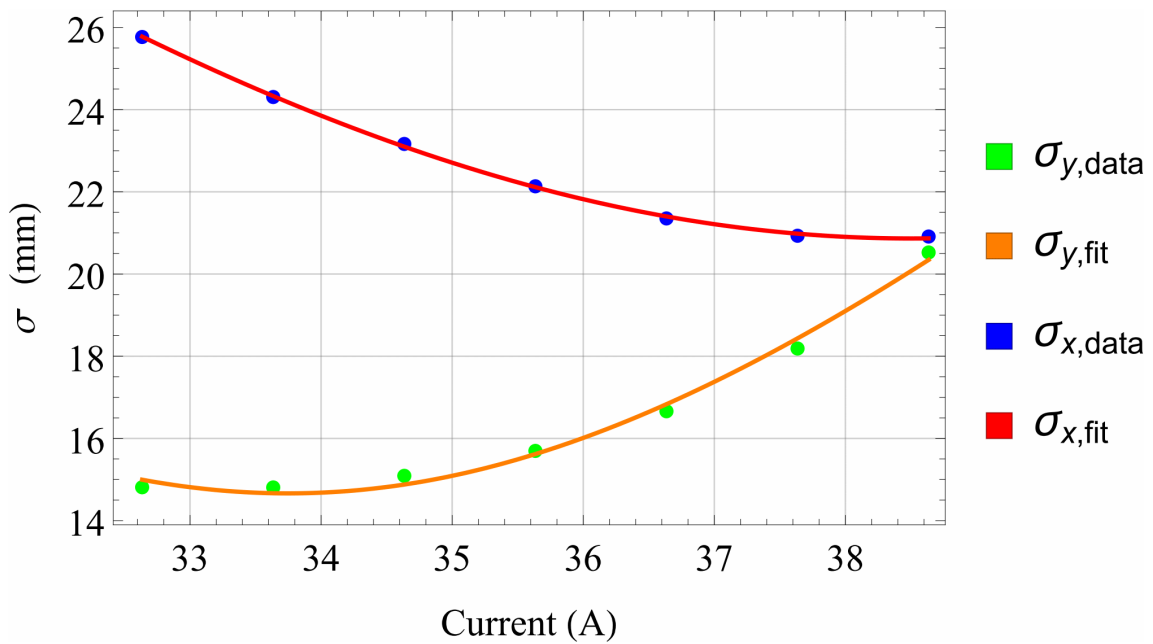
Figure 2.69.: *QSK43 phase space measurements with QSM optics. All magnets US of Pill1 were set to the final focus values. The QSK43 was tuned and the phase space information was extracted as previously described. The 1σ phase space parameters are: α_x=-2.30, β_x=1.59 m, ϵ_x=838.54 mm·mrad, x_m=36.51 mm, θ_m=57.62 mrad, $\rho_{x\theta}$=0.9172 − α_y=12.07, β_y=5.99 m, ϵ_y=380 mm·mrad, y_m=47.72 mm, ϕ_m=96.40 mrad, $\rho_{y\phi}$=-0.9966*
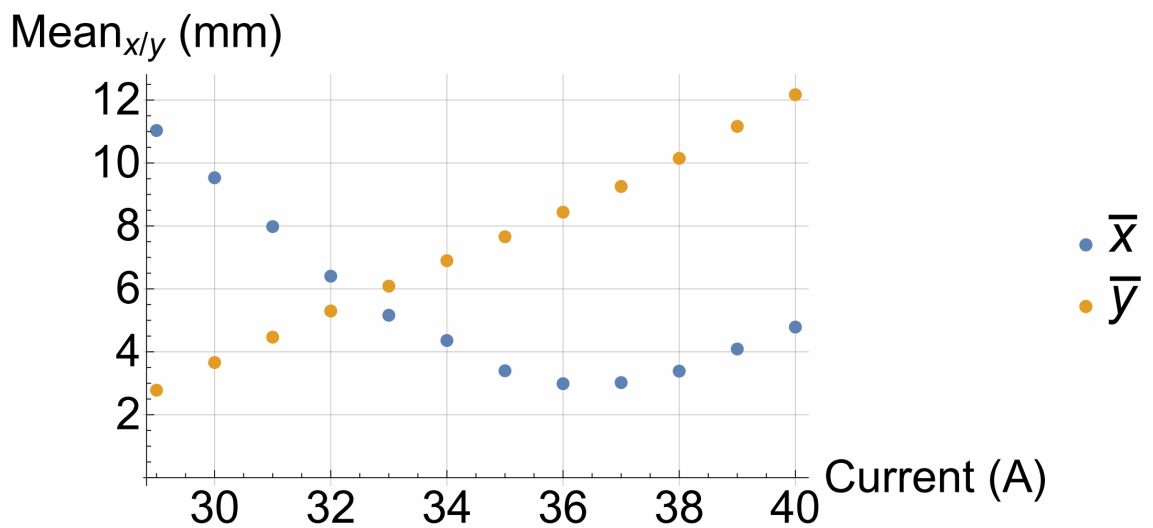
Figure 2.70.: *The beam centroid shift was extracted from the profiles that were measured during the QSK43 quadrupole tuning for the final focus beam line optics.*

5 mm Profile Phase I (2015)
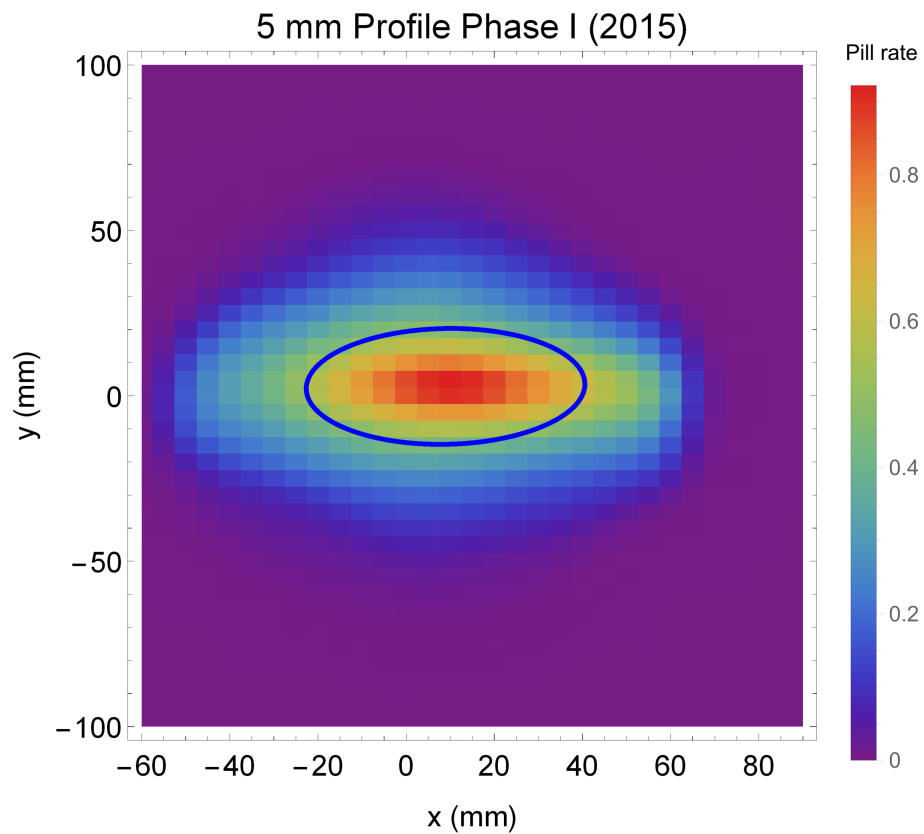
Figure 2.71.: *The raster scan was taken at the Pill1 position with the beam line set to final focus optics. The parametres extracted from a 2D Gauss fit are: $\bar{x}=8.95$ mm, $\bar{y}=2.83$ mm, $\sigma_x=31.59$ mm, $\sigma_y=17.52$ mm, $\rho_{xy}=-0.0390$. The absolute rate calculated from the scaled sum of the points of the raster scan is $1.09 \cdot 10^8$ μ+/s at 2.2 mA proton current.*
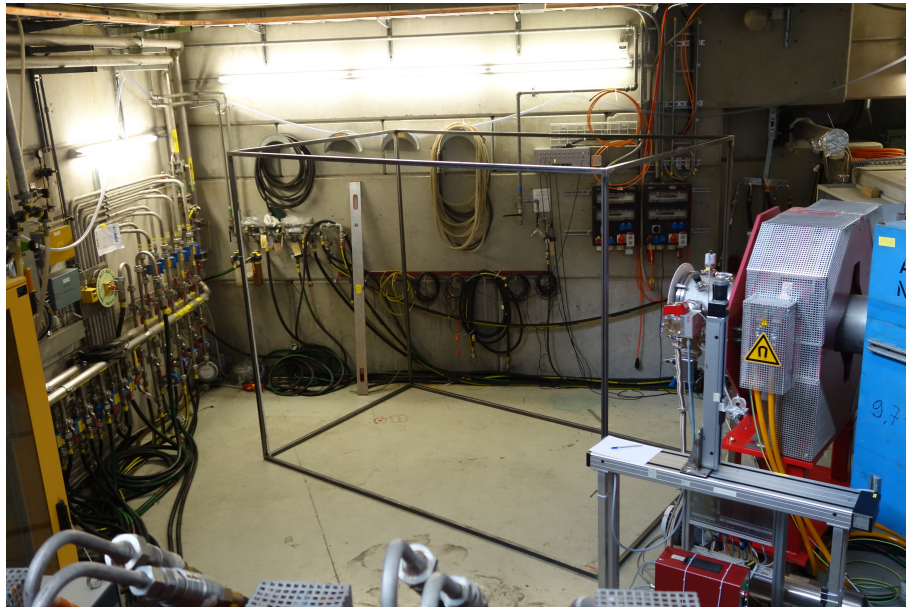
Figure 2.72.: *The image shows a steel frame mock-up of the outer dimensions of the Mu3e solenoid at the end of the CMBL*

Additional measurements of the muon momentum spectrum were undertaken during this beam time, that allow to determine the momentum byte and the kinematic edge from which the central beam momentum can be obtained. Therefore the beam line was tuned to different momenta around the theoretical kinematic edge and cross-scans were taken at the Pill1 position. Figure 2.73 shows the measured spectrum together with the fit function that was used to extract the rate. The fit function is given by the theoretical $p^{3.5}$ increase
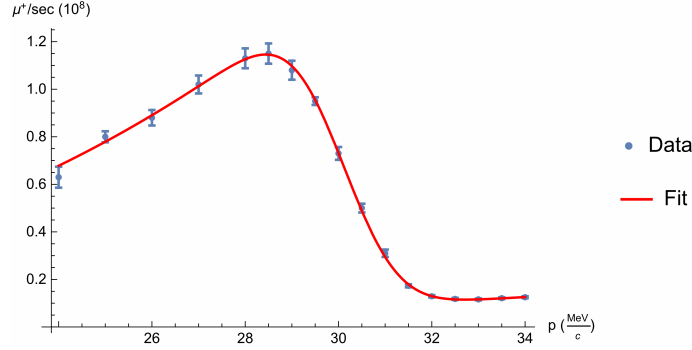
Figure 2.73.: *Shown is the muon momentum of the $\pi E5$ beam line. Therefore the beam line was tuned to different momenta around the kinematic edge. The fit function yields a momentum acceptance $\sigma_p = 0.95$ MeV/c and $k_{edge} = 29.93$ MeV/c for the kinematic edge.*

[27] multiplied by the convolution of a step function and a Gaussian resolution function, which reflects the blurring of the kinematic edge k_{edge} by the momentum acceptance σ_p of the beam line. An exponential background contribution accounts for the cloud muons, that are not due to stopped pions. The reduced χ^2 of the fit is $\frac{\chi^2}{d.o.f.} = 0.92$.

$$I(p) = p^{3.5} \cdot \int \hat{a} \cdot e^{-\frac{p'^2}{2 \cdot \sigma_p^2}} \Theta\left(k_{edge} - p'\right) dp' + c_{bkgd1} + c_{bkgd2} \cdot p^{c_{bkgd3}} \qquad (2.33)$$

The kinematic edge is slightly higher than the theoretical value of 29.79, which determines the calibration for the $\pi E5$ beam line momentum, as well as the momentum byte of the beam. The final values are:
central beam momentum $P_0 = 27.86$ MeV/c
momentum byte $\frac{\delta P}{P}$ (FWHM) $= 8\%$
this is obtained by scaling the 28 MeV/c (our assumed central momentum) by (29.792/29.93), and $\frac{\delta P}{P}$ (FWHM)$= (0.95/27.87) \cdot 2.35$.

2.6. Accurate G4BL Simulation of the CMBL & simulation based optimization post 2014/2015 commissioning tests

In order to improve the transmission to the end of the CMBL a more refined G4BL model of the last part of the beam line was created. All elements were positioned according to alignment measurements in the area that were made at the end of the CMBL beam time 2014 /2015. The beam for the simulation was extracted from the phase space measurements that were carried out at the stage I position with the "final focus" optics (shown in

figure 2.69). All drawings were checked again and vacuum chamber apertures were implemented accurately. The currents that were applied in the simulation were directly taken from the "final focus" optics setting, that was determined in the CMBL setup. In order to simulate comparable beam profiles at the end also the Mylar vacuum window and the air column between the window and the pill counter were implemented in the simulation. The results of this simulation are presented below. Figure 2.74 shows the graphical output of the G4BL simulation. The beam profile that is extracted at the position that corresponds
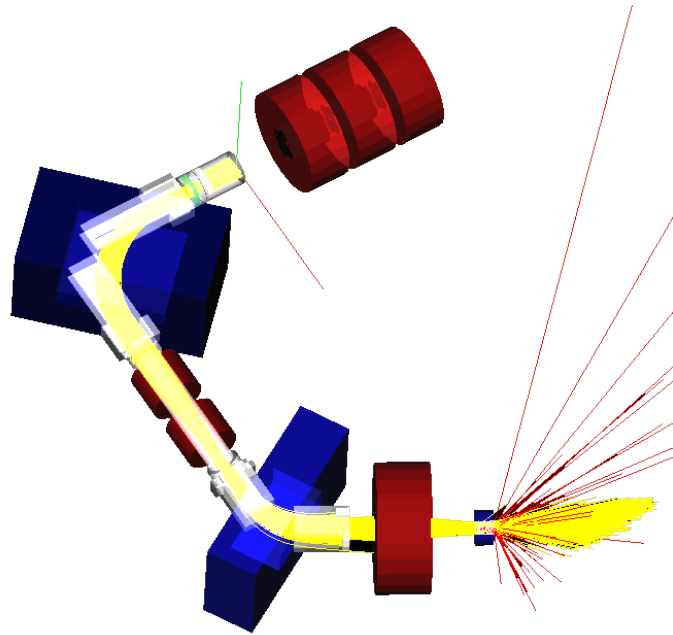
Figure 2.74.: *The graphical output shows the muon beam (yellow trajectories) propagation through the CMBL to the final focus position. The implementation of the Mylar window and the air column at the end leads to scattering of the muon beam.*

to the position of the pill counter during the beam time is shown in figure 2.75. The beam profile shows a good agreement with figure 2.64. The beam profile parameters for both simulation and measurement are listed in table 2.4. The beam widths, correlations and the transmission show a good agreement. Deviations of the beam centroid can be explained by the fact, that the simulated beam starts on-axis parallel to the centreline, whereas the quadrupole tuning in figure 2.70 implied an offset. For further validation the QSM current was tuned in the simulation to the same values that were used for the phase space measurements at the final focus. The comparison plot is shown in figure 2.76. Over a wide range of applied QSM currents a good agreement between the measured beam size and the simulation result is observed. This implies that not only the profile for the final focus setting is correctly modelled but also the phase space is well described. The deviations in the horizontal direction can be partially attributed to contributions from the coupling associated with dispersion, since the beam spot is only regarded to be achromatic around the final focus setting. Further sources of deviations are due to the first-order beam implementation and contributions e.g. from hysteresis. The beam envelopes are shown in figure 2.77. Discontinuities in the envelope plot can mainly be identified with particle losses as
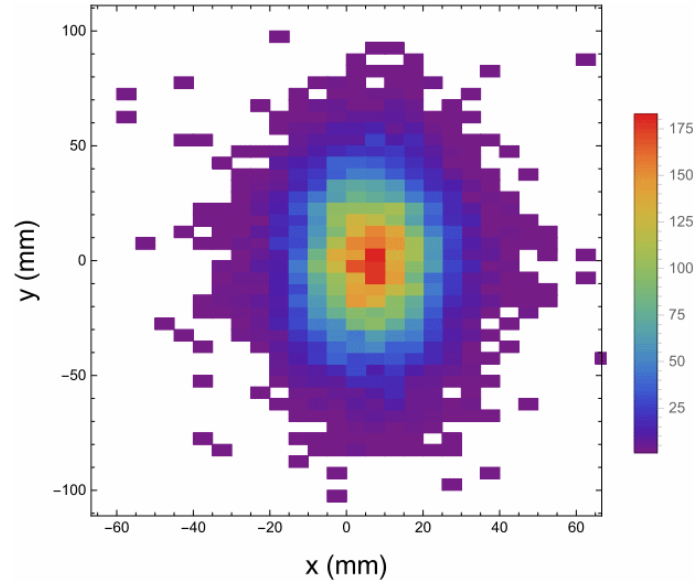
Figure 2.75.: *The muon beam profile was extracted from the G4BL simulation at the corresponding Pill3 position and shows a good agreement with the measured beam profile in figure 2.64.*

Table 2.4.: *Comparison between the measurements during the CMBL test beam 2014/2015 and the G4BL simulation results. The measured transmission is given as the range from the results obtained at the final focus in 2015 and 2014.*

Beam Parameter	Measurement CMBL 2014/2015	G4BL simulation
$\bar{x}$ (mm)	0.4	6.1
$\bar{y}$ (mm)	3.8	-0.1
σ_x (mm)	10.4	11.1
σ_y (mm)	25.4	25.0
$\rho_{x,y}$	0.026	-0.015
Transmission from stage I to the end (%)	58.0 - 61.3	60.6
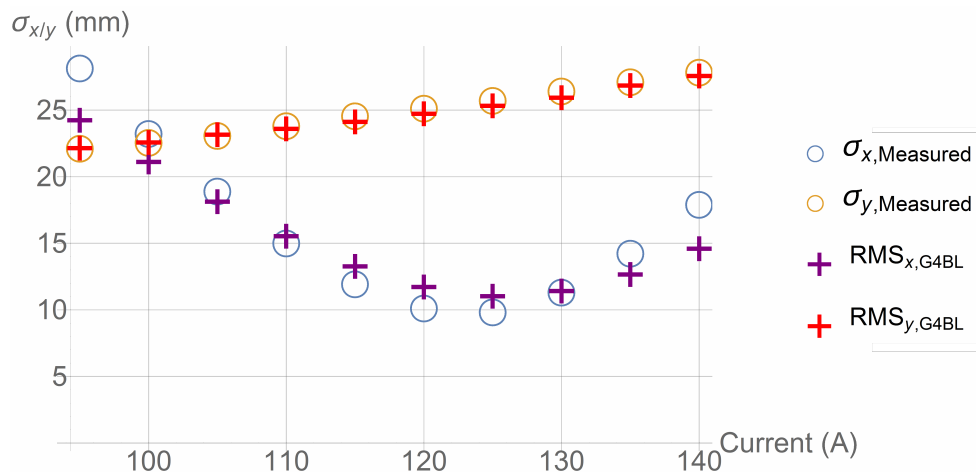
Figure 2.76.: *The QSM in the G4BL simulation was tuned to the same current values as for the phase space measurements in the experimental area. The plot compares the respective widths for the measurements and the simulation.*
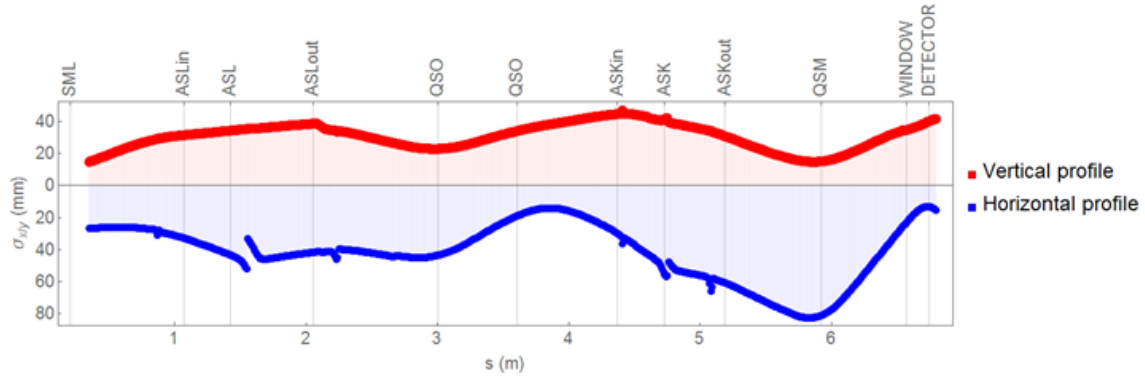
Figure 2.77.: *Shown are the beam envelopes for the G4BL simulation with final focus settings applied to the magnets.*

illustrated in figure 2.78. Finally the transmission efficiency has to be multiplied by the survival probability of ~96.5 %, since the simulation was done with muon decay disabled. The corrected transmission from the Pill1 to the Pill3 position amounts to 60.6 %. Figure
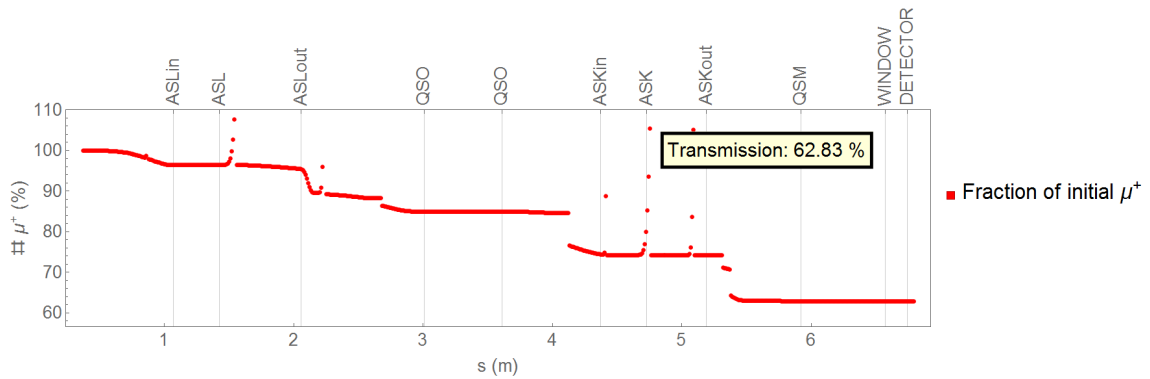
Figure 2.78.: *The plot shows the beam losses that occur on the beam line apertures according to the G4BL simulation for final focus magnet settings. The simulation was done with disabled muon decay. Therefore the transmission has to be scaled with the survival probability between the beginning and the end, yielding 60.6 %.*

2.79 shows the profile at the stage I measurement position for both the simulation and the measurement.

The validation checks described in this section show that the simulation based on the reconstructed phase space is able to properly reproduce the transverse phase space, the central profiles and the transmission. Therefore the simulation is used as a basis to identify regions of particle losses. Figure 2.78 illustrates that these regions are mainly at the dipole vacuum chambers. Therefore new fieldmaps of the ASL and the ASK were generated in TOSCA that have a larger gap. Running the simulation with loose aperture constraints shows that after optimization of the beam line with the *Optima G4BL* code a total transmission of up to 87 % can be achieved by introducing larger vacuum chambers.
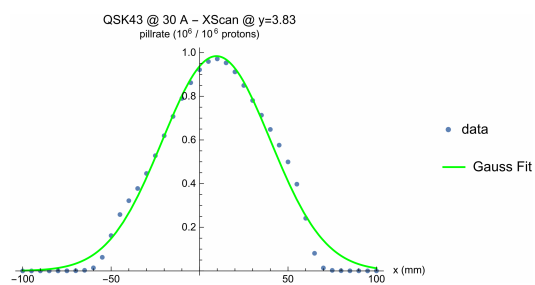
(a) Measured beam profile at the Pill1 position for final focus optics
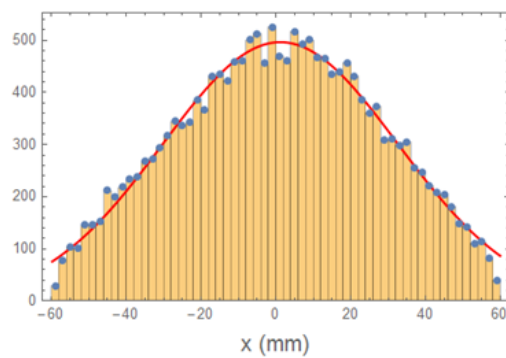
(b) Simulated beam profile at the Pill1 position for final focus optics

Figure 2.79.: *The horizontally cut measured profile at the Pill1 position for the final focus tune is shown on the left. The simulation based on the reconstructed phase space on the right shows a comparable cut.*

2.7. Design of new vacuum chambers for the CMBL dipole magnets

After the 2015 test beam much effort was spent on the refinement of the simulation and the source of losses. Modifications to both dipole magnets ASL & ASK were found to be necessary:

- Pole-gap widening vertically for both magnets

- Corresponding new vacuum chambers for both

- Change of the current 60° bending angle of the ASK magnet to 65° to allow sufficient space for the Mu3e solenoid

- Optimal vacuum chamber design to allow the beam to pass through the most homogeneous part of the dipole field

The solution for the ASL magnet came in form of a large 330 mm pole-gap spare ASL magnet in storage. Although the corresponding vacuum chamber had the wrong deflection angle it could be relatively easily modified to a 90° bend due to its flexible design - split into the chamber body and the two dismountable end-plates with the coupling flanges. Hence only new end flanges had to be made. In the case of the ASK magnet the pole-gap had to be widened and a new complete vacuum chamber made, modelled on the ASL design. Figure 2.80 shows the original ASL magnet together with the final end-plates for the ASK magnet. For the construction of the end-plate flanges of both chambers

(a) The picture shows the 330 mm gap ASL in storage

(b) End-plates that need to be mounted to the body of the ASK vacuum chamber

Figure 2.80.: *The spare ASL magnet shown on the left was acquired for the CMBL setup, although the end-plate flanges needed to be replaced. The ASK vacuum chamber uses a similar but shorter vacuum chamber design that also consists of a central body and attached end-plate flanges.*

the intersection point of both in- and outgoing centrelines with the flange plane had to be determined. Therefore TOSCA models of both magnets (with 330 mm gap) were generated and the corresponding fieldmaps for both magnets were implemented into a small G4BL tracking simulation. In the following iterative process a 28 MeV/c reference particle is tracked through the fieldmap of each magnet, which is initially positioned according to

the previous setup, with the strength of the fieldmap adjusted to provide the desired 90°
/ 65° bending angle. The initial trajectory in the magnetic midplane of e.g. the ASK
is illustrated in figure 2.81. It can be seen that the reference trajectory does not pass
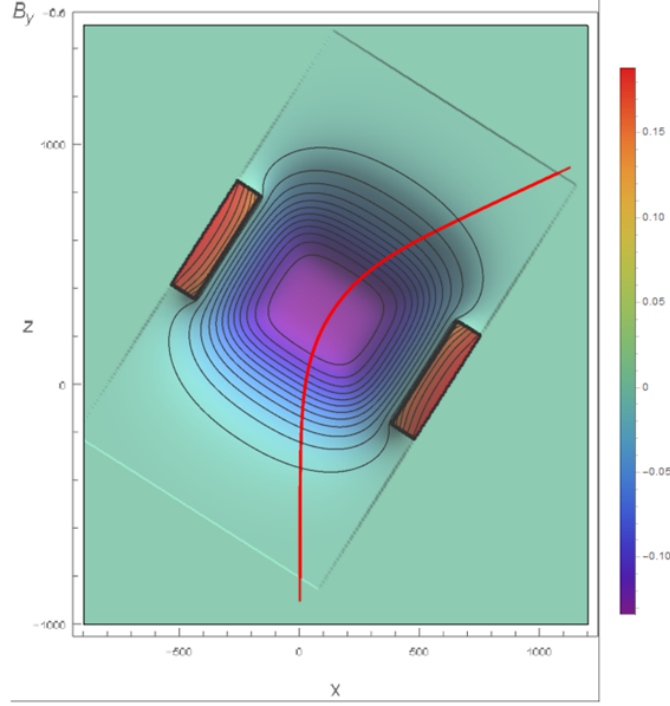
Figure 2.81.: *Shown is the field of the calculated 330 mm gap ASK dipole in the magnetic midplane together with a 28 MeV/c reference trajectory. As can be seen the trajectory does not pass the most homogeneous inner region of the magnetic field and traverses a curved fringe field at the injection/extraction.*

the innermost field region with the highest homogenouity optimally. The field that acts
on the particle, plotted against the distance covered during its propagation through the
fieldmap is shown in figure 2.82. From this the effective length can be determined to be
$l_{eff,ASK,\text{first try}}$=792.2 mm, leading to the corresponding radius:

$$r_{eff,ASK,\text{first try}} = \frac{l_{eff,ASK,\text{first try}}}{65°} = 698.3mm \qquad (2.34)$$

In a next step, the fieldmap in the simulation has to be shifted in order use the most
homogeneous part of the dipole field for the central trajectory. The amount by which the
fieldmap has to be shifted is extracted from the difference between the magnet centre and
the centre of the rectangle enclosing the lower left and right sides of the arc trajectory and
its sagitta.
Once determined, the simulation is restarted and the new effective length is extracted. The
whole procedure is then repeated until the desired convergence found. The final positioning
of the ASK and the ASL is shown in figure 2.83. The effective lengths are $l_{eff,ASK}$= 802.3
mm and $l_{eff,ASL}$= 1373.7 mm. To check the horizontal alignment figure 2.84 shows the
horizontal displacements from the centrelines in front of and behind the magnet. The
spikes (ASL: z∼0,700,1400 & ASK z∼0,400,800) near the vertex in G4BL are due to the

Minimum of B_y on reference orbit: -0.133745 T

l_eff= 792.229
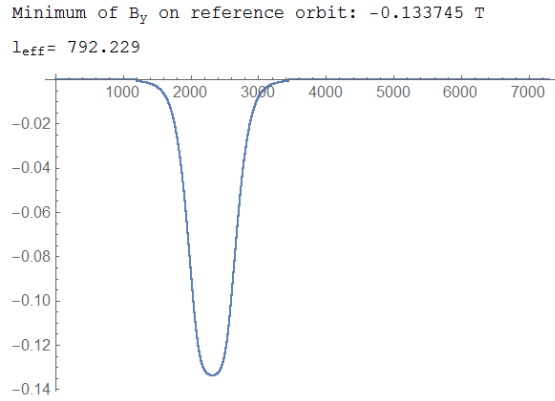
Figure 2.82.: *Shown is the B_y field that is "seen" by the reference particle in figure 2.81. From this the effective length is extracted as $l_{eff,ASK,first\ try}$=792.2 mm.*
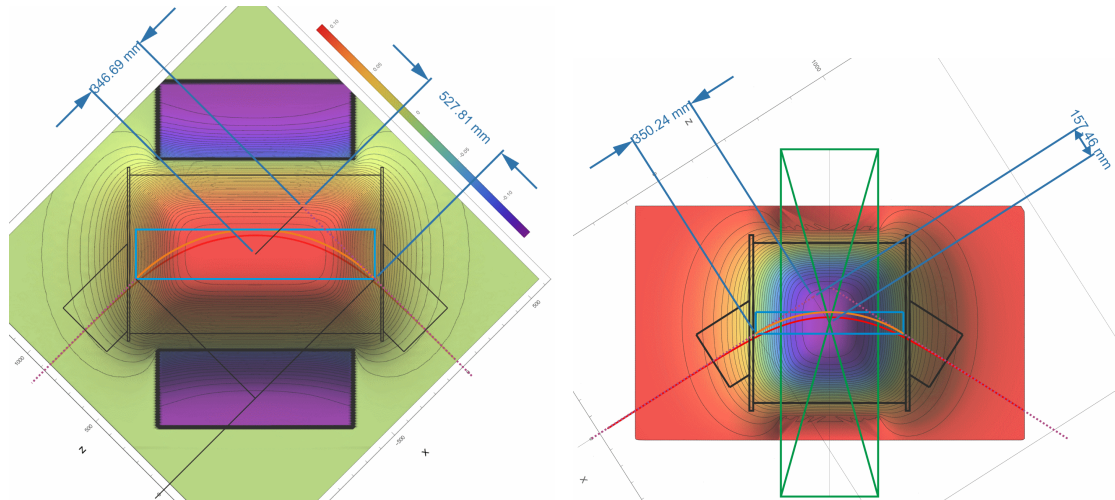
(a) Field and central trajectory in the midplane of the ASL

(b) Field and central trajectory in the midplane of the ASK

Figure 2.83.: *The central trajectories (red lines) are overlayed on a heatplot of the magnetic field in the midplane of the ASL and ASK. The orange arc trajectories indicate the ideal orbit according to the extracted effective lengths. The centres of the dipoles match the centres of the cyan rectangles that are given by the orange ideal trajectories for the shown alignment. The centred vacuum chambers are inidacted with black lines.*

position output near vertices, however the displacement of the optimum trajectory from the ideal orbit given by arcs can be seen in figure 2.83.
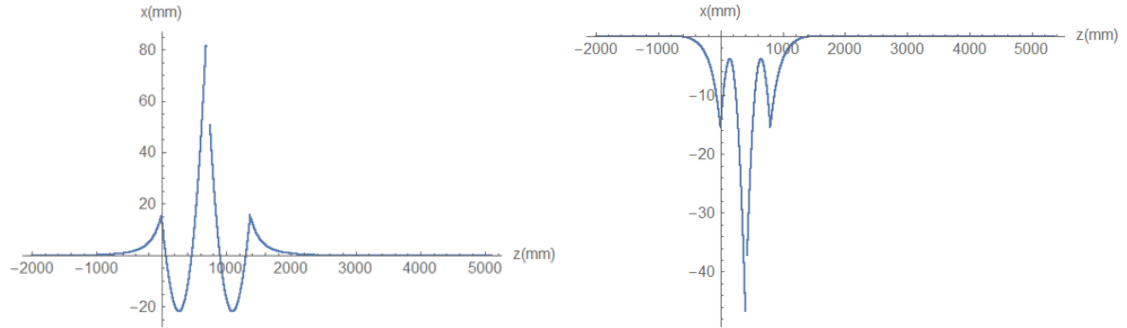
(a) $\bar{x}$ of reference particle injected on-axis to the ASL field

(b) $\bar{x}$ of reference particle injected on-axis to the ASK field

Figure 2.84.: *To check the alignment for the positioning that was shown in figure 2.83 the horizontal deviation from the centreline is checked for both magnets. The plots show the horizontal offset $\bar{x}$ of a reference particle that is injected on-axis after being deflected by 90°/65°. The spikes at the magnets' central positions are due to an artefact in the G4BL position reconstruction near a vertex.*

2.8. Final CMBL beam time 2016

For the CMBL beam time at the end of 2016 the new ASL with a full yoke and new end-plate flanges as well as the ASK with increased gap and new vacuum chamber were prepared. After a first beam tuning period at the Pill1 position the CMBL elements were installed in the area and the measurements were continued at the final focus. All elements DS of the Triplet II were aligned by the PSI survey group. After beam optimization at the final focus the beam was again characterized at the Pill1 position by removing the bellows flange between the ASL dipole and the SML collimator system. The measurement results are presented below. For the CMBL beam time 2016 a novel thin foil Luminophore beam monitoring system with a camera was installed between the Triplet II and the SML/collimator system, which could be moved in and out of the beam. This tool helped in the beam optimization procedure, mainly because it provdided the capability to monitor the beam a) in vacuum and b) US of the Pill1 while optimizing at the final focus. The characterization and results of the validation studies for the Luminophore will be given in [66].

The first beam optimization at the Pill1 position yielded a final rate of $1.11 \cdot 10^8$ μ^+/s @ 2.2 mA proton current and the raster scan that was taken is shown in figure 2.85. As
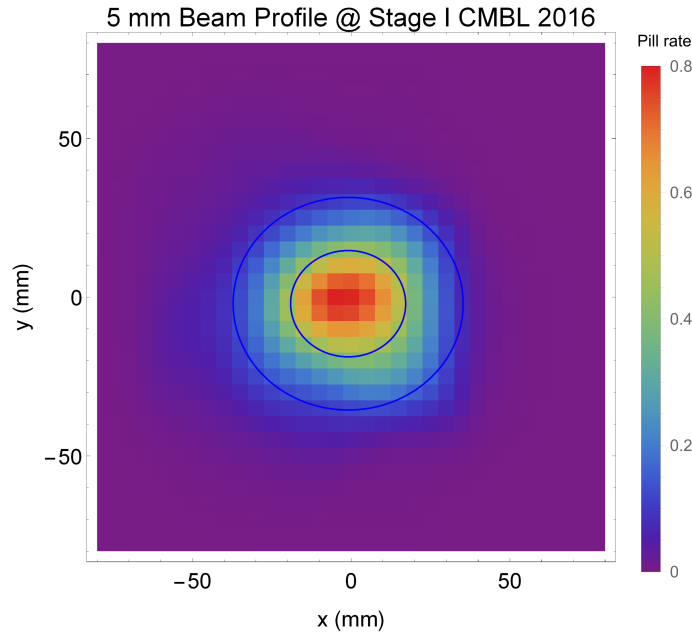
Figure 2.85.: *The beam line was optimized for the Pill1 position. The raster scan and a 2D Gauss fit yield the following parametres: $\bar{x}$=-0.94 mm, $\bar{y}$=-2.08, σ_x=18.12 mm, σ_y=16.73 mm, ρ_{xy}=0.0016. The rate according to the scaled sum of all measurement points is $1.11 \cdot 10^8$ μ^+/s @ 2.2 mA proton current*

expected the results for the beam profile and the rates are similar to what was measured in the previous runs. In the following the remaining magnets were installed and the alignment was also made by the PSI survey group. The beam optimization at the final QSM focus position that followed, proved to be very challenging and great effort was spent to determine a proper tune that yielded the highest flux of muons. In order to enhance the

transmission the inner collimator was removed DS of Triplet II, which then provided a square $165{\times}165$ mm^2 aperture instead of the previous 120 mm round aperture. Further optimization to the end of the beam line yielded a surface muon rate at the final focus of $8.44{\cdot}10^7$ μ^+/s at 2.2 mA proton current. Since the inner part of the collimator system had been removed for this measurement a low trigger threshold raster scan was required to characterize the beam e^+ contamination. Therefore the scanner DAQ was set up to record both low and high threshold pulses in parallel while the global triggering was made by the low threshold. The corresponding high threshold (muons only) raster scan is shown in figure 2.86(a) while figure 2.86(b) shows the low threshold results measuring the combined rate of muons, beam positrons and positrons from Michel decay. In addition to the Michel positrons a band of beam positrons is visible at the top of the low threshold profile. In order to reduce the background from beam positrons the inner collimator was reinstalled and the optimization was continued for this setting. The muon beam profile for the final beam tune with the inner collimator reinstalled is shown in figure 2.87(a). The scanner configuration was kept as before and the low trigger threshold profile was again extracted with the same scan. The result is shown in figure 2.87(b). The contamination of beam positrons is still visible at the top of the scanned profile though in much reduced number. Therefore to investigate their origin, information on the beam optics at the Pill1 position close to the collimator is required. As previously done the bellows between the SML/collimator system was removed and the scanner system set up. The beam profiles for high and low trigger thresholds for the previous optics are shown in figure 2.88(a) and 2.88(b). The shown raster scans imply that a major contribution of beam e^+ makes it through the collimator system. The implications and possible solutions for this problem will be discussed at the end of this section. For a further investigation the inner collimator was removed again for additional measurements. Raster scans at the Pill1 position with the collimator taken out are shown in figure 2.89(a) (high trigger threshold) and figure 2.89(b) (low trigger threshold). Comparing the muon rates for the final focus tune with the collimator in/out shows, that the transmission to the Pill1 position increases by $\sim$10 % and by $\sim$8 % for the final focus position, when the collimator is removed.

The last measurement of the CMBL that is presented here is the low threshold vertical distribution taken at the Pill1 position. This was done for different quadrupole tunes of the QSK43 and shows the influence of the QSK43 setting on the beam e^+ contamination. Four dedicated low threshold cross scans were taken horizontally centred on the low threshold distribution. The other low threshold scans were taken parasitically with the same electronics setup as in the case of the previously shown raster scans and therefore measure the low threshold profile going through the centre of the muon distribution. Both types of scans yield comparable distributions but the amplitude can differ between the different techniques and only the relative profile dependence can be extracted in this way. Figure 2.90 shows the vertical profiles measured at the Pill1 position with the inner collimator still removed for different QSK43 currents. It can be observed that for lower QSK43 currents the lower part of the distribution, that corresponds to the beam positrons, is shifted from the bottom of the profile towards the centre. The lower current setting however is important in achieving maximal rate for the final focus tune implying that the beam focus is shifted DS with respect to former MEG settings, suggesting that for the Mu3e CMBL tune at the final focus, the collimator is not at the optimal position. Hence the beam positron contamination can be explained by two facts. Since the focus position after Triplet II is
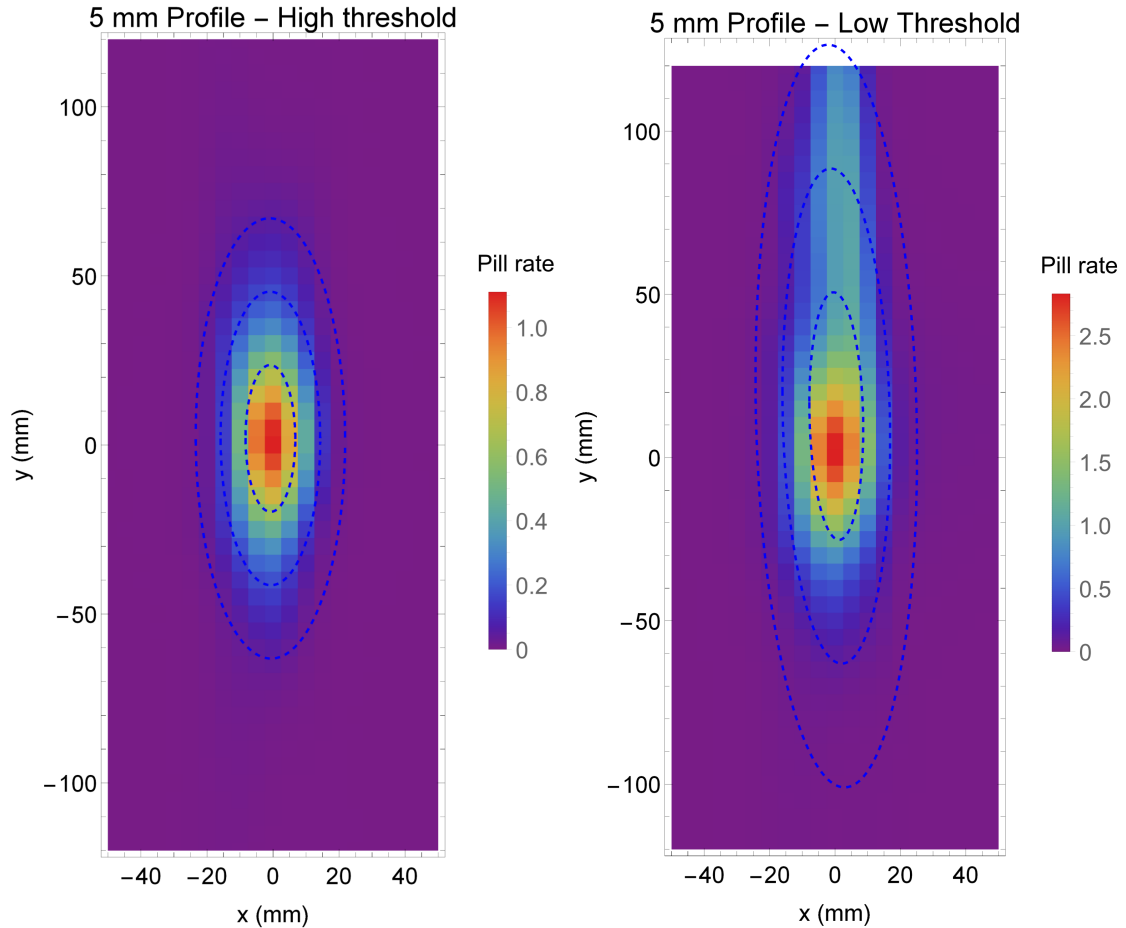
(a) Raster scan of muons only at the final focus with the inner collimator taken out

(b) Raster scan of the combined rate of muons and positrons at the final focus with the inner collimator taken out

Figure 2.86.: *For the shown raster scans at the final focus position the collimator was removed. The high threshold scan (left) takes into account only muons and the low threshold (right) also counts Michel and beam positrons. The evaluation of the high threshold scan yields:*
$\bar{x}$=-0.80 mm, $\bar{y}$=1.92, σ_x=7.54 mm, σ_y=21.71 mm, ρ_{xy}=0.0104. *The rate extracted from the scaled sum of the grid points is* $8.44 \cdot 10^7$ μ^+/s *at 2.2 mA proton current. Although the main profile contribution in the low threshold case matches the muon distribution shown in figure 2.86(a) and is attributed to muons and Michel positrons, a band of beam positrons comes in from the top of the profile. The evaluation of the low threshold scan yields a rate of* $3.38 \cdot 10^8$ $(\mu^+ + e^+)/s$ *at 2.2 mA proton current.*
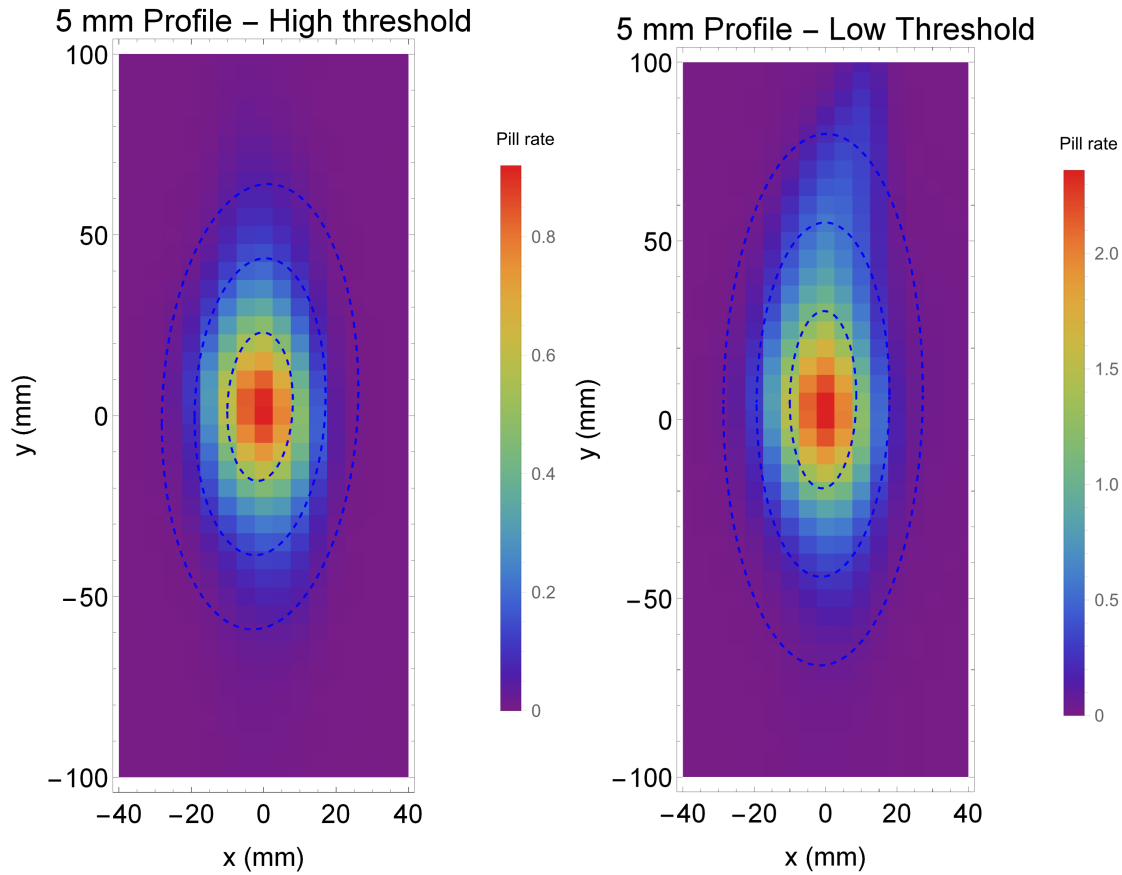
5 mm Profile – High threshold

5 mm Profile – Low Threshold

(a) Raster scan of muons only at the final focus with the inner collimator in place

(b) Raster scan of the combined rate of muons and positrons at the final focus with the inner collimator in place

Figure 2.87.: *For the shown raster scans at the final focus position the collimator was in place. The high threshold scan (left) takes into account only muons and the low threshold (right) also counts Michel and beam positrons. The evaluation of the high threshold scan yields:*
$\bar{x}$=-1.00 mm, $\bar{y}$=2.47, σ_x=9.05 mm, σ_y=20.52 mm, ρ_{xy}=-0.0785. The scaled sum of all measured points yields a normalized rate of 7.81 ·10^7 μ^+/s at 2.2 mA proton current. Although the inner collimator was reinstalled for this measurement the beam positrons are still visible at the top of the profile in the low threshold scan. The scaled sum of the measured points yield a rate of 2.46·10^8 (μ^++e^+)/s at 2.2 mA proton current.
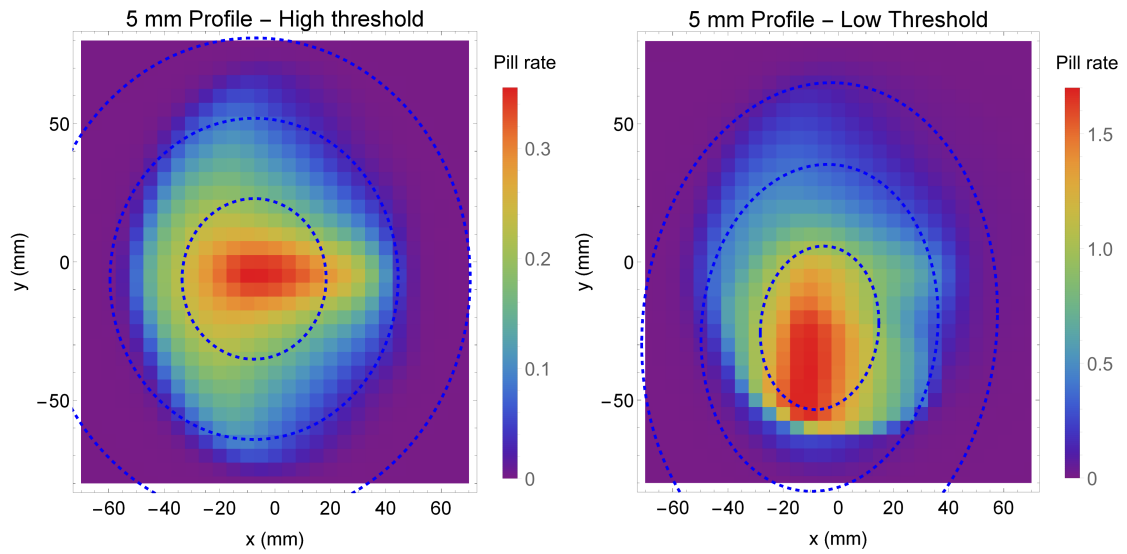
(a) Raster scan of muons only at the Pill1 position with the inner collimator in place

(b) Raster scan of the combined rate of muons and positrons at the Pill1 position with the inner collimator in place

Figure 2.88.: *For the shown raster scans at the Pill1 position the collimator was in place. The high threshold scan (left) takes into account only muons and the low threshold (right) also counts Michel and beam positrons. The evaluation of the high threshold scan yields:*
$\bar{x}$=-7.55 mm, $\bar{y}$=-6.12, σ_x=26.00 mm, σ_y=29.01 mm, ρ_{xy}=-0.0024. The scaled sum of the measured points yield the rate $1.08 \cdot 10^8$ μ^+/s at 2.2 mA proton current. The low trigger threshold profile shows a high contribution from positrons. Comparing with the high threshold profile implies that the major fraction is due to beam positrons. The scaled sum yields a rate of $4.79 \cdot 10^8$ $(\mu^+ + e^+)/s$ at 2.2 mA proton current.
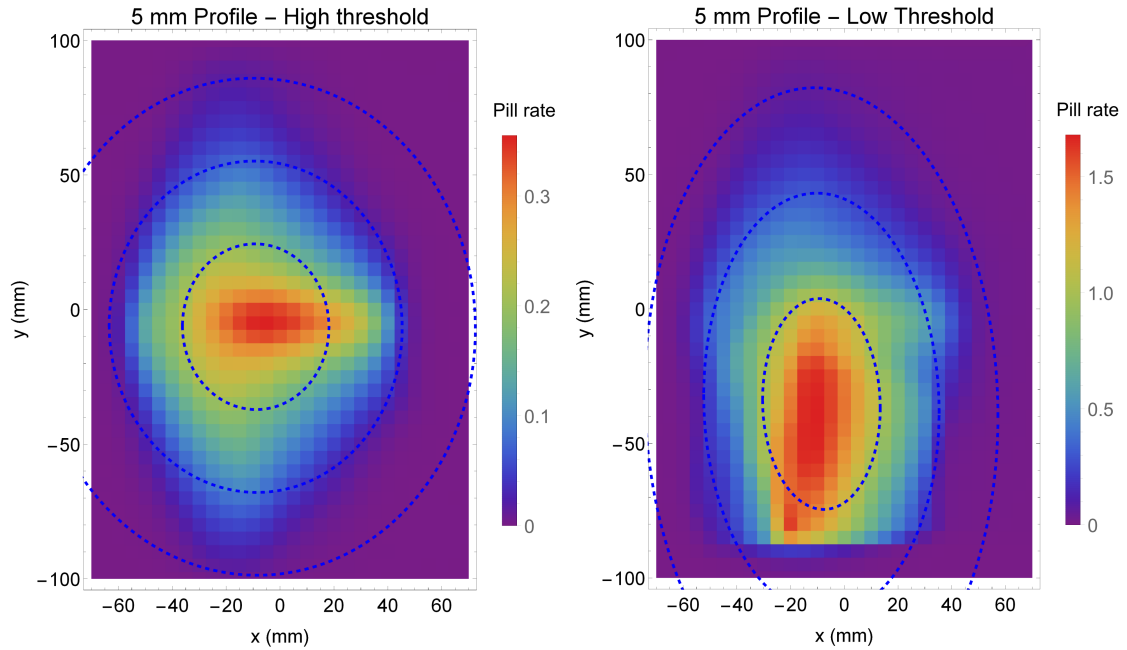
(a) Raster scan of muons only at the Pill1 position with the inner collimator removed

(b) Raster scan of the combined rate of muons and positrons at the Pill1 position with the inner collimator removed

Figure 2.89.: *For the shown raster scans at the Pill1 position the inner collimator had been removed. The high threshold scan (left) takes into account only muons and the low threshold (right) also counts Michel and beam positrons. The evaluation of the high threshold scan yields: $\bar{x}$=-9.04 mm, $\bar{y}$=-6.36, σ_x=27.12 mm, σ_y=30.77 mm, ρ_{xy}=0.0084. The scaled sum of the measured points yields a normalized rate of $1.19 \cdot 10^8$ μ^+/s at 2.2 mA proton current. The combined rate (μ^+ & all e^+) in the low threshold profile is dominated by the positrons on the bottom of the scanner range. The rate accoridng to the scaled sum of the measured points is $6.41 \cdot 10^8$ ($\mu^+ + e^+$)/s at 2.2 mA proton current. This should be compared to figure 2.88(b). The $\sim$34% more beam e^+ with the inner collimator removed are consistent with the same situation at the final focus $\sim$37 %. $\rightarrow$ Virtually all e^+ contamination at the collimator is transmitted to the final focus.*
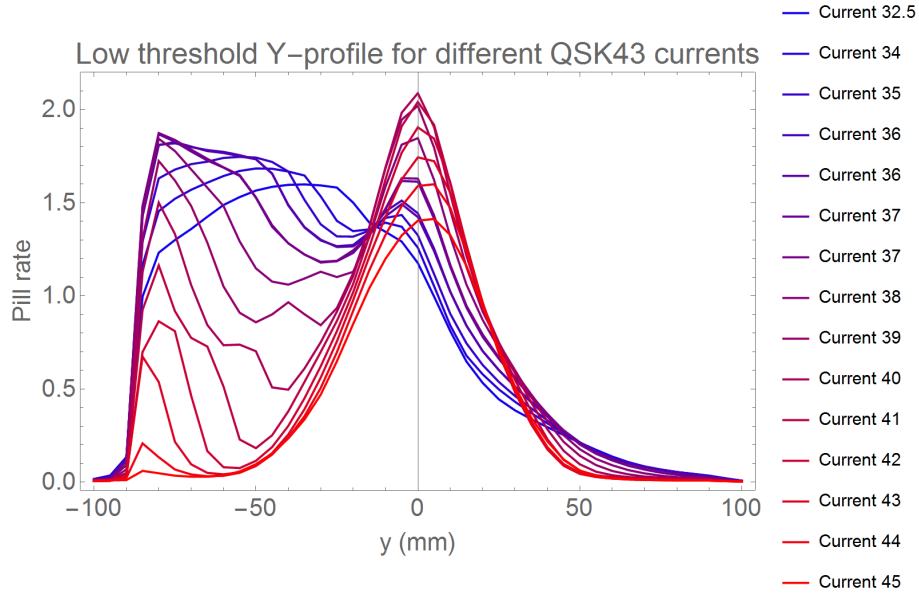
Figure 2.90.: *Shown are vertical scans for different QSK43 currents at the Pill1 position. The scans were taken on a vertical line for slightly different horizontal offsets. It can be observed, that for the lower currents the beam positrons, corresponding to the low y-value part of the distribution, are shifted towards the centre.*

shifted DS the beam size of both the muon and the beam positron fraction is larger at the collimator position. In the case of the muons this led to a cut of the muon beam, especially in the horizontal direction. However, for the beam positrons this means that a part of the larger beam makes it through the collimator inner diameter. The second part of the explanation covers the behaviour of the positron beam centroid that is shown in figure 2.90. Figure 2.91 shows a qualitative explanation for the centroid shift towards the collimator centre for lower QSK43 currents. As expected the muons (orange) are not deflected by the separator but pass the collimator system on the centreline. The beam positrons however are deflected in the Triplet II. The violet trajectories correspond to QSK43 set to 44 A, the yellow trajectories correspond to QSK43 set to 28 A. The behaviour of the beam centroid shift can be qualitatively reproduced with the simulation.

Further analysis of the CMBL 2016 measured data in combination with simulation studies are planned for the near future, to a) look for ways to further enhance the rate at the end and b) determine a new position for the collimator that garantuees a pure muon beam at the end of the beam line, that is essentially free from positron contamination.
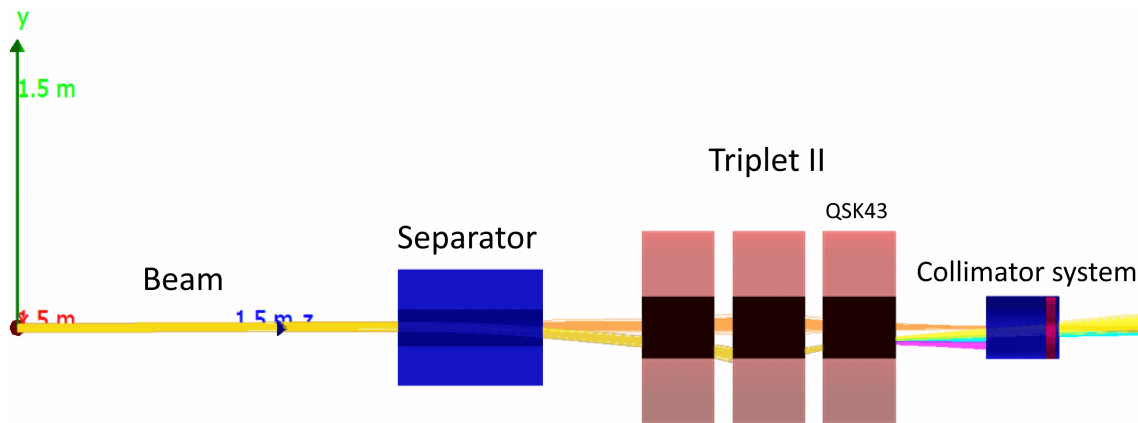
Figure 2.91.: *Shown is the graphical output of G4BL. The simulation comprises of the particle separator, with the fields set to the CMBL 2016 settings, Triplet II with currents close to the final focus settings and the SML/collimator system. The orange trajectories correspond to a reduced phase space subset of muons. The yellow trajectories are beam positrons tracked with the QSK43 set to 28 A, the cyan trajectories correspond to QSK43 at 36 A and the violet trajectries are simulated for the 44 A.*

2.9. G4BL beam optimization study for the Mu3e spectrometer

In the following, the short version of the G4BL simulation is used to simulate the beam that can be expected on target of the Mu3e experiment. Therefore the short version of the beam line with the upgraded ASL and ASK magnets has been further extended with a realistic implementation of the Mu3e solenoid magnet. The design of the inner beam tube of the Mu3e solenoid has not yet been finalized and is implemented in the simulation with a conical entrance followed by a 60 mm diameter beam tube. The graphical output of the simulation geometry and a representative subset of trajectories is shown in figure 2.92. For
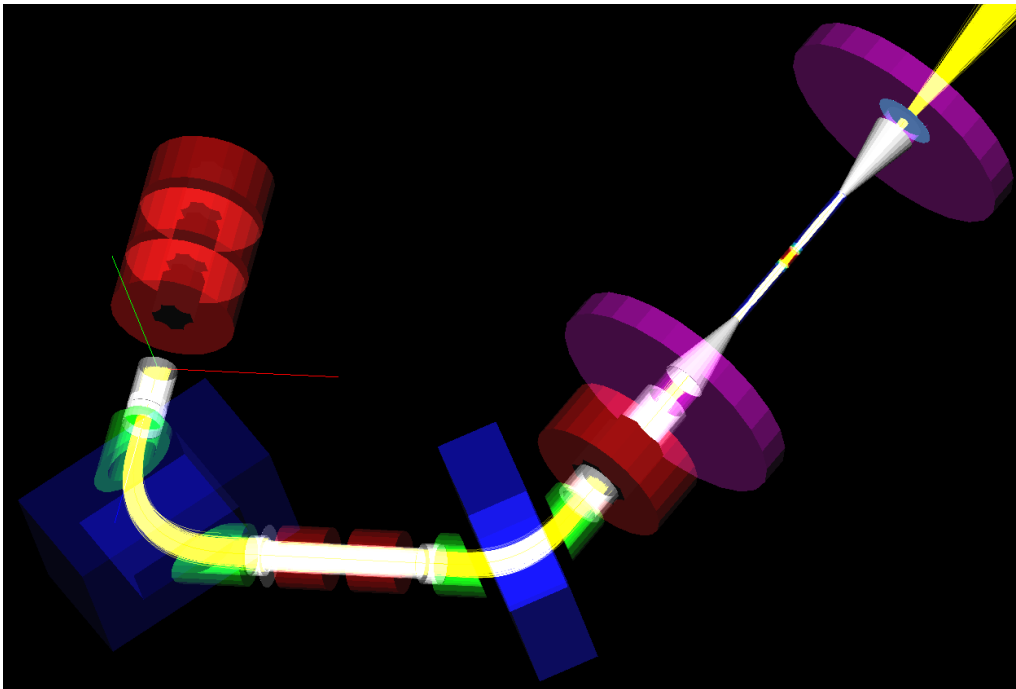
Figure 2.92.: *The graphical output of the G4BL simulation shows the CMBL elements and the Mu3e solenoid, represented by the corresponding fieldmap and a conical entrance and exit aperture with a 60 mm diameter beam-pipe in-between.*

the optimization 10^5 muons, distributed according to the CMBL 2014/2015 phase space, were tracked through the CMBL, including the Mu3e solenoid. The beam line elements SML, ASL, QSO41, QSO42, ASK, QSM were tuned to yield the highest rate within the planned 19 mm target radius at the centre of the solenoid. The computation was done with the *Optima G4BL* code (appendix 4.4).
Figure 2.93 shows the simulated horizontal and vertical beam envelopes and centroids along the CMBL. The corresponding beam losses are shown in figure 2.94. The simulation shows, that a transmission from the Pill1 position to the Mu3e target of 68.1 %, after scaling with the survival probability, is possible. The beam profile at the centre is shown in figure 2.95(a) and the fraction of the transmitted particles that reaches the solenoid centre within a given target radius is shown in figure 2.95(b). The major fraction of beam losses throughout the CMBL occur at the injection to the Mu3e solenoid where a
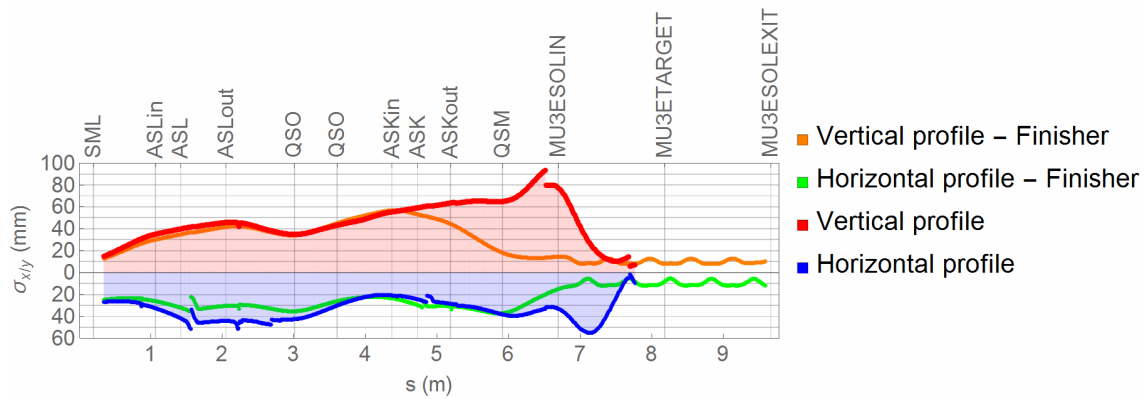
(a) Beam envelopes for the optimization of the CMBL on a 19 mm radius Mu3e target
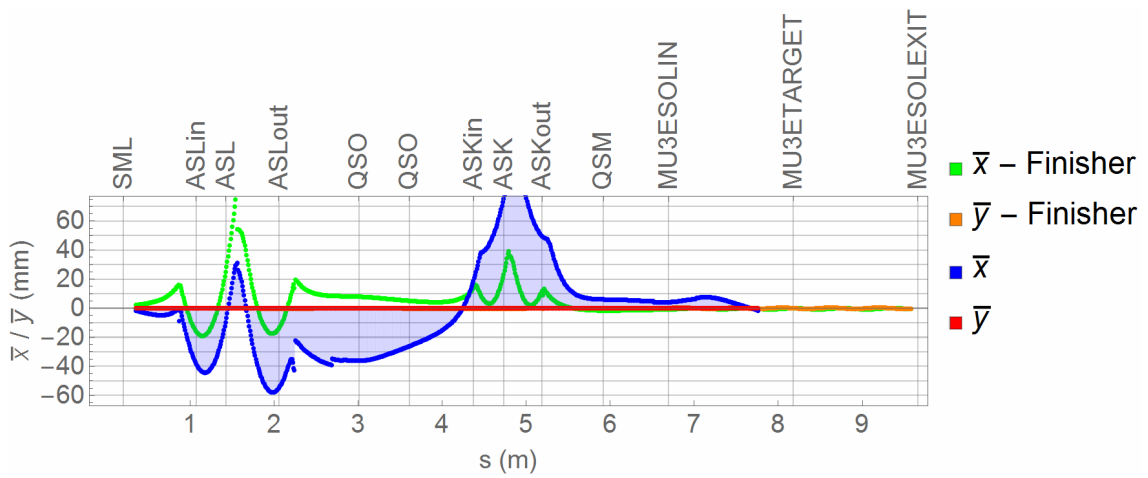
(b) Beam centroid for the optimization of the CMBL on a 19 mm radius Mu3e target

Figure 2.93.: *The shown beam envelopes and centroid plots correspond to the phase space propagation of the 2014/2015 transverse phase space in the CMBL. The beam line elements are optimized to achieve a maximum rate on a 19 mm radius target at the centre of the Mu3e solenoid.*
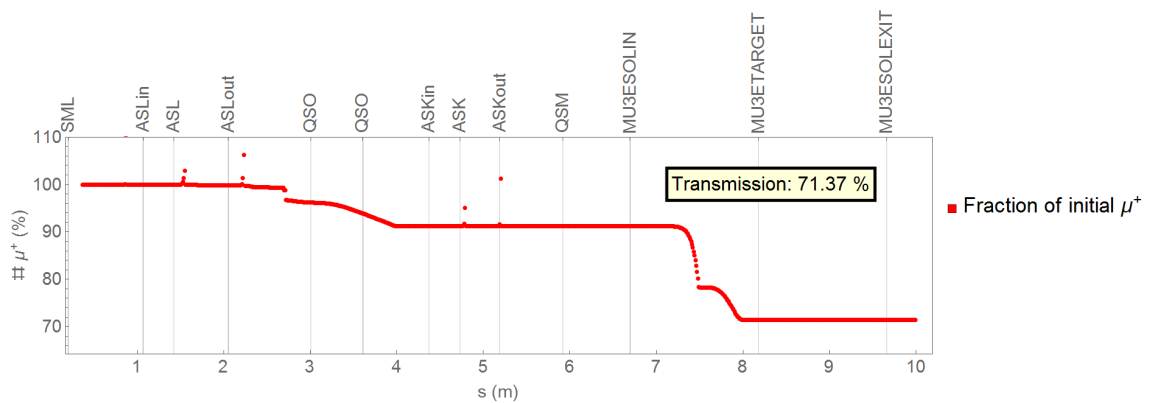
Figure 2.94.: *The shown beam losses correspond to an optimized beam tune of the CMBL elements for maximal rate on the target at the centre of the Mu3e solenoid.*
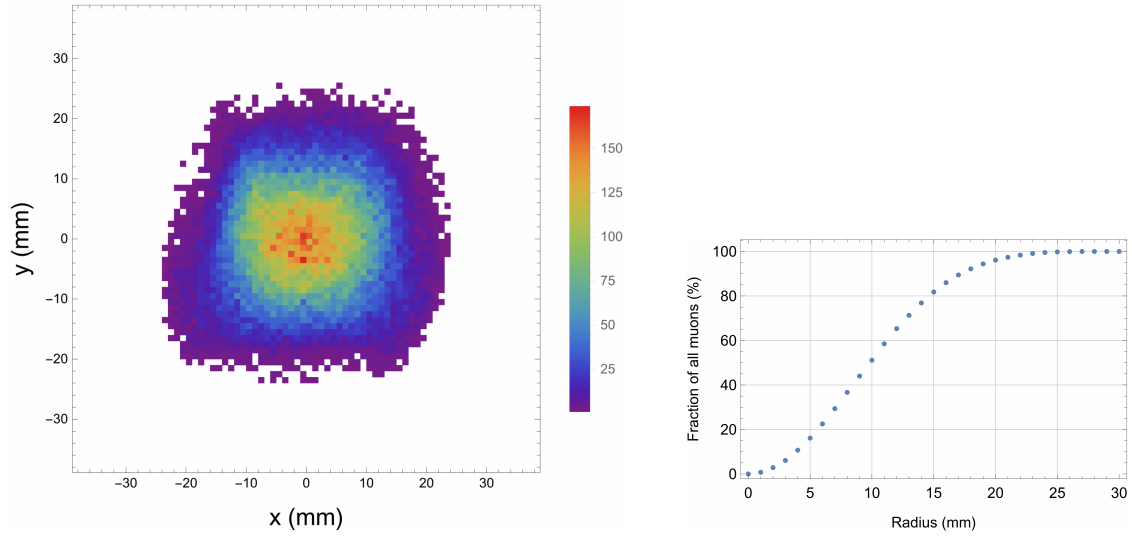
(a) Beam Profile for the optimized tune at the centre of the Mu3e solenoid

(b) Fraction of muons that reach the centre of the Mu3e solenoid vs. target radius

Figure 2.95.: *Shown is the beam profile according to the optimized G4BL simulation. The 19 mm target radius contains ∼95 % of all muons that reach the centre of the Mu3e solenoid.*

conical transition between the standard 320 mm diameter beam-pipe to the inner detector support beam tube of 60 mm diameter takes place. The latter diameter is governed by the inner silicon tracking detector size which also determines the maximum target diameter. Although not well matched to the beam emittance of such a secondary beam line, it is a compromise betwenn occupancy, number of channels, vertex resolution and stopping rate. To overcome part of these losses the possibility of a short air-core coupling solenoid should be investigated.

The status of the simulation is not yet final, as the newer phase space of the CMBL 2016 test beam measurements still need to be evaluated and implemented in the simulation.

2.10. Conclusions & Outlook on the CMBL setup, measurements and simulation status

The Mu3e experiment plans for a first engineering run in 2019. In order to reach the final sensitivity, a staged approach is foreseen with different detector setups requiring a stepwise increase in muon beam rates. The initial phase I using the CMBL will be carried out in the πE5 area at PSI. The shared use together with the MEG II experiment necessiated a challenging beam line design with the main constraints imposed by the limited available space and the requirement for the highest intensity available.

A solution to fit into the front part of the πE5 area, while still having a high $\sim$8·10^7 μ^+/s rate at the injection to the Mu3e solenoid was found in the presented CMBL design and first commissionig runs have proved very succesful. The CMBL allows for a fully independent operation of the front and the rear part of the experimental area, which means that work on the MEG II setup is not compromised by Mu3e beam times. With the current CMBL design all beam line elements can in principle stay in place and only the ASL magnet has to be replaced by the BTS when switching between the Mu3e and the MEG II setups. Furthermore, an economic solution concerning the beam elements for the CMBL was found using spare elements, that had already been used in other experiments. As a result of the 2014/2015 beam time the vacuum chambers of the ASL and the ASK and the yoke of the latter dipole were modified to enhance the acceptance and transmission of the CMBL. The investigations that led to these modifiactions were based on an accurate G4BL simulation of the last part of the beam line, which made use of realistic field maps and a reconstruction of the transverse phase space that showed a good agreement with the 2014/2015 test beam setup. The 2016 test beam with the modified ASL and ASK vacuum chambers yielded a significantly increased final rate of $\sim$7.8·10^7 μ^+/s for the inner collimator in place and $\sim$8.4·10^7 μ^+/s with the inner collimator taken out, all measured at 2.2 mA proton current. However these rates are still less than what was expected from the previous simulation. This can partially be explained with the missing momentum correlation, which led to an underestimated beam spread from dispersion at the QSO doublet. It is also possible that the actual optimum setting has not yet been found, since time constraints had an influence on the schedule during the 2016 beam time.

The 250 mm diameter vacuum-pipe of the QSO doublet represents the smallest diameter aperture that follows the longest distance without active focussing in the entire πE5 beam line. A possible replacement with the initially planned QSN doublet, that has a larger cross-shaped vacuum chamber is not feasible in the current setup due to transverse spatial constraints imposed by the concrete shielding walls.

The beam contamination, that was observed in the 2016 test beam requires further investigation and can be improved either via a modified beam line tune or a different collimator setup. The beam tune for the CMBL however requires comparable Triplet II values to minimize the beam losses at the injection to the QSO doublet. Therefore the available data has to be further analyzed and a new collimator position further DS determined for Mu3e. The proposed new collimator should in addition not be round, but rather have an asymmetric design to cut vertically and to be less restrictive in the horizontal direction. The final rate can therefore be expected to lie between the rates that were measured in 2016 with the collimator in and out.

The simulation of the Mu3e beam line together with the Mu3e solenoid showed a maximum transmission to the 19 mm stopping target of 68 %. The normalization of all quoted rates to 2.2 mA reflects the status of the proton current during most of the beam times. However, already in 2016 the PSI HIPA accelerator complex recieved the permission to operate at 2.4 mA with possible further increased intensities foreseen in the near future [71], which will directly increase the muon rates. Furthermore, for all measurements, that were presented, the muon production target had a length of 40 mm. However most recent measurements in 2017 using a former production target with a length of 60 mm, show an enhanced rate at the intermediate focus position of ∼30 %. Therefore surface muon rates at the centre of the Mu3e solenoid close to 10^8 μ^+/s can be expected for the run using the 60 mm long TgE.

The Mu3e innermost pixel detector requires shielding from muons that do not hit the centre of the target. Figure 2.93(a) can be used to evaluate a suitable collimator position, by studying the difference in envelopes representing the entire beam and the subset of muons that end on the Mu3e target.

Although initially planned solely for the Mu3e experiment, the CMBL has already been used by several experiments:

- the AlCap Collaboration, a combined Mu2e/Comet test experiment to study muon capture for $\mu \to e$ conversion experiments [72]
- Hyperfine splitting in μH and $\mu^3 He^+$ [73]
- MuX, measuring the charge radius of Radium [74]

Once the beam positron background situation has been solved with a new collimator design the CMBL will provide an excellent environment for those experiments that require a low background, benefitting from the two bending magnets and far distance to the collimator, which reduces the Michel positron background from muons decaying in flight and γs from particle stops in the collimator.

In conclusion it can be stated, that the CMBL successfully passed its first commissioning tests and the beam could be characterized at three distinct measurement locations, which will also be benefitial to future πE5 users. Several issues concerning the beam line could be identified and improvements applied. In the future the CMBL offers a high rate surface muon beam, with a potential low background from Michels and γs, to Mu3e, enabling a three orders of magnituded more sensitive measurement than the current experimental limit, and enabling the possibilities for other experiments at PSI.

Furthermore, the simulation studies turned out to be a powerful tool showing good agreement with the 2014/2015 test beam results. The long version of the full beam line starting from TgE promises to significantly contribute to a deeper understanding of the complex πE5 beam line and show potential ways to enhance the beam rates for all experiments in πE5.

3. The MEG II Scintillation Target

The general requirements for the MEG target are still valid for the MEG II target and are:

- High muon stopping efficiency
- Minimization of annihilation-in-flight (AIF) or Radiative Muon Decay (RMD) photon production in the target
- Minimization of Multiple Scattering and Bremsstrahlung production from the e^+ leaving the target after muon decay
- Consideration of the e^+ angular asymmetry due to the muon polarization
- Allow the e^+ decay vertex reconstruction and e^+ direction at the target plane to be determined
- Dimensionally stable and remotely movable target

To satisfy these requirements for MEG a thin, low-Z, low density, elliptical layered structure of Polyethylene (PE) and Polyester (PET) was chosen as a target and placed at ~20.5° to the beam-axis. In MEG II these essential features are also required, however, based on the upgrade performance of the detectors more stringent requirements must be met concerning the stopping rate, positron multiple scattering and photon background production, leading to a new optimized target design.

A study of the optimal beam momentum and target characteristics was undertaken as outlined in the MEG upgrade proposal [4]. The baseline solution chosen was the combination of a surface muon beam of 28 MeV/c together with a 140 μm thick PE (CH_2) target placed at 15° to the beam-axis, rather than a sub-surface muon beam of 25 MeV/c. This reduction in thickness and angle for example reduces the multiple scattering in the MEG target by a factor 1.5.

Further candidate targets have since been studied and are summarized in table 3.1. Each target has an equivalent thickness to the baseline solution of a 140 μm of CH_2, so achieving an equivalent stopping efficiency. Apparent from table 3.1 is that all candidate targets have similar properties with the multiple scattering estimates varying less than 10 % from the average. The equivalent thickness in radiation lengths however does vary by as much as 25 % from the average, with different materials outperforming each other in different categories. Beryllium shows an overall good performance though from the thickness & size required as well as the safety aspect is not so favoured. Diamond which is mechanically stable and known to be more radiation resistant as well as having scintillation properties has however, the second largest radiation length equivalent thickness and is currently not commercially available in the size required for MEG II. The scintillation target (Scint. PVT) shows mid-range performance characteristics though with the substantial benefit of online beam monitoring capabilities comprising of full information about the beam profile as well as the relative intensity at the centre of the COBRA solenoid. The most promising

Table 3.1.: *The table lists the possible target candidates that were considered for MEG II and their properties based on calculations. All candidate targets have an 15° inclination angle and are preceeded by a 350 μm Mylar degrader. The data was provided by [75, 76]*

Material	Thickness (μm)	t/X_0	Density (g/cm^3)	Stop Efficiency (%)	Multiple Scatt. $\mu^{+(18MeV)}$ e$^{+(52MeV)}$ (mrad)	
CH$_2$	140	$2.8 \cdot 10^{-4}$	0.893	83	52.0	3.0
Be	90	$2.6 \cdot 10^{-4}$	1.848	83	49.3	2.9
MYLAR	100	$3.5 \cdot 10^{-4}$	1.390	84	58.5	3.4
Scint. PVT	130	$3.1 \cdot 10^{-4}$	1.032	84	54.5	3.2
Diamond	40	$3.3 \cdot 10^{-4}$	3.515	81	56.8	3.3

candidate for a scintillation target is BC400 from Saint-Gobain [77], which is only available with thicknesses down to 150 μm in a sufficent size for MEG II. A scintillation target made from such a thin slab of BC400 was tested during two beam times - at an intermediate focus position of the πE5 beamline at the end of 2015 and used as a stopping target in COBRA during the Pre-Engineering Run in 2016.

3.1. Introduction to Scintillation Characteristics

Scintillators are fast and energy sensitive detector materials for different types of radiation which work based on luminescence. The emitted light is usually part of the visible spectrum and for moderate energy depositions the Light Yield (LY) is proportional to the energy loss in the medium. Scintillators are available in liquid form, e.g. the LXe as used in the MEG calorimeter as a γ-detector, or in gaseous or solid form. The compounds of solid scintillators are either inorganic such as e.g. the Bismuth Germanium Oxide (Bismuth Germanate) $Bi_4Ge_3O_{12}$ (BGO) crystal, as used during the MEG CEX calibration runs, or organic as in the case of the common plastic scintillators Polystyrene (PS) and PVT. Light from inorganic crystals is due to band-gap transitions in the crystal, whereas organic scintillators emit light due to transitions between the energy levels in aromatic molecules. Compared to inorganic scintillators, plastic scintillators have a lower density and lower-Z (nuclear charge) comparable to PE and therefore predestined as a MEG stopping target. The physics involved in the generation of scintillation light is similar for the various organic scintillators, though their individual properties can be steered by the addition of different types and proportions of base material and dopants allowing for different optical characteristics such as LY, rise/decay time and spectral distribution as well as other parameters such as radiation hardness or chemical and mechanical robustness to be influenced. The envisaged material for the MEG II scintillation target is BC400B from Saint Gobain, which is designed as a multi purpose scintillator and the only scintillator available with the thickness and size required. The base material of BC400B is PVT and the primary dopant is para-Terphenyl (1,4-Diphenylbenzene). In order to increase the so-called Stokes-shift, the separation between the emission and absorption spectrum, an additional wavelength shifting fluor 1,4-bis(5-phenyloxazol-2-yl) benzene known as POPOP is added in small con-

centration. The chemical structures of the compounds of BC400B are shown in figure 3.1.

(a) (b) (c)
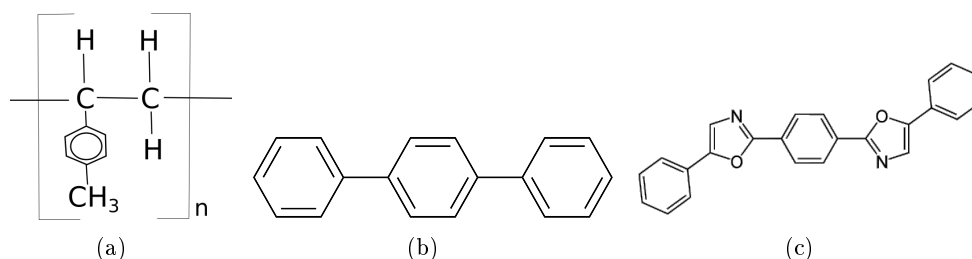
Figure 3.1.: *Ingredients of BC400B from Saint-Gobain:*
a) base material: $[CH_2CH(C_6H_4CH_3)]_n$ PVT [78]
b) primary dopant: $C_{18}H_{14}$ Para-terphenyl[79]
c) secondary fluor: $C_{24}H_{16}N_2O_2$ POPOP[80]

3.1.1. Scintillation mechanism in organic scintillators

The purpose of scintillators is the conversion of energy that is deposited in the detector into visible/detectable light. In the case of an organic scintillator, ground state valence electrons from the 3 covalent or π-bonds in a benzene ring are excited to higher singlet states. Fast radiationless de-excitation via vibrational sub-levels ν_i lead to the vibrational ground level ν_0 of the first excited singlet state. Subsequent transitions to ground state levels are accompanied by the emission of fluorescence light. In the case of fluorescence the full chain of energy loss in the material and the emission of light occurs on the order of a few nanoseconds. Intersystem crossing (ISC) between the first excited singlet and triplet states leads to a several orders of magnitude slower deexcitation via phosphorescence. Figure 3.2 illustrates the excited states of an organic scintillator. Organic scintillators that
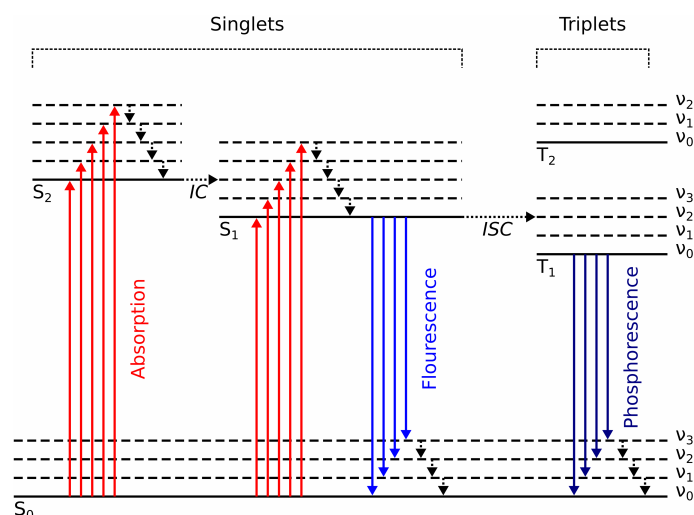
Figure 3.2.: *Shown is the Jablonski diagram for an organic scintillator molecule. Figure was taken from [38]*

occur as polymers (plastic scintillators) show an inferior fluorescence efficiency compared to e.g. crystalline Anthracene but alternative de-excitation channels can be enhanced. Hence additional fluors have to be added to the base material. In the following the scintillation principle is briefly explained by taking the example of BC400.

Once the scintillator is irradiated, a part of the energy loss $\frac{dE}{dx}$ is absorbed in the scintillator base material PVT. The PVT transfers its excitation energy to the primary dopant p-Terphenyl. A concentration on the order of $\sim 1\%$ ensures a short mean distance between base material and primary solvent molecules. Therefore the energy is transfered mainly via radiationless Förster resonance energy transfer (FRET) i.e. dipole-dipole interactions. In order to avoid self-absorption a small concentration of a second wavelength-shifting fluor 1,4-bis(5-phenyloxazol-2-yl) benzene (POPOP) is added [81]. The Stokes shift of POPOP separates the emission spectrum of the POPOP and the overall absorption spectrum in order to minimize light loss in the scintillator material. The corresponding spectra are shown in figure 3.3. In contrast to other setups where scintillators are employed, the
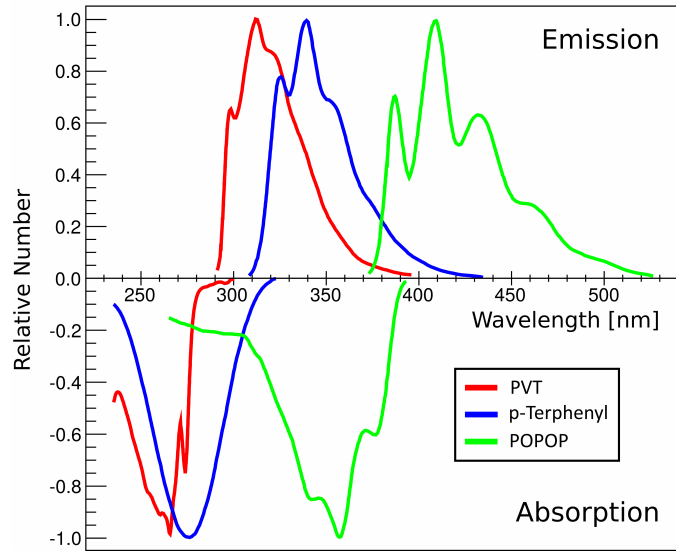
Figure 3.3.: *Shown are the emission and absorption spectra of PVT, p-Terphenyl and POPOP. Figure has been adapted from [38]*

working principle of the scintillation target with a CCD camera and exposure times of the order of tens of seconds does not require a scintillator response on a nanosecond scale, which would also allow for other phosphorescent materials. Other aspects such as quenching effects induced by high energy depositions by single particles causing a non-linear response of the LY play only a minor role in the case of the MEG II target as the camera exposure time integrates the LY of a large number of particles $\frac{\mathcal{O}\left(10^9 \rightarrow 10^{10}\right)\mu^+}{t(frame)}$. However considering the properties of plastic scintillators, especially the low nuclear charge, density and LY, makes them the favoured choice for MEG II.

3.1.2. Radiation Damage in plastic scintillators

Plastic scintillators have properties that are favourable for the use as a stopping target such as a low density, low nuclear charge Z, good homogeneity and a good reproducibility. However for certain applications a dose-dependent degradation of the light output has been observed. Up to now there is no comprehensive framework that quantitatively describes radiation damage for arbitrary setups. Nevertheless a variety of literature is available, the major part dating back to the late 80's and early 90's in the context of detector developments for the Superconducting Super Collider[82]. However radiation damage in plastic scintillators is still the subject of more recent research projects, e.g. in the context of radiation hard detector components for the Large Hadron Collider at CERN[83]. Reliable data on radiation damage in PVT is rare and the available data spans a large parameter space, showing different results depending on the environment, geometry, dose, dose rate, particle type[1] and the scintillator compounds. An attempt to provide a theoretical framework for radiation damage in PS which quantitatively links the observed degradation to the formation of radicals and the associated chemical reaction channels can be found in [86]. Neglecting the influence of oxygen as a potential annealing agent and dose rate dependence, the radiation damage in plastic scintillators is described by an exponential decay of the initial LY in [83]:

$$L(d) = L_0 \cdot e^{-\frac{d}{D}} \tag{3.1}$$

where L is the actual LY, L_0 is the initial LY before irradiation, d is the absorbed dose and D the material decay constant which depends on the sample properties, the sample environment and the nature of the irradiation.

Although the majority of publications cover the radiation damage in PS, radiation damage in PVT is expected to be based on qualitatively the same effects [87]. The remainder of this section provides a brief overview of the phenomena commonly described in literature and how it relates to the use of a scintillation target for MEG II.

Light loss during irradiation is usually accompanied by a change of the appearance of the sample. The former clear and transparent sample becomes yellow-brown [88]. After irradiation a partial annealing of the scintillation properties can be observed, that is also reflected in a bleaching of the sample. The reduction in LY can be mainly associated with a wavelength-dependend decrease in transmission in the solvent [89]. This is related to the creation of absorption centres formed by radicals in the base material [82, 90]. Absolute numbers for the loss of scintillation light in BC400 after irradiation with a Cs-137 source in air are presented in [91]. The relative LY was measured with a FEU-110 PMT and therefore shows the convolution of the wavelength-dependent quantum efficiency of the PMT and the generated light. After exposure to $3.4 \cdot 10^4$ Gy the light output degraded to 44.4 %. Further irradiation up to 10^5 Gy resulted in a decreased output corresponding to 31.0 % of the unirradiated sample. Figure 3.4 illustrates the asymmetric degradation of the transmission spectrum of NE102a for different irradiation doses. The light transmission degrades strongest on the short wavelength side, which implies that a search for future radiation hard plastic scintillators should not only focus on the base material and additives that support its annealing but also on the wavelength shifting fluors[93]. The underlying principle in the creation of absorption centres is commonly described as follows:

---

[1]Related to the linear energy transfer during energy loss[84, 85] in the medium.
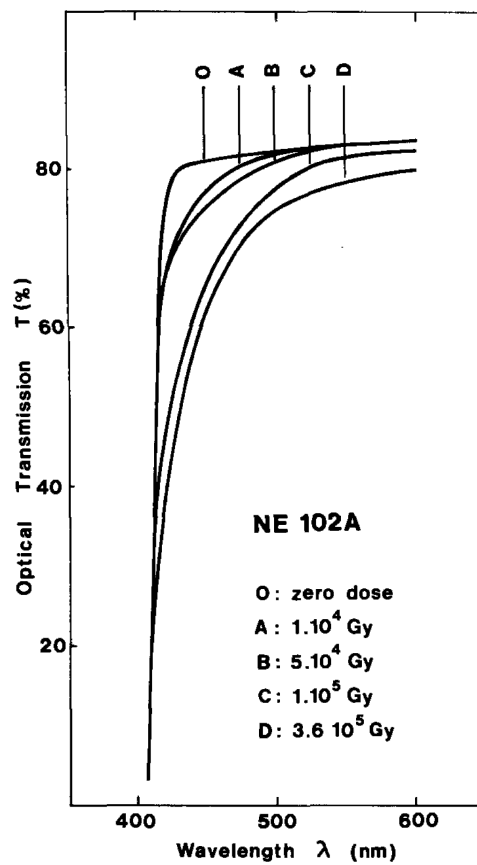
Figure 3.4.: *Shown are the transmission spectra of NE102a, which is equivalent to BC400B, taken after different radiation exposures. As can be seen most of the absorption/LY loss occurs on the short-wavelength side. The figure was taken from [92].*

Energy that is deposited in the base material can break up the polymer chains and build up radicals. During this process the environment plays an important role. Due to its high electron affinity the presence of oxygen has a considerable influence in this context. Literature provides contradictory information on this point. On the one hand oxygen is suspected to increase the radiation damage [88, 85] since it offers more reaction channels in the formation of radicals, while on the other hand a more recent source [86] shows an increased radiation hardness in the presence of oxygen. Measurements presented in the same publication indicate that oxygen dissolved in the sample (due to previous storage in air) reduces the initial radiation damage until the oxygen is "used up", when irradiated in an inert Argon atmosphere. The benefit of oxygen in the annealing process after irradiation is commonly accepted. As a conclusion three different types of absorption centres can be identified [86]:

- Short-lived damage, with life times on the order of minutes to hours, that anneals even quicker in an oxygen environment
- Long-lived radiation damage that can anneal when exposed to oxygen
- Permanent radiation damage, that can not anneal

More information concerning radiation damage in plastic scintillators is available. However the limited data and the variance of the radiation damage for different setups still necessitates dedicated tests before application. This is certainly the case for the MEG II stopping target. One of the particular advantages in the MEG-case, using a camera to sample the light from a thin slab is, that one is sensitive to light-paths of the order of the thickness of the scintillator, i.e. path lengths several orders of magnitude less than the attenuation length in PVT [77], rather than, in the usual case of an edge read-out of the scintillator slab, where the light propagates parallel to the surface of the slab.

3.2. Motivation for a scintillation stopping target in MEG II

For the upgrade from MEG to MEG II not only higher beam rates are required but also a direct feedback on the beam properties is desireable. In MEG the trigger rates of the individual sub detectors were the only continuous measure of the muon stopping rate, once data-taking had started. Similarly the beam profile information, apart from dedicated measurements made at the start of each run period, was deduced from the accumulated vertex distribution of detected decays using a minimum bias trigger. The heatplot in figure 3.5 shows the vertices of all reconstructed events during the 2012 physics run. However
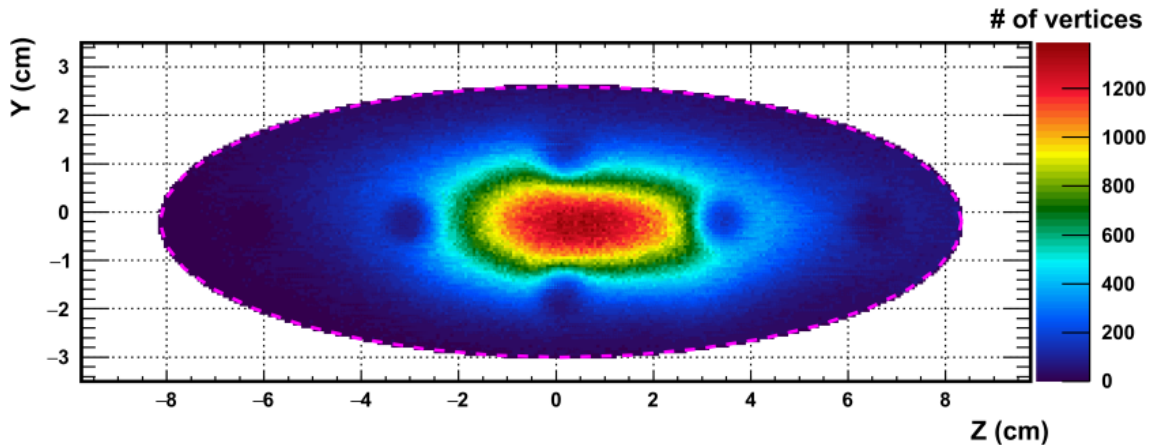
Figure 3.5.: *Vertex positions (2012 Run) in the plane of the MEG stopping target [6]. The holes in the distribution, correspond to holes in the target material, that are used for the reconstruction of the target alignment relative to the Drift Chambers [94].*

the full calibrated beam information was not directly available on a short time scale, which potentially meant the necessity for further beam scanner measurements after returning to the muon beam setup post e.g. CEX calibrations using pions or for beam trouble shooting. Replacing the former PE/PET target material with a sheet of BC400B provides the ability to directly monitor the footprint of the stopped muons by viewing the emitted scintillation light with a camera from outside COBRA, without comprimising the target stopping characteristics significantly [76]. As most cameras nowadays show a good linearity between their ADC value and incident light intensity, the recorded intensity of the camera picture is proportional to the muon beam intensity. Once calibrated against a single particle counting device as for example the Avalanche Photodiode (APD) scanner system used, a scintillation target can so provide information about both, the beam profile and the absolute intensity of muons stopped in the target.

The main benefits from online beam information in MEG II would be:

- A substantial saving in both time and effort at the beginning of a run period. The scintillation target would replace the need for installing a dedicated APD based 2-D scanner system at the centre of the COBRA magnet, involving removing the C-W beam line & replacing it with a rail system for the scanner. Furthermore the actual beam measurements could be substantiallly shortened from a full 2-D raster scan with a 3 mm step-size lasting about 2 hours or a horizontal/vertical cross-scan taking $\sim$ 20 minutes, to a single CCD exposure of only 100 sec. The latter can be further

reduced by a superior cooled CCD camera with a much better signal/noise ratio so achieving similar exposures within 10 sec.

- The possibility of online beam re-optimization after an accelerator shut-down for a muon production target change which is associated with a position change of the proton beam on the target as well as a potential muon beam shift due to hysteresis effects in the front channel momentum selection dipole magnet. Both of these situations can lead to a change of the muon beam footprint on the MEG II target, as demonstrated during the test beam in 2016 (see subsection 3.5.4).

- The muon beam footprint on the MEG II target can conversely be used to monitor the position of the proton beam on the main production target.

- The accurate knowledge of the muon stopping distribution history and intensity obtained from the CCD pictures of the scintillation target can serve as an independent cross check and input to the MEG II analysis and simulation. On the one hand by relating the reconstructed vertex position to the actual stopping distribution. On the other hand having the possibility of studying the detector spatial acceptance by steering the stopping distribution on the target using the horizontal and vertical steering magnets mounted on the BTS.

- Act as an additional monitoring tool for the shift crew, thereby helping to identify potential problems as early as possible - an example is given in section 3.6.

- One of the biggest advantages is the access to the true stopping distribution in the slanted target, unlike previous raster scan measurements that were performed in a plane centred on the target but perpendicular to the beam axis.

- Access to possible planarity deformation in the target from stresses associated with the support suspension mechanism, the He-environment, or from radiation damage.

This shows the overwhelming advantages of a scintillation target in MEG II however, the only feature not accessible is particle identification via pulse-height discrimination in the same distribution.

3.3. Requirements for MEG stopping target

For a statistically and resolution limited experiment such as MEG the optimization of the stopping target is a key element. A tradeoff between target parameters, affecting the target geometry and materials have to be optimized to reach the physics goals. Obviously the extent of the target has to be chosen to contain the full beam spot at the centre of the COBRA magnet. Throughout the MEG runs the projection of the stopped muons perpendicular to the beam axis shows an almost round Gaussian distribution with $\sigma_x \approx \sigma_y \approx 10$mm. Therefore the projection of the horizontal axis of the target has to equal approximately the vertical axis and both have to be bigger than 60 mm to so contain 98.9% of the beam.

$$\int_{r=0}^{r=30} \int_{\phi=0}^{\phi=2\pi} \frac{r}{2\pi \cdot \sigma_x \cdot \sigma_y} e^{\frac{-1}{2}\left(\frac{(r \cdot \cos(\phi))^2}{\sigma_x^2} + \frac{(r \cdot \sin(\phi))^2}{\sigma_y^2}\right)} = 98.9\% \tag{3.2}$$

The need for a high rate is met on the one hand by one of the world's most intense muon beams provided at PSI by the πE5 channel and on the other hand by a high stopping

efficiency in the target. The stopping power scales with the nuclear charge Z of the target material[95].

$$-\frac{dE}{dx} = \rho z^2 \frac{Z}{A} f(\beta, I) \qquad (3.3)$$

with ρ the density of the stopping target,
z the incident particle's charge,
Z the effective charge of the stopping material,
A the mass number of the stopping material,
$\beta = \frac{v}{c}$ the ratio of velocity to the speed of light
and I the mean excitation potential of the stopping material. There is a roughly linear relation between I and Z for higher Z elements, whereas measured data are available for lower Z materials. The nuclear charge Z as well as the thickness of the stopping material do not only have an impact on the muon stopping rate but also affect the trajectories of the decay positrons. More material and a higher nuclear charge Z of the stopping material enhance mainly three effects:

- Higher contribution from Multiple Coulomb Scattering (MSC) of outgoing positrons leading to a higher uncertainty on the relative angles $\theta_{e+\gamma}$ and $\phi_{e+\gamma}$

- Increase of the photon background from Annihilation in Flight (AIF) events of decay positrons

- Increase of the photon background induced by Bremsstrahlung of outgoing positrons

In order to maximize the stopping efficiency while minimizing the material budget for outgoing decay positrons and reducing the chance of photon background production the target is mounted at an angle with respect to the beam axis. Hence the projected target thickness d^* is given by:

$$d^* = \frac{d}{\sin \alpha} \qquad (3.4)$$

where d is the bulk thickness of the target and α is the mounting angle. In order to improve the reconstruction of the positron emission angle (θ_{e+}, ϕ_{e+}) the multiple scattering in the target has to be reduced, which is achieved by the use of materials with a low effective nuclear charge Z. Most suitable low Z candidates are low density hydrocarbons such as Mylar, polyethylene or PVT (see table 3.1). Figure 3.6 shows the Polyethylene target as used in MEG between 2010 and the end of the run 2013. Apart from a different target thickness, slant angle and the absolute beam intensity the parallel projection of the profiles at COBRA centre are similar for MEG and MEG II. Before reaching COBRA the incoming muon beam passes through a 300 μm thick degrader foil (Mylar, $\rho_{Myl,139} = 1.390 \frac{g}{cm^3}$) at the centre of the BTS and a 190 μm lower density Mylar window ($\rho = 1.377 \frac{g}{cm^3}$), which separates the beam line vacuum from the COBRA Helium/air mixture ~ 1475 mm upstream the target centre. Based on the residual momentum ($\sim 19.8 \frac{MeV}{c}$) at the MEG target a stopping efficiency of $\sim 82\%$ was achieved taking into account the range straggling of the muon beam. A small fraction of muons pass through the holes in the target (see figure 3.6), which are used for the relative alignment between target and detector based on reconstructed events[6]. The baseline solution for the MEG II experiment as outlined in the MEG upgrade proposal [4] foresees a 140 μm thick PE target mounted at 15° with
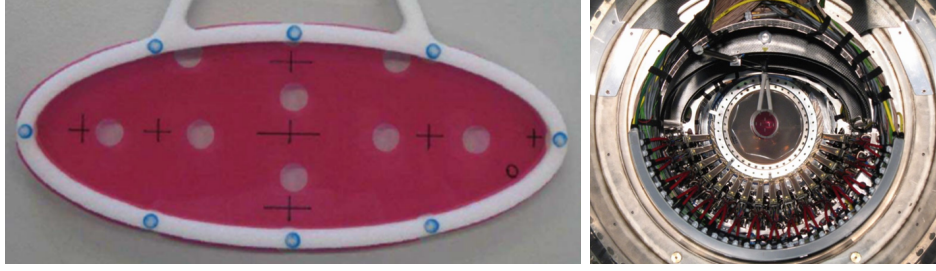
Figure 3.6.: *The MEG target consists of an elliptical 205 μm thin polyethylene/polyester foil (density $\rho_{CH2} = 0.895$ g/cm^3) loosely held in a Rohacell frame with a major axis of 200.5 mm and a minor axis of 79.8 mm. The right picture shows the implementation inside COBRA. With a slant angle of 20.5° the projected area has an almost circular shape, when looking at the target in beam direction, corresponding to the round beam spot.*

respect to the beam axis, a degrader thickness of $t_{deg,CH2} = 320\mu m$ and a pure Helium environment inside the COBRA volume. The entire amount of material up to the target centre corresponds to 870 μm Mylar ($\rho_{Myl,139} = 1.390 \frac{g}{cm^3}$) equivalent. Considering the thinnest commercially available 150 μm PVT scintillation target material, a suitable Mylar degrader thickness $t_{deg,scint}$ is given by:

$$t_{deg,scint} = t_{deg,CH2} - \left(\frac{\frac{t_{PVT}}{2\cdot\sin 15°} \cdot \rho_{PVT} \cdot \frac{Z_{PVT}}{A_{PVT}} - \frac{t_{CH2}}{2\cdot\sin 15°} \cdot \rho_{CH2} \cdot \frac{Z_{CH2}}{A_{CH2}}}{\rho_{Mylar,139} \cdot \frac{Z_{Mylar}}{A_{Mylar}}} \right) \qquad (3.5)$$

Therefore the degrader thickness t_{degr} has to be reduced to 290 μm. The target major (horizontal) axis attains 26 cm length and the minor (vertical) axis 7 cm. Figure 3.7 shows a top view schematics of the target setup in COBRA.
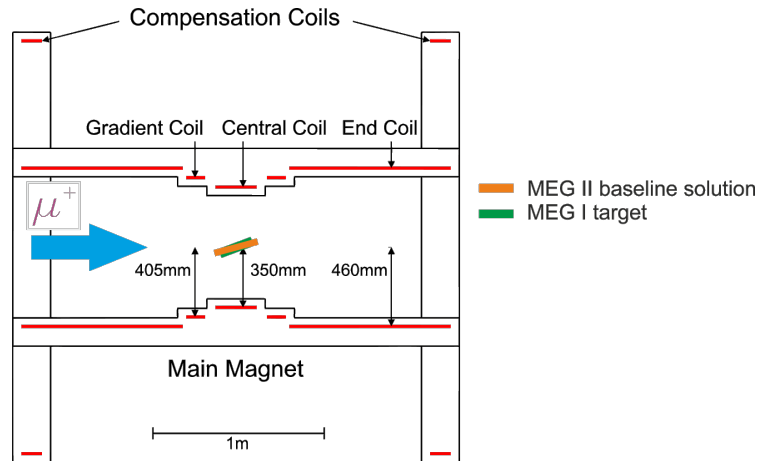
Figure 3.7.: *The schematics shows both the old MEG and the new baseline solution for the MEG II stopping targets (image adapted from [96]). The target angle and extent is to scale whereby the thickness is enhanced for a better visibility.*

3.3.1. Target long-term durability

The reconstruction of decay vertex positions in MEG/MEG II makes use of the small target thickness which constrains the region of highest probability for muon decays to the overlap of the incoming beam and the well-defined target volume. This necessiates the target to stay at the same position and to maintain its shape for the duration of the run. To minimize the influence of external forces (e.g. due to different thermal expansions), that act on the MEG target, the PE/PET foil was loosely held in its Rohacell frame. During the run the target is moved to a parking position off axis e.g. for beam tuning with the APD scanner and frequent calibration runs of the LXe calorimeter which require different target types. For example a Lithium-Boron target is inserted to produce a monochromatic source of gamma rays from the MEG C-W proton accelerator or a liquid hydrogen target can be inserted for the production of γs from π^0 decay. The target frame in MEG as in MEG II is held by an arm that is mounted on the upstream side of COBRA and is moved pneumatically between measurement position and parking position. The position of the stopping target in both position is precisely reproducable. Although the target movement is rather smooth a sufficiently sturdy and stable target material and mount is necessary. The target stability should not only take into account the mechanical stability but also the ability to withstand the dry He environment inside COBRA as well as being resistant to radiation damage from the substantial accumulated doses of $\mathcal{O}\left(10^{15}\right)$ stopped muons. Measurements made at the end of the 2013 physics run showed planarity imperfection of the PE/PET target. Figure 3.8 shows a "point cloud", that represents the target surface. The measurements were made after the 2013 physics run with a FARO laser measurement arm. Deviations from a plane surface up to a few mm over the full target area were found affecting the detector resolutions. For the final analysis a paraboloidal approximation of the target surface with a linear increment for each year were applied in order to partially recover the resolution [6]. The observed warping is thought to originate from the dry gas environment as well as from radiation damage. The MEG PE/PET target used between 2010 to 2013, was exposed in total to $6.9 \cdot 10^{14}$ stopped muons corresponding to 41 Mrad radiation dose within the 1σ-region, 13 Mrad dose between the 1- and 2σ-region and 1.5 Mrad dose beyond the 2σ-region [98]. For doses greater than ~ 10 Mrad the mechanical properties of polyethylene change significantly [99, 84]. The elastic modulus and the tear strength increase whereby the maximum elongation at the breaking point is reduced. Taking the inhomogenuous irradiation into account the sum of these effects could possibly account for the observed target shape. Preservation of the target surface under irradiation is therefore also an important criterium for a scintillation target. However in general optical properties are more readily affected than mechanical properties in organic materials, which places great emphasis on radiation damage of a scintillation target made of plastic. A more detailed discussion of the radiation hardness of the scintillation target follows in subsection 3.5.8. The overview in figure 3.9 summarizes the main target design goals and the involved physical aspects.
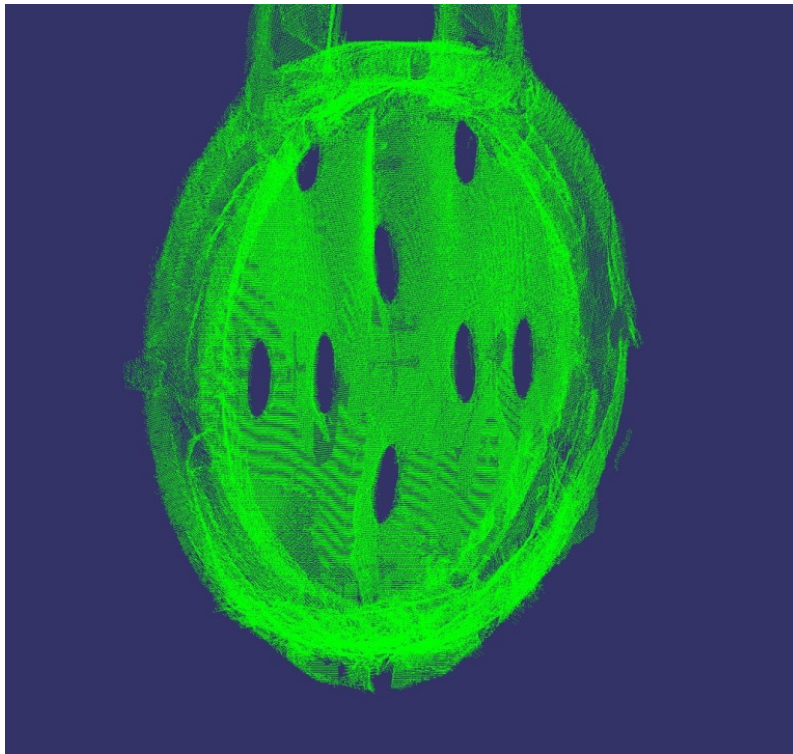
Figure 3.8.: *The green points measured with the FARO arm 3D laser measuring system define the surface of the target and the Rohacell mounting frame. [97]*
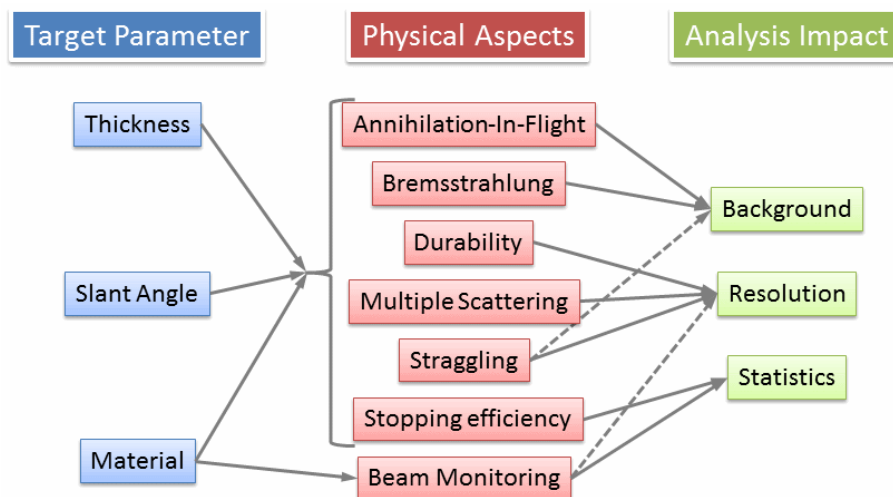
Figure 3.9.: *A careful choice of the target parameters offers the possibility to find a good compromise between physical benefits for the experiment and minor drawbacks from unwanted effects.*

3.3.2. Assessment of the Scintillation Target

The 150 μm thin scintillator BC400B that was used for the test beams is also foreseen for a future use in MEG II. Figure 3.10 shows its emission spectrum and the wavelength dependent efficiency of the camera used in both test beams. The spectra suggest the use of a scintillator type with enhanced emission at somewhat longer wavelengths rather than BC400B. However, BC400B was the only plastic scintillator available with a suitable thickness of only 150 μm and sufficient lateral size. Table 3.2 lists the main physical properties of the scintillator. In order to not interfere with detector components and
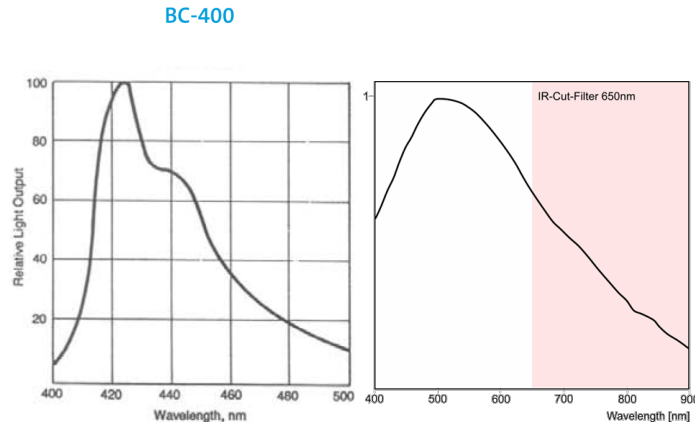
Figure 3.10.: *The left graph shows the emission spectrum of BC400B. The right graph shows the relative photon efficiency of the iDS camera that was used in the test beams. [77, 100]*

Table 3.2.: *Main physical properties of BC400 [77]*

Light Output (in % Anthracene)	65
Light Output (Photons/MeV)	$2.5 \cdot 10^4$
Rise Time (ns)	0.9
Decay Constant of main component (ns)	2.4
Pulse Width - FWHM (ns)	2.7
Wavelength of Maximum Emission (nm)	423
Light Attenuation Length (cm)	160
Refractive Index	1.58
No. of H atoms per cm^3	5.23×10^{22}
No. of C atoms per cm^3	4.74×10^{22}
H:C Ratio	1.103
Density (g cm^{-3})	1.032
No. of electrons cm^{-3}	3.37×10^{23}
Softening Point (°C)	70

due to spatial constraints imposed by the beam line the positioning of the camera and the mirror system proved challenging. A possible installation of the mirror on the beam axis DS of COBRA is excluded due to the C-W beam line that is installed for calibration runs. Currently a permanent implementation of the mirror and camera system is foreseen in the
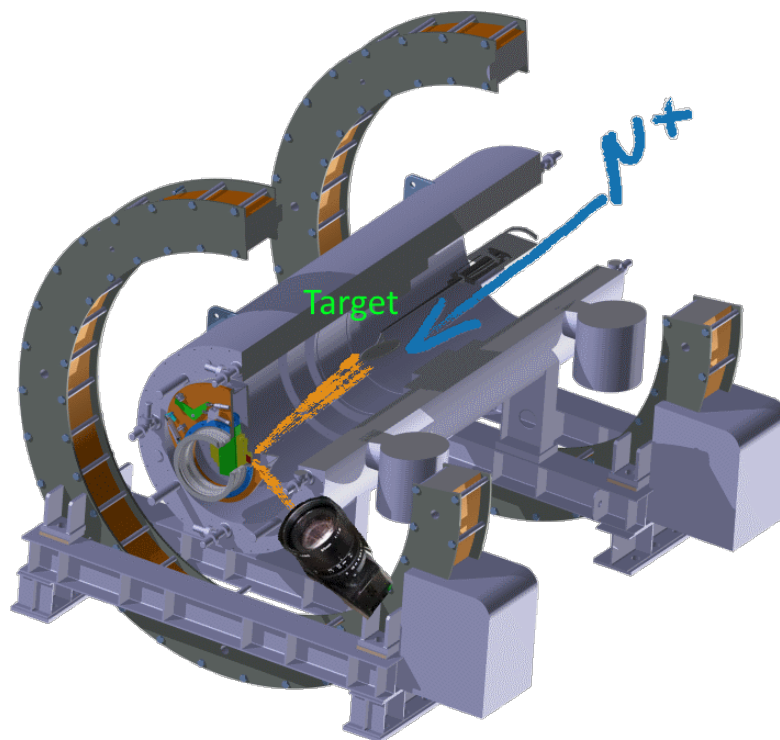
Figure 3.11.: *The envisaged mounting solution foresees a mirror in the downstream RDC flange. The light passes a ~4 cm gap between RDC counter and insertion system, which couples to the downstream side of COBRA, and is reflected by a mirror towards the camera. For the test beam period in 2016 the camera and mirror were mounted downstream in front of the C-W insertion system.*

downstream RDC flange as shown schematically in figure 3.11. However the final implementation of the scintillation target monitoring system still requires further investigation, whereby the spatial distribution of the emitted light has to be taken into account.

3.3.3. Light distribution and mirror positioning

In order to assess possible mounting positions the angular dependent relative yield has to be determined for the case of light produced in the PVT target. The following considerations are based on several simplifications and assumptions:

- only the horizontal direction is taken into account
- Any absorption is neglected
- Influence of a window is neglected $\rightarrow$ reflexion only occurs at the PVT - Helium interface
- Source is assumed to be pointlike and propagation length inside the scintillator is small
- Assume a horizontal angular acceptance of $\theta_{cam,accept} = 1.2°$ corresponding approximately to a 4 cm lens aperture acceptance at a distance of 1.9 m
- no wavelength dependence on the refractive indices of the scintillator $n_{PVT} = 1.58$ and the Helium atmosphere $n_{He} = 1$
- smooth PVT surface

Scintillation light in the PVT is produced isotropically. When impinging on the PVT - Helium interface, angles smaller than the critical angle $\theta_{PVT-He,crit} = 39.27°$ are partially transmitted. The transmitted fraction of light that reaches the interface once at an angle θ_{PVT} is given by the Fresnel formulae:

$$T(\theta_{PVT}) = 1 - R(\theta_{PVT}) = 1 - \frac{1}{2}\left(R_\perp(\theta_{PVT}) + R_\parallel(\theta_{PVT})\right) \tag{3.6}$$

$$= 1 - \frac{1}{2}\left(\left|\frac{n_{PVT}\cos(\theta_{PVT}) - n_{He}\sqrt{1 - \left(\frac{n_{PVT}}{n_{He}}\sin(\theta_{PVT})\right)^2}}{n_{PVT}\cos(\theta_{PVT}) + n_{He}\sqrt{1 - \left(\frac{n_{PVT}}{n_{He}}\sin(\theta_{PVT})\right)^2}}\right|^2\right.$$
$$\left. + \left|\frac{n_{PVT}\sqrt{1 - \left(\frac{n_{PVT}}{n_{He}}\sin(\theta_{PVT})\right)^2} - n_{He}\cos(\theta_{PVT})}{n_{PVT}\sqrt{1 - \left(\frac{n_{PVT}}{n_{He}}\sin(\theta_{PVT})\right)^2} + n_{He}\cos(\theta_{PVT})}\right|^2\right) \tag{3.7}$$

Transmitted light is refracted at the PVT - Helium interface according to Snell's law:

$$\theta_{He}(\theta_{PVT}) = \arcsin\left(\sin(\theta_{PVT})\frac{n_{PVT}}{n_{He}}\right) \tag{3.8}$$

whereby θ_{He} is the angle in Helium and analogue θ_{PVT} in PVT. Incoming light with angles greater than the critical angle $\theta_{PVT-He,crit}$ undergoes total internal reflexion back into the
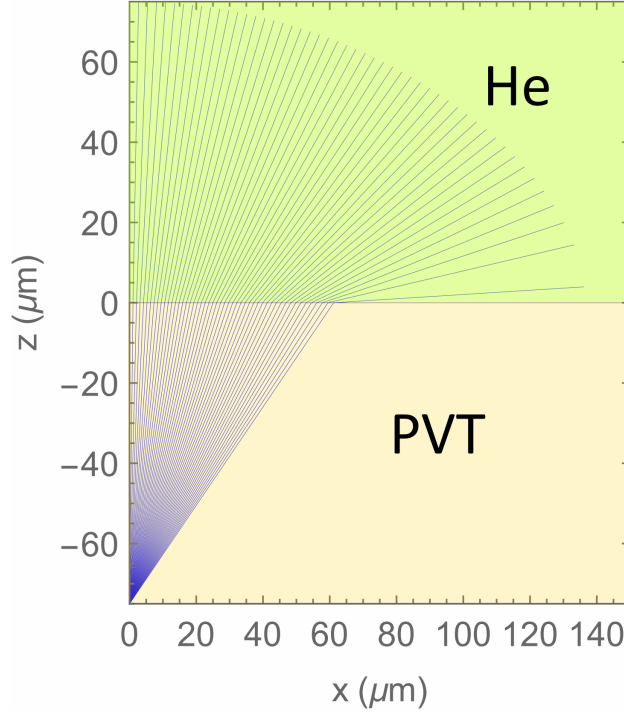
Figure 3.12.: *Scintillation light is produced at (x=0, z=-75) with an isotropic angular distribution ranging from $\theta_{PVT} = 0°$ to $\theta_{PVT} = 39.2°$. Refraction at the PVT - Helium interface at z=0 leads to an angular distribution in Helium with the peak at 0°.*

scintillator volume. As illustrated qualitatively in figure 3.12 angles close to the critical angle are supressed. In the case of mounting the mirror on the beam axis the angle between the visual axis and the normal direction with respect to the scintillator surface amounts to $\theta_{He} = 75°$ which corresponds to $\theta_{PVT} = 37.69°$ in PVT. Therefore the absolute fraction $\frac{I_{cam,accept}}{I_0}(\theta_{He})$ of light emitted directly from the scintillator surface without undergoing reflections in the PVT and that matches the horizontal acceptance angle $\theta_{cam,accept}$ of the mirror-camera system is given by:

$$\frac{I_{cam,accept}}{I_0}(\theta_{He}) = \frac{\theta_{PVT-He,crit}}{360°} \times \frac{\#(\theta_{He})}{\#(0° \leq \theta_{He} < 90°)} \times T(\theta_{He}) \tag{3.9}$$

whereby $\frac{\#(\theta_{He})}{\#(0° \leq \theta_{He} < 90°)}$ is the fraction of the light that leaves the PVT at a certain angle in the quadrant facing towards the camera with respect to the total amount of light emitted on the corresponding surface of the scintillator at first impact. In the case of reflections in the scintillator the situation is illustrated in figure 3.13. Therefore the absolute transmission in the direction facing towards the mirror-camera system is given by:

$$I(\theta_{He}) = \sum_{k=0}^{\infty} T \cdot R^k = \frac{T}{1-R} = 1 \tag{3.10}$$

The resulting angluar distribution of the relative LY is plotted in figure 3.14 for both cases of direct and direct + reflected light. The blue line illustrates the fraction of initially generated light for a 1.2° angular acceptance allowing for internal reflexions in the PVT
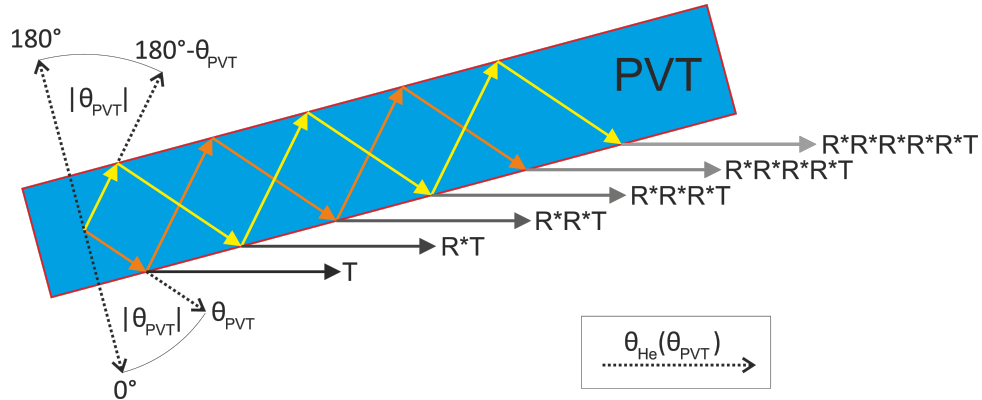
Figure 3.13.: *The absolute light emission with direction $\theta_{He}(\theta_{PVT})$ from the surface facing the mirror-camera system is the sum of the direct transmission and the reflected components. Therefore also the corresponding angle in PVT $180° - \theta_{PVT}$ directed to the opposite face of the scintillation target has to be taken into account.*
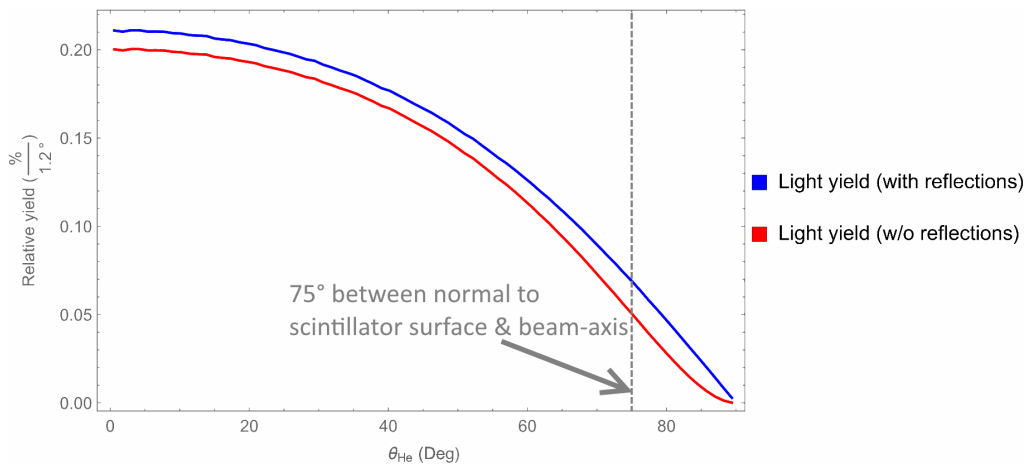
Figure 3.14.: *Shown is the fraction of initially generated light that is emitted in a 1.2° wide angle centered around the angle θ_{He} according to equation 3.9. The red curve only takes into account the first time the light reaches the PVT-Helium interface. The blue curve reflects the case of multiple reflections in the scintillator. The dashed line indicates an axial emission as during the test beam 2016.*

and the red line only takes the first impact on the surface into account. The position of the mirror-camera system not only influences the resolution by the $\frac{CCD\ pixel}{mm}$ ratio in the horizontal direction, but plot 3.14 also emphasizes that the relative angle between the mirror and the scintillator leads to significantly different LYs for a possible installation of the mirror on either the left or right DS side. The light emission at steep angles close to 75° could be significantly enhanced with a diffuse surface, which could be applied to the target by homogenously distributed scratches. In that case care has to be taken in order to not falsify the profile results, by guiding the light away from the centre, leading to larger profiles implied by the increased light emission rather than the actual muon distribution, or even providing a too rough granularity of scattering centres and thereby corrupting the spatial resolution.

3.4. Beam monitoring test December 2015

The testbeam in 2015 was mainly dedictated to the proof-of-principle of the scintillation target, which included the reconstruction of the beam profile from images, confirmation of linearity which allows for intensity measurements and a long range test viewing of the scintillator from approximately the same distance as it would be viewed at COBRA centre. The scintillator used was a 150 μm thin sheet BC400B, also used for the test beam at COBRA centre in 2016.

3.4.1. Setup for the Scintillator Beam Test 2015

In December 2015 a prototype scintillation target with rectangular shape was mounted in a test setup downstream of the triplet II in the πE5 area. Figure 3.15 shows the setup between the BTS and the collimator system (discernable by the $\cos\theta$ type steering magnet (SML) mounted on the same vacuum tube). The scintillator is mounted on a gray polyethylene
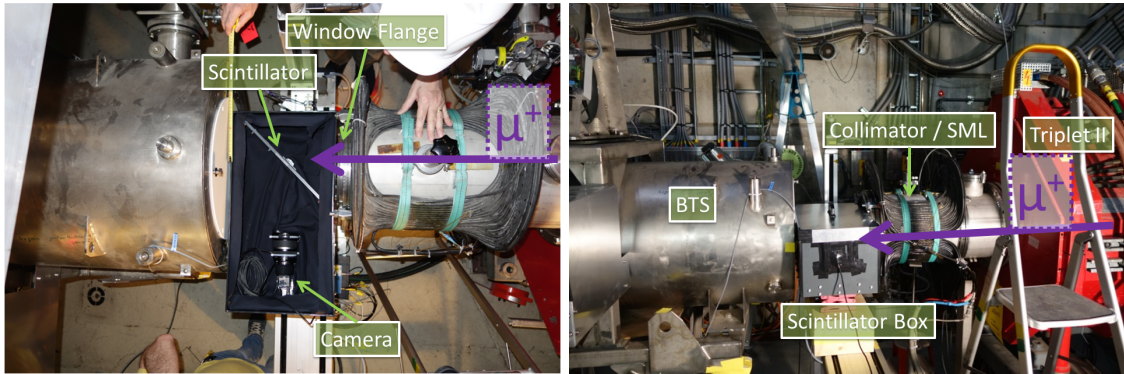
Figure 3.15.: *Testbeam setup, the muon beam comes in from the quadrupole Triplet II on the right, passes a collimator system and leaves the beam vacuum through a 190 μm thin Mylar window. The light tight box containing the scintillator has an aluminum window on the entrance side. The scintillator is mounted with at 45° to the beam axis. The camera views the scintillator also at 45° and perpendicular to the beam axis.*

frame with a 45° angle to the incoming beam in a light tight box. The muon beam first leaves the beam vacuum through a 190 μm thin Mylar window and passes (besides the air) the 20 μm aluminum entrance window of the light-tight box before it impinges on the scintillator. The camera, a UI-2220SE-M-GL Rev.3 from iDS [100] is a monochrome, C-mount CCD camera with a 768 × 576 pixels resolution and a pixel size of 8.3 μm × 8.3 μm. The camera was mounted perpendicular to the beam axis viewing the scintillator under a 45° angle, which ensures sufficient distance from the beam to protect the camera from radiation damage. In order to focus the scintillation light on the CCD a Canon Telefoto lens EF-S 18-200mm f/3.5-5.6 IS was used. The camera was triggered in parallel to a Scaler, which recorded the proton signal provided by the MHC4 current monitor in the proton beam line just upstream of the main production TgE for the duration of the camera exposure time. The electronics is schematically shown in figure 3.16.
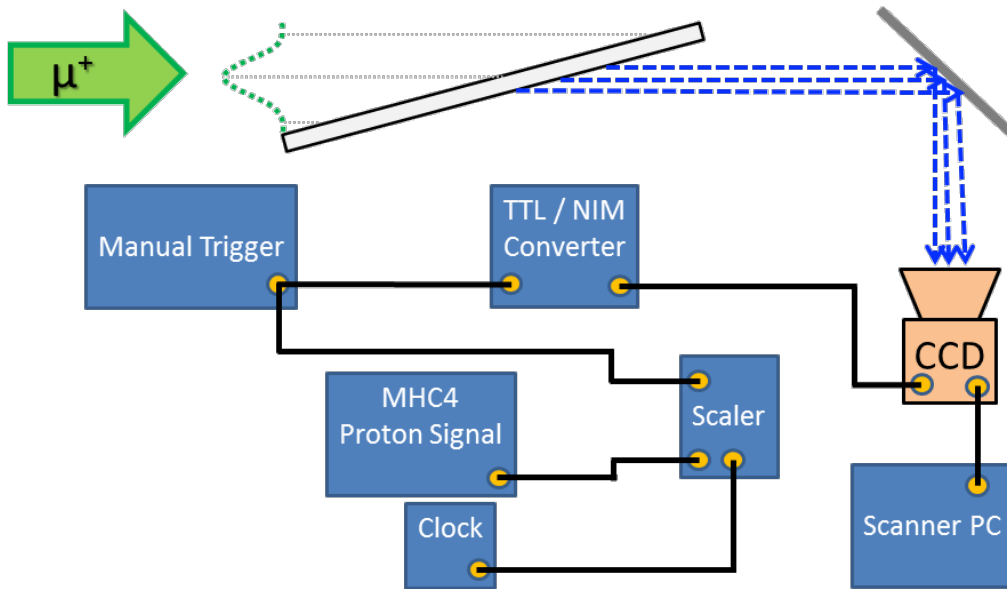
Figure 3.16.: *Readout scheme, the TTL signal output is send to the camera, whereby it is first converted to NIM matching the camera trigger input and in parallel to the start input of the scaler module. The scaler once started counts the MHC4 signal and stops when the number of clock counts matches the exposure time of the camera.*

3.4.2. Pre-test with ^{90}Sr

Before installing the light-tight box in the experimental area, a source test with a ^{90}Sr β^- emitter (~ 1.7 MBq) was carried out. The setup is shown in figure 3.17. A small C-mount lens was used for this pre-test. By comparison between the different lenses available the Canon Telephoto lens was found to be the most suitable for the later beam test. The ^{90}Sr source was positioned behind and directed towards the scintillator which was viewed by the iDS camera at 45°. The camera images with the lid of the light-tight box open and closed are shown in figure 3.18. The exposure time was set to 100 sec. For alignment purposes thin <1 mm strings were fixed diagonal on the side of the scintillator frame facing towards the camera and vertical and horizontal strings were fixed on the opposite side facing towards the source. Therefore the diagonal strings block the scintillation light directed to the camera whereby the vertical line in the image corresponds to areas of the scintillator which are shielded by the strings from incoming electrons. The scintillation light image on the right illustrates qualitatively the sub-millimeter resolving power of the scintillator monitoring method. This showed that the LY expected from the high intensity muon beam in πE5 should be sufficient. However for an implementation at COBRA centre two factors counteract each other, on the one hand the steeper angle of ~75° between the target surface and the direction of the mirror position increases the energy deposit and therefore leads to a higher LY but on the other hand the accepted LY at 75° is significantly smaller - see section 3.3.3.
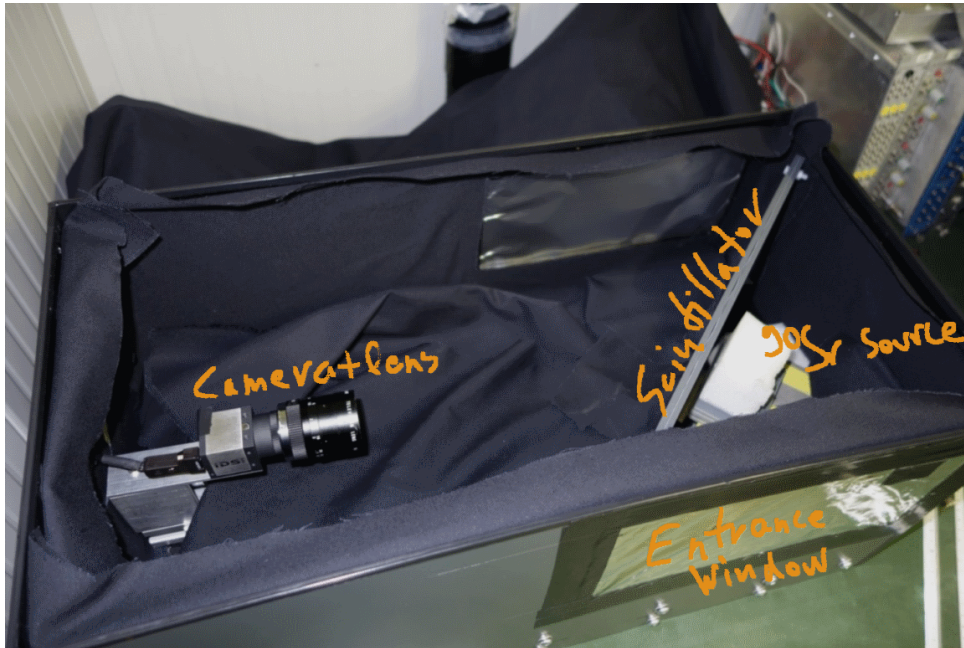
Figure 3.17.: *Source test setup, the camera and scintillator are mounted in the same way as for the later muon beam test, except the lens that was replaced by a Canon Telephoto lens. The ^{90}Sr source is placed on the back side close to the centre of the scintillator frame.*
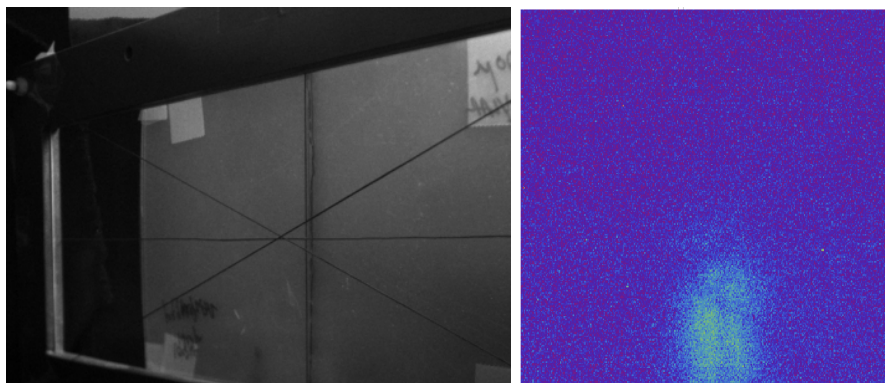
Figure 3.18.: *Fine cotton strings were attached to the front and the back side of the scintillator holder. On the right picture you can see the scintillation light image of the source. The light spot at the bottom of the picture is interrupted by lines that correspond to the attached strings. The diagonal lines are caused by the strings attached to the side facing the camera and therefore block light. The vertical string on the side facing the ^{90}Sr source scatters the electrons.*

156

3.4.3. Quantitative profile information via perspective correction

Viewing the scintillator at an angle causes objects further away to appear smaller in the image, which is known as perspective distortion. To correct for this a non-affine perspective transformation has to be applied [101]:

$$\begin{pmatrix} w_0 x_{tg} \\ w_0 y_{tg} \\ w_0 \end{pmatrix} = \mathcal{M} \times \begin{pmatrix} x_{im} \\ y_{im} \\ 1 \end{pmatrix} \tag{3.11}$$

$$\rightarrow x_{tg} = \frac{\mathcal{M}_{11} \cdot x_{im} + \mathcal{M}_{12} \cdot y_{im} + \mathcal{M}_{13}}{\mathcal{M}_{31} \cdot x_{im} + \mathcal{M}_{32} \cdot y_{im} + \mathcal{M}_{33}} \tag{3.12}$$

$$\rightarrow y_{tg} = \frac{\mathcal{M}_{21} \cdot x_{im} + \mathcal{M}_{22} \cdot y_{im} + \mathcal{M}_{23}}{\mathcal{M}_{31} \cdot x_{im} + \mathcal{M}_{32} \cdot y_{im} + \mathcal{M}_{33}} \tag{3.13}$$

where x_{tg} / y_{tg} are the coordinates in the target plane, x_{im} / y_{im} are the pixel coordinates
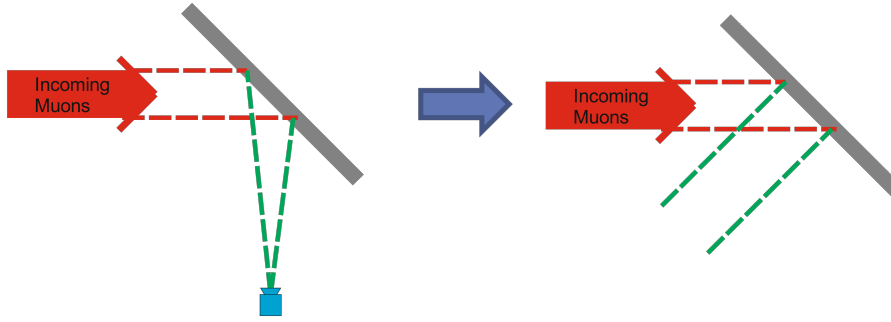
Figure 3.19.: *Due to the slant angle of the scintillator and the finite extent of the sensitve area objects further away appear smaller in the image. In order to extract quantitative beam information the image must be transformed to recover correct proportions in the image plane.*

in the image, w_0 is the projection scale and $\mathcal{M}$ is the 3×3 transformation matrix with $\mathcal{M}_{33}$=1. The 8 remaining coefficients of $\mathcal{M}$ are determined by a set of 4 points in the image and the corresponding coordinates in the scintillator plane. Graphpaper was attached to the scintillator holder to provide the well-defined points that are needed to reconstruct the perspective transformation - see figure 3.20. Determination of the transformation matrix coefficients as well as the back transformation to the non-distorted image is done with the open source software OpenCV [102]. In order to loose as little information as possible the image was scaled up during transformation using a linear interpolation method. The reason for scaling up was that otherwise a part of the image (with parts of the scintilllator further away from the lens) would have been compressed resulting in a loss of information. The transformation was also adjusted to provide a pixel/mm ratio of 10. In addition the horizontal pixel coordinates must be scaled by $\frac{1}{\sqrt{2}}$ to derive the projection of the beam profile in beam direction to compensate for the 45° angle to the scintillator. The lower picture in figure 3.20 illustrates the effect of the perspective correction; the horizontal lines are now parallel and vertical and horizontal lines perpendicular to each other.
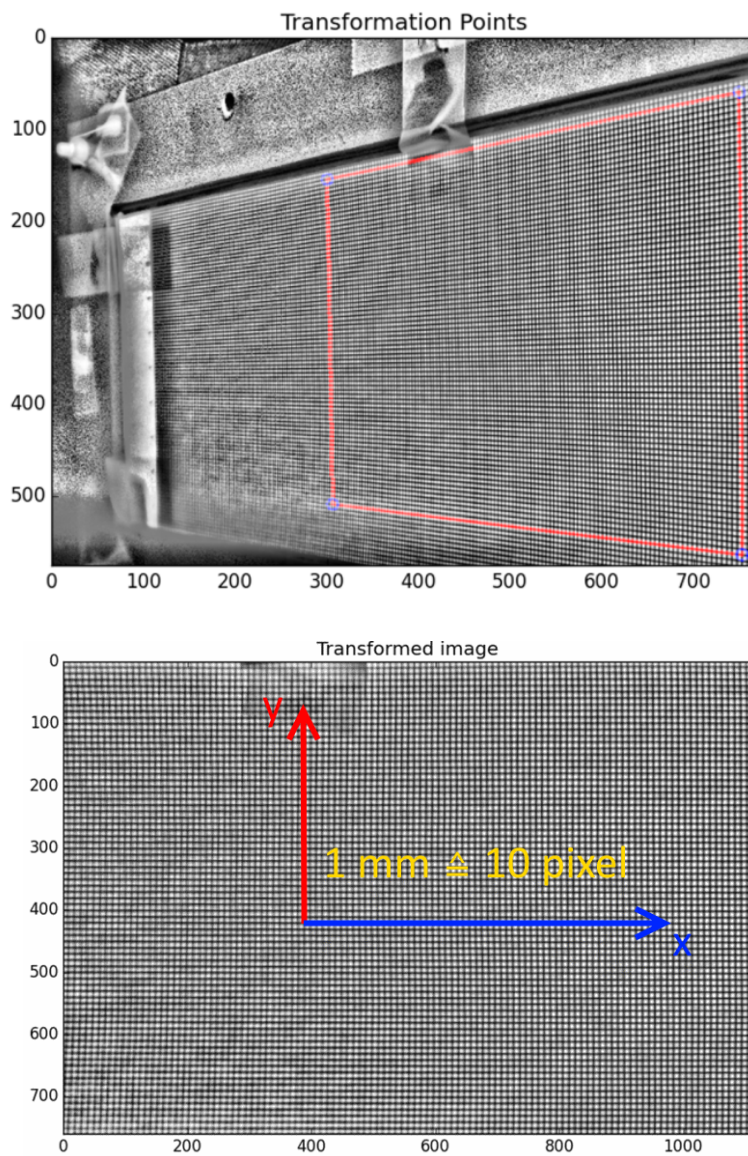
Figure 3.20.: *The upper picture taken by the camera (gray values inverted) shows the natural perspective distortion of the lines on the graph paper. The edgepoints of the red quadrangle are used for the reconstruction. The lower picture shows the corrected fiducial area of the left picture.*

3.4.4. Results of the beam monitoring test Dec 2015

First pictures taken with the setup shown in figure 3.15 were used to determine the best camera settings. The most suitable exposure time for the measurements was a tradeoff between an increase in the background level and the quantization error due to the 8-Bit limitation of the camera and the readout noise. The exposure time was finally been fixed at 100 sec with a master gain amplification of ≈12, with the resulting pixel intensities at the centre of the beam spot using ~ 2/3 of the dynamic range, which ensures values in the linear range of the CCD ADC. The linearity of the ADC is shown in figure 4.1[103]. One of the first pictures taken with the 28MeV/c surface muon beam impinging on the scintillator foil is shown in figure 3.21(a). The heatplots are generated from the intensity levels of the pixels. The muon beam spot is clearly visible. However the camera shows a considerable dark noise level that is also non-uniform, showing a bright spot in the top left region. This can be clearly a dark current phenomenon, confirmed by taking a background frame with the beam blocker closed. The righthand picture in the same figure shows the background image with the same accumulation of hotpixels in the top left region. Subtracting the background image (subfigure 3.21(b)) from the beam image (subfigure 3.21(a)) solves this issue. The result (subfigure 3.21(d)) is an image that shows intensities that are proportional to the scintillation light originating from the muon beam spot. Image subtraction in this context means a pixel per pixel subtraction of the individual ADC values. The muon distribution is clearly seen in the image of the scintillation light. A closer look at the background subtracted image shows highlighted lines which on investigation proved to be surface scratches. This implies that the handling of the scintillator has to be improved in order to avoid scratches on the scintillator surface. Nevertheless since the "scratches" seem to be ~uniformly distributed across the surface (see figure 3.22) and the fraction of the areas with "scratches" is small the overall influence on the evaluation of the beam profiles can be regarded as small. As described above the image now has to be transformed in order to correct for the perpective distortion thereby defining a Field-of-view (FOV) that is used for the further evaluation of the beam profiles. No further filters are applied to the the background subtracted and transformed image. The so derived intensity distribution is fitted with a 2D Gaussian distribution:

$$f\left(x,y\right) = A_0 + \hat{A} \cdot \mathrm{e}^{-\frac{1}{2\cdot\left(1-\rho_{xy}^2\right)}\left(\frac{(x-\bar{x})^2}{\sigma_x^2} + \frac{(y-\bar{y})^2}{\sigma_y^2} - \frac{2\cdot\rho_{xy}(x-\bar{x})\cdot(y-\bar{y})}{\sigma_x\cdot\sigma_y}\right)} \tag{3.14}$$

with the coordinates in the FOV being x and y. The beam profile parameters that are derived from the fit are $\hat{A}$ the intensity amplitude, the horizontal/vertical centre of the fit $\bar{x}/\bar{y}$, the corresponding standard deviations σ_x / σ_y and the Pearson correlation parameter ρ_{xy}. The offset term A_0 takes into account the residual homogeneous background illumination from for example stray light. The fit result is illustrated as a 1-σ outline and shown together with the background subtracted and transformed image in figure 3.23. For comparison a beam profile raster scan was taken at approximately the same position along the beam axis with the XY-scanner, described in section 2.5.2, which measures the profile perpendicular to the beam axis. The result is shown in figure 3.24. A comparison of the fit results derived from the scintillation image and the pill raster scan discriminating on low threshold (muons and positrons are counted) and discriminating on high threshold (only muons counted) is given in table 3.3. Due to the rough alignment the values for the centre

(a) BB open.

(b) BB closed.

(c) = (a) - (b)
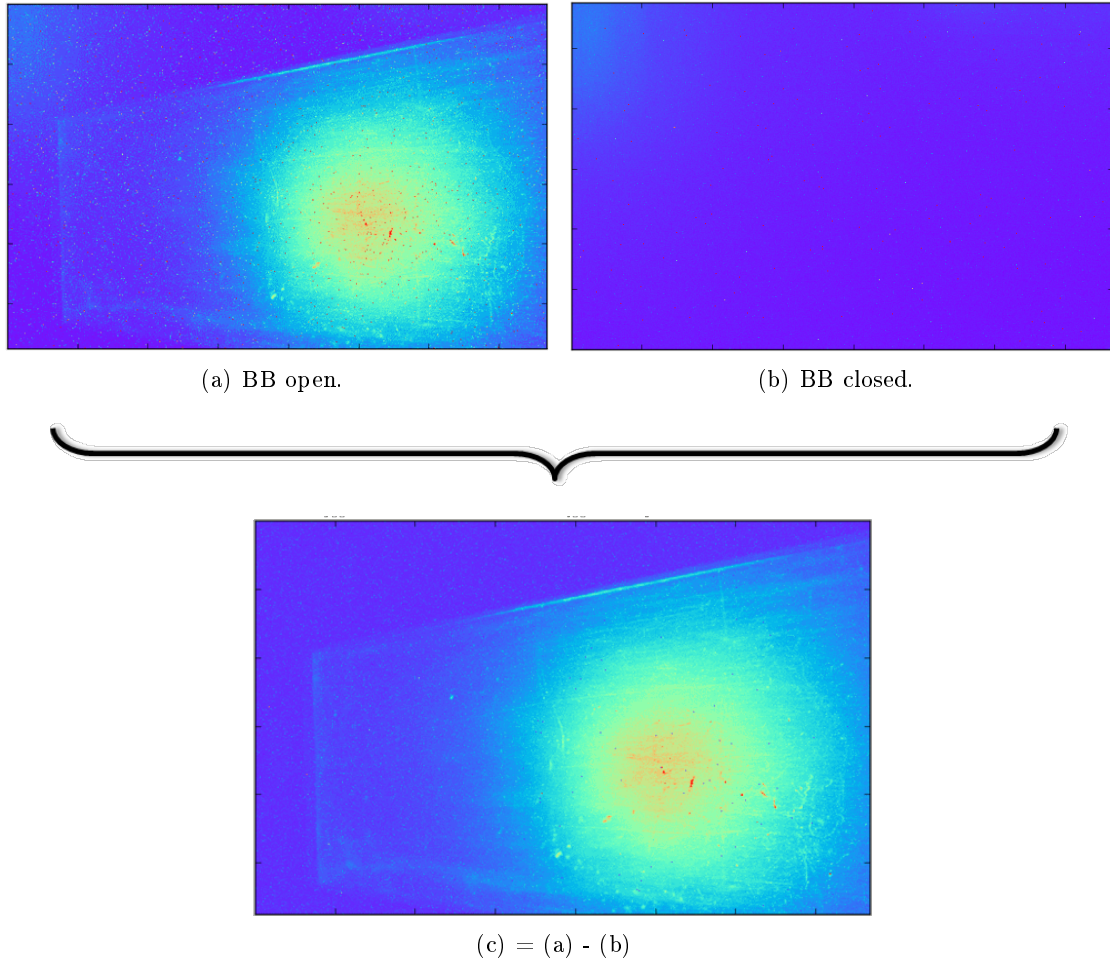
Figure 3.21.: *Shown the image processing sequence. Image (a) was captured with BB open at ∼nominal beam intensity (beam picture). The beam spot is clearly visible - however several continuous areas / lines, that show an enhanced LY, can be attributed to defects on the scintillator surface. Image (b) was taken with BB closed i.e. without muon stops in the target (background picture). From (b) two types of noise-related artefacts can be identified, namely isolated hot pixels and areas of high excitation (e.g. glow of "light" on the top left). Subtracting the ADC values of the background image from the beam image for each pixel individually is called background correction and shown in (c).*

Table 3.3.: *Beam Profile Comparison between XY beam scanner and scintillation light distribution.*

	$\sigma_x(mm)$	$\sigma_y(mm)$	ρ_{xy}	$\Delta\ \sigma_x$ (mm)	$\Delta\ \sigma_y$ (mm)
Scintillator Image	20.9	24.8	-0.01	-	-
Pill High Threshold	18.3	19.8	-0.04	+2.6	+5.0
Pill Low Threshold	19.4	20.8	-0.04	+1.5	+4.0
G4BL Phase Space propagation	26.6	24.4	-	-5.7	+0.4
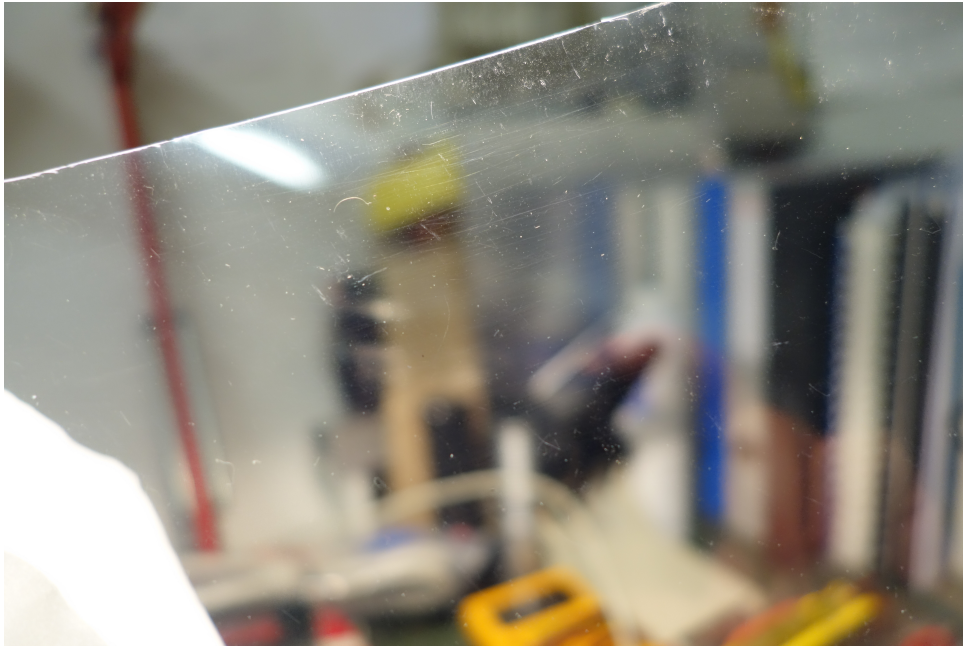
Figure 3.22.: *The close-up image shows inhomogenities and scratches in the scintillator surface that can be identified in the beam picture 3.21.*
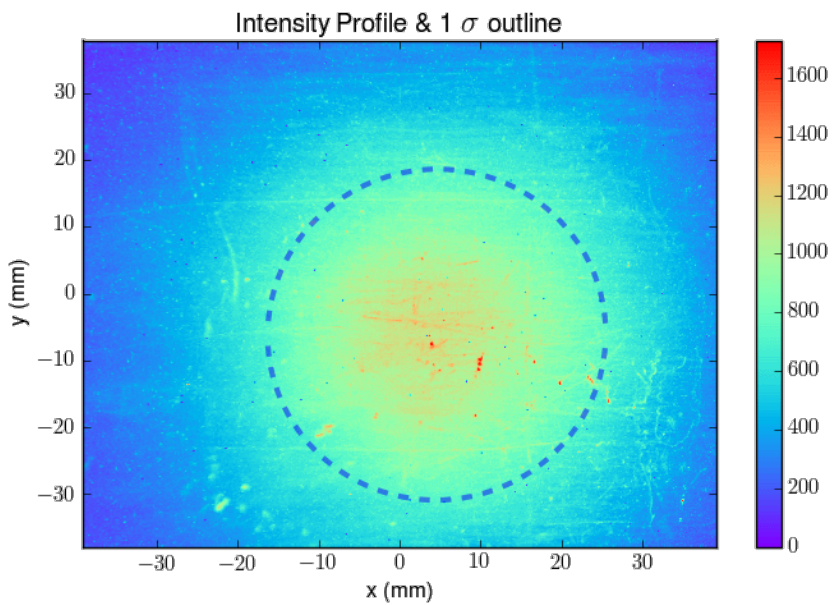
Figure 3.23.: *The background subtracted and transformed image is shown together with the 1-σ outline of the fitted distribution. The picture already shows qualitatively that x and y are essentially uncorrelated, consistent with the small xy-coupling throughout the πE5 beam line.*
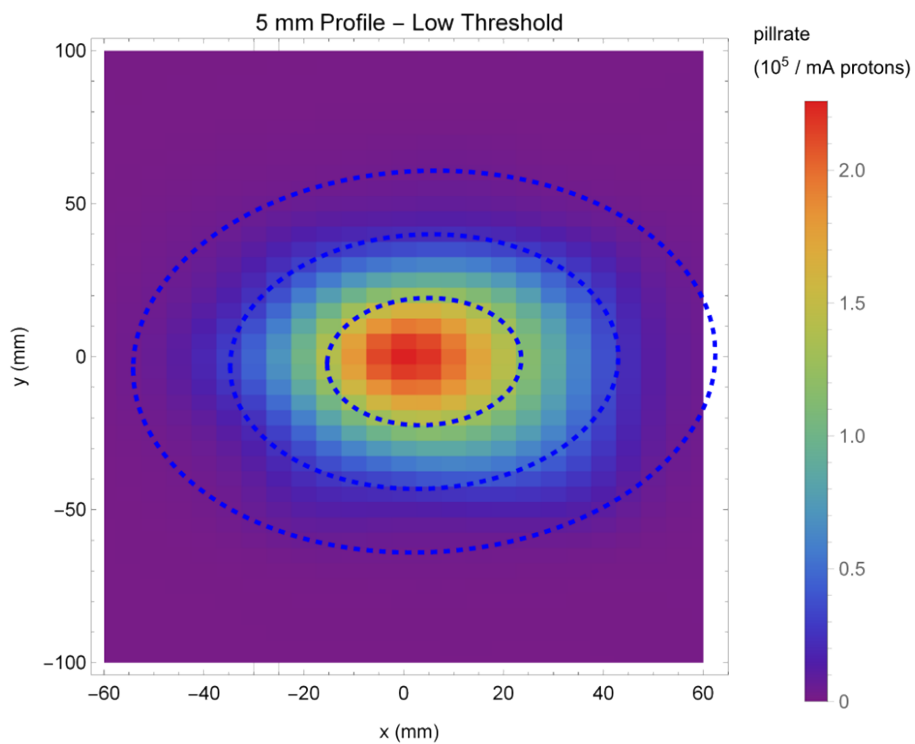
Figure 3.24.: *The plot shows a pill raster scan carried out with the scanner system that has been described in section 2.5.2 discriminating at low threshold. The blue dashed lines indicate the 1-, 2- and 3-σ outline respectively, (note the scales are not the same).*

162

$\bar{x}/\bar{y}$ of the 2D Gauss distributions are not compared. The scintillator image is considered to show a beam size slightly broader than the pure muon distribution due to scattering of emitted light and excitation by Michel positrons. The previously qualitatively observed neglibable coupling between x and y is confirmed by the small correlation coefficients ρ_{xy}. However the comparison between the two methods needs more refinement. The pill scanner measurement being perpendicular to the incoming beam can be used to simulate the beam at the 45° slant angle scintillator with its centre ∼15 cm downstream of the scanner measurement plane.

The more refined method is based on phase space measurements at the entrance to QSK43, upstream of the scintillation target. The phase space is calculated in a similar way as in section 2 of the Compact Beam Line setup. Figure 3.25(a) shows the TRANSPORT envelopes for a multi-envelope fit constrained by the pill scanner measurements carried out for 10 different quadrupole settings. The measured and the simulated beam size based on the reconstructed phasespace are compared in figure 3.25(b). Based on these parameters a beam is tracked in TURTLE [52] and extracted 40 cm upstream the centre of the scintillator. The beam file is then converted to the G4BL compatible G4BLTrackfile format. The geometry in the G4BL simulation encompasses a simplified Mylar vacuum window, the air between the Mylar and the aluminum window of the light-tight box and the air up to the scintillator screen - see figure 3.26. The muon distribution on a virtualdetector representing the slanted scintillator is then projected onto the x-y plane. The projected beam size is then compared to the scintillator results in table 3.3. The vertical direction is in good agreement, whereas the horizontal profile is found to be 5.7 mm larger than measured. Possible reasons for this deviation can be found in the difficult alignment in the horizontal direction. Furthermore, the scratches are mostly in the horizontal direction and therefore affect the horizontal phase space more. The phase space for the simulation was derived in a paraxial approximation first order matrix description. The profiles measured with the pill scanner show a strong dependence $\sim 1.6 \ \frac{mm}{A}$ on the current applied to the preceeding quadrupole (QSK43) as shown in plot 3.27. Thus one can conclude that the muon beam passes the last quadrupole of Triplet II off axis and propagates with an angle to the reference orbit which also predominantly affects the horizontal direction.

3.4.5. Slit Curve measurements

As described in section 3.1 the scintillation light intensity is proportional to the muon flux. Therefore normalizing the scintillation light intensity to the proton beam provides a linear and sensitive measure for changes in the muon rate. In order to adjust the beam intensity for different experiments the πE5 channel has several slit systems. Usually the FSH41 horizontal slit system is used to trim the rates though due to the non-zero dispersion at that location it influences the momentum band. For a linearity check the scintillation light intensity (sum of ADC values after background subtraction) is compared to the integrated pill signal measured on the beam axis; each for different slit settings. Figure 3.28 shows the relative intensities of both devices normalized to the 250/280 setting, whereby the left side FSH41L is set to 250 and the right side is set to 280 which essentially corresponds to a fully open slit. Both devices are in good agreement. Slight deviations stem from a temperature dependence that is discussed in subsection 3.5.2 and a slightly non-Gaussian
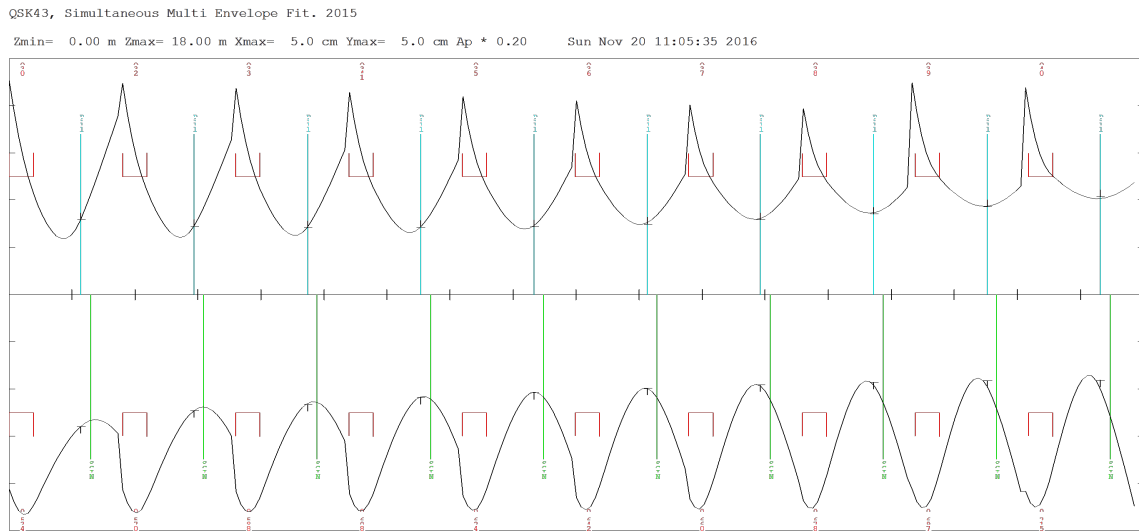
(a) TRANSPORT multi-envelope fit.
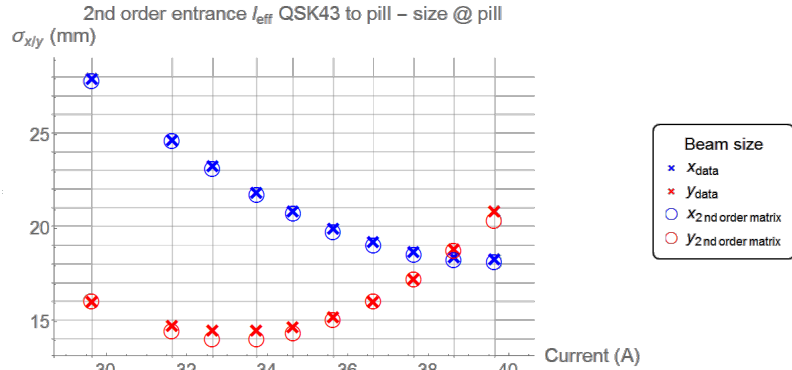
(b) Fitted phasespace at the QSK43 quadrupole magnet.

Figure 3.25.: *The horizontal phase space parameters are fitted for the beam size constraints determined from profiles measured downstream of the intermediate MEG collimator for different quadrupole currents.*
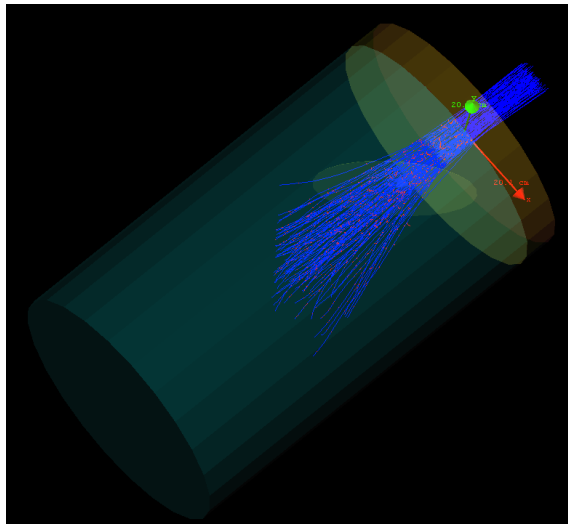
Figure 3.26.: *The graphical output of the G4BL simulation shows the propagation of the beam to the slanted scintillator, based on phase space determination.*
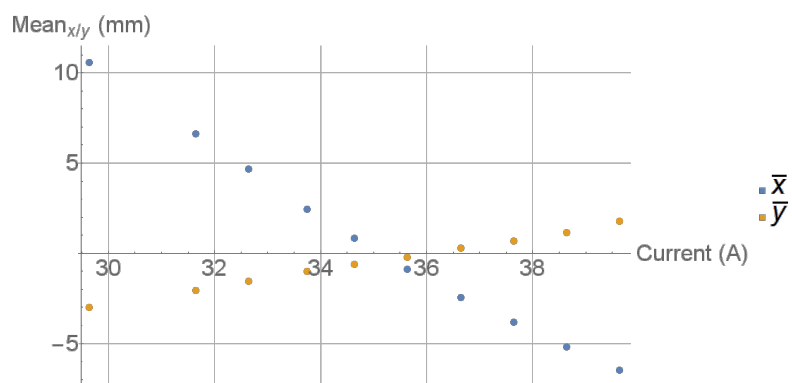
Figure 3.27.: *The centre of the muon distribution on the scintillator shifts for different applied quadrupole currents, implying steering and an off-axis or inclined beam.*

shape of the beam since the pill measures only the central 1 mm radius and the scintillator records the full beam spot.
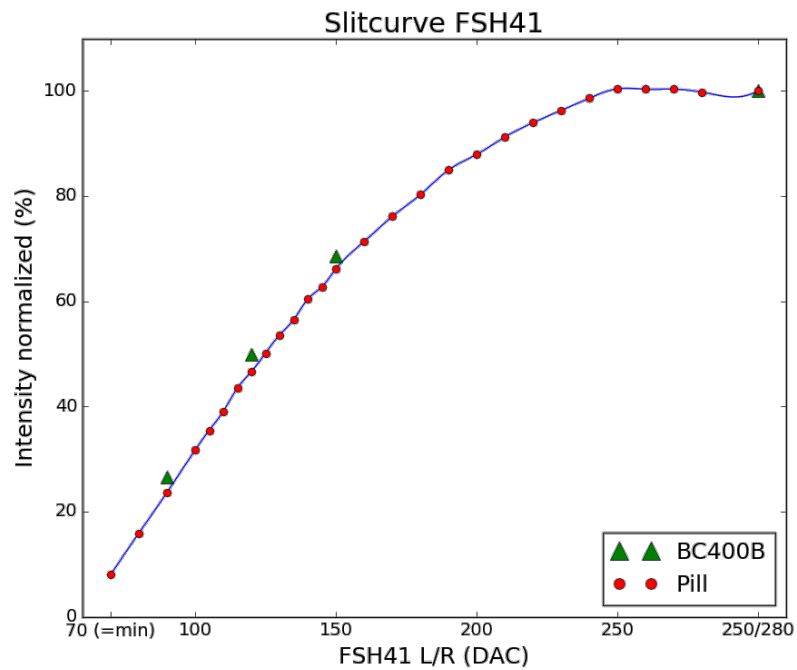
Figure 3.28.: *Comparison of the scintillator LY and pill intensity measured by adjusting the FS41 L/R slit opening in the front part of the $\pi E5$ channel. For both devices the measurements are normalized to the 250/280 setting of FSH41. In all other cases the FSH41 is opened symmetrically. A good agreement is shown.*

3.4.5.1. Conclusions of the 2015 scintillator beam monitoring test

During the first test a 150 μm thin slab of BC400B was mounted at 45° with respect to the beam axis and the camera, as a prototype for the MEG II scintillation target setup. A 100 second exposure time corresponds to a dynamic range $\gtrsim 2/3$, which in turn confirms that the target mounted in COBRA should yield a sufficient signal when viewed from DS. At the end of the test beam a long tube was attached to the light-tight box in order to view the scintillator from ~ 1.8 m distance showing consistent results with the camera mounted inside the light tight box - see figure 3.29. Finally one can conclude that the use
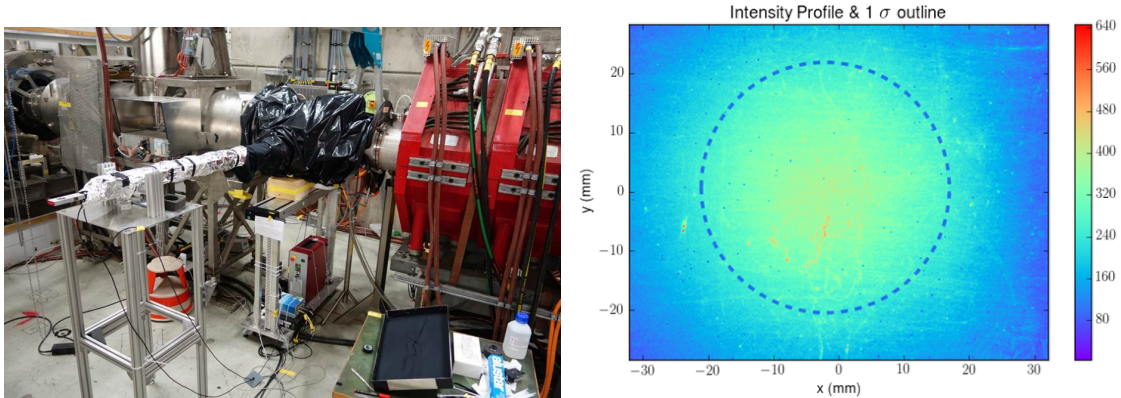
Figure 3.29.: *The left picture shows the long range test setup and the right picture the resulting beam picture. Although less light reaches the CCD the profiles are still clear and consistent with the previous test pictures.*

of the scintillator as a slanted beam monitor located in air and downstream of the MEG collimator showed promising results.

- As can be seen from the scratches on the scintillator surface submillimeter structures are easily resolved which confirms the results from the source pre-test.

- Beam measurements are very fast compared to pill raster scans that usually take $\gtrsim 1$ hour[2]

- Good agreement between the vertical profile determined with the scintillator and that of a combination of pill scanner measurements and a simplified G4Beamline simulation. However there is a significant deviation in the horizontal profile. This can most likely be attributed to several sources. The difficult horizontal alignment, furthermore the incoming muon beam is not paraxial but has an angle. This was identified by the beam centroid dependence, in the horizontal direction, of the quadrupole setting. Both mentioned alignment aspects influence the uncertainty of the G4Beamline model. The very prominent scratches on the surface are predominantly oriented in the horizontal direction. A careful treatment of the scintillator surface is therefore necessary in the future.

- The relative beam intensities for different FSH41 slit openings show a good agreement between pill and scintillator measurement.

---

[2]A new in-vacuum beam monitoring system based on a thin CsI scintillator is currently being developed and has recently been tested in the πE5 beam line [66].

3.5. Testbeam 2016 at COBRA center

The evaluation of the 2015 test beam period provided the techniques and knowledge necessary for the usage of the scintillation target. However the 2016 beam time proved to essential in the understanding of so far undiscovered effects and influences. In order to produce a background subtracted image with the resulting muon beam intensity and beam profile parameters determined, the following known and discovered effects had to be taken into account:

- Lens depth-of-field (DOF) adjustment for a slanted target
- Perspective transformation
- Normalization to the measured proton beam intensity
- Sensitivity to the scintillator surface structure e.g. scratches
- Dark current sensitivity to temperature
- Dark current sensitivity to magnetic field
- Sensitivity to the proton beam centring on the production target TgE causing both a muon intensity change as well as a steering effect on the scintillation target
- Effect of radiation damage on the scintillation LY

A perspective correction has to be applied for the target mounted at 15° although the effect is smaller when viewed from further away. Therefore a calibration paper grid is attached to the carbon-fibre target frame that holds the scintillator and is mounted as parallel as possible with the scintillator surface. The plane of the graph paper and the plane of the scintillator are therefore offset in the horizontal direction by $\frac{frame\ thickness}{2} \cdot \cos{(15°)} = 2.7mm$, when viewed axial from DS of COBRA. The scintillation target with the graph paper attached is shown in figure 3.30. For the operation at COBRA centre further aspects proved challenging.
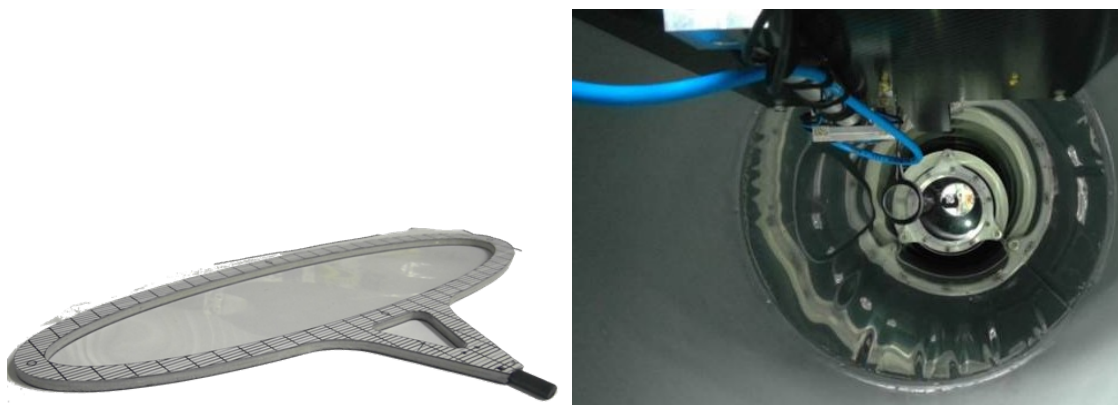
Figure 3.30.: *The left picture shows the target frame with the scintillator mounted. The scintillator was glued between two halfs of a Rohacell frame which is covered with a thin mask made of carbon fibre to enhance the rigidity of the target. The graph paper has been glued to the carbon frame, whereby care has been taken for a good alignment and planarity. The right image is taken from US COBRA*

3.5.0.1. Operational aspects of the setup

The following features are either required or must be taken into account in order to succesfully monitor the scintillation target:

- Long-term operation requires automated image capturing:

    - An automated image capturing software was written in C, providing image capture with a timestamp as well as the averaged proton current $\bar{I}_{p+}$ during the exposure obtained from a DRS evaluation board [66].

- Frequent capture and short-term exposure:

    - Capture frames were automatically taken every 10 minutes for an exposure time of 100 sec.

- Perspective transformation and pixel-to-mm calibration:

    - Requires a good view of the calibration scale on the target frame which is $\sim$2.5 m from the camera requiring the light to pass through and be reflected by several different media involving air/He/Eval-window/Mylar mirror

- depth-of-field (DOF) compensation:

    - The use of the Canon Telephoto lens is necessary to image the target at a distance of $\sim$2.5 m however due to the slanted position not all regions of the target are in focus when the aperture is fully open. Therefore a compromise between image intensity and image sharpness must be made by "stopping down" the lens aperture.

- Illumination of the Calibration Scale

    - Intially a LED was installed above the target system allowing the callibration scale to be illuminated, later it was found a UV LED could both excite the scintillator and the callibration graph paper allowing also surface features to be monitored.

The scintillation target setup DS of the COBRA magnet is shown in figure 3.31.

3.5.0.2. Camera-related aspects of the setup

- Camera system to function in the fringe-field of the COBRA magnet

    - With an average magnetic field of $\sim$0.3 T in this region, the planned, cooled 4M-pixel Hamamatsu Orca Flash 4.0 camera was not suitable due to its built-in power supply. This was substituted by our iDS 0.4M-pixel camera that was tested above 1 T.

- No manual shutter:

    - This restricted the number of background frames that could be taken during data-taking as for this the BB had to be closed.

- Camera dark current and temperature:
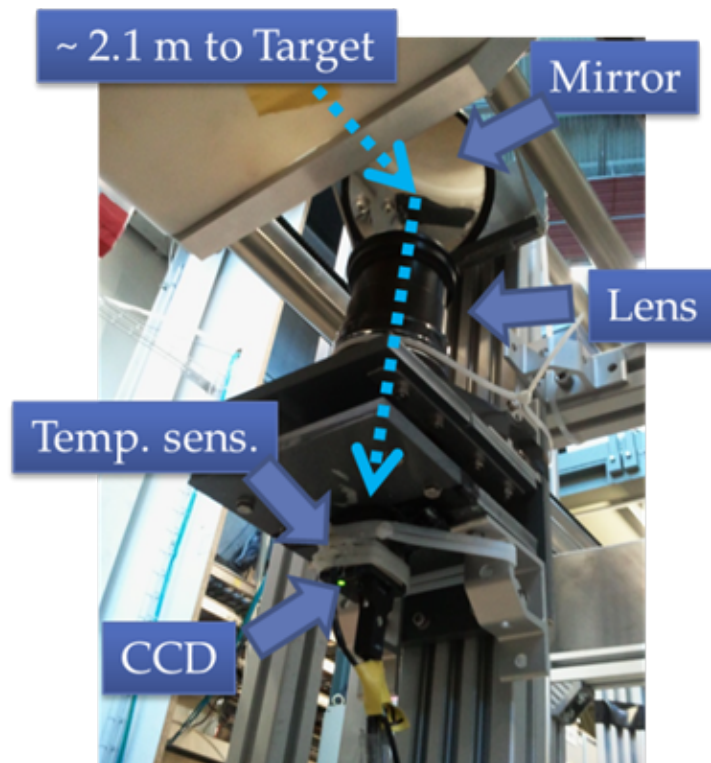
(a) The iDS camera mounted together with the mirror

(b) Light-tight plastic foil covers the camera-mirror support

Figure 3.31.: *COBRA scintillation target setup, the iDS camera views the scintillation target at the centre of COBRA via a mirror. The polyethylene coupling flange on the DS-side is not completely opaque necessiating light-tight wrapping together with the camera.*

- The iDS camera has no internal or external cooling so that the thermal noise in the form of dark current in the sensor plays a major role in achieving a reasonable signal/noise (S/N) ratio of the final image. As described in [104] the main contribution to the dark current is the temperature of the sensor. The iDS camera housing was subsequently fitted with an AD590 [105] temperature transducer using a thermal paste, so giving a measure of the thermal equilibrium temperature of the sensor and its environment. The temperature is recorded by an SCS2000 [49] module as part of the MEG MIDAS Slow Control System. Figure 3.32 shows the S/N ratio for a raw beam and background image showing clearly the high background level.

(a) Heatplot of a raw beam image - no background subtraction & no transformation applied

(b) Heatplot of a successive background frame (Beam Blocker closed)

(c) Histogram of intensity levels of the beam picture a.

(d) Histogram of the intensity levels of the background image.
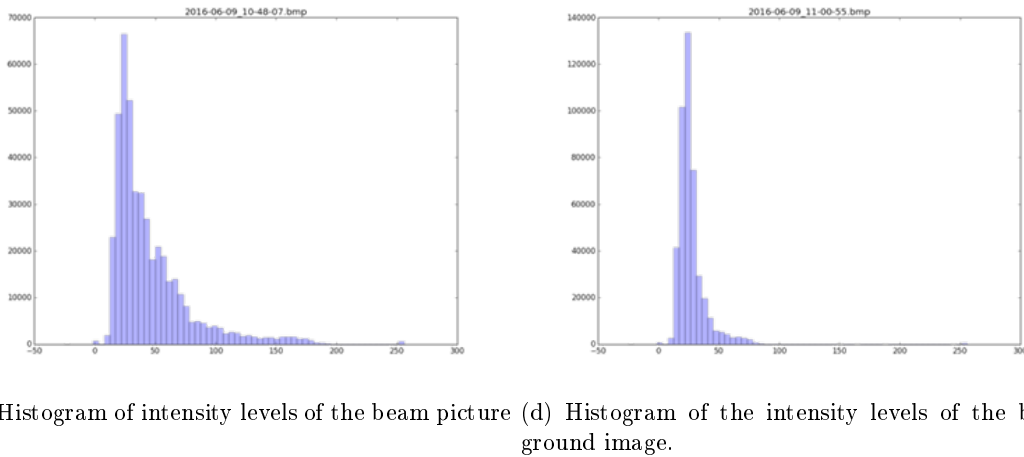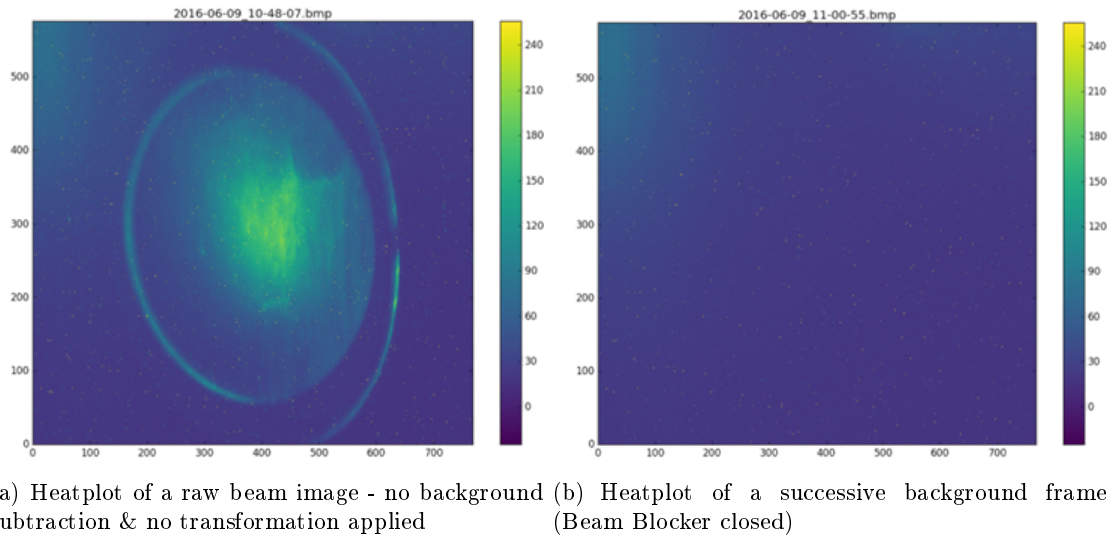
Figure 3.32.: *Shown are heatplots and histograms of the ADC levels for a beam and a successive background image. The summed ADC value of all pixels for a raw beam picture amounts to 20300k whereby the sum of all background pixels amounts to 11965k for the same exposure time.*

3.5.1. 2016 Scintillation Target Beamtime Overview

The scintillation target was implemented as the MEG II muon stopping target at the centre of the COBRA magnet during the Pre-Engineering Run 2016. The beam setup period at the beginning allowed the setup and testing of the camera, the capture software written as well as the offline reconstruction procedure. The run period dedicated to the Timing Counter (TC) and Radiative Decay Counter (RDC) commissioning was between 21$^{\text{st}}$ May and the 10$^{\text{th}}$ July 2016, this period also served as a commissioning run of the scintillation target as a beam monitoring system.

The beam monitoring period was split into 3 distinct slots caused by an unplanned accelerator outage requiring a production target replacement and once by the planned measurement with the RDC requiring the camera and mirror assembly to be removed.

During the first period a light leak was discovered by chance during a frame capture with the beam momentarily down but open vacuum valves at the separator, that are normally closed with the BB. The affected captured frame can be seen in figure 3.33(b) showing a bright spot which was found to come from a small uncovered window feed-through some 10 m upstream in the separator. Once made light-tight dark background images were also produced without beam and were also taken repeatedly with the BB either closed or open during the accelerator down period, together with multiple LED illuminated target pictures for calibration.

An overview of the beam monitoring period is shown in figure 3.34 with the detailed chronology given below:

- Period I: [29/5-12/6]

    - 29/5 - 10/6 11:15 data-taking, unaware of light leak

    - 10/6 11:15 - 12/6 0:00 good conditions I_{p+}>1 mA

- Target Repair: [12/6 0:00 - 20/6 13:00]

    - accelerator outage due to production target change
      background & calibration frames taken repeatedly

- Period II: [20/6 13:00 - 27/6 12:00]

    - good data-taking parallel to TC measurements

- RDC Run: [27/6 - 9/7]

    - camera and mirror system removed

- Period III: [9/7 - 10/7]

    - camera and mirror assembly reinstalled & final data-taking

Compared to the 2015 test beam the perspective correction for the 2016 run is more challenging due to the shallow mounting angle of 15° and the low resolution of the camera. However, figure 3.35 illustrates that the correction works well. As can be seen in 3.35(b) gridlines generated to be positioned at pixel values corresponding to $x = \pm k \cdot 20mm$ and $y = \pm k \cdot 4mm$ from target centre for integer numbers k match the the lines of the attached graphpaper.
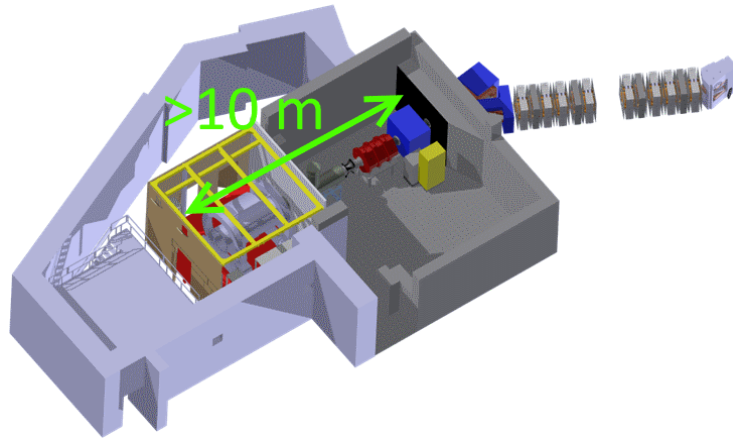
(a) Distance between camera and separator $\gtrsim$ 10 m.
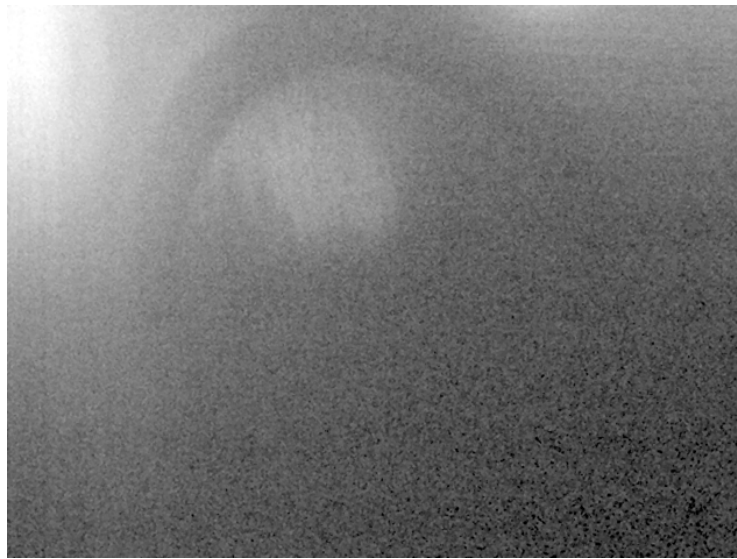
(b) The picture was captured without beam but with beam blocker open (contrasts are enhanced by software).

Figure 3.33.: *Light entering the beam line through an uncovered window flange at the separator travels $\gtrsim$ 10 m. Despite the long distance the light is sufficient to influence the monitoring capabilities.*
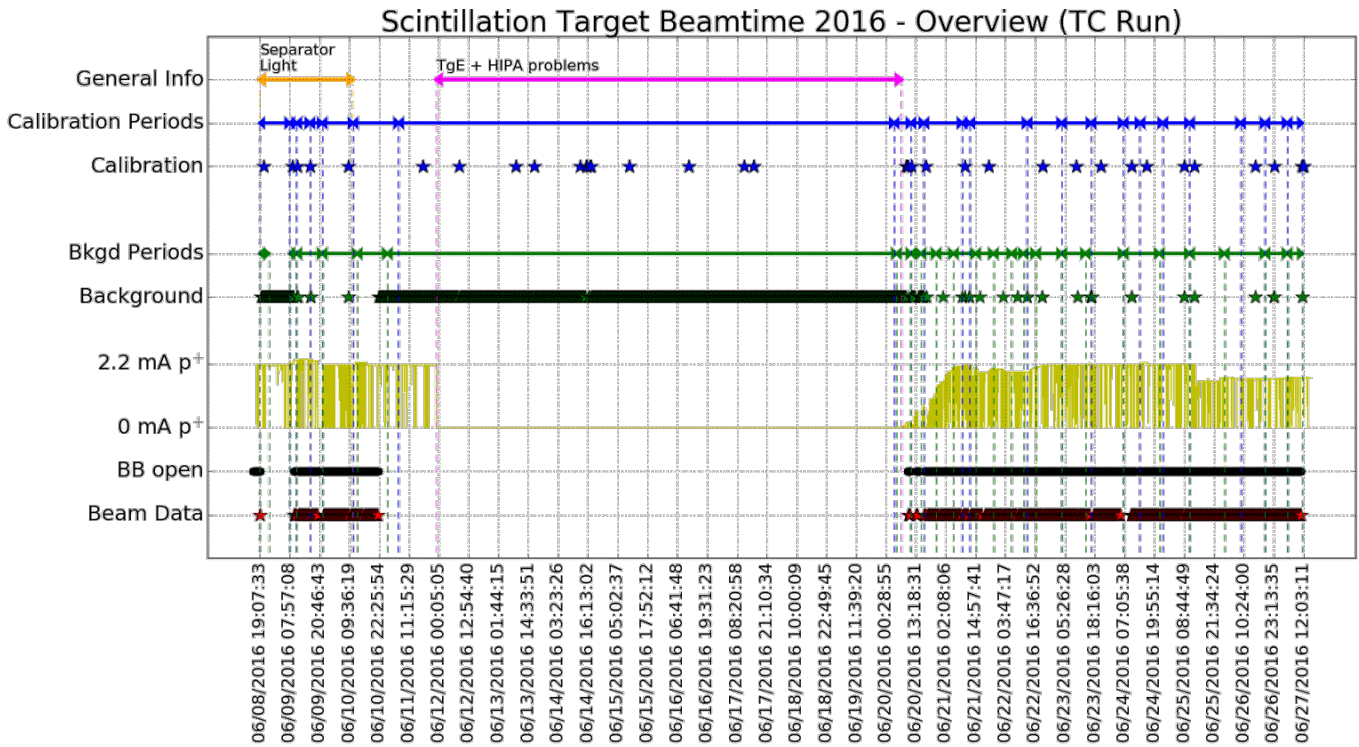
Figure 3.34.: *The main data taking period started with the discovery of a light leak in the beam line. After this had been fixed, beam pictures (red stars) were taken until severe problems occured at TgE and the HIPA proton accelerator causing an interruption of approximately one week. During that time the continuous image capturing continued in order to get good statistics for the background (green stars). Restarting from 20th June, images were captured in parallel to the Timing Counter data taking for ∼1 week. Periods safely regarded to have a coherent reproducibility are marked as either Calibration Periods describing periods that garantuee the same perspective view on the target or as Background Periods garantueeing same light-tight conditions. The proton beam (yellow line) is used for intensity normalization. The Beam Blocker BB (black points) indicate whether the beam blocker was open or closed.*
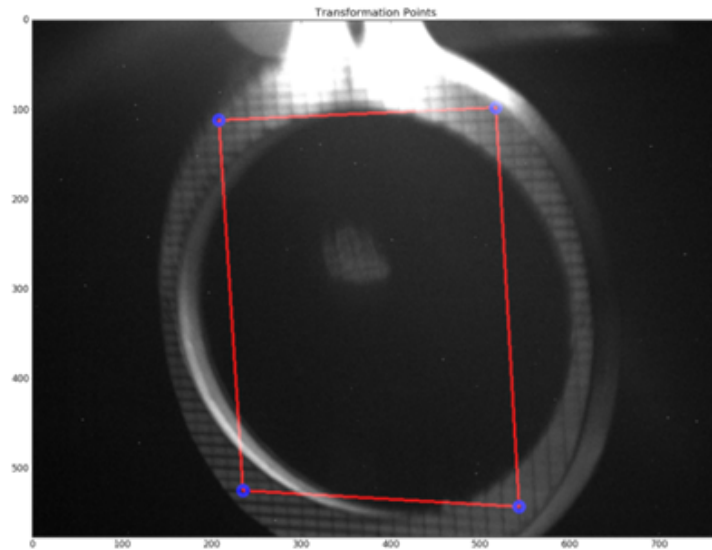
(a) Image of the target showing the 4 points on the graph paper used for the reconstruction.
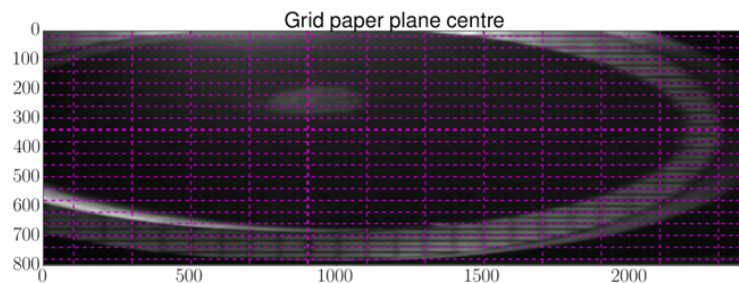
(b) Corrected image after perspective transformation.

Figure 3.35.: *The perspective transformation provides an undistorted parallel view perpendicular to the target which is proven by the gridlines drawn according to the well defined spacing of the graph paper lines.*

3.5.2. Background Subtraction with temperature scaling

A proper determination of the background is essential for measuring relative intensities. During the data-taking of the Timing Counter the involved groups agreed on closing the beam blocker ~twice per day for a few minutes in order to take several background frames in a row. All beam pictures taken in between have to be corrected by those backgrounds. Hence a stable background level is very important. As a measure for this the summed ADC values for all pixels in an image are drawn in figure 3.36. As seen from the plot the background intensity levels fluctuate in time ranging from $\sim 9.5 \cdot 10^{6}$ to $\sim 1.5 \cdot 10^{7}$ summed bitlevels. This would mean a severe drawback ruling out most of the captured frames
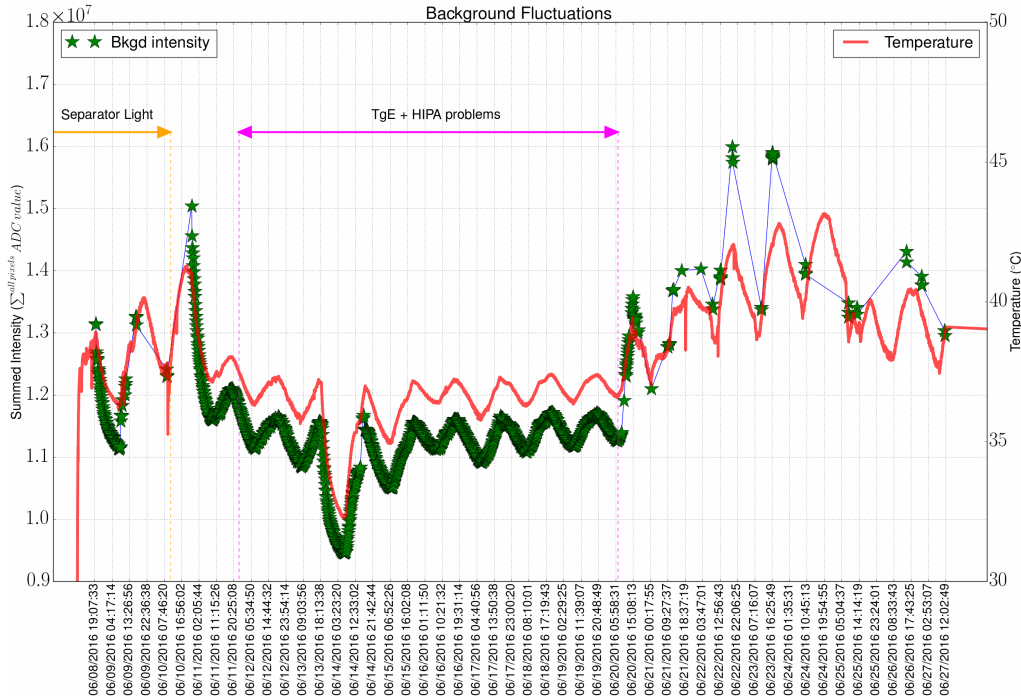
Figure 3.36.: *The summed ADC values of the background images show significant fluctuations over time. However the temperature sensor mounted on the iDS camera housing shows a clear correlation with the background intensity levels.*

for analysis unless being properly corrected for. The camera temperature read out by the AD590 is expected to be correlated with the intensity levels. Since the camera temperature can change within the 100 seconds exposure time, for example when the main door of the experimental hall is opened (see figure 3.37), the temperature that is assigned to a single frame is given by the integral for the exposure time of the linear interpolated temperature values. For the further evaluation the timeline plots for the status of the beam blocker, the magnetic field and the LEM's rate are also linearly interpolated.

$$T_{assign}\left(frame\right) = \frac{1}{t_{end\ frame} - t_{start\ frame}} \cdot \int_{t_{start\ frame}}^{t_{end\ frame}} T_{interpolation}\left(t\right) dt \qquad (3.15)$$

Figure 3.38 shows the summed background intensity levels drawn against the integrated temperature. This also confirms the correlation between temperature and the background
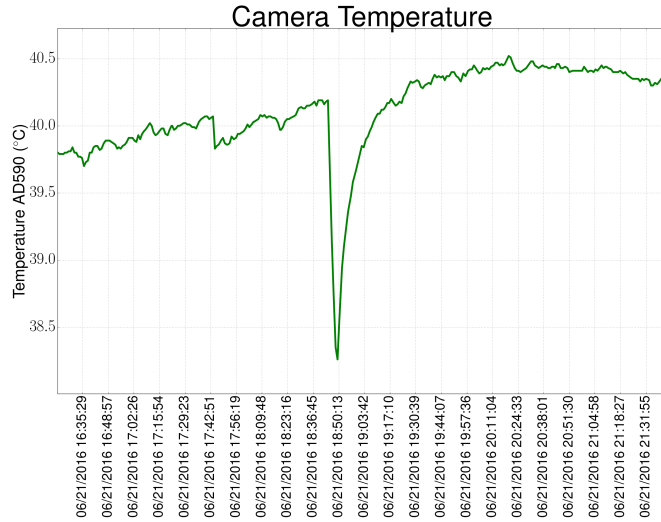
Figure 3.37.: *The time scale needed for the camera to cool down is of the same order of magnitude as the exposure time.*
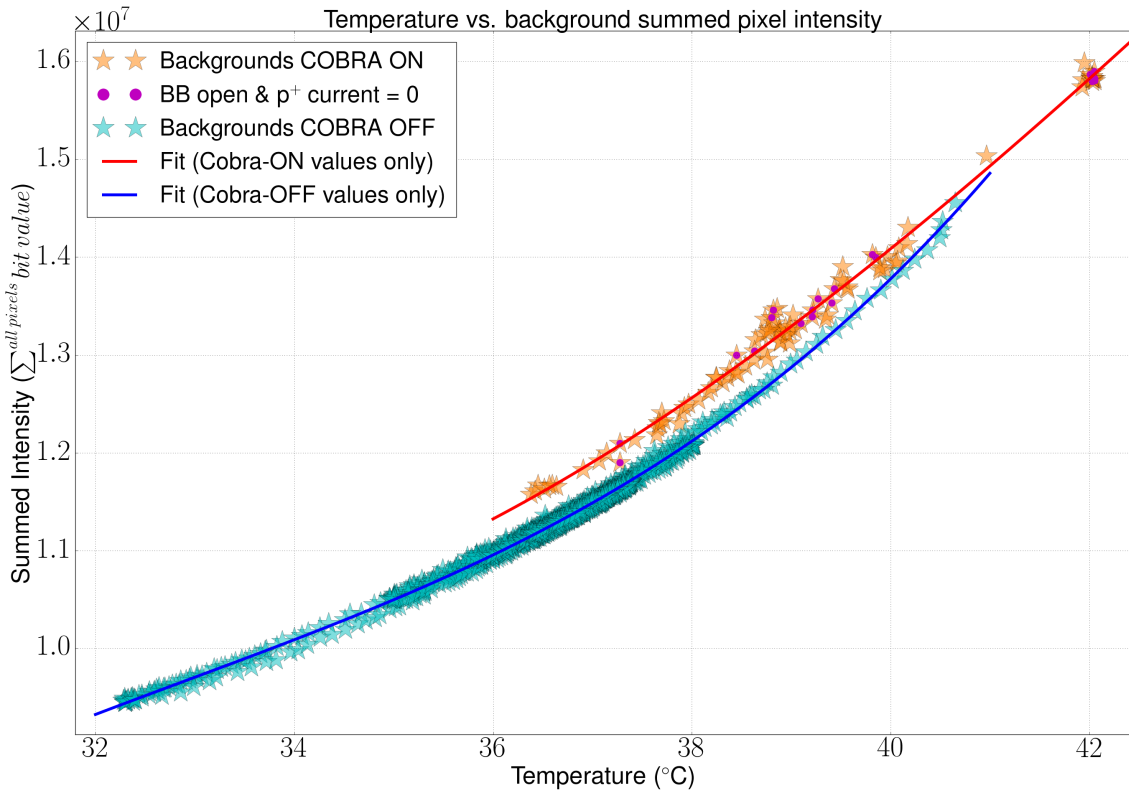
Figure 3.38.: *The summed background intensity levels show a clear nonlinear correlation with the temperature and can therefore be fitted by polynomial functions. The background frames taken with excited coils show a higher dark current level with a slightly different trend compared to background frames with COBRA OFF.*

Table 3.4.: *Polynomial functions and their coefficients used to fit the dark current levels:* $I_{fit}(T) = a_0 + a_1 \cdot x + a_2 \cdot x^2 + a_3 \cdot x^3 + a_4 \cdot x^4 + a_5 \cdot x^5$

	COBRA ON	COBRA OFF
Number of frames		
	99	1421
Polynomial coefficient		
a_0	$+7.32 \cdot 10^9$	$5.60 \cdot 10^8$
a_1	$+1.70 \cdot 10^6$	$-1.19 \cdot 10^8$
a_2	$-2.35 \cdot 10^5$	$3.16 \cdot 10^5$
a_3	$-1.75 \cdot 10^2$	$4.31 \cdot 10^3$
a_4	$+4.27 \cdot 10^0$	$-2.20 \cdot 10^1$
a_5	$-6.80 \cdot 10^{-3}$	$2.83 \cdot 10^{-2}$
RMS after normalization		
	0.78%	0.33 %

level. There are two obvious main bands in which the points accumulate. Applying corresponding cuts, the two main distinguishable types of (temperature|intensity) points can be identified. The lower band with many more points is identified as background frames taken while the coils of COBRA are not excited and vice versa. This means that the setup is sensitive to the magnetic field. In principle the AD590 sensor could cause a similar effect by a B-field dependent temperature read back. however, this can be ruled out as the major source since there are no temperature jumps of recognizable size in figure 3.36 observed while ramping up or down COBRA.

There is not only a gap between the backgrounds taken with "COBRA ON" (i.e. nominal current) and "COBRA OFF" but furthermore both bands have a different shape. This implies that the higher order dependence between the summed intensity I and the temperature or the B-field cannot be treated independently. A mixing term of the magnetic field B and the temperature T would be required:

$$I(T,B) = f(T,B) \neq g(T) + h(B)$$

with f, g, h being functions of temperature and/or the magnetic field. However for a spatially stable camera position the B-field contribution is constant and can therefore be absorbed in the coefficients of two different polynomials that only show a temperature dependence. Hence both cases "COBRA ON" and "COBRA OFF" can be fitted independently. Since we do not have the exact CCD and electronics temperature, we can not apply a common theory to describe the dark current [104]. Hence a 5th order polynomial is fitted to each, the COBRA OFF and the COBRA ON data points in order to evaluate the beam intensities. Different degree polynomials were tested in order to determine the best trade-off between good agreement and overfitting. The resulting fit parameters are summarized in table 3.4. Unfortunately the backgrounds taken with COBRA ON cover a smaller temperature range and less in number than those for COBRA OFF. An initial idea to put the camera in a thermal chamber at the end of the run and produce more background frames covering a wider temperature was given up due to the strong dependence on the B-field which can not be reproduced in the thermal chamber. In order to check

the validity of the fits all summed background intensity levels are normalized according to equation 3.16 and drawn in figure 3.39.

$$I_{norm}(frame) = \frac{I\left(frame\right)}{I_{fit}\left(T_{int}\left(t\left(frame\right)\right)\right)} \tag{3.16}$$

whereby I_{norm} is the normalized intensity, $I\left(frame\right)$ is the summed intensity of the frame, I_{fit} is the polynomial value with coefficients a_n from table 3.4 and $T_{int}\left(t\left(frame\right)\right)$ is the temperature derived from integration of the interpolated temperature values from data as in equation 3.15. The histograms in figure 3.40 show the deviations from 1 for the norma-
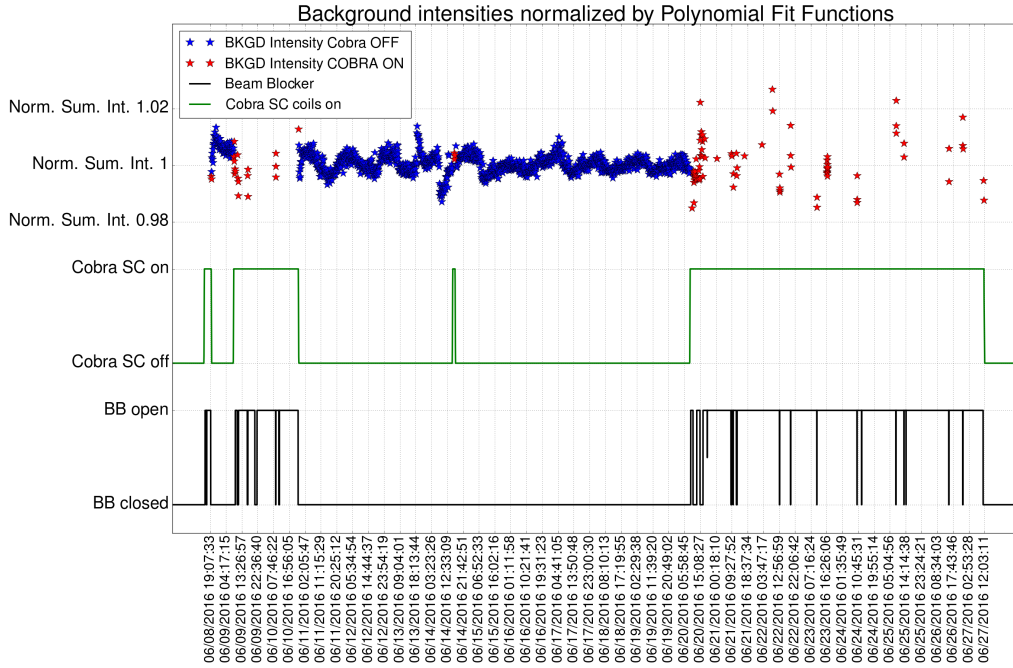
Figure 3.39.: *Normalizing the background intensities assigned to the frames by the corresponding polynomial fits derived from figure 3.38 illustrates the strongly reduced residual fluctuation of this method when compared to figure 3.36.*

lized values for COBRA ON / OFF. The RMS values for the temperature normalization are 0.33% in the case of no current is applied to the COBRA coils and 0.78% with the nominal coil excitation. This does not only imply a higher dark current level when the coils are excited, which could be avoided in the future with a temperature stabilized camera, but also a larger spread of the background intensities. The susceptibility to the field of COBRA will strongly depend on the field strength at the final mounting position and the individual response of the camera electronics, which is difficult to predict. Therefore functionality tests are necessary when deciding on a new camera. Thorlabs, a candidate company, offer a loan of a temperature controlled CMOS camera [106] for careful tests, which are envisaged in the near future. The temperature scaling method shows a residual scattering < 1% RMS for the backgrounds taken with excited COBRA coils.
Applying this procedure to beam pictures with background subtraction allows the ex-
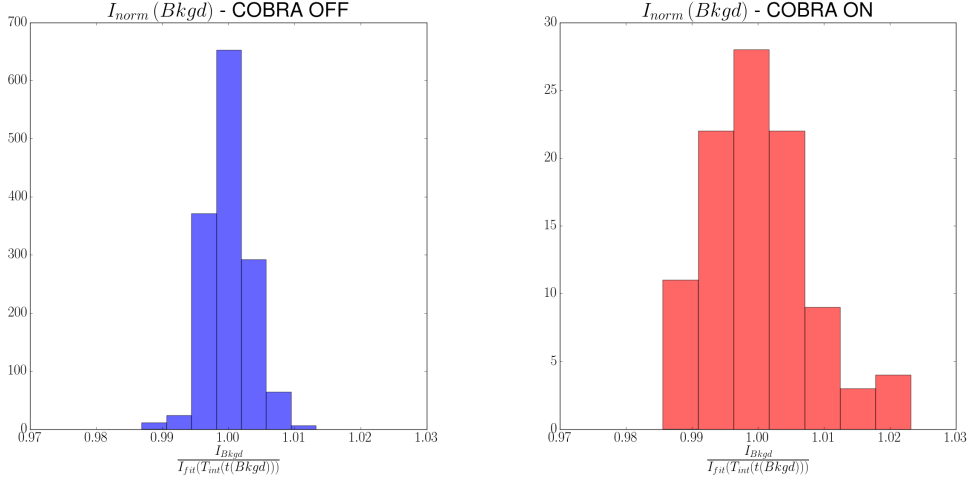
(a) Distribution of the temperature normalized
background intensities with COBRA OFF

(b) Distribution of the temperature normalized
background intensities with COBRA ON

Figure 3.40.: *The noise levels of the dark frames after normalization correspond to* $RMS_{dark,norm,COBRAOFF} = 0.33\%$ *and* $RMS_{dark,norm,COBRAFF} = 0.78\%$.

traction of a beam intensity $I_{\propto\mu}$ which is approximately proportional to the number of incoming muons. The intensities have to be scaled according to equation 3.17.

$$I_{\propto\mu} = I_{frame,beam} - \frac{1}{n} \sum_n \left(\frac{I_{fit}\left(T_{int}\left(t\left(frame,beam\right)\right)\right)}{I_{fit}\left(T_{int}\left(t\left(frame,bkgd_n\right)\right)\right)} \cdot I_{frame,bkgd_n} \right) \qquad (3.17)$$

where $I_{frame,beam}$ is the intensity level of the beam picture under investigation,
$I_{fit}\left(T_{int}\left(t\left(frame,beam\right)\right)\right)$ is the result of the background fit function ("COBRA ON") for the integrated average temperature T_{int} during the exposure time of the beam picture from $t\left(frame,beam\right) - exposure\ time$ to $t\left(frame,beam\right)$, similarly for $I_{fit}\left(T_{int}\left(t\left(frame,bkgd_n\right)\right)\right)$ the exposure time of the background frames. $I_{frame,bkgd_n}$ are the intensities of the background frames that are averaged for background subtraction. Equation 3.17 is only valid as long as the scintillator shows no degradation due to radiation damage. However since the number of muons also depends on the proton current and proton beam centring on TgE this information can be used to determine the radiation damage of the scintillation target. The required relationships between these quantities are derived in the following subsections.

3.5.3. Scintillation target profiles and comparison with the APD scanner results

In the following, the steps necessary to extract the beam profile information are summarized:

| Median Filter on Beam and Bkgd images | $\rightarrow$ | Subtract average of adjacent Bkgds | $\rightarrow$ | Perspective transformation | $\rightarrow$ | Apply Cuts | $\rightarrow$ | Profile parameters from 2D Gauss Fit |

- Median Filter:
  - As already seen in the previous 2015 run the iDS camera suffers from a number of "hot pixels" that immediately saturate. Those are corrected for by means of a small window size Median Filter which is applied to both, beam and background images. Table 3.5 lists the fit results of a 2D Gaussian for one beam profile image of the scintillation target for different Median filter window sizes. By choosing the smallest non-trivial window size=3 the hot pixels can be removed without affecting the fit results.

- Background subtraction:
  - Background subtraction comprises of taking the average of 4 background frames adjacent in time within a coherent background period (see figure 3.34) and assigning them to each beam picture. All background periods contain at least 4 background frames. The temperature dependence of the sum of the background ADC levels can be described well as outlined in subsection 3.5.2. This allows for an accurate determination of the absolute intensity. However the temperature scaling of the background levels is not uniform across the CCD which leads to distortions of the subtracted profiles. Therefore in the case of beam profile evaluation the backgrounds are averaged before subtraction without temperature scaling. The major uniform part of the temperature dependent background level is absorbed in the offset coefficient A_0 and the amplitude $\hat{A}$ in the fit function 3.14 and does not affect the remaining beam profile parameters. The residual temperature dependence can be seen and is discussed in subsection 3.5.6.

- Perspective Transformation:
  - The background corrected image contains the extracted muon footprint and to a small extent artefacts such as stray light, reflections and enhanced LY regions caused by surface imperfections of the scintillator. In a next step the image has to be corrected for the perspective distortion, as outlined in subsection 3.4.3 and 3.5.1, which yields the parallel projection of the profiles along the beam axis. Individual sets of points used for the perspective correction are assigned to different calibration periods (see figure 3.34).

- Cut application:

- In order to restrict the fitted data only to the scintillator surface with a sufficient distance from the Rohacell frame, a first circular and centred cut with a 29 mm radius is introduced. The scintillator images show distinct bright regions of $\mathcal{O}\left(millimeter\right)$ size which are associated with inhomogenities on the scintillator surface. Therefore additional rectangular cuts are applied which exclude the most affected regions from the Gauss Fit. The cuts are valid for all images throughout the run since they are assigned to regions on the target after carrying out the perspective transformation.

- Fitting:
  - Finally the remaining data are fitted with equation 3.14 in order to extract the beam size, beam position and correlation of the axially projected muon beam profile on the target.

Table 3.5.: *Comparison of Profile Parameters for different Median Filter settings. Example image taken on 10th July.*

Median filter kernel size	$\bar{x}(mm)$	$\bar{y}(mm)$	σ_x (mm)	σ_y (mm)
1	5.37	2.38	11.28	11.74
3	5.37	2.39	11.28	11.74
5	5.37	2.39	11.29	11.74
7	5.37	2.39	11.29	11.74
9	5.37	2.39	11.29	11.74
11	5.37	2.39	11.30	11.75
13	5.37	2.39	11.30	11.76
15	5.37	2.40	11.31	11.77
21	5.38	2.40	11.32	11.78

Since the beam line for the MEG Pre-Engineering Run 2016 was set up using the APD-mounted, long-armed 2-D scanner system described in section 4.5, the results of the APD scans can be compared with the profiles provided by the scintillation target. Figure 3.41 shows the result of an APD raster scan. The corresponding beam profile derived from the scintillation target is shown in figure 3.42. Both plots are overlayed with the corresponding 1 σ-and 2 σ outlines. In both cases larger x-values correspond to the left-direction when viewed in beam direction. Positive y-values are above the beam line midplane. The point $(0/0)$ is defined by the beam centreline. The profile results are compared in table 3.6. The values for the Gauss Fit of the two methods agree within 0.3 mm in σ_x and 1 mm in σ_y which confirms the usability of the scintillation target as profile monitor. However the means $\bar{x}$ and $\bar{y}$ are off by several mm in both directions and is most likely due to a scanner misalignment of the APD caused by the 5 m long lever-arm and the parallelism of the scanner rail system. The remaining deviations can also be assigned to systematic uncertainties, that are listed below:

- Dependence of the muon beam envelope in COBRA due to the different positions along the beam line, in the vincinity of the target and the slanting angle, whereby the APD scan has been acquired some cm downstream of the US-side of the inclined scintillation target in a plane perpendicular to the incoming muon beam
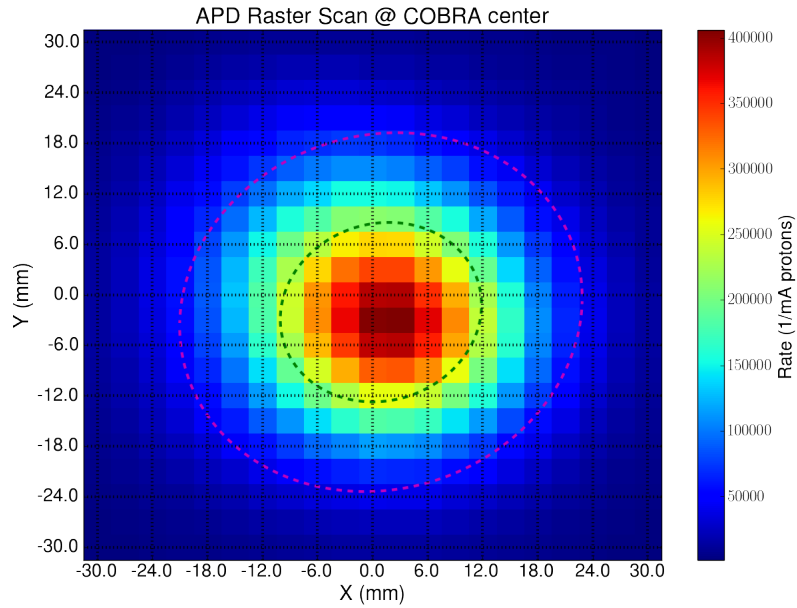
Figure 3.41.: *The plot shows the result of the 3 mm APD raster scan measured in a plane perpendicular to the beam direction at COBRA centre. The raster scan yielded $9.16 \cdot 10^7 \mu^+/s$. The profile parameters are listed in table 3.6.*
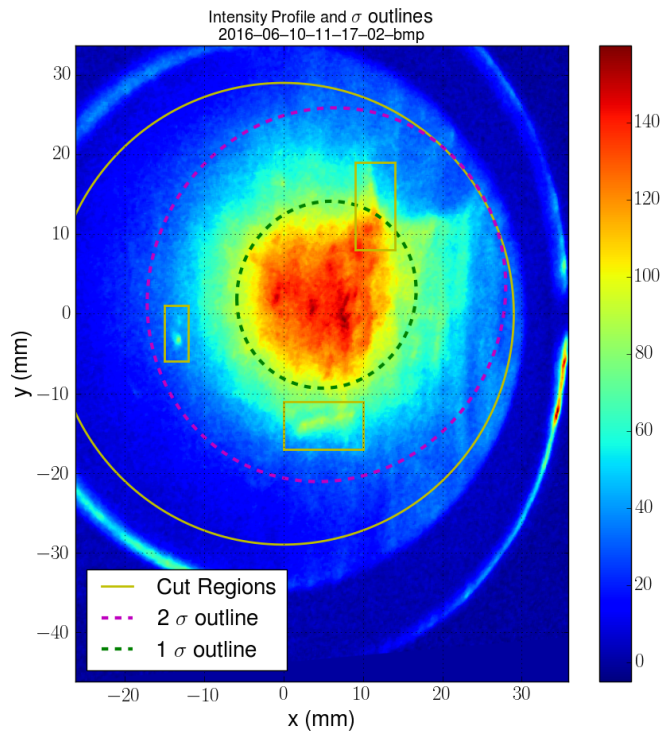
Figure 3.42.: *Shown is the corresponding heatplot of the corrected first beam image that was captured on the 10th of June, after fixing the light leak with an average proton current $\bar{I}_{proton} = 2.15mA$. The yellow lines indicate the regions of the image that were excluded from fitting.*

Table 3.6.: *Comparison between result of the APD raster scan and the scintialltion target profile measurement from 10th June at normal beam intensity after fixing the light leak and a profile captured on the 23rd June at low beam intensity.*

	APD Raster	Scintillation target @ $\bar{I}_{p^+} = 2.15 \ mA$	Scintillation target @ $\bar{I}_{p^+} = 0.05 \ mA$
$\bar{x}$ (mm)	0.9	5.4	5.6
$\bar{y}$ (mm)	-2.1	2.4	2.1
σ_x (mm)	11.0	11.3	12.8
σ_y (mm)	10.7	11.7	13.4
ρ_{xy}	-0.08	-0.05	-0.07

- Defficiencies on the surface of the scintillator, such as scratches, that are not excluded by cuts

- As outlined in subsection 3.5 the scintillator is glued between two Rohacell parts that are covered with a thin sheet of carbon fibre to enhance the rigidity of the target. Already before the run it was observed that the scintillator surface was somewhat warped - see figure 3.64.

- Inhomogeneities of the camera, such as dark current temperature dependency and linearity in the spatial distribution of the LY

- In the 2016 COBRA centre setup the scintillation light has to pass the curved and not-so-clean 20 μm EVAL window of the End-cap insertion system leading to a possible position dependent absorption.

- As can be seen in the right picture in 3.30 the walls of the new cylindrical drift chamber are made of reflective aluminized Mylar foil. Picture 3.35(a) shows an unwanted reflection on the scintillator, however the light emanates not from the target itself but from the Light Emitting Diode (LED), during calibration measurements.

- Residual light leaks

- The source of the striations on the right side of the beam images (see figure 3.42) is not clear. Though the muon beam can be assumed to have a rather smooth distribution. Therefore small structures with big gradients on the edges are most likely indicative of systematic effects.

Despite the above mentioned systematic effects the sensitivity of this method allows even monitoring of rather weak beam signals. Figure 3.43 shows a beam picture that was captured with a corresponding average proton current $\bar{I}_{p^+} \lesssim 50\mu A$, ~2 % of the nominal current. The Gauss Fit still shows consistent results so demonstrating the use of the stopping target for limited beam currents, large displacements from centreline, or allowing a reduction in exposure time in order to have a faster feedback for example during beam tuning. Furthermore this proves the possibility to deal with lower LYs as a consequence of radiation damage. The fit parameters assigned to the beam profiles shown in this subsection are listed in table 3.6. The profile fit results of the 1122 beam images captured during the run are shown and discussed in subsection 3.5.6.
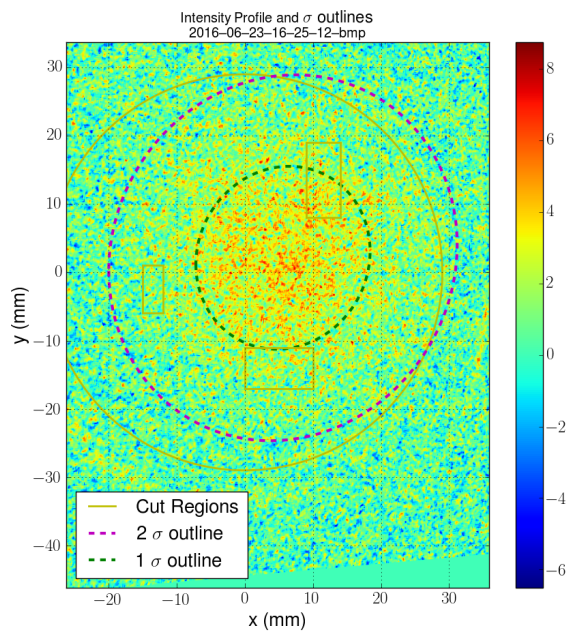
Figure 3.43.: *Single beam picture taken on the 23rd of June with an average proton beam current of $\bar{I}_{p^+} \lesssim 50\mu A$, $\sim$2 % of the nominal current.*

3.5.4. A proton beam scan of TgE

A CAD model of the MEG beam line including the πE5 extraction dipole AHSW and the muon production target TgE was shown in figure 1.21. The close-up CAD sketch 3.44 illustrates how the proton beam traverses TgE. The proton beam position on TgE can
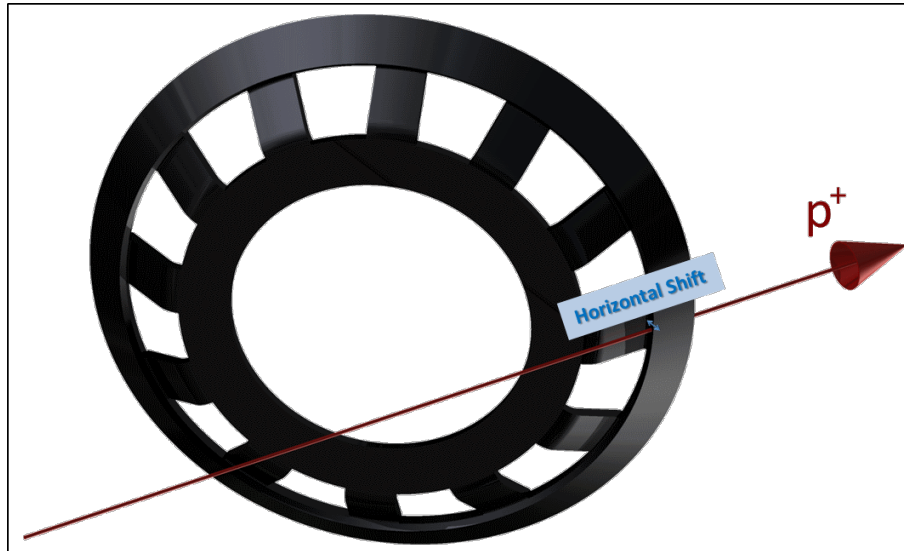
Figure 3.44.: *Close view on the muon production target TgE (CAD model). The proton beam indicated by the red arrow can be shifted in a small range horizontally across the target.*

be adjusted by up to $\pm \sim 1.2$ mm by tuning the three dipole magnets AHU, AHV and AHSW as illustrated in figure 3.45. Different impact locations of the proton beam on TgE lead to a shifted pion stopping distribution and consequently affect the muon distribution from pion decay. Figure 3.46 shows the projected pion stopping distribution that has been calculated in [69], whereby a novel physics model based on a low-energy parametrization of pion generation has been employed. Results show that an increased surface muon yield towards the side to which the proton beam is shifted can be expected. In πE5 there is no permanent beam monitoring tool up to now but the NE102 scintillator pill XY-scanner system can be used to that purpose. On the opposite side of TgE a positron counter at the junction between the secondary μE4 beam line and the coupled tertiary Low Energy Muon (LEM) [107] beam line counts decay positrons that are proportional to the muon beam intensity that reaches the LEM moderator. This provides a continuous but relative measure of the muon beam intensity on the opposite side to πE5. It is only relative since the rate depends not only on the phase space of the generated muons but also on the magnet tune in the μE4 beam line, the high-voltage and threshold of the positron counter used. After an initial setup period these settings usually stay rather constant throughout the run. Therefore the rates can be used to provide information on the proton beam position on TgE.

Shifting the proton beam across the production target by means of the preceeding dipole magnets is called an "AHPOS scan". The AHPOS scan can be used to determine the correct proton beam centring on the production target or to check the target state by determining the extent of the flat region in a beam loss plot[28]. The centring of the
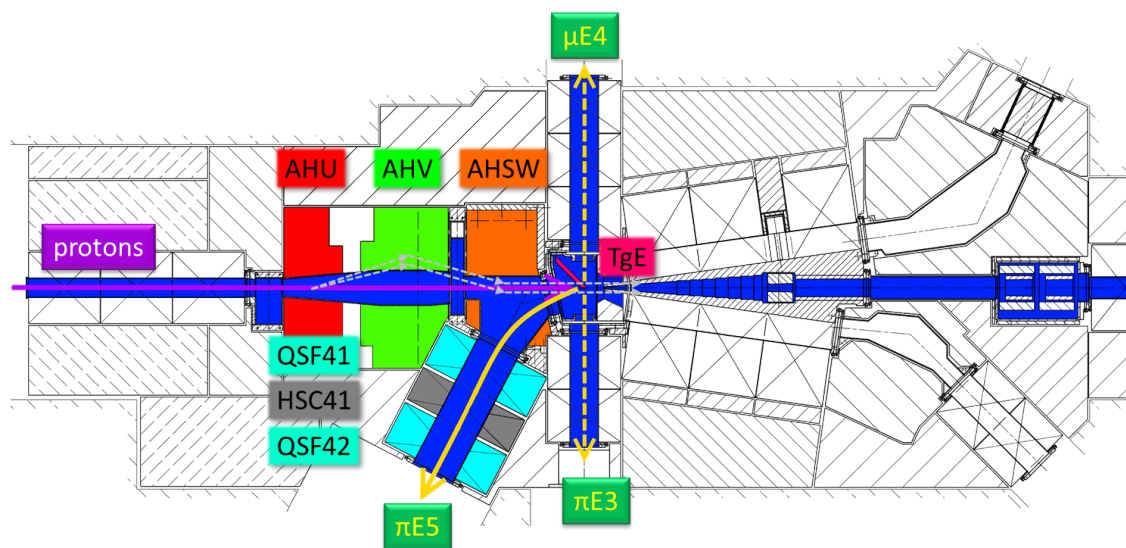
Figure 3.45.: *The AHPOS scan is done with the dipole magnets AHU and AHV which allow for a horizontal shift of the proton beam across the production target. The central orbit is schematically shown with dashed gray arrows. The field strengths are constrained by the need to compensate for the deflection caused by the AHSW extraction magnet for the $\pi E5$ beam line, while allowing a horizontal scan of the proton beam across TgE.*
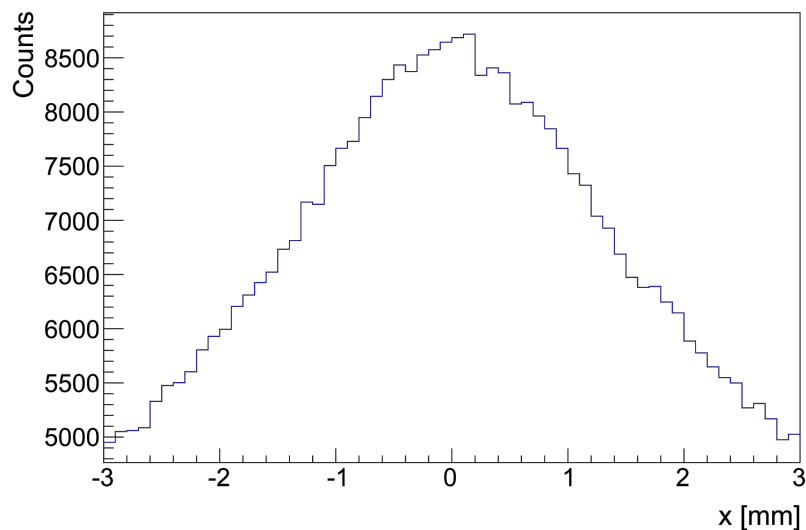
Figure 3.46.: *Shown is the horizontal pion stop distribution integrated along the target length for an incoming centred proton beam. Plot taken from [69].*

proton beam on TgE by use of the LEM counter is achieved by determining the magnet settings that give the average of the minimum and the maximum LEM rate. Since there is no active feedback on the proton beam line magnets, the proton beam can "drift" over time whereby the LEM rate depends approximately linear on the proton beam position on TgE, which enables the control room crew to manually correct the proton beam centring if required. Centring of the proton beam on TgE is usually done at the beginning of each run period as was the case on the 17$^{\text{th}}$ May, when both LEMs and πE5 measurements were undertaken simultaneously. These measurements also showed that the muon rate in πE5 depends $\sim$linearly on the proton beam position on the production target. The rates that were measured in both beam lines are shown in figure 3.47, whereby a LEM rate vs. proton beam position calibration from a former AHPOS scan was applied and both data sets are normalized to the maximum rate. The proton beam centring position was determined to
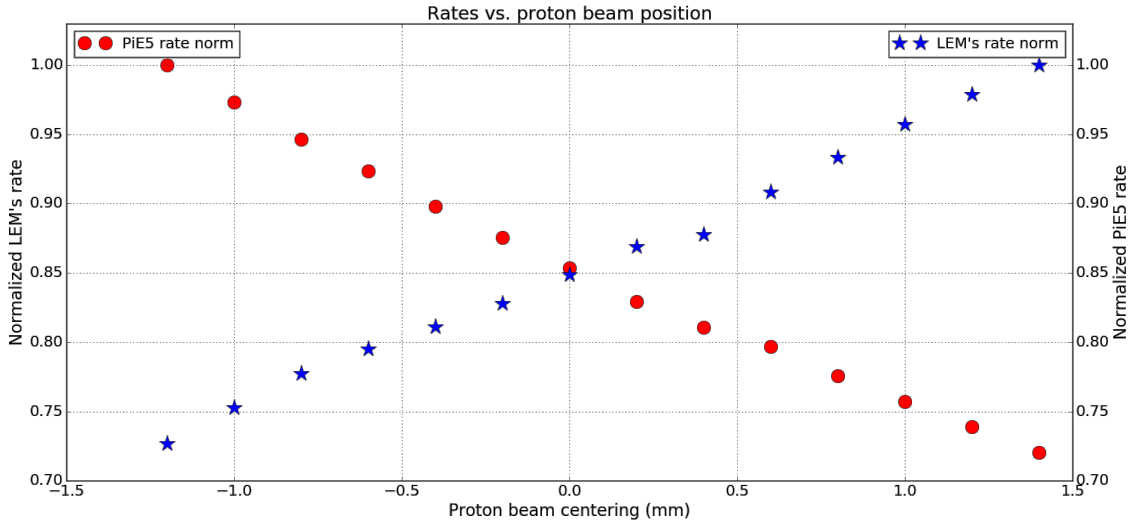
Figure 3.47.: *The rates in the πE5 (scintillator pill) and μE4 (positron counter) beam lines are plotted versus the proton beam impact position on the muon production target. The position is derived from a former LEMs rate calibration. The rate dependence is approximately linear on both sides as implied by figure 3.46.*

correspond to a LEM rate of $174\frac{kcounts}{sec}$, whereby all the quoted LEM rates in this text are already normalized by the MHC4 proton current monitor.

After the beam interruption (11$^{\text{th}}$ June - 20$^{\text{th}}$ June) the proton beam centring on TgE had to be repeated on the 23$^{\text{rd}}$ of June due to a different magnet setting US of TgE. The AHPOS scan was stopped at different proton beam displacements for a few minutes in order to provide enough time to capture images with the scintillation target setup, including the outermost extrema. Background frames were captured right before and after this procedure. For the evaluation of the beam intensities the summed ADC levels of the background frames are scaled for subtraction as described in subsection 3.5.2 and subtracted from the beam images. The residual "pure" signal is then normalized to its associated average proton current $\bar{I}_{p^+}$. Different sources of uncertainty are discussed and the according equation and uncertainty propagation shown in appendix subsection A. During this long AHPOS scan the proton beam was not as stable as during normal operation. The beam picture shown in 3.43 was excluded due to its low intensity and a second frame

(2016-06-23-16-18-46) was excluded from evaluation due to a complete proton beam loss during the exposure time. The remaining associated average proton currents range from $\bar{I}_{p^+} = 1.41\ mA$ to $\bar{I}_{p^+} = 2.15\ mA$. The approximate linear behaviour that was observed for the pill measurement on the centreline after Triplet II was confirmed for the full beam spot on the target, as measured with the scintillation target setup at COBRA centre - see figure 3.48. The new proton beam centre position corresponds to a LEM rate of $168\frac{kcounts}{sec}$. The
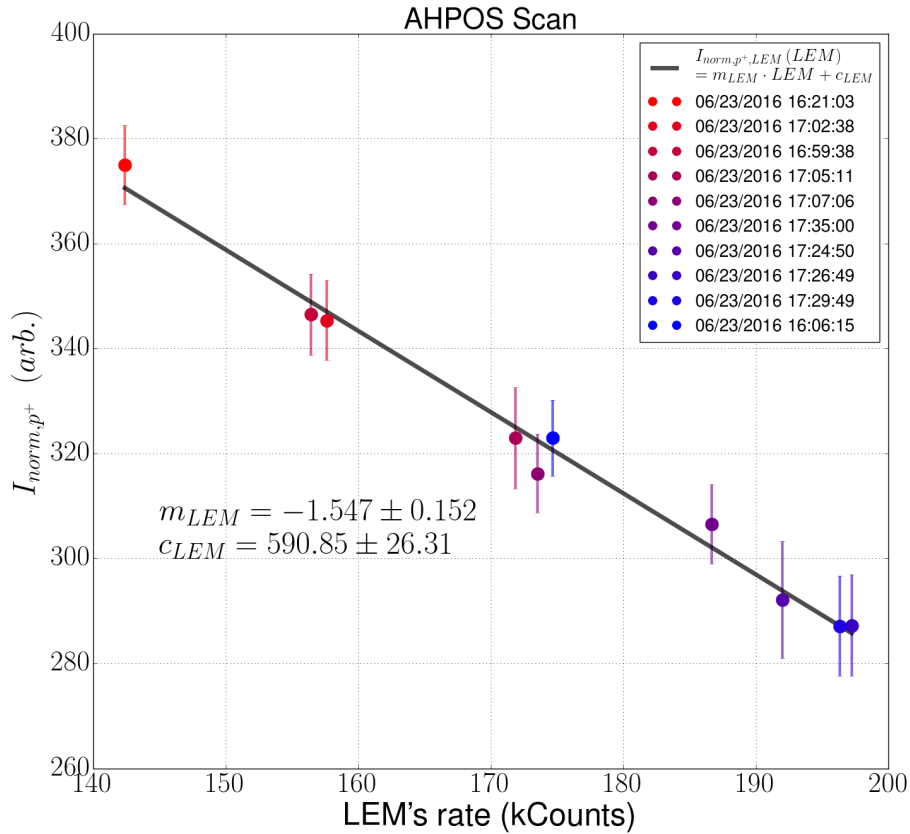
Figure 3.48.: *Scintillation target summed and normalized beam picture intensities plotted against the LEMs positron rate. The points are shown with the individual time stamps to illustrate, on the one hand, the time needed for this difficult measurement and on the other hand, to exclude a systematic time dependence. The reduced χ^2 is $\frac{\chi^2}{d.o.f.} = 0.21$.*

normalized intensities of both, the pill measurement and the scintillation target, are shown in figure 3.49 drawn against the LEM rate. The pill data indicates a rate dependence of $\sim \frac{0.51\%}{LEMSkcount}$ and the scintillator data yields $\sim \frac{0.41\%}{LEMSkcount}$ with respect to the maximum
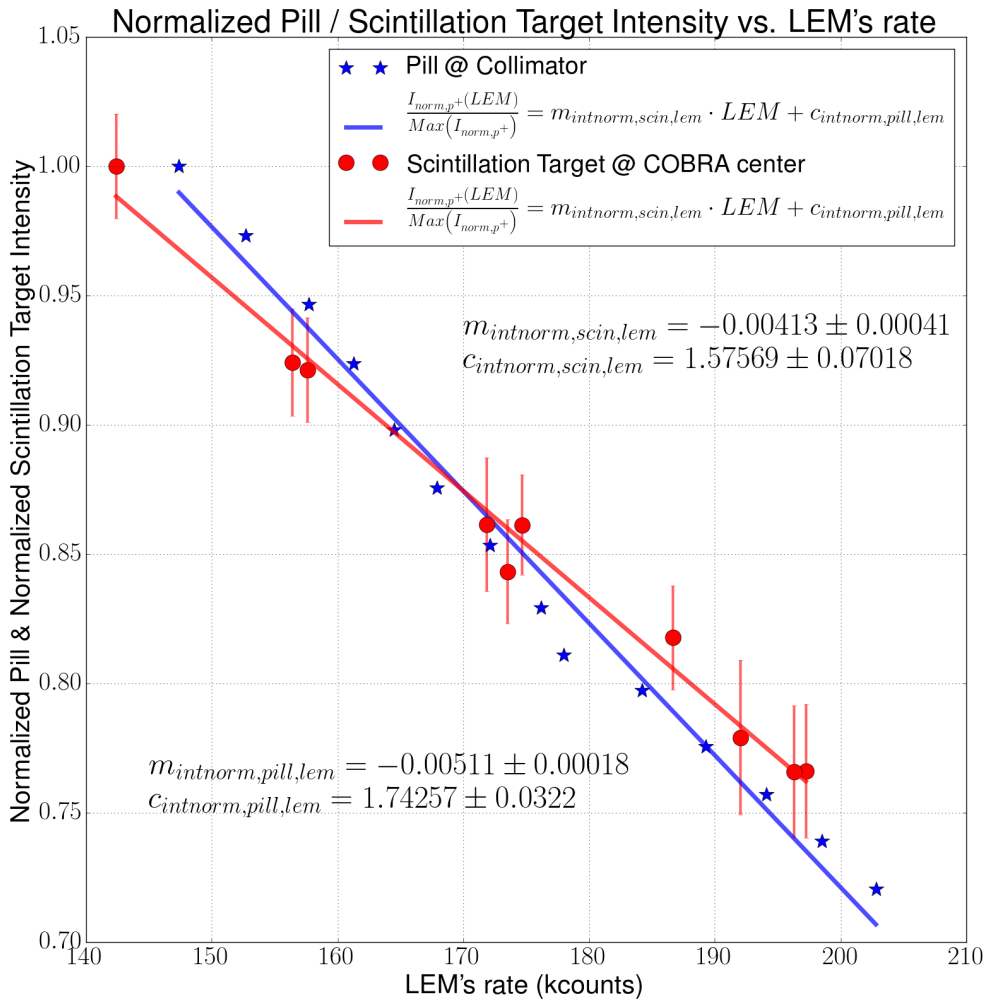
Figure 3.49.: *Comparative plot of normalized beam intensities versus LEM rate. The measurements were done with the scintillation target at COBRA centre and on another day with the scintillator pill on the beam axis just DS the intermediate collimator system. Normalized by their maximum values both graphs show a linear behaviour whereby the slope of the pill measurement is steeper.*

values in both beamlines. The difference in gradient obtained between using the pil or the scintillation target lead to a small difference of a few percent at the extremities. This can be understood by the fact that the the position of the two detectors is very different and subject to a non-unity transmission factor. Furthermore there is a big difference in beam-spot coverage between the two measurements, full coverage in the case of the scintillation target and only $\sim$3 mm^2 in the pill case.

The linear fit to the data points derived from the scintillation target serves in section 3.5.8 as a further normalization for the beam picture intensities. Finally with a normalizing measurement of the absolute muon rate using an APD raster scan (see figure 3.41), the actual muon rate during the run is completely determined by the proton current I_{p+} and the actual LEM rate. However any AHPOS scan changes must be taken into account.

3.5.4.1. Beam spot shift on the stopping target

Surface muons at generation are non-uniformly distributed along the length of the production target. The properties of a backward extracted muon beam that also views the side of the target, as in the case of πE5 (see figure 3.45) therefore depends on the lateral shift of the proton beam on the production target. This spatial shift of the muon source is associated with a displaced beam centroid and a minor change of the beam distribution at extraction, which is then further propagated down the beam line. The size as well as the sign of the displacement changes during propagation through the individual elements of πE5.

As this effect is small and requires a simultaneous measurement during a so-called AHPOS scan it has not been measured before in any of the secondary beam lines at PSI. The scintillation target data collected in parallel to the AHPOS scan on the 23$^{\text{rd}}$ June allowed this effect to be quantified for the first time in the MEG beam line. The profiles have been evaluated in the same way as described in subsection 3.5.3. Figure 3.50 shows an overview from 14:30 - 20:30 on the 23$^{\text{rd}}$ June, the beam size and centroid of the muon beam on the target, together with the proton beam and the normalized LEM rate share the same time axis. A clear and almost linear correlation between the LEM rate, reflecting the proton beam position on TgE and the position of the muon beam on the MEG target can be seen. Figure 3.51 shows the horizontal shift of the muon beam across the stopping target plotted against the LEM rate. A linear Fit yields a horizontal muon beam spot displacement of 0.014 mm per kCounts that are measured in the LEM positron counter. Due to the 15° slanting angle of the stopping target this corressponds to a 0.054 mm/kCounts shift in the axial direction on the target. An intensity dependence of $\bar{x}$, that could e.g. be introduced by a non-uniform linearity of the CCD pixels, can be excluded, as demonstrated in figure 3.52. This shows the central position $\bar{x}$ of the stopped muons plotted against the summed intensity of all pixels after background subtraction and without scaling by the average proton beam $\bar{I}_{p+}$, no correlation is seen. Temperature effects can also be excluded as a dominating effect by the small temperature variation during the scan and the fact that the data points were acquired in a non-regular order as can be seen in the legend of figure 3.48, which also excludes a time dependence.

The influence of a proton beam shift on the vertical beam centroid $\bar{y}$ and the beam widths $\sigma_{x/y}$ is not as clear as in the horizontal case, whereas the variation of the beam widths σ_x and σ_y appear small compared to the scattering of the data, which can partially attributed to the unstable beam conditions. The vertical mean $\bar{y}$ shows a monotonous increase with LEM rate apart from 2 frames at $\sim$142 kCounts and at 174 kCounts, which were both taken before the beam interruption during the AHPOS scan. Figure 3.53 illustrates the dependence of the remaining beam profile parameters on the proton beam centring.
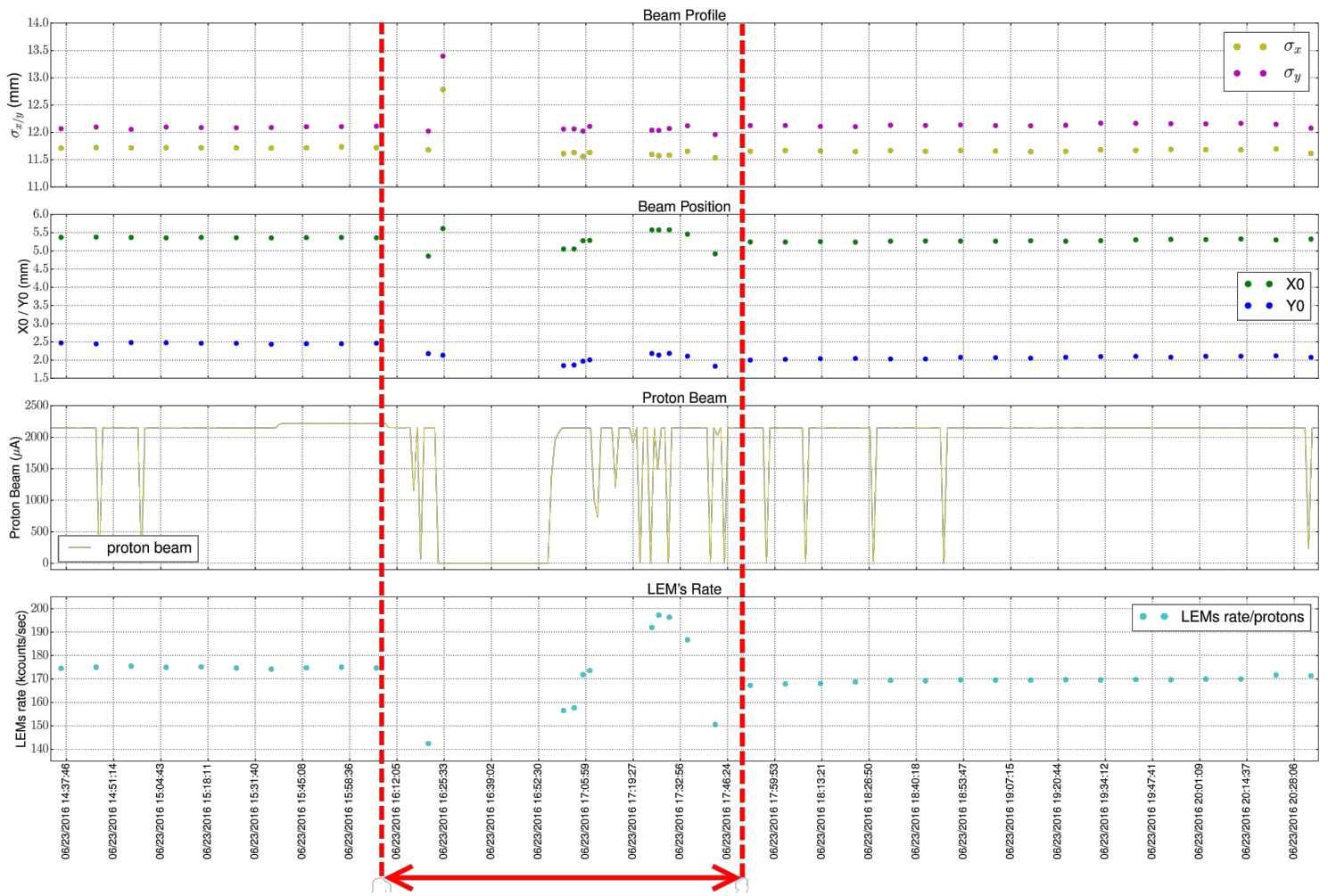
Figure 3.50.: *Shown are the beam profile parameters, proton beam current and the normalized LEM rate before, during and after the AHPOS scan (outlined with dashed red lines). The second point during the scan was captured when the proton beam went down after ~2% of the exposure time, for which reason this point is not used for the further analysis.*
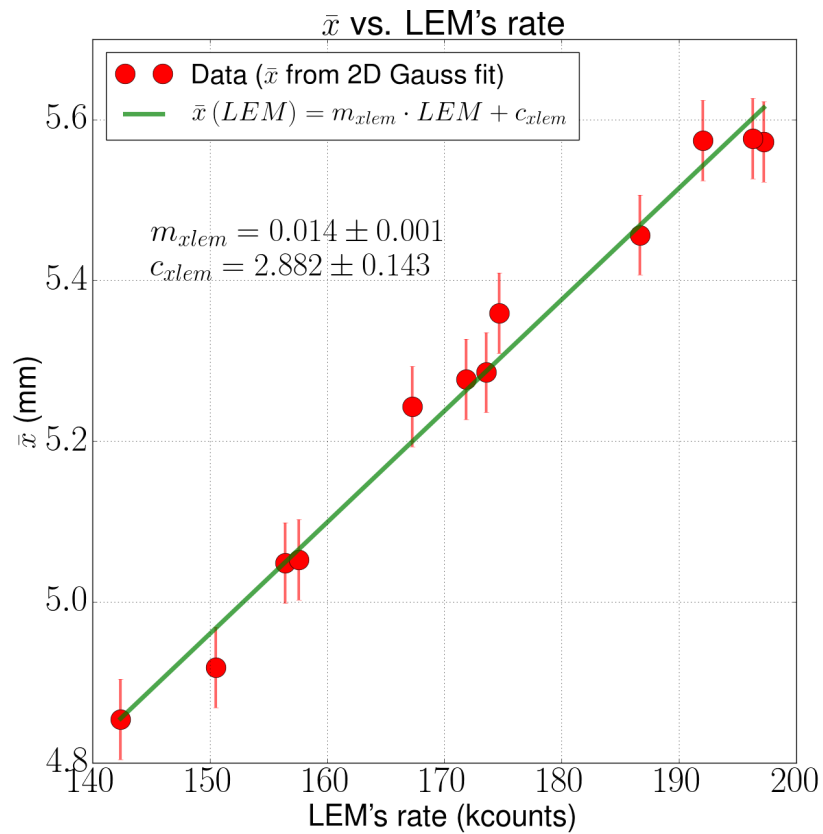
Figure 3.51.: *Shown is the relationship between the centroid of the muon beam Gauss fit result from the scintillation target and the normalized $\frac{LEM}{I_{p^+}}$ rate which is a linearly measure of the proton beam centring on TgE. The reduced χ^2 is $\frac{\chi^2}{d.o.f.} = 0.36$.*
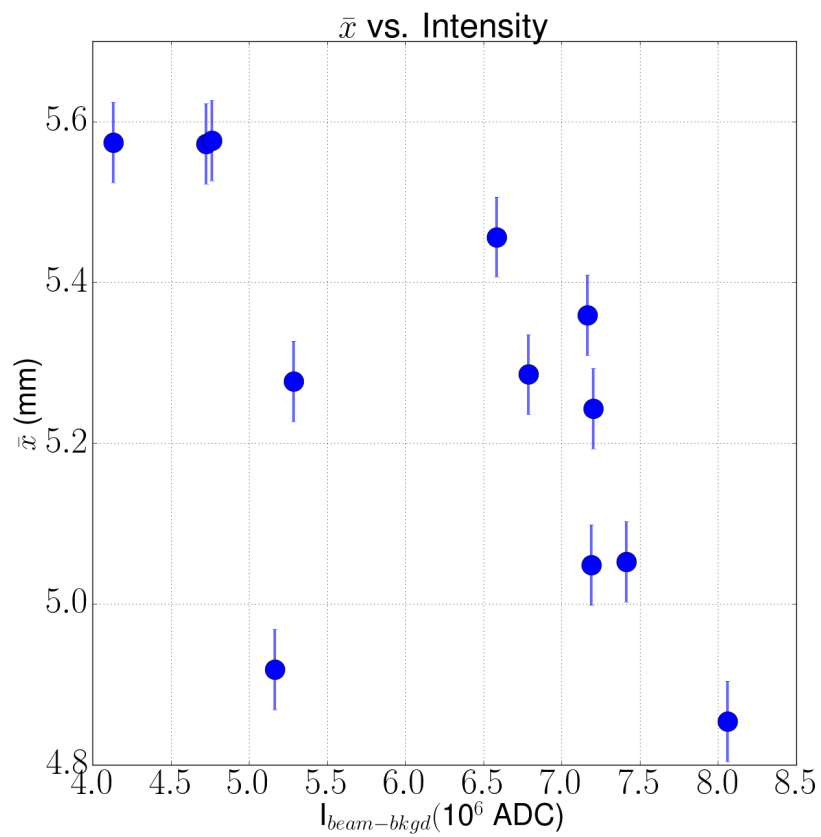
Figure 3.52.: *Shown is the horizontal centre of the 2D Gauss Fit X0 plotted against the summed pixel intensity after background subtraction, no correlation is seen.*
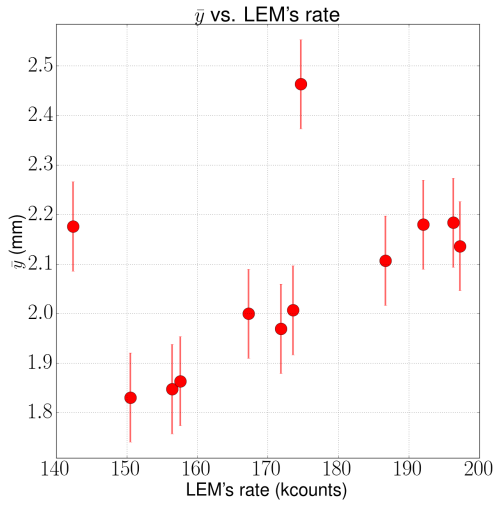
(a) y_0 vs. LEM
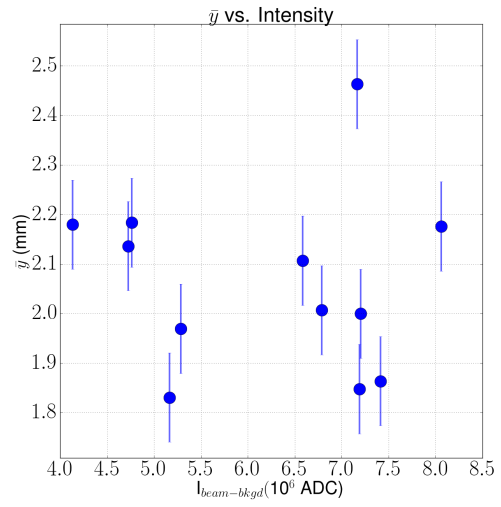
(b) y_0 vs. Int
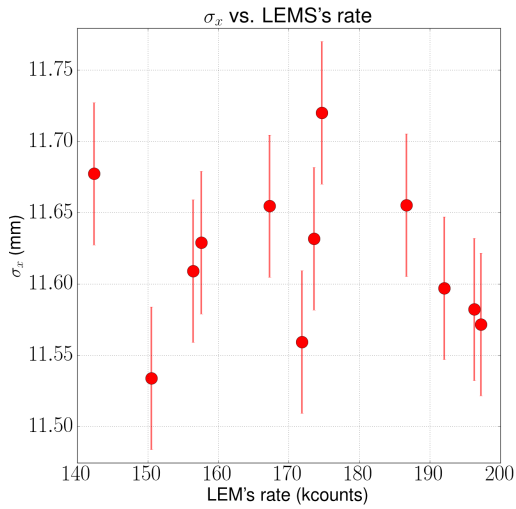
(c) σ_x vs. LEM
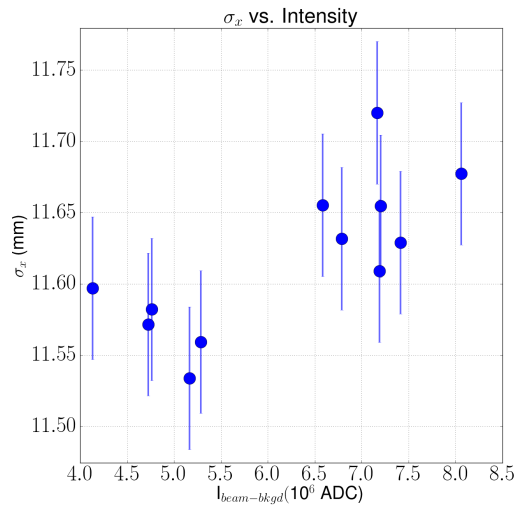
(d) σ_x vs. Int
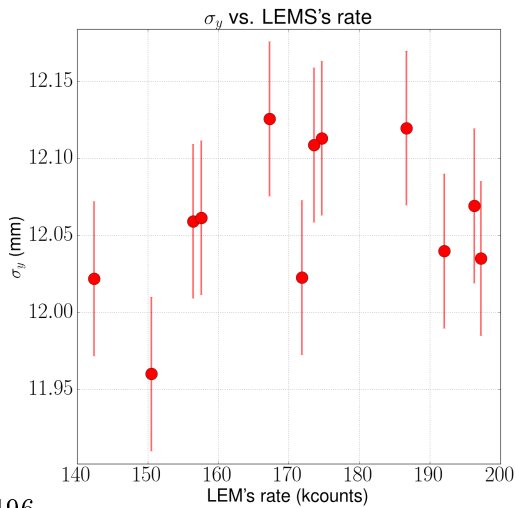
(e) σ_y vs. LEM
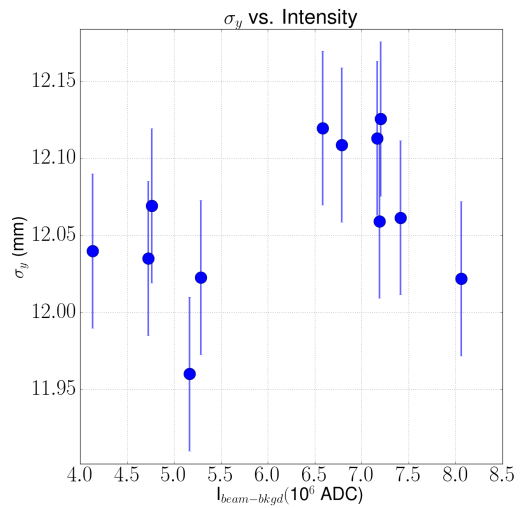
(f) σ_y vs. Int

Figure 3.53.: *Beam Profile parameters vs. LEM positron counter rate and vs. background subtracted image intensity*

3.5.5. Conclusion from AHPOS scan

Images of the scintillation target were captured in parallel with a planned AHPOS scan on the 23$^{\text{rd}}$ June 2016. The duration of the scan was extended to allow image capturing with a normal exposure time at distinct lateral proton beam shifts on the muon production target, covering the full range of $\sim \pm 1.2$ mm. In accordance with a previous measurement using the scintillator pill, the scintillation target setup confirmed the linear dependence of the muon rate on the proton beam centring for the full beam spot.

A significant change in the beam parameters could be demonstrated from the evaluation of frames that were captured before and after the scan compared to those during the scan (figure 3.50). Furthermore it was shown for the first time at the PSI secondary beam lines, that not only the intensity, but also the muon beam centroid depends on the proton beam centring on TgE. The effect amounts to a ~ 0.54 mm shift in the axial direction and ~ 0.14 mm laterally for an assumed variation of 10 kCounts in LEM rate during a full MEG run. False effects mimicking such changes to the beam intensity and the profiles, associated with temperature, time and absolute beam intensity could be ruled out as dominating by comparison and the continuous temperature monitoring using the MEG slow control system.

The measurements strongly demonstrate the high precision that can be achieved by the scintillation target setup as well as providing useful information on the beam dynamics for MEG II and for the rest of the πE5 users community. A full simulation of πE5 as described in section 2.4.3.1 requires the reproduction of such effects for validation. From the experimental side the LEM rate had been the basis for a continous monitoring of the proton beam centre for the full run period. However, the rates are subject to several external influences such as from the magnet tune or the positron detector operation itself. The scintillation target setup can provide an additional independent measure of the proton beam centring on TgE in the future, as it is sensitive not only to the intensity but also to the muon beam position.

In order to quantify the dependence of $\bar{y}$, σ_x and σ_y on the proton beam centring further data with an improved setup is required in the future.

3.5.6. Long-term Monitoring

The use of a scintillation target for MEG II depends on its capabilities for monitoring the muon beam over a full run period. This requires the characterization of the achievable precision of this method and the ease to acquire useful information on specific beam-related aspects during such a measuring period.

All beam images captured during the 2016 Pre-Engineering run were analyzed as described in section 3.5.3 to extract the profile information and a subset has already been shown in figure 3.50. The background frames and calibration pictures are arranged in intervals to ensure mechanically optical stable conditions for all associated beam images. Figure 3.54 illustrates the profile widths and centroid of all 1122 beam images that were recorded parallel to the TC run, together with additional information on the calibration periods, that use a common perspective transformation matrix, and LEM rate, that both directly affect the beam profile analysis. The proton current history and general information on the test beam period complement the comprehensive overview. The key-observations following from the combined information shown in figure 3.54 are listed below:

- Fluctuations at the beginning:
  - The beam profile parameters $\bar{x}$, $\bar{y}$, σ_x and σ_y show large variations at the beginning of the test beam, which is due to falsely determined beam parameters caused by a residual light leak. This is reflected in the daylight cycle where the fluctuation directions agree with figure 3.33(b). During the night the profile parameters stay almost constant and the fluctuations are immediately stopped as soon as the light leak at the separator was closed.

- Discontinuities in the beam centroid:
  - Although most adjacent profile parameter data points show only minor variations jumps of $\bar{y}$ and to a minor extend also $\bar{x}$ occur coincident at distinct times. These jumps of the centroid are caused by different sets of coefficients for the perspective reconstruction. The coherent intervals for which a certain set of transformation coefficients is valid are marked with dashed blue lines.

- Drift of $\bar{y}$ with a daily period:
  - Shifts of $\bar{y}$ on the order of few 100 μm can be observed with a daily period. This is associated with the spatial non-uniform temperature scaling of the background intensity levels as can be seen in figure 3.55.

- Long-term drift of $\bar{x}$:
  - In agreement with figure 3.51 $\bar{x}$ follows the overall trend of the LEM rate, whereby a jump is observed on 23rd June when the proton beam line upstream of TgE was tuned and a new proton beam centring was determined during the AHPOS scan.

- Overall increase of profile width:
  - An overall increase of the beam widths σ_x σ_y can be observed, which flattens out towards the end of the observed period. Radiation damage yields a natural explanation for the broadening of the beam profile widths σ_x and σ_y as a result of reduced scintillation light output in the centre of the distribution, where the expected degradation is most significant. This leads to an artificial broadening
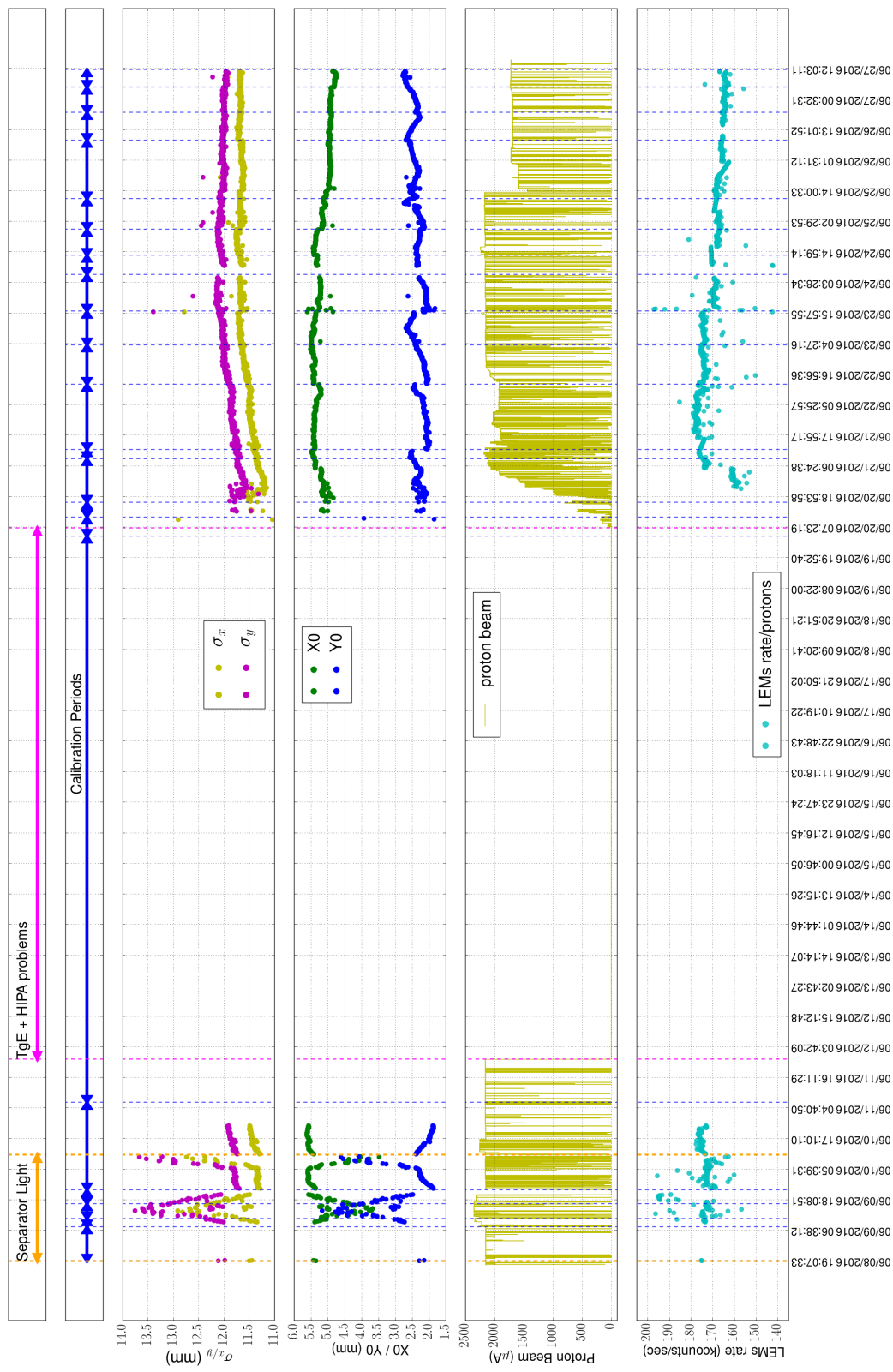
Figure 3.54:: *Beam monitoring during the TC Run period. The centroid $\bar{x}/\bar{y}$ as well as the beam widths σ_x/σ_y suffer significantly from residual light until the 10th June 11:15 a.m. Discontinuities at the junction of adjacent calibration periods are the result of redefined perspective transformations. Apart from that, the centre of the y-direction shows a periodical fluctuation of a few 100 nm due to temperature inhomogeneities of the CCD*

Table 3.7.: *Shown are the Mean, RMS and the maximum deviation from the mean of the beam profile parameters corresponding to the evaluation of those images in the time interval from 25th June 11:03:48 until 26th June 8:40:28.*

	$\bar{x}$ (mm)	$\bar{y}$ (mm)	σ_x (mm)	σ_y (mm)
Mean	4.96	2.45	11.65	12.02
RMS	0.05	0.09	0.05	0.05
Max($|\Delta_{val,mean}|$)	0.16	0.23	0.43	0.39

of the fitted widths. This explanation is briefly investigated and confirmed in subsubsection 3.5.6.1 by applying a spatial cut and fitting only the tails of the distribution in the images.

- Achievable precision:

  - Despite the observed systematic effects associated with temperature, proton beam centring and radiation damage the reproducibility of the profile parameters from successive beam images can be determined for bounded periods. The mean, RMS and the maximum deviation from the mean of the beam profile widths and centroid for the 128 image frames in the time interval from 25th June 11:03:48 until 26th June 8:40:28 are listed in table 3.7. These values represent a good estimate of the high precision that is achievable with an improved setup, calbrations and algorithms that compensate for the influence of radiation damage - envisaged improvements are listed at the end of this chapter.
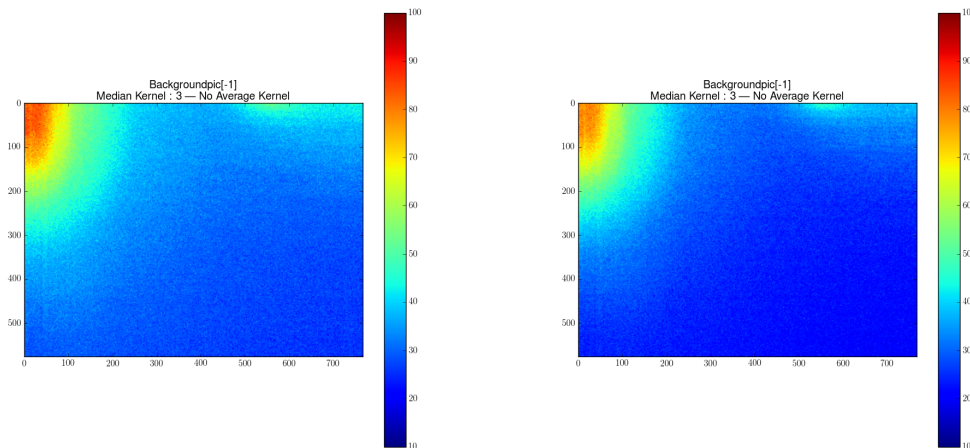
Figure 3.55.: *Shown is the effect of the temperature on the background image, the (left) background frame captured on the 22nd June at 19:35:23 at **41.9 °C**, (right) background frame captured on the next day at 10:46:46 at **39.3 °C**.*

3.5.6.1. Profile reconstruction based on distribution tails

The central region of the scintillation target is exposed to the highest rates and therefore experiences the strongest degradation in LY due to radiation damage. Therefore the tails of the LY-distribution appear relatively enhanced, which causes an artificial broadening of the profile widths derived from equation 3.14. This is confirmed in figure 3.56 which shows an evaluation of the 2D Gauss fit on all beam images but with an additional cut that excludes the innermost 12 mm radius of the distribution. Although the profiles are affected
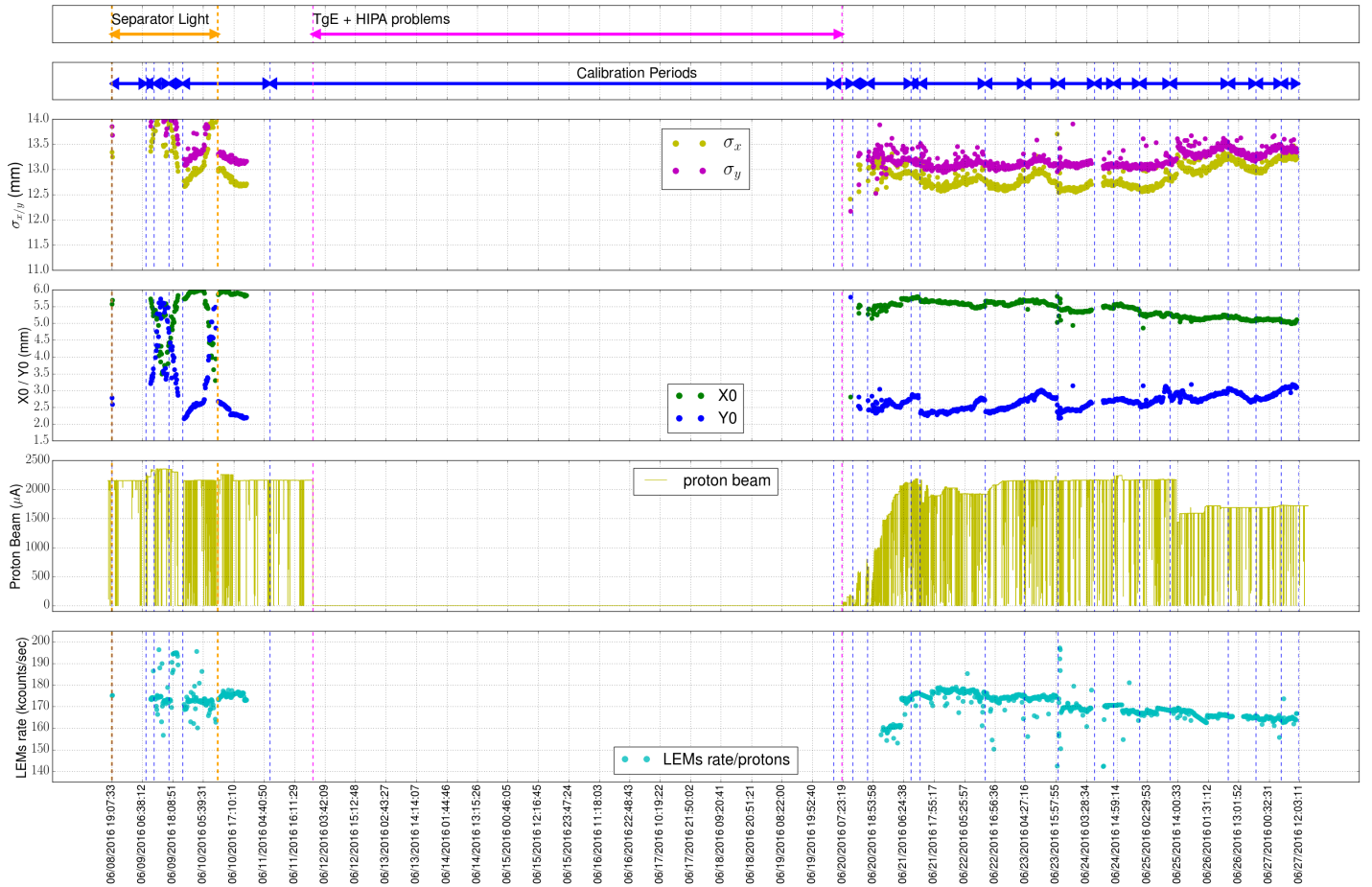
Figure 3.56.: *Beam monitoring during the TC Run period. Beam size and position are taken from 2D Gauss Fit, whereby an additional cut excludes all pixels within a 12 mm radius around (x=5.5/y=1.8). The trend of the beam profiles during this period is constant although the profile widths show higher values and are more affected by temperature fluctuations as in figure 3.54.*

more by the camera temperature dependence (see figure 3.55) the overall broadening of the beam widths during this period is supressed. The temperature induced fluctuations in this case affect both the fitted beam centroid and the σs, which also are strongly affected. In addition the deviations from a pure Gaussian distribution cause the beam profiles to show larger fit results $\sigma_{x,y}$ compared to figure 3.54 already right from the beginning.
The reduction of the proton beam from $\sim$2.2 mA to $\sim$1.6 mA on the 25th June leads

to a further increase of the profile width, which can be explained by the more dominant influence of the broadening due to temperature dependent dark current.

3.5.7. Conclusions and perspectives for long-term use of the scintillation target

The beam monitoring data derived from the scintillation target over the full period, parallel to the TC run, illustrates the excellent reproducibility of successive frames. The RMS and maximum deviation from the mean value of σ_x, σ_y, $\bar{x}$ and $\bar{y}$ was determined for a subset of the images corresponding to $\sim$1 day of data-taking. According to table 3.7 a precision on the order of a few tens of microns can be achieved which is competitive with the beam scanner system, which is the standard beam measurement device implemented by MEG and now used at the PSI secondary beam lines.

These numbers serve as an estimate on the achievable precision of the final scintillation target setup, which requires further improvements to master the several systematic effects that were observed during the test beam:

- The mechanical stability of the setup required to redetermine the perspective transformation, which caused distinct jumps between adjacent "calibration periods"
- The temperature dependence of the used camera affected the profile parameter evaluation and was a dominant limiting factor of the overall precision
- Radiation damage yields a natural explanation for the observed broadening of the beam profiles, as a result of a strong LY-degradation at the beam centre. The intensity degradation due to radiation damage is quantitatively analyzed and discussed in the next section.

The results presented in this section confirm the importance of the scintillation target for monitoring the muon beam properties during a longer run period. A variety of information can be accessed by correlating the image data with available data from different sources. There is still more information contained that has not been investigated in detail, as for example the behaviour of the profile widths in figure 3.54 when the proton beam was reduced on the 25$^{\text{th}}$ June. Further data-taking with an improved setup and improved analysis methods promise important results in the future that on the one hand provide a better understanding of the muon beam and its correlations with other observed quantities and on the other hand help to characterize and understand the scintillation target monitoring setup/technique in more detail. In conclusion the scintillation target monitoring system has demonstrated the important usage of such a system for MEG II, whereby beam profile characteristics and beam centring information on the target can directly be used to realign the beam during data-taking, should an offset occur due to e.g. a proton beam shift on the production TgE. The ultimate implementation of such a target in MEG II will depend on further important tests of radiation induced changes which will be adressed in the next section.

3.5.8. Radiation Damage

In order to quantify muon induced radiation damage effects in the scintillation target, during the 2016 Pre-Engineering Run, the following are required to assess the LY variation with increasing muon radiation dose.

(a) the net LY due to muons

(b) the calibration ratio of muons/I_{p+} (proton current) and the actual muon rate

(c) the total number of accumulated muons at any given time

(d) mean energy deposit by a target muon.

The first three points have been adressed in the previous sections. The full evaluation scheme is summarized in figure 3.57.

→(a): The net LY (LY) is assumed from background subtracted beam images using the following steps:

- background is assessed from the four nearest background frame intensities within an assigned background period
- these are then scaled according to their temperature, averaged and subtracted from the beam intensity picture
- the resultant beam intensity picture is normalized to the average proton current $\bar{I}_{p+}$ during the exposure
- this is further normalized to the integrated LEM rate during the exposure, using the LEM fit function and procedure outlined in section 3.5.4

→(b): The actual muon rate and the calibration ratio of muons/(proton signal) are assessed from an initial COBRA-centre APD raster scan which measures the total muon spot-rate normalized to the proton current, hence giving the calibration constant of muons in the beam spot per proton signal and a given LEM rate.

→(c): The accumulated number of muons at any time is then assessed by integrating the proton current with applied LEM rate correction factor. The so accumulated number of muons for the radiation damage study test period amounted to ∼5.5·10^{13} μ^+ on target, based on a COBRA centre APD raster scan measurement of 9.16·10^7 μ^+/s at $\bar{I}_{p+}$=2.2 mA and an average LEM count rate ∼178k.

→(d): In order to estimate the radiation dose from the accumulated number of muons in the target, the mean energy deposit per muon is needed. This was determined from a G4BL simulation, in which muons were first tracked through to the target taking into account the full material budget (see section 3.3), though simulating the COBRA magnet as a constant field solenoid rather than a gradient field one. The so obtained momentum distribution and beam parameters were then used to generate a new Gaussian beam of σ_x=σ_y=11.5 mm, yielding a total energy deposit in the PVT of ∼1.7 MeV per muon and daughter particles.

The resultant scintillation target relative LY curve and the accumulated muon dose, together with the chronology of the associated parameters is shown in figure 3.58. The LY degradation is determined by fitting an exponential model (equation 3.1) to the LY curve however, neglecting possible annealing effects due to longer beam breaks in either a He- or
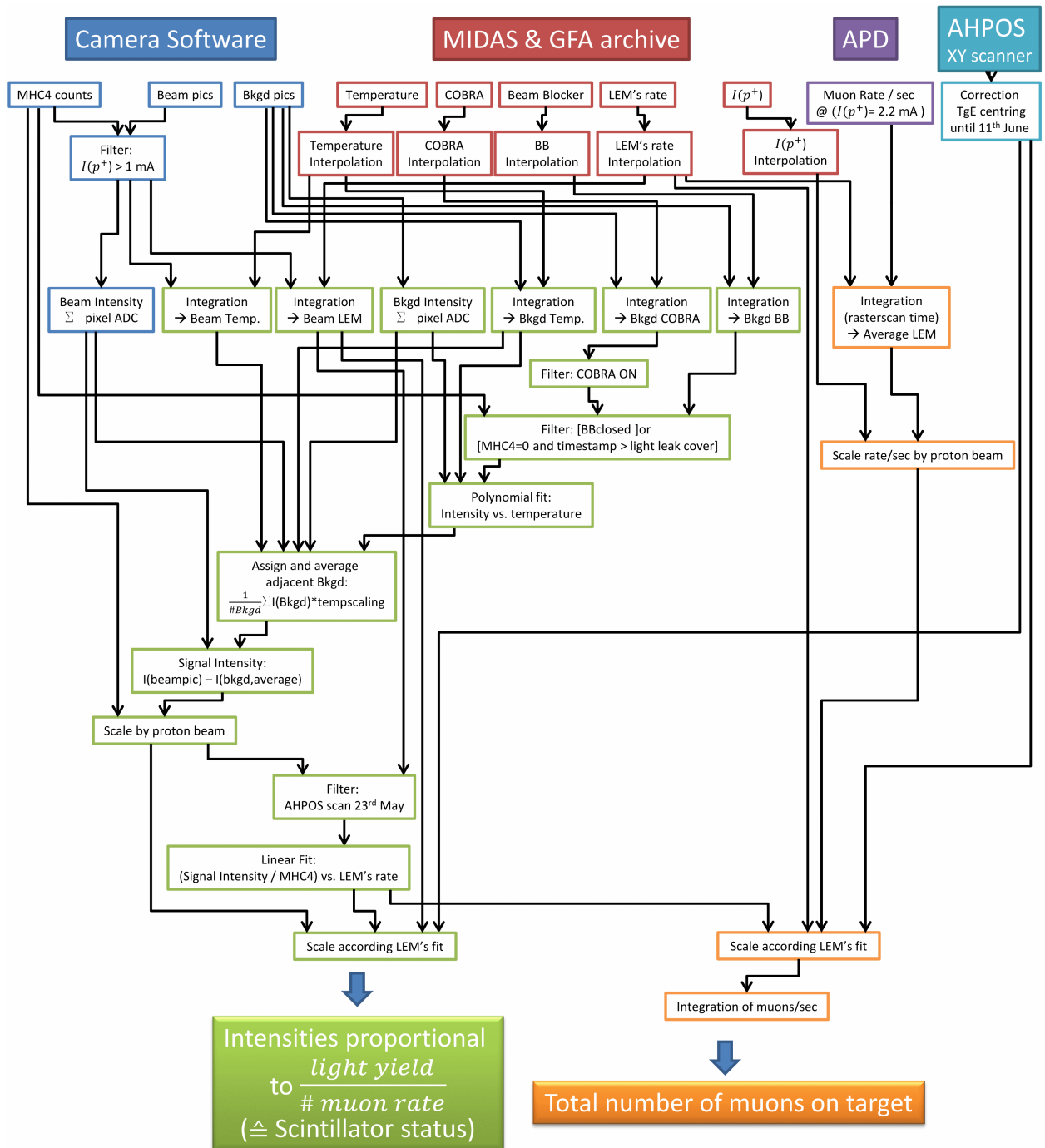
Figure 3.57.: *Shown is a summary of the evaluation scheme that was used in order to determine the residual LY intensities normalized to the number of muons. The individual steps are explained in more detail throughout this chapter.*

Figure 3.58.: *Shows the relative scintillation target LY versus the accumulated number of muons on target and equivalent radiation dose, as well as the MHC4 signal, BB information and the LEM rate.*

O_2-environment (possible effects of O_2 only affects data from 10th July. Furthermore the fitting region excludes LY values obtained during the separator light leak period as well as LY values below a threshold of LY ≤ 0.8 due to a wrong LEM rate readout.

The LY degradation curve for the full beam spot is shown in figure 3.59 giving a decay constant D=$(2.793\pm0.041)\cdot10^{14}$ μ^+. This corresponds to ~ 35 days, at the previously mentioned instantaneous rate, for the LY to drop to $\frac{1}{e}$.

Table 3.8 lists the accumulated number of muons reached for each of the MEG run periods
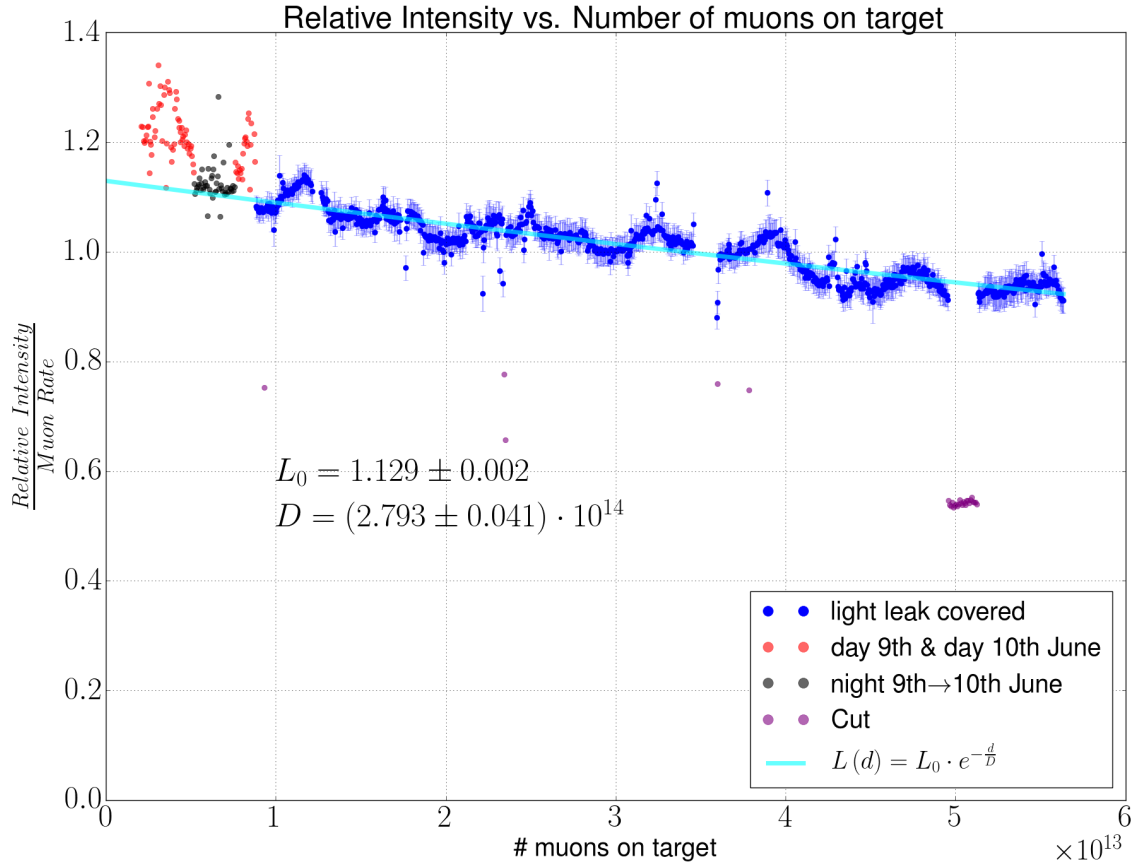
Figure 3.59.: *Shown are the relative beam picture intensities normalized by the proton current and the LEM rate plotted against the sum of all muons on target. The values that were taken under light-tight conditions and that are above the threshold of 0.8 are fitted with an exponential model. The reduced χ^2 is $\frac{\chi^2}{d.o.f.} = 1.11$.*

at an average stopping rate of $3\cdot10^7$ μ^+/s. Extrapolating the maximum number for the 2012 period to an equivalent MEG II run with a planned stopping rate of $7\cdot10^7$ μ^+/s yields:

$$\text{MEG II } \mu^+/\text{Run} \sim 2.32\cdot10^{14} \cdot \frac{7\cdot10^7}{3\cdot10^7} = 5.41\cdot10^{14} \ \mu^+$$

Hence with a full spot decay constant of D=$(2.793\pm0.04)\cdot10^{14}$ μ^+ would lead to a LY value of $\sim 14\%$ at the end of the run. Neglecting any distortions of the reconstructed beam

Table 3.8.: *Statistics from MEG runs 2008-2013. The third column shows the ratio of the number of muons divided by the radiation decay constant D for the full spot.*

MEG run	No. muons on target	$\frac{No.muons}{D}$
2008	$9.5 \cdot 10^{13}$	0.34
2009	$6.1 \cdot 10^{13}$	0.22
2010	$1.12 \cdot 10^{14}$	0.40
2011	$1.85 \cdot 10^{14}$	0.66
2012	$2.32 \cdot 10^{14}$	0.83
2013	$1.63 \cdot 10^{14}$	0.58

profiles, due to radiation damage, the amount of light would still be sufficient for imaging which is confirmed with the beam profile in figure 3.43.

3.5.8.1. Radiation damage and its spatial variation

Since the muon beam profile is Gaussian at the target the radiation damage can be expected to vary across the beam spot. This was confirmed by comparing the LY degradation fit for the innermost 1-σ region of the beam spot and the complete spot as shown in figure 3.59. Applying the same procedure to the selected 1-σ region of the beam images as applied to the full beam images maintains both the relative LEM rate calibration within the uncertainty as well as giving similar results for the temperature scaling. The fit to the 1-σ intensity profiles yields a LY decay constant D=$(2.204\pm0.007)\cdot10^{14}$ μ^+ which is $\sim$21 % smaller than the full beam spot value, as expected. The fit is shown in figure 3.60.

Finally, at the end of the RDC run for which the CCD camera system had to be removed, a final measurement (10th July) was made in order to see the effect of a further $2.8\cdot10^{13}$ μ^+ reaching the target. The effect can be seen on the extended chronology plot of figure 3.61. The beam centroid and the vertical profile width are consistent with the values prior to the RDC run. However, there is a significant jump in the horizontal profile width of $\sim$0.8 mm to smaller values. The most plausible explanation was a horizontal misalignment when remounting the camera system, this was confirmed by comparing target calibration pictures with "LED ON" to e.g. figure 3.35(a), which then showed an image shift. Furthermore, an associated radiation damage explanation would also have to affect the vertical profile. Including these last data-points into the light degradation fit of figure 3.59 shows clearly the mismatch to the previous full image decay constant as shown in figure 3.62. D is modified by less than 2 % and within the uncertainties, showing the validity of the previously quoted D value in figure 3.59. Further possible influences causing a jump in the LY could be:

- A transmission change of the total LY caused by a different viewing angle
- Possible annealing effects caused by the presence of oxygen during the few days extraction of the RDC
- A change in the influence of the COBRA fringe field due to a change in position

A change in the temperature dependence of the associated 10th July background images can also be seen in the plot of figure 3.63.
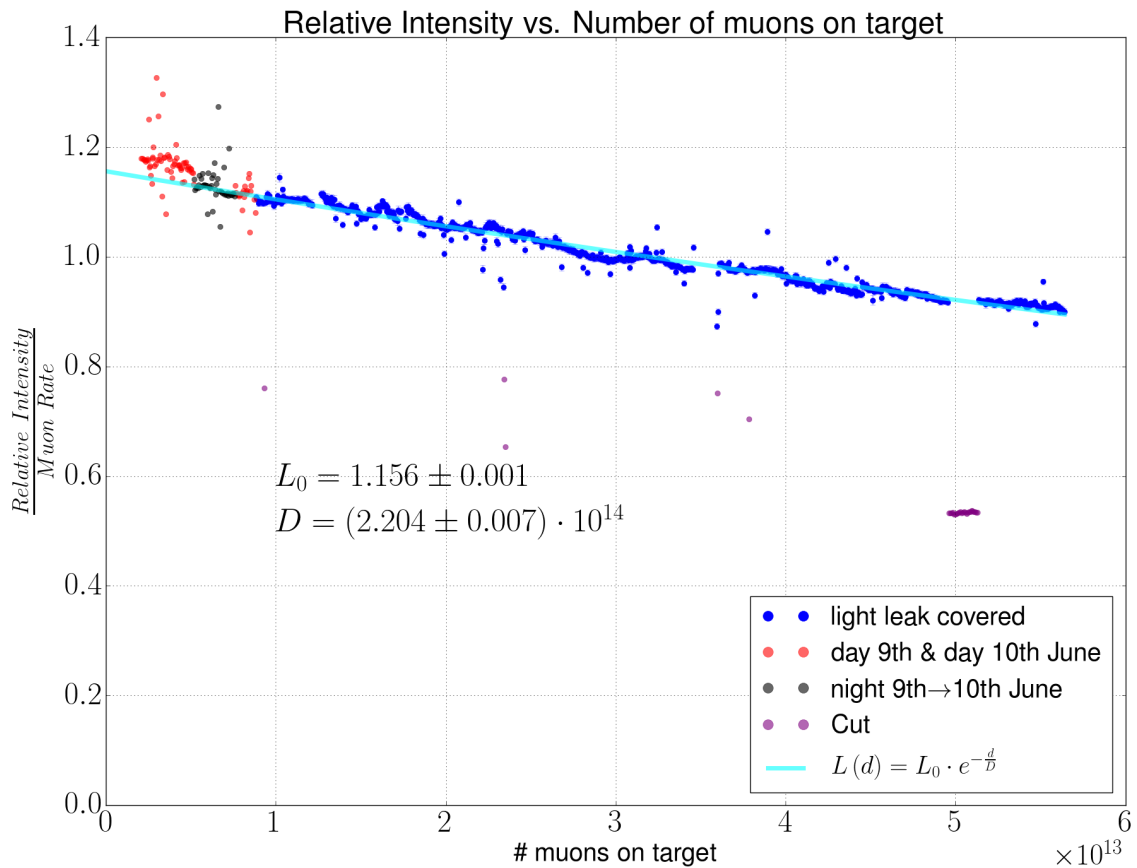
Figure 3.60.: *Shown are the relative beam picture intensities normalized by the proton current and the LEM rate plotted against the sum of all muons on target, after a 1-σ cut has been applied on the transformed image. The values that were taken under light-tight conditions and that are above the threshold at 0.8 are fitted with an exponential model. The reduced χ^2 is $\frac{\chi^2}{d.o.f.} = 4.39$.*
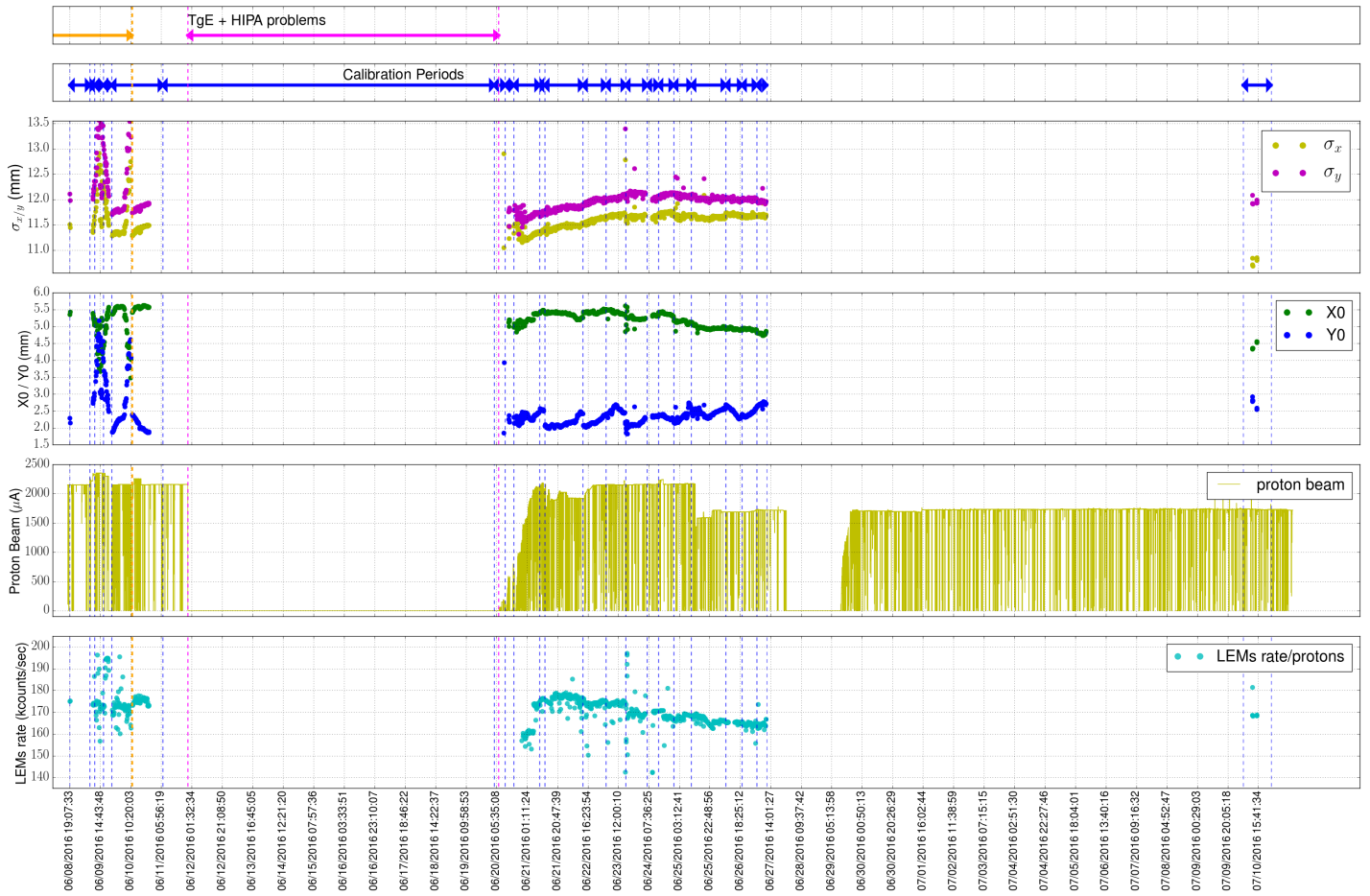
Figure 3.61.: *Shown are the beam profile parameters from figure 3.54 with additional data recorded on the 10th July.*
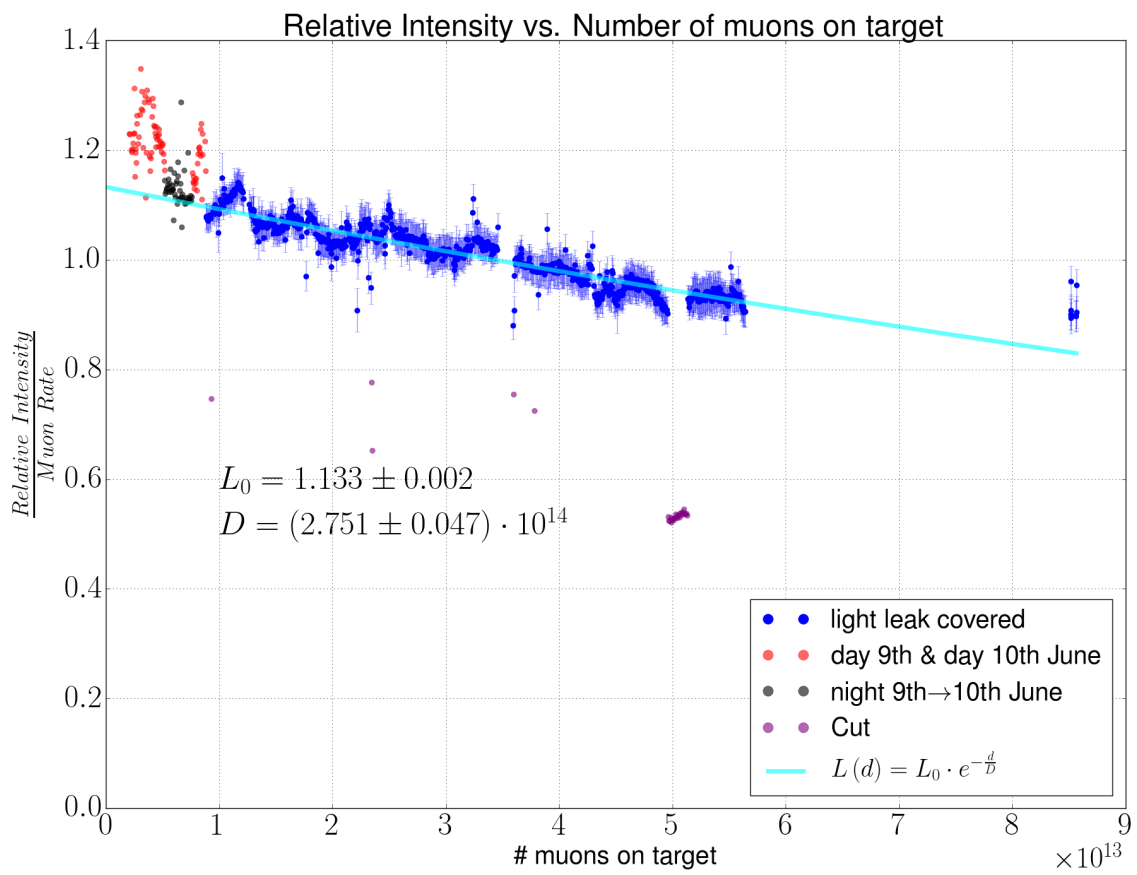
Figure 3.62.: *The light intensities of the full images are processed as for figure 3.59 with the additional data points from the 10th July.*
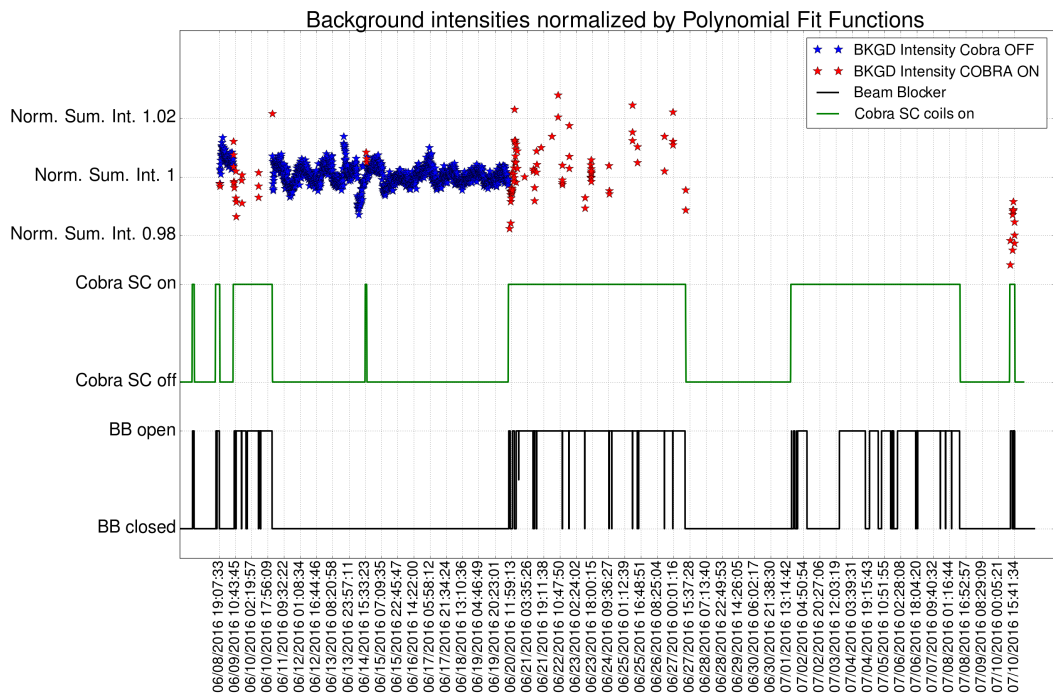
Figure 3.63.: *Shown are the normalized background intensities as in figure 3.39 but including the data from the 10th July. Although fitted and normalized the same way as the previous data the background intensities derived from the 10th July data are clearly overestimated by the fit, which leads to lower values for the normalized intensities.*

3.6. Conclusions & outlook regarding the scintillation target

The scintillation target has been progressively tested in two beam times and the usability confirmed. During the Pre-Engineering Run 2016 a contiuous data-taking provided several thousand images which could be correlated with a diversity of information from various sources. Fitting the profiles with a 2D Gaussian with an offset showed a very high precision could be obtained on the order of a few tens of microns for the centroid $(\bar{x}/\bar{y})$ and the profile widths (σ_x/σ_y) for "short-term" observations. However systematic effects such as radiation damage cause the profile widths to change already within days. The LY degradation that is considered most likely responsible for the broadening of the projected profiles could be determined by taking into account the following aspects. The strong temperature dependence of the background level, which necessiated an appropriate description by means of a 5th-order polynomial; a significant camera dependence on the B-field of COBRA; the influence of both the proton beam current, used for normalizing the background subtracted beam pictures, and the influence of a proton beam shift on TgE causing a change in intensity and a shift on the muon scintillation target, an effect that could be quantitatively measured for the first time.

Taking into account the above effects the LY degradation was fitted with an exponential model as employed by the LHC CMS collaboration for the radiation damage in the modules of the hadron calorimeter endcaps. The decay constant was determined to be D=$(2.793 \pm 0.041) \cdot 10^{14}$ μ^+ for the full image and to D$_{1\sigma}$=$(2.204 \pm 0.007) \cdot 10^{14}$ for a 1-σ region of the beam.

An estimate of the LY at the end of a MEG II data run, based on the maximum length of a MEG data-taking period shows a LY drop to 14 %. However, the camera setup has proven to be sensitive to very low beam intensities at the level of 2 % of the nominal intensity or 50 μA average proton current. Radiation damage occurs mainly at the centre where most muons deposit their energy, which leads to somewhat distorted profiles as could be seen after a few days of irradiation. There are several different ways to solve the problem for a final MEG II solution:

- Successively increase the inner cut region for evaluation and keep the setup as it is. This would mean a loss of the profile width information early during the run but information on the centroid should still be available for a longer period

- Install a stable UV-LED that illuminates the scintillation target e.g. once per day (the LED spectrum must have no overlap with the camera spectrum). This UV picture could be used to determine the accumulated radiation damage and correct each pixel continously throughout the run. Assuming that the beam picture covers a considerable part of the dynamic range of the camera at the beginning of the run, this solution is regarded as a suitable means to recovering the full information for the complete run though with an increasing uncertainty. A stabilized photo-diode [108] that measures the UV LED light could be used for further stabilization of this system. An additional benefit from this method would be an accurate long-term observation of the muon-induced radiation damage in PVT.

- More recent tests of a new system show promising results from the beam monitoring point of view, the very thin CsI(Ti) coated Mylar [66] foils are also regarded as a possible MEG target candidate. However although the CsI layer can be thinned

down to a few microns the high nuclear charge would enhance the multiple scattering of the outgoing positrons. Therefore careful simulation studies are necessary if the collaboration would favour such a solution.

- Another alternative approach is the use of a pure diamond scintillation screen. The working principle has been tested in [109]. Due to the high density the slab would have to be thinned down to only 40 micron. A recent publication [110] has shown that this has been achieved in a size that is sufficient for the use as a MEG target. Simulation studies concerning the use of diamond are envisaged for the near future. A major advantage of the diamond solution would be the high resistance to radiation damage that is known for both the optical as well as for the mechanical properties.

The study and experimental investigations undertaken with a prototype scintillation target have led to a number of issues having been found as well as solutions which would make such a target a viable MEG II target solution. Hence in the case of the PVT solution further improvements and investigations are required. These fall into two main categories: Target and mounting improvements and camera and imaging system improvements.

From the point of view of the target and mounting improvements a major issue was the surface planarity, the original PVT slabs appeared flat and rigid however after mounting warping was observed as can be seen in figure 3.64. This leads directly to distortions of

Figure 3.64.: *The reflections on the target qualitatively show the wavy surface of the scintillator already before installation in COBRA. The scintillator was plane and showed a good mechanical stability before glueing to the Rohacell frame. For a final installation in MEG II the mounting technique of the target has to be improved in order to reach a better planarity which is not only benefitial for the profile reconstruction in a scintillation target but is of utmost importance for the MEG II analysis, independent of the stopping material used.*

the beam profiles and to an angular dependence. This non-planarity is attributed to the mounting method in the scintillator frame which involved spot gluing and is not suitable due to differential expansion. The second aspect concerns the target surface handling as the current target suffers from surface scratches that are clearly visible on the recorded beam profiles. Even though the highest quality surface was ordered, post handling was not optimal. The surface quality can be qualitatively judged by the 3D-plot in figure 3.65. Polishing could be applied to regain a homogeneous clear surface [111] or a homogeneously roughened surface could be applied to also enhance the total LY at $\sim75°$ to the normal of the target surface. The final point concerning the target is the susceptibility to mechanical deformations such as surface crazing or cracking introduced by a dry helium atmosphere or from radiation damage. Unlike the polyethylene target used in MEG, a PVT target
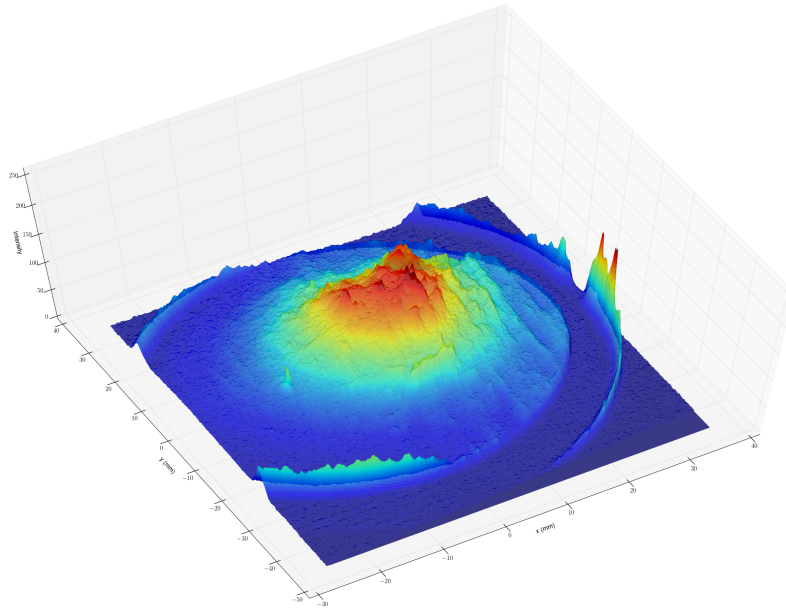
Figure 3.65.: *Shown is a 3D plot of a single beam image captured on the 10th June after background subtraction and application of a minimum window size median filter.*

would have to be replaced each year/measuring period.

The camera aspects to be improved are:

- The possibility of using a tilt-shift lens to optimize the DOF when viewing a 27 cm long inclined object without "stopping down" the lens to have a sharp focus, at the cost of cutting down the light intensity

- A higher resolution camera than the iDS 8-Bit 0.4 Mpixel from which imaging in the horizontal direction of the target benefits most, which is viewed under a shallow angle

- A higher Bit depth camera miminimizes quantization effects especially at low intensities associated with radiation damage

- A cooled camera is mandatory to minimize the thermal noise and the strong temperature dependence of the iDS camera

- Minimum susceptibility to magnetic fields of the order of 1 T

- Have a mechanical shutter to allow background images to be taken without interrupting the beam

- Finally a sturdy fixed camera mounting ensuring a reproducible and fixed viewing angle

With the above outlined improvements the scintillation target can be regarded as a powerful tool that provides valuable information on the muon beam for MEG II. It can also be considered to save beam tuning in MEG II that would then be available for physics data-taking. Already during the Pre-Engineering run 2016 the target proved its worth as an independent tool by confirming that no muon beam reached COBRA centre even though the accelerator had beam. This could later be adressed to a severe misaligned proton beam

in the TgE region by the HIPA control room crew. Furthermore, due to problems with the MEG II gas system the stopping target was unwantedly moved to its parking position which could be seen on pictures with the target LED illumination. The permanent optical monitoring of the beam on target allows an intermediate intervention during data-taking of a beam misalignment caused by the steering of the proton beam on TgE. Despite the positive characteristics of such a target, further irradiations of PVT are required to check the susceptibility to mechanical deformations as this turned out to be a major issue in MEG.

4. Appendices

4.1. IDS camera linearity
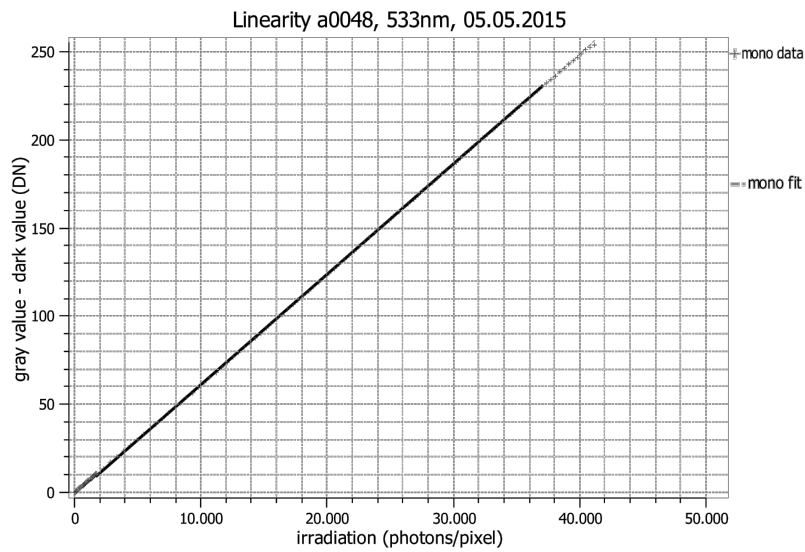
Figure 4.1.: *Shown is the linearity of the iDS camera, that was used for the scintillation target test beams. Approximately 160 photons are needed for an increment of the ADC level by 1. The overall nonlinearity amounts to 0.37 % [103]. The plot is taken from [103]*

4.2. Uncertainties in the Scintillation Target Measurements 2016

A. Uncertainties on the MHC4 normalized beam intensities during the AHPOS scan

The number of muons on the stopping target is mainly determined by the proton current on TgE. In section 3.5.4 further information about the proton beam centring on the production target allows the dependence of the normalized light intensity on the proton beam centring on TgE to be determined for the next steps of the analysis. The intensities that are used to extract the relationship to the LEM rate are given by the summed ADC levels after background subtraction and normalization by their associated average proton currents $\bar{I}_{p^+}$ during the exposure time. The so derived intensities I_{norm,p^+} are given by:

$$I_{norm,p^+} = \frac{I_{frame,beam} - \frac{1}{n}\sum_{n=1}^{4}\left(\frac{I_{fit}(T_{int}(t(frame,beam)))}{I_{fit}(T_{int}(t(frame,bkgd_n)))}\cdot I_{frame,bkgd_n}\right)}{\bar{I}_{p^+}} \qquad (4.1)$$

The individual terms are explained in the text below equation 3.17. Introducing the following abbreviations:

$$I_{fit}\left(T_{int}\left(t\left(frame,beam\right)\right)\right) \mathrel{\widehat{=}} fbeam$$

$$\frac{I_{frame,bkgd_n}}{I_{fit}\left(T_{int}\left(t\left(frame,bkgd_n\right)\right)\right)} \mathrel{\widehat{=}} I_{norm}\left(bkgd_n\right) \qquad \text{(equation 3.16)}$$

shortens equation 4.1 to:

$$I_{norm,p^+} = \frac{I_{frame,beam} - \frac{1}{n}\sum_{n=1}^{4}\left(fbeam\cdot I_{norm}\left(bkgd_n\right)\right)}{\bar{I}_{p^+}} \qquad (4.2)$$

Gaussian error propagation therefore yields:

$$\Delta I_{norm,p^+} = \left(\left(\frac{\partial I_{norm,p^+}}{\partial I_{frame,beam}} \cdot \Delta I_{frame,beam}\right)^2\right.$$
$$+ \left(\frac{\partial I_{norm,p^+}}{\partial fbeam} \cdot \Delta fbeam\right)^2$$
$$+ \left(\frac{\partial I_{norm,p^+}}{\partial \bar{I}_{p^+}} \cdot \Delta \bar{I}_{p^+}\right)^2$$
$$+ \left(\frac{\partial I_{norm,p^+}}{\partial I_{norm}(bkgd_1)} \cdot \Delta I_{norm}(bkgd_1)\right)^2$$
$$+ \left(\frac{\partial I_{norm,p^+}}{\partial I_{norm}(bkgd_2)} \cdot \Delta I_{norm}(bkgd_2)\right)^2$$
$$+ \left(\frac{\partial I_{norm,p^+}}{\partial I_{norm}(bkgd_3)} \cdot \Delta I_{norm}(bkgd_3)\right)^2$$
$$\left. + \left(\frac{\partial I_{norm,p^+}}{\partial I_{norm}(bkgd_4)} \cdot \Delta I_{norm}(bkgd_4)\right)^2\right)^{\frac{1}{2}} \tag{4.3}$$

The individual sources of uncertainty are listed below:

- $\Delta I_{frame,beam} = 0.0037 \cdot I_{frame,beam}$ is due to the nonlinearity of the camera [103].
- $\Delta \bar{I}_{p^+} \approx 0$ is determined by the quantization error $< 10^{-4}$ that is introduced by prescaling the MHC4 signal and can be neglected.
- $\Delta I_{norm}(bkgd_{1..4}) = 0.0078$ was derived in subsection 3.5.2 and illustrated in figure 3.40(b).
- $\Delta fbeam = 0.0087 \cdot fbeam$ is an estimate based on the uncertainty of the normalized backgrounds.

The uncertainty on the LEM rate depends on the high voltage and threshold setting of the detector used as well as on the magnet settings in the μE4 beam line. During the AHPOS scan the MHC4 proton signal and LEM rate were monitored. Since frames were only captured as soon as those parameters stabilized the variations on the LEM rate during an exposure turned out to be small and slow parameter drifts can be neglected due to the short duration of the full scan ~ 1 hour. Hence an uncertainty on the LEM rate is not taken into account. Furthermore, there is no accurate knowledge of the proton beam envelope on TgE. Hence extreme shifts of the proton beam with respect to the target centre, as experienced during an AHPOS-scan, lead to an uncertainty in the proton beam current DS of MHC4 and hence to an uncertainty in the muon beam intensity, which is not taken into account for such a scan. This was exemplified by the incident on June 20th where the proton beam was steered and missed the target but with MHC4 still registering a current.

B. Uncertainties on the profile information during the AHPOS scan

The uncertainties for the profile parameters are taken from table 3.7. These values partially overestimate the uncertainties on the profiles since variations due to systematic effects

(radiation damage) that occured during one day of data taking are reflected in these values.

C. Uncertainties in the normalized intensities for the quantification of radiation damage

In order to determine the radiation damage in subsection 3.5.8 the image intensities need to be normalized to the muon intensity. Therefore equation 4.1 is further refined by applying the LEM scaling as derived in section 3.5.4, which means that for the calculation of the relative muon intensity not only the proton current is taken into account but also the proton beam centring on TgE. The so normalized intensities are given by equation 4.4:

$$
I_{norm,p^+,LEM} = \frac{\dfrac{I_{frame,beam} - \frac{1}{n}\sum\limits_{n=1}^{4}\left(\frac{I_{fit}\left(T_{int}(t(frame,beam))\right)}{I_{fit}\left(T_{int}(t(frame,bkgd_n))\right)}\cdot I_{frame,bkgd_n}\right)}{\bar{I}_{p+}}}{m_{LEM}\cdot LEM + c_{LEM}} \tag{4.4}
$$

The uncertainty on $I_{norm,p^+,LEM}$ is again determined via Gaussian uncertainty propagation. The uncertainties are the same as in subsection A and in addition the uncertainties $\Delta m_{LEM} = 0.152$ and $\Delta c_{LEM} = 26.31$ derived from the fit in subsection 3.5.4 are introduced for the LEM scaling parameters. Uncertainties on the LEM rate, the proton current are again not taken into account.

4.3. Thoughts on how to enhance the πE5 beam intensity with an optimized extraction from TgE

Particles produced at TgE usually do not emanate from a common origin but come either from the target surface, as in the case of positive muons close to the kinematic edge of stopped pion decay, from the bulk as in the case of positrons, or from an extended volume around the target in the case of cloud muons. Furthermore, up to date valid alignment data for the front part of πE5 is not available, whereby a sag of the production target station compared to the time of construction has been observed. Misalignment or a mismatch between design and the real mean particle origin leads to an off-axis beam as schematically shown in figure 4.2. This leads for example to the difficult task of aligning the muon
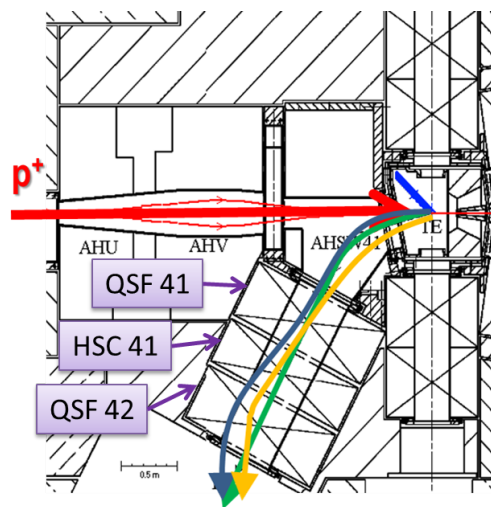
Figure 4.2.: *Shown is the muon production target region, the preceeding dipoles in the proton beam line and the first elements of πE5. For surface muons the first quadrupole QSF41 after the extraction dipole AHSW is defocussing in the horizontal direction as well as the subsequent sextupole HSC41 although the sextupole is operated at a rather low strength. The QSF42 therefore is horizontal focussing. The centred and parallel design trajectory is shown in green. The blue and the yellow trajectory represent, on the one hand a configuration in which the AHSW is set to provide the correct deflection angle and on the other hand a setting that centers the beam in the QSF41.*

beam along the beam line while maintaining the rate. The off-axis central trajectories are proven by the ability to steer the beam with the magnets that are usually foreseen only for focussing. The G4BL simulation of the πE5 beam line starting from TgE, presented in section 2.4.3.1, shows a displacement of the beam at the centre of the QSF41. Although the simulation shows deviations of the beam centroid at the Pill1 position, the parts of the simulation close to TgE are regarded to reasonably reflect the real conditions.

Figure 4.3 shows the muon beam profile at the centre of the QSF41, derived from the simulation. The distribution of those muons that would reach the Pill1 position shows two dense spots stemming from the back- and the side-face of TgE both of which contribute to the surface muon beam in πE5. The horizontal phase space of the corresponding surface muon beam, that reaches Pill1, is shown in figure 4.4. Considering the whole muon subset,

(a) Beam profile of all muons

(b) Beam profile of muons that would reach the Pill1 position
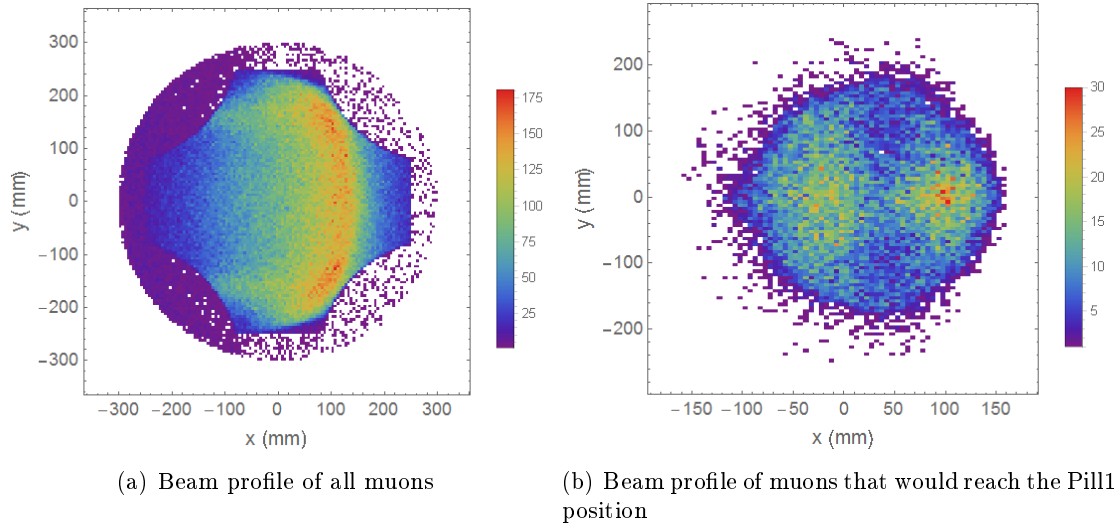
Figure 4.3.: *Shown is the muon beam profile at the centre of the QSF41 derived from the simulation, that was described in section 2.4.3.1. The left profile shows all muons that reach the QSF41 and the right plot shows only the subset of muons that would reach the Pill1 position.*
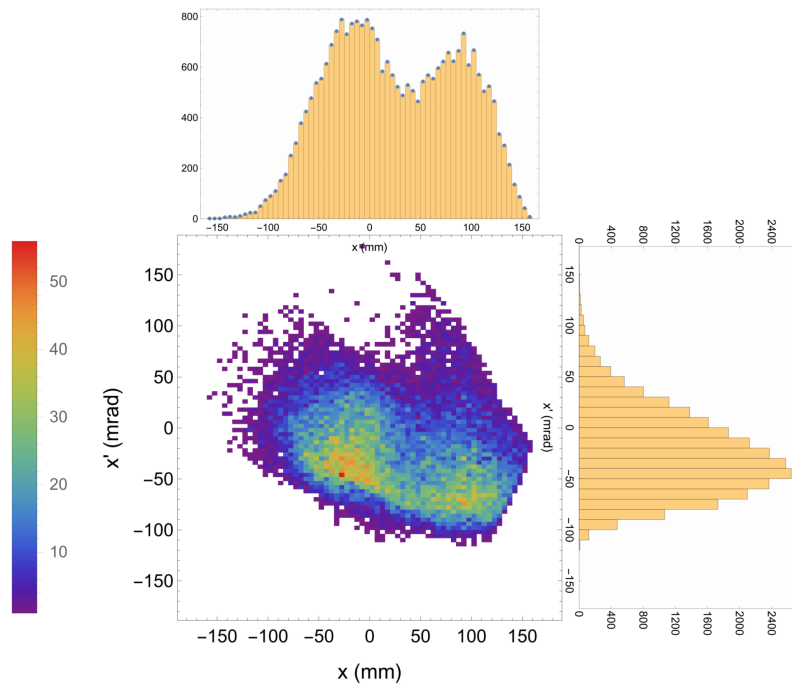
Figure 4.4.: *Shown is the horizontal phase space of surface muons at the centre of the first quadrupole QSF41 after extraction into $\pi E5$. Only particles that are transported to the intermediate collimator are taken into account. The origin of the surface muons are from the side- and backward facing target faces and clearly show two dense spots. The means of the distribution are: $\bar{x} = 25.4$ mm and $\bar{x}' = -25.3$ mrad.*

the means of the horizontal spatial distribution ($\bar{x} = 25.4$) mm and angular distribution ($\bar{x}' = -25.3$) mrad indicate a clear compromise between the two possible non-ideal alignment solutions shown in figure 4.2 (blue and yellow trajectories). Figure 2.42(b) shows the resulting beam displacement of up to several cm with respect to the centreline of the multipole channel. The total transmission from TgE to the final experimental focus is expected to be reduced due to this observation. Other elements of the Mu3e beam line that are further DS offer at least partially, the ability to compensate for a non-ideal deflection angle and off-axis displacement, which requires at least two degrees of freedom. The deflection by the AST dipole magnet can be complemented by the ASC in the horizontal direction and the combined horizontal steering by SML and ASK offer the possiblity to achieve a good alignment in the QSO doublet.

A. Operating QSF41 with asymmetric coil currents

In order to improve the transmission from TgE a second steering magnet close to the AHSW would be required, although there is no free space to implement such a device. However by operating the coils of the QSF41 indepently, one can add steering capability while still maintaining its focussing properties. Figure 4.5 shows such an example of the steering properties of a quadrupole when operating the coils independently. The quadrupole coils can either be operated as a subset of two coils as shown in figure 4.5(b) or with at least 2 coils operated fully independently and maximum one pair of coils connected in series. Maintaining one symmetry as in the first case allows the beam to be deflected in this symmetry plane. A slightly different current value of one of the coils with respect to the other coils as in figure 4.5(a) steers the beam in the diagonal direction. A combination of both modes therefore provides additional steering capabilities in both transverse directions.

B. Challenges in the modification of QSF41 & Discussion

In order to operate the QSF41 coils independently, brazed connections that normally connect the coils in series have to be cut. Obviously, additional cables would also be required. Furthermore, at least one additional power supply is required in case of steering power in only one direction and two additional power supplies for steering capabilities in both transverse directions. Due to the high radiation levels in the TgE region modifications are difficult. However, possible future upgrades to this region might allow a QSF41 upgrade. Further estimates on the work needed for such modifications are necessary.
Most importantly comprehensive simulation studies are required to validate the complete G4BL model of πE5 and to quantify the possible enhancement of the beam intensity throughout the beam line. A possible failure resulting in less beam intensity than at present can be excluded, since the electrical properties can either be mimicked by setting the power supplies to equal values or by reconnecting the cables outside the πE5 channel for operation with one power supply only. The quality of the quadrupole field and the superimposed dipole field for asymmetric currents needs to be investigated with respect to higher order contributions and XY-couplings as well as the maximum steering power, this requires further FEM calculations and tracking simulations. Exploiting the steering capabilities of the QSF41 could improve the extraction and hence beam intensity and quality in the experimental area. Hysteresis effects of the iron yokes of the dipole magnets in the

(a)

(b)
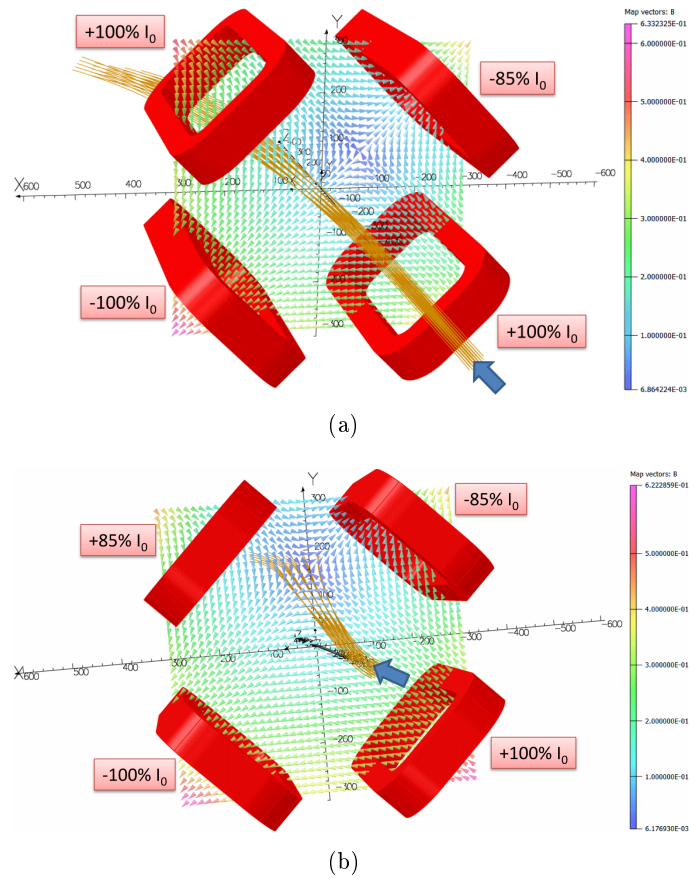
Figure 4.5.: *Action of a horizontally defocussing quadrupole on a parallel beam with slightly asymmetric coil currents (the color coded fieldline arrows show the quadrupole field displacement):*
a) Tuning the upper right coil allows for a deflection in the diagonal direction
b) Tuning independently the upper coils as a set allows to deflect the beam in the vertical direction

beam line have been demonstrated each time the momentum or particularly the polarity of the πE5 beam is changed. This effect can be reduced if the magnets are cycled, which means a repeated excitation to the maximum positive and negative currents before setting the actual setpoint. The AHSW however can only be changed by the HIPA control room crew. The AHSW is usually not cycled which is not a problem for the proton beam since the preceeding dipoles AHU and AHV are used for compensation. Steering power at the QSF41 could therefore also be used to partially compensate for the hysteresis of the AHSW extraction magnet.

4.4. Optimization software for G4BL

As shown in section 2 the fieldmap-based particle tracking in G4Beamline agrees with the transport matrix formalism for neglegible fringe field contributions, particle loss and paraxial approximation. Vice versa the optimum beam line setup can only be found by taking these effects into account. Therefore the detailed simulation and beam line optimization studies that were described in section 2 required an automated optimization tool for the G4Beamline[5] tracking simulations. Such a tool was not available. Therefore the Python[68] based code *Optima G4BL* that makes use of Numpy[112], Tkinter and Matplotlib[113] has been developed to run on Linux, MacOS and Windows operating systems, as part of this work. The parameters provided to G4Beamline can be of any type and the number of optimization parameters is not limited, except by computation time and power respectively. For each new parameter set G4Beamline is called and results are reported and provided in various output formats.

The *Optima G4BL* Graphical User Interface

A Graphical User Interface (GUI) provides easy access to all settings, without a need for editing the Python script, as well as monitoring the overall optimization progress. The GUI is shown in figure 4.6. The top frame (A) is used to input for each of the different parameters the parameter name, the initial value and a prescaling factor, separated by square brackets. The prescaling factor allows one to take into account the different sensitivities of the individual parameters on the optimization result. If G4Beamline has been built with MPI support (only for Linux and Mac) the number of parallel threads can be set in the second frame (B). Frame C contains the file paths to the G4Beamline script, the G4Beamline simulation output table and where to save the optimization progress history. The next part allows the selection of one of three optimization methods, whereby the optimum is determined sequential via nested intervals for each single parameter as:

- Highest value in interval
- Maximum of a cubic spline interpolation
- Maximum of a linear method (here called Pseudo Gradient)

The input on frame E sets the number and size of intervals as well as the steplength. Changes of the parameter settings in each step of the optimization can be applied either in relative or in absolute terms. Most important, the target radius is specified within which the number of particles is optimized. The next frame F can be used to follow the progress during optimization by an auto-updating plot that summarizes the main quantities. The bottom of the GUI is used to start and quit the optimization, call the manual (Help) and save all above entries for later reuse.

Optimization principle

Optima G4BL scans parameter by parameter over the defined range and determines the optimum based on the selected method. Figure 4.7 illustrates the simple but robust working principle. The highest value method simply determines the highest value of the recent interval scan of a parameter. The cubic interpolation can be chosen for a faster convergence
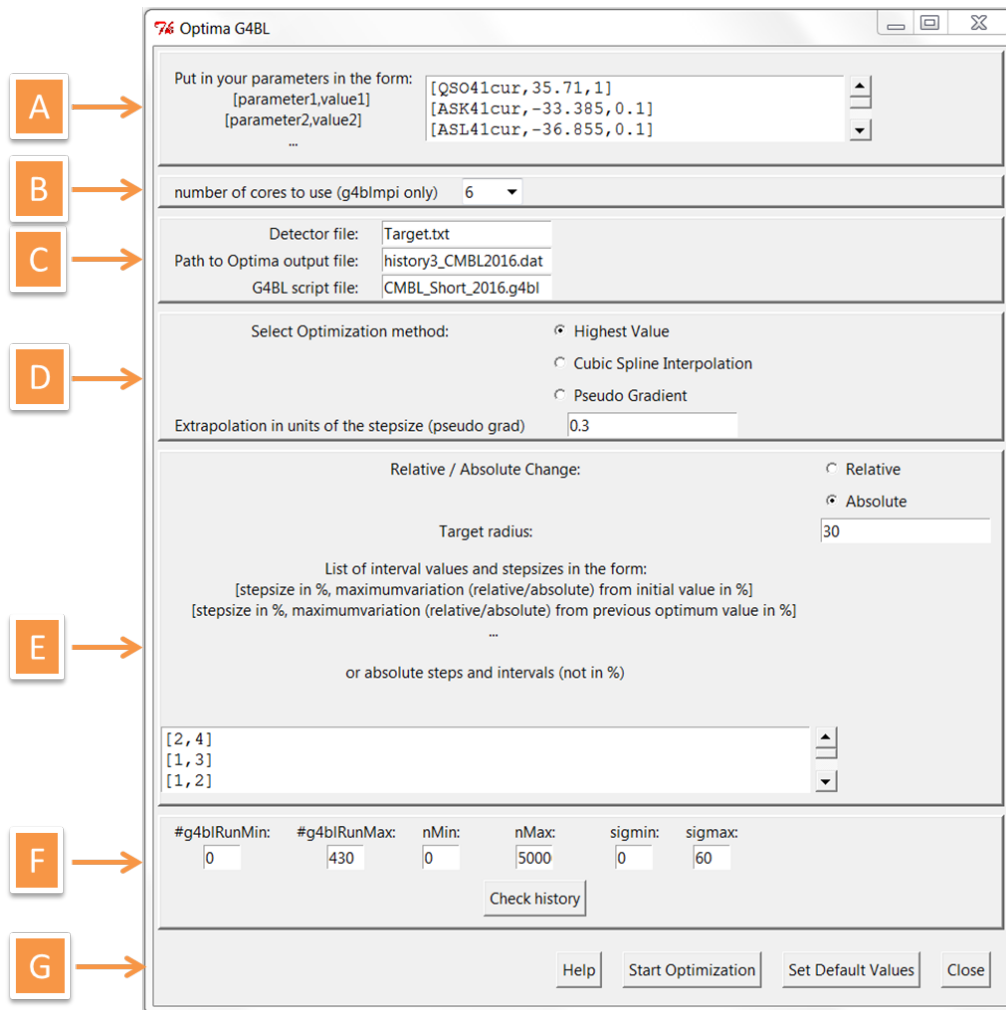
Figure 4.6.: *The graphical user interface for Optima G4BL. A specifies the parameters. B sets the number of threads. File paths are set in C. Selection of the optimization method is made in D. The optimization acceptance radius as well as the interval ranges and step-sizes are input in E. F provides a progress monitor and G is mainly used for saving the default values and starting the optimization procedure.*
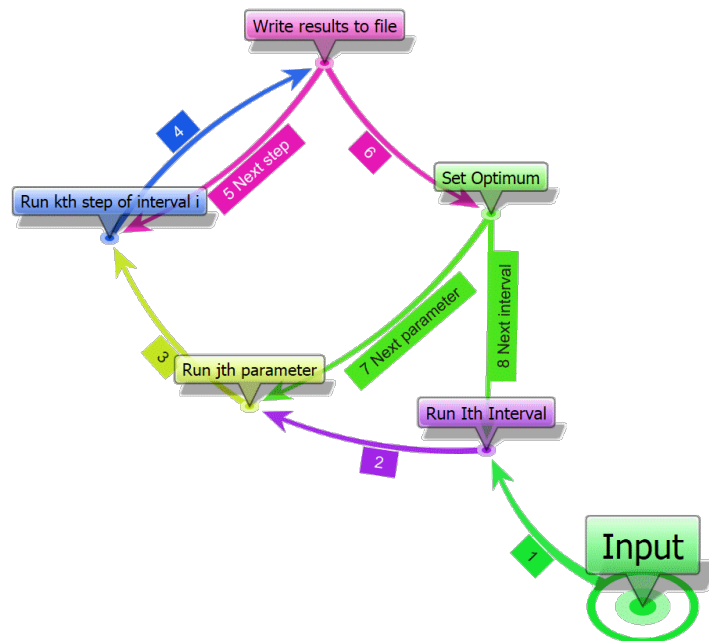
Figure 4.7.: *Shown is the optimization scheme. At start-up the GUI takes default values for the optimization parameters from a file (1). These default values can be overwritten for easier reuse with similar settings. Once the optimization is started the first element (2) is set to the lower edge of the first interval and a G4BL run is started (3). The target data is recorded and written to a history file. After that the parameter is succesively varied by the given steplength and successive G4BL runs started (4-5). At the end of the interval (6) the optimum value is determined, depending on the chosen method and set for this particular parameter. After that the procedure is repeated for the next parameter in the list to be optimized (7). Once all parameters have been optimized in the range of the first interval a PDF output summary is produced and the next interval is initiated, starting again with the first parameter specified in the input (8).*

in some cases. If the optimum value lies within the interval range the 'Pseudo Gradient' provides the same value as the 'High value' method. However, the parameter range scanned is extrapolated by a parameter that can be specified in the GUI. For a smooth parameter dependence the Pseudo Gradient method with a well-chosen extrapolation range will lead to a fast convergence. Figure 4.8 shows an extract of the Run summary PDF output as an example for the different optimization methods. The main limitation of the optimization
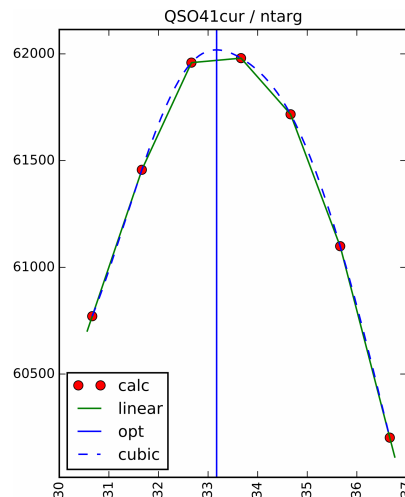
Figure 4.8.: *Illustration of the different optimization methods. The optimum in this example is determined by the highest value of a cubic spline interpolation.*

is given by the statistics that is provided by the G4Beamline simulation. Therefore it can make sense to start off with different numbers of tracked particles and / or a bigger optimization radius and to adapt the settings later. The optimization status can be checked by several outputs.

Optimization Output

Immediately after starting the optimization from the GUI a summary of all the settings appears in the shell from which *Optima G4BL* was started. After that the optimization goes through the intervals for all the parameters and outputs information on the run line by line, as can be seen in figure 4.9. A history file, the name of which has been specified in the GUI, has the form of a table, summarizing the parameter names, the actual parameter settings and the corresponding results for total transmission, transmission to be within the acceptance radius, RMS sizes and horizontal / vertical mean of the beam on the target. This table can in principle later be used further for a sensitivity analysis. The history file is immediately updated after each individual G4Beamline run. At the end of each interval a PDF is generated containing the interval scan for each parameter as shown in figure 4.8. A convenient way to monitor the progress of the optimization is provided by pushing the 'Check history' button on the GUI. This opens the following auto-updating plot in figure 4.10.

```
Parameters: [0.0801, -0.022, 0.58]  -  Number of particles on target: 167
Parameters: [0.08455, -0.022, 0.58]  -  Number of particles on target: 185
Parameters: [0.089, -0.022, 0.58]  -  Number of particles on target: 184
Parameters: [0.09345, -0.022, 0.58]  -  Number of particles on target: 177
Parameters: [0.0979, -0.022, 0.58]  -  Number of particles on target: 167
Optimum of parameter QSN1cur is 0.08455 with 185 particles on 15 mm radius target - (Opt=Max(calculated))
Parameters: [0.08455, -0.01979999999999998, 0.58]  -  Number of particles on target: 181
Parameters: [0.08455, -0.020900000000000002, 0.58]  -  Number of particles on target: 183
Parameters: [0.08455, -0.022, 0.58]  -  Number of particles on target: 185
Parameters: [0.08455, -0.0231, 0.58]  -  Number of particles on target: 186
Parameters: [0.08455, -0.0242, 0.58]  -  Number of particles on target: 180
Optimum of parameter QSN2cur is -0.0231 with 186 particles on 15 mm radius target - (Opt=Max(calculated))
Parameters: [0.08455, -0.0231, 0.522]  -  Number of particles on target: 172
Parameters: [0.08455, -0.0231, 0.551]  -  Number of particles on target: 184
Parameters: [0.08455, -0.0231, 0.58]  -  Number of particles on target: 186
Parameters: [0.08455, -0.0231, 0.609]  -  Number of particles on target: 174
Parameters: [0.08455, -0.0231, 0.638]  -  Number of particles on target: 158
Optimum of parameter QSMcur is 0.58 with 186 particles on 15 mm radius target - (Opt=Max(calculated))
Run 0 finished.
Parameters: [0.0820135, -0.0231, 0.58]  -  Number of particles on target: 173
```

Figure 4.9.: *The shell output of the optimization code provides online information about the current status of the optimization.*
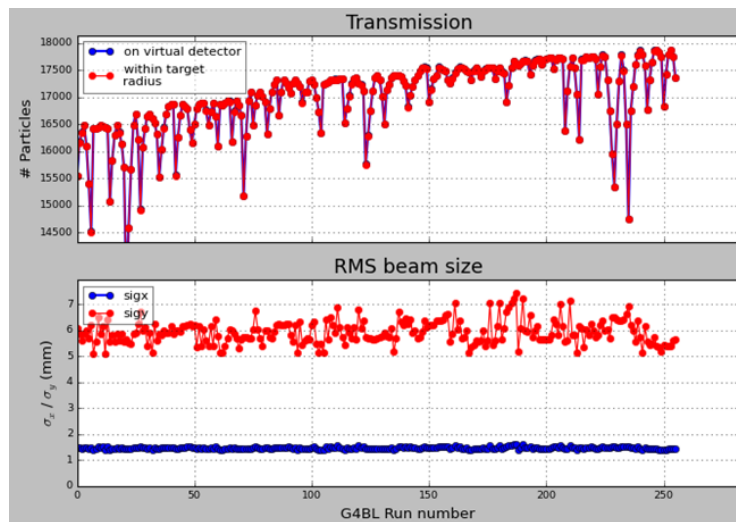
Figure 4.10.: *The progress plot provides the main information during the optimization procedure.*

Outlook on the *Optima G4BL*

The software had turned out to be valuable for tracking and beam tuning problems and has been employed for the G4Beamline optimizations shown in this thesis. Furthermore it has already been used by other groups e.g. at the Max-Planck Institute for Nuclear Physics in Heidelberg for beam optics calculations of the source platform extraction of the cryogenic storage ring (CSR) [114]. Although the nested interval method is slow, it is regarded to garantuee a uniform convergence and provides an accesible overview of the parameter dependencies and sensitivities. However, in the future more optimization methods that are not interval based will be implemented. For specific applications or if desired, operation without the GUI is feasible by editing one variable in the code. Depending on the progress of the optimization a reasonable number of G4BL runs are carried out which predestines the history output table for a further evaluation. The implementation of a surrogate model based on a least squares Polynomial Chaos Expansion [115], with its versatile benefits for optimization and sensitivity analysis, is foreseen to be investigated in the future.

4.5. Beam Scanner Improvements

In 2013 a new automated beam scanner was introduced by the PSI High Energy Beam lines group [116], (see figure 4.11) that utilizes the same scintillator pill and PMT combination as the previous scanner. Step motors in the horizontal and the vertical axis together
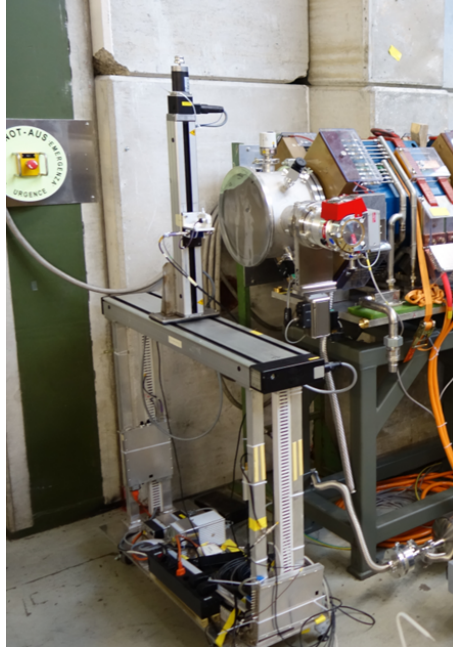
Figure 4.11.: *Shown is the new XY-scanner that has been employed for all measurements in the front part of the $\pi E5$ area, that are presented in this thesis.*

with the rigid and robust construction allow for a positioning precision of <0.1 mm with the limiting accuracy determined by the alignment during the scanner setup procedure. The scanner is controlled by a LabVIEW interface which in turn controls the movement, by software boundaries, movement speed, stepsize and scanner range. Furthermore rates provided by a DRS evaluation board are acquired and displayed in the LabVIEW software. The acquired rates are normalized to the proton current provided by the MHC4 current monitor that is connected to one channel of the DRS.

A. Improvements to the new mobile automated scanner system

At the time the scanner system was provided a simple cross scan mode was implemented allowing the normalized muon rates at points on a horizontal and a vertical line to be measured. The software fits the data from both lines independently with a Gaussian distribution and outputs the corresponding means $\bar{x}$, $\bar{y}$ and widths σ_x and σ_y of the 1-dimensional distributions. In order to increase the accuracy of this method the software was modified as part of this thesis, to incorporate a second scan, which is initiated at the $\bar{x}$ and $\bar{y}$ means of the first scan, to give an intensity measurement based on the true maxima of the distributions. A larger step size during the first run can be chosen in order to reduce the measurement time to determine the profile centroid while a smaller step size during

the second scan provides accurate results. The method is illustrated schematically on a representative muon distribution in figure 4.12. The horizontal and the vertical phase space
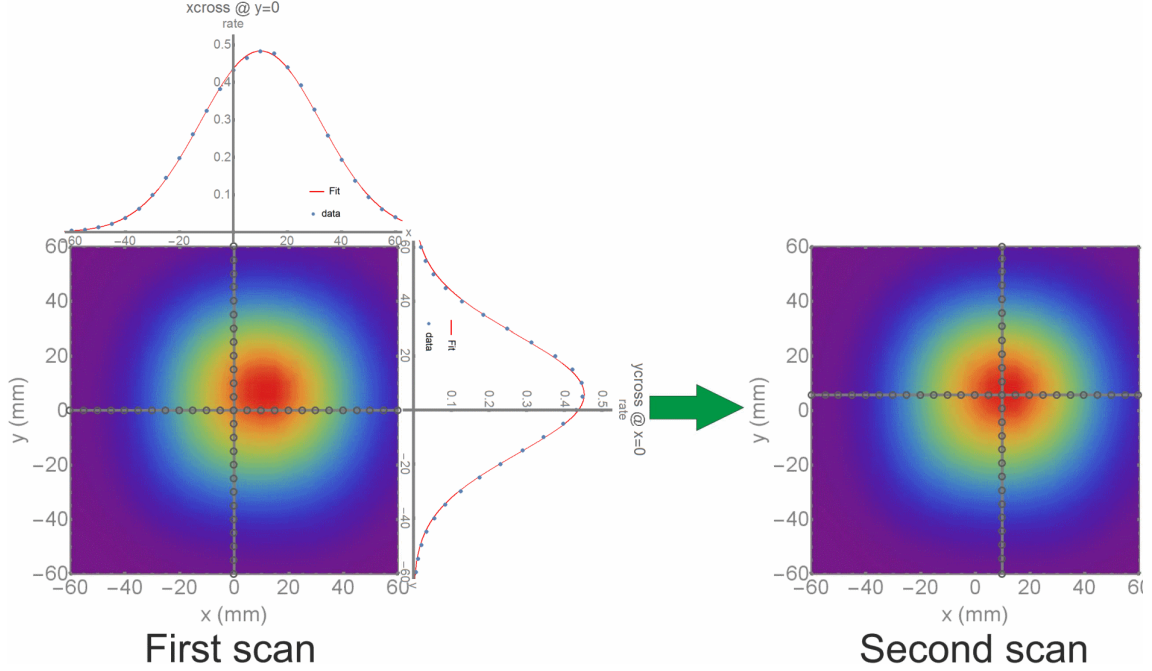
Figure 4.12.: *Shown is the principle to determine the rates of the full muon profiles with cross scans. A first cross scan yields the beam centroid, which is taken as offset for the second scan.*

are only weakly coupled in the πE5 beam line by the sextupole magnets that are operated at low currents. Therefore, also the beam profiles show mostly a vanishing correlation $\rho_{x,y}$. Hence the method described above provides the full information on the beam spot and gives direct access to the rates. Furthermore, three different ways to calculate and output the rates have been implemented. Assuming a pure Gaussian shaped beam, the full rate R_{beam} of the beam spot is calculated with equation 4.5:

$$R_{beam} = \frac{2 \cdot \pi \cdot R_{pill,center} \cdot \sigma_x \cdot \sigma_y}{A_{pill}} \tag{4.5}$$

where $R_{pill,center}$ is the rate measured with the pill counter at the beam centroid, $\sigma_{x,y}$ are determined by the fit to the horizontal and vertical distributions and A_{pill} is the area of scintillator pill. In case of a Gaussian distribution with cut tails a second output provides the rate R_{beam} based on the integrated Gaussians within the range of the scan. The last method is also constrained to the integration within the scanned range but uses a cubic interpolation of the data points. The integration based rates are calculated by:

$$R_{beam} = \frac{1}{R_{pill,center}} \frac{\Delta x \cdot \Delta y \cdot \int\limits_{Xrange} f(x)\,dx \cdot \int\limits_{Yrange} f(y)\,dy}{A_{pill}} \tag{4.6}$$

where $\Delta x, y$ are the scanner step size in the horizontal / vertical directions and $f(x/y)$ are either the Gauss fits or the cubic interpolations in both directions. The rate at the

centre for all methods is determined by the maximum of the distribution that is used to approximate the data. In case of the cubic interpolation the second cross scan through the centre determined from the first scan still yields reliable results for non-Gaussian but still symmetric beams that show no XY-coupling. All rate outputs of the software are normalized to a 2.2 mA proton beam intensity.

A raster scan option, that was already foreseen but neither activated nor tested was activated in the raw non-compiled LabVIEW firmware. Figure 4.13 shows schematically the grid on which the pill rates $R_{pill,1mA}(x,y)$ are acquired for a preset time and normalized to a 1 mA proton current equivalent. In order to obtain the full beam rate R_{beam} all normalized
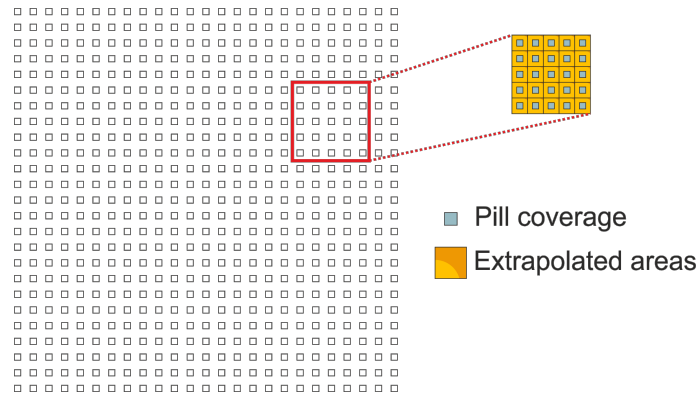
Figure 4.13.: *In raster scan mode the beam scanner acquires the rates on a grid of XY coordinates. In order to extract most reliable beam rates the normalized pill (shown as light blue squares) rates are scaled by the ratio $\frac{step_X \cdot step_Y}{A_{pill}}$ so that the full beam rate is given by a scaled summation of all gridpoints.*

rates are summed and scaled by the ratio $\frac{step_X \cdot step_Y}{A_{pill}}$ corresponding to a stepwise constant approximation to the beam distribution.

$$R_{beam} = \frac{step_X \cdot step_Y}{A_{pill}} \cdot 2.2 \cdot \sum_{(x,y) \in XY\,grid} R_{pill,1mA}(x,y) \qquad (4.7)$$

The step grid spacings are $step_X$ and $step_Y$ and A_{pill} is the cross sectional area of the pill seen by the beam. $R_{pill,1mA}(x,y)$ is the pill rate at specific coordinates normalized to 1 mA proton current equivalent. The factor 2.2 represents the reference proton current 2.2 mA that accounts for all pill scanner measurements presented in this thesis. The advantage of this method is that the beam rate R_{beam} does not depend on a specific model that is fitted to the data but fluxes from arbitrary beam shapes are determined and in fact most often a $\lesssim 3$ % higher rate has been observed in the raster scan, compared to the cross scan fit result. This could be shown to be due to non-Gaussian tails in the distribution. In the following the error introduced by this method is estimated for a Gaussian shaped beam.

The fraction of the full profile intensity that is lost in the stepwise constant approximation F_{loss}, for a given set of profile parameters $\bar{x}$, $\bar{y}$, σ_x, σ_y, $\rho xy = 0$ can be determined via:

$$F_{loss} = 1 - \frac{step_X \cdot step_Y}{A_{pill}} \left(\sum_{(x,y) \in XYgrid} \int\limits_{x-\frac{w_{pill}}{2}}^{x+\frac{w_{pill}}{2}} \int\limits_{y-\frac{h_{pill}}{2}}^{y+\frac{h_{pill}}{2}} \frac{1}{2\pi\sigma_x\sigma_y} e^{-\frac{1}{2}\left(\frac{(x^*-\bar{x})^2}{\sigma_x^2} + \frac{(y^*-\bar{y})^2}{\sigma_y^2}\right)} dx^* dy^* \right)$$
(4.8)

with w_{pill} and h_{pill} being the width and the height of a rectangular pill scintillator. The maximum absolute value of F_{loss} for different centroid shifts with assumed profile widths $\sigma_x = \sigma_y = 10$ mm, a horizontal and vertical scanner range of ± 100 mm, step sizes $step_X = step_Y = 5$ mm and $w_{pill} = h_{pill} = 2$ mm is at the ppm level. Most of the quoted rates in this thesis are based on these raster scans which usually require at least >1 h for measurement.

B. Improvements on the APD scanner for COBRA centre measurements

Beam measurements for MEG at COBRA centre were previously performed with the same XY-scanner from CERN as was used for the measurements in the area, which has also been replaced with a similar new scanner system. Due to the 1.27 T B-field at COBRA center the detector type, consisting of a small NE102a scintillator pill and a PMT cannot be used. Instead an APD of circular shape and 3 mm diameter is installed and particles that pass the depletion layer generate a signal according to the energy deposited. The muon signal can clearly be separated from the positron signal, however the higher noise level compared to the PMT denies a clear discrimination between positrons and background. In order to carry out the measurements at the centre of COBRA the scanner is mounted on a rail system on the DS side of COBRA and a ~ 4 m long aluminum profile is attached with the APD at its tip.

For the MEG Pre-Engineering run at the end of 2015 beam tuning at COBRA centre was undertaken for the first time with the new automated scanner system. A new support structure and adapter plate were manufactured in order to match the new scanner to the rail system and measurement arm - see figure 4.14. In addition endswitches have been attached on the horizontal and the vertical axis and connected to the interlock output of the scanner controller box. The endswitch positions were determined to protect the insertion system (an extendable bellows system allowing devices to be remotely inserted to COBRA centre, without having to break the inner Helium environment) from damage by the scanner arm. Screws on the aluminum profile and aluminum plate allow for a fine adjustment of the vertical and horizontal angle before moving the scanner arm inside COBRA. Determination of the reference orbit position inside COBRA is difficult and has been done as in the past, by visual observation of the reflections of light from a self-leveling cross line laser on a polished aluminum ball that is mounted at a well-defined position with respect to the APD at the tip of the aluminum arm. Since the ball is inside the reflective and non-illuminated COBRA volume this method depends on the subjective judgement of the person that is doing the alignment. Therefore an automatic alignment was implemented using a non-magnetic Hamamatsu photo diode (2.5×2.5 mm^2), which was mounted at the tip of the aluminum profile near the APD facing backwards to the
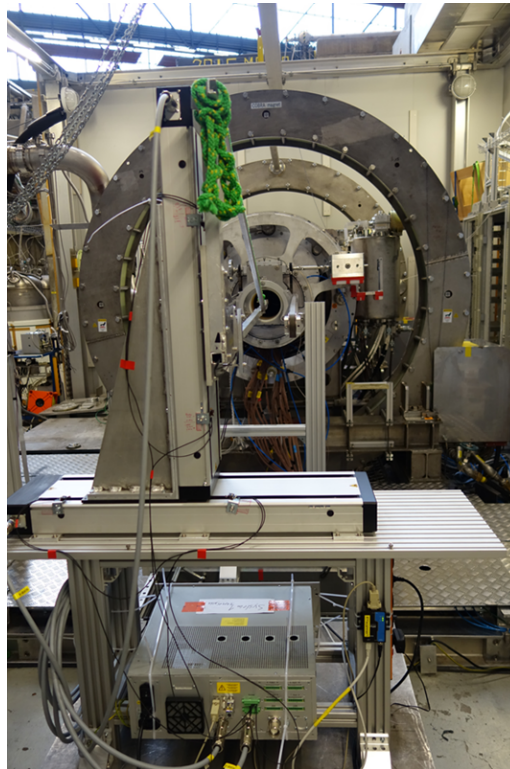
Figure 4.14.: *View of the APD scanner from the DS COBRA side. The APD scanner is moved to the measurement position. The endswitches that can be seen on the horizontal and the vertical axis are connected with the interlock connector on the controller box underneath.*

scanner. An electronic circuit that is shown in figure 4.15 has been integrated into a small housing and converts the photo diode current into a ~ 300 mV amplitude signal with a monotonously increasing frequency for higher light exposures. The output of the circuit
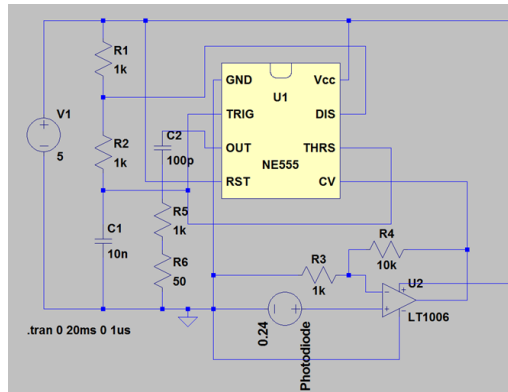
Figure 4.15.: *The designed circuit shown, converts the photo diode current into a frequency in the range of several tens of kHz that matches the scanner DAQ and reflects the light intensity on the sensitive area of the diode. The resistor R6 represent the DRS input impedance.*

matches the DAQ system of the scanner, that is mainly based on a DRS4 evaluation board and a LabVIEW [70] interface. Therefore once the cross line laser has been adjusted the normal measurement software can be used in the same way as for beam scans, whereby the particle counts are mimicked by the photo diode current dependent signal output of the circuit. Figure 4.16 shows the result for a vertical alignment scan with a step size of 0.1 mm. Due to the square shape of the used photo diode a rhombus-like orientation improved
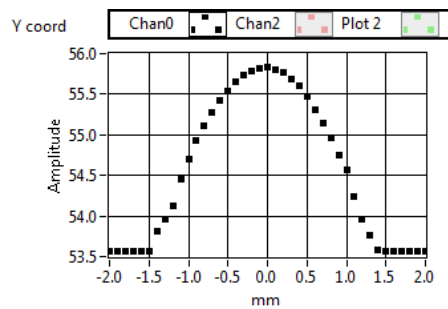
Figure 4.16.: *Shown is the alignment scan when moving the photo diode through the horizontal cross-hair line of the laser that is setup to match the vertical centre.*

the resolution. This method allows for an easy and reproducable alignment of the APD scanner at the centre of COBRA.

Acknowledgements / Danksagung

Bibliography

[1] Y. Kuno and Y. Okada, "Muon decay and physics beyond the standard model," *Rev. Mod. Phys.* **73** (2001) 151–202, `arXiv:hep-ph/9909265 [hep-ph]`. `https://doi.org/10.1103/RevModPhys.73.151`.

[2] P.-R. Kettle, "The "Golden" cLFV channels $\mu \to e\gamma$ and $\mu \to eee$ — the high-intensity frontier," *Hyperfine Interactions* **214** no. 1, (2013) 47–54. `https://doi.org/10.1007/s10751-013-0789-6`.

[3] A. Blondel, A. Bravar, M. Pohl, *et al.*, "Research Proposal for an Experiment to Search for the Decay $\mu \to eee$," `arXiv:1301.6113 [physics.ins-det]`.

[4] A. M. Baldini, F. Cei, C. Cerri, *et al.*, "MEG Upgrade Proposal," `arXiv:1301.7225 [physics.ins-det]`.

[5] T. Roberts, *G4beamline User 's Guide*, second ed., 2013. `http://www.muonsinternal.com/muons3/G4beamline`. [Online; accessed 16-April-2016].

[6] A. M. Baldini, Y. Bao, E. Baracchini, *et al.*, "Search for the lepton flavour violating decay $\mu^+ \to e^+\gamma$ with the full dataset of the MEG experiment," *The European Physical Journal C* **76** no. 8, (Aug, 2016) 434, `arXiv:1605.05081 [hep-ex]`. `https://doi.org/10.1140/epjc/s10052-016-4271-x`.

[7] U. Bellgardt, G. Otter, R. Eichler, *et al.*, "Search for the Decay $\mu^+ \to e^+e^+e^-$," *Nucl. Phys.* **B299** (1988) 1–6. `https://doi.org/10.1016/0550-3213(88)90462-2`.

[8] W. Bertl, R. Engfer, E. A. Hermes, *et al.*, "A Search for muon to electron conversion in muonic gold," *Eur. Phys. J.* **C47** (2006) 337–346. `https://doi.org/10.1140/epjc/s2006-02582-x`.

[9] Wikipedia, "Standard model." `https://en.wikipedia.org/wiki/Standard_Model`. [Online; accessed 5-April-2017].

[10] S. Chatrchyan, V. Khachatryan, A. M. Sirunyan, *et al.*, "Observation of a new boson at a mass of 125 GeV with the CMS experiment at the LHC," *Phys. Lett.* **B716** (2012) 30–61, `arXiv:1207.7235 [hep-ex]`. `https://doi.org/10.1016/j.physletb.2012.08.021`.

[11] G. Aad, T. Abajyan, B. Abbott, *et al.*, "Observation of a new particle in the search for the Standard Model Higgs boson with the ATLAS detector at the LHC," *Phys. Lett.* **B716** (2012) 1–29, `arXiv:1207.7214 [hep-ex]`. `https://doi.org/10.1016/j.physletb.2012.08.020`.

[12] B. T. Cleveland, T. Daily, R. Davis, Jr., *et al.*, "Measurement of the Solar Electron Neutrino Flux with the Homestake Chlorine Detector," *The Astrophysical Journal* **496** no. 1, (19985) 505–526. `https://doi.org/10.1086/305343`.

[13] Z. Maki, M. Nakagawa, and S. Sakata, "Remarks on the Unified Model of Elementary Particles," *Progress of Theoretical Physics* **28** no. 5, (1962) 870–880. `https://doi.org/10.1143/PTP.28.870`.

[14] B. Pontecorvo, "Inverse beta processes and nonconservation of lepton charge," *Sov. Phys. JETP* **7** (1958) 172–173. [Zh. Eksp. Teor. Fiz.34,247(1957)].

[15] J. Bagdonaite, P. Jansen, C. Henkel, H. L. Bethlem, K. M. Menten, and W. Ubachs, "A Stringent Limit on a Drifting Proton-to-Electron Mass Ratio from Alcohol in the Early Universe," *Science* **339** no. 6115, (2013) 46–48. `https://doi.org/10.1126/science.1224898`.

[16] J. M. Pendlebury, S. Afach, N. J. Ayres, *et al.*, "Revised experimental upper limit on the electric dipole moment of the neutron," *Phys. Rev. D* **92** (Nov, 2015) 092003, `arXiv:1509.04411 [hep-ex]`. `https://doi.org/10.1103/PhysRevD.92.092003`.

[17] M. Otani, "Status of the Muon g-2/EDM Experiment at J-PARC (E34)," *JPS Conf. Proc.* **8** (2015) 025008. `https://doi.org/10.7566/JPSCP.8.025008`.

[18] R. Pohl, A. Antognini, F. Nez, *et al.*, "The size of the proton," *Nature* **466** (2010) 213–216. `https://doi.org/10.1038/nature09250`.

[19] C. Blocker, "Searches for Charged Lepton Flavor Violation with the ATLAS Detector at the LHC," in *Proceedings, 17th International Workshop on Neutrino Factories and Future Neutrino Facilities (NuFact15): Rio de Janeiro, Brazil, August 10-15, 2015.* 2015. `https://cdsweb.cern.ch/record/2110264/files/ATL-PHYS-PROC-2015-164.pdf`.

[20] **Mu3e** Collaboration. Mu3e collaboration internal notes.

[21] B. W. Lee and R. E. Shrock, "Natural suppression of symmetry violation in gauge theories: Muon- and electron-lepton-number nonconservation," *Phys. Rev. D* **16** (Sep, 1977) 1444–1473. `https://doi.org/10.1103/PhysRevD.16.1444`.

[22] Y. G. Cui, R. Palmer, Y. Arimoto, *et al.*, "Conceptual design report for experimental search for lepton flavor violating $\mu^- - e^-$ conversion at sensitivity of 10^{-16} with a slow-extracted bunched proton beam (COMET),".

[23] R. M. Carey, K. R. Lynch, J. P. Milleand, *et al.*, "Proposal to search for $\mu^- N \to e^- N$ with a single event sensitivity below 10^{-16}," 2008.

[24] R. Giada, *In Search of Charged Lepton Flavor Violating Decays at PSI - R&D of a Fiber Hodoscope for the Mu3e Experiment and Study of Novel Calibration Methods for the MEG / MEG II Experiment.* PhD thesis, ETH Zürich, 2017. `https://doi.org/10.3929/ethz-b-000174750`.

[25] A. de Gouvea and P. Vogel, "Lepton Flavor and Number Conservation, and Physics Beyond the Standard Model," *Progress in Particle and Nuclear Physics* **71** (2013) 75–92, `arXiv:1303.4097 [hep-ph]`.
`https://doi.org/10.1016/j.ppnp.2013.03.006`.

[26] G. M. Pruna and A. Signer, "Lepton-flavour violating decays in theories with dimension 6 operators," *EPJ Web Conf.* **118** (2016) 01031, `arXiv:1511.04421 [hep-ph]`. `https://doi.org/10.1051/epjconf/201611801031`.

[27] A. E. Pifer, T. Bowen, and K. R. Kendall, "A high stopping density μ^+ beam," *Nuclear Instruments and Methods* **135** no. 1, (1976) 39 – 46.
`https://doi.org/10.1016/0029-554X(76)90823-5`.

[28] K. Deiters, F. Foroughi, G. Heidenreich, *et al.*, "Reduction of Target-E length from 60 mm to 40 mm.". Paul-Scherrer Institut Internal Report.

[29] P.-R. Kettle, "Muon beam prospects - present & future," in *MAX 2016 - Workshop on Muonic Atom Spectroscopy*. Paul Scherrer Institut, Villigen, Switzerland, Oct. 21, 2016.

[30] "The Swiss Spallation Neutron Source SINQ." `https://www.psi.ch/sinq/`. Accessed: 2017-04-21.

[31] M. Seidel, S. Adam, A. Adelmann, *et al.*, "Production of a 1.3 MW Proton Beam at PSI," *Conf. Proc.* **C100523** (2010) TUYRA03.

[32] S. D. Holmes, S. D. Henderson, R. Kephart, *et al.*, "Project X functional requirements specification," *Conf. Proc.* **C1205201** (2012) 3945–3947, `arXiv:1205.3082 [physics.acc-ph]`.

[33] Y. Miyake, K. Shimomura, N. Kawamura, *et al.*, "J-PARC muon facility, MUSE," *J. Phys. Conf. Ser.* **225** (2010) 012036.
`https://doi.org/10.1088/1742-6596/225/1/012036`.

[34] I. Perić, "A novel monolithic pixelated particle detector implemented in high-voltage CMOS technology," *Nuclear Instruments and Methods in Physics Research Section A: Accelerators, Spectrometers, Detectors and Associated Equipment* **582** no. 3, (2007) 876 – 885. `https://doi.org/10.1016/j.nima.2007.07.115`. VERTEX 2006Proceedings of the 15th International Workshop on Vertex Detectors.

[35] H. Augustin, N. Berger, S. Dittmeier, *et al.*, "MuPix7—A fast monolithic HV-CMOS pixel chip for Mu3e," *Journal of Instrumentation* **11** no. 11, (2016) C11029, `arXiv:1610.02210 [physics.ins-det]`.
`https://doi.org/10.1088/1748-0221/11/11/C11029`.

[36] R. Gredig, *Scintillating Fiber Detector for the Mu3e Experiment*. PhD thesis, Universität Zürich, 2016. `https://doi.org/10.5167/uzh-127074`.

[37] T. Harion, K. Briggl, H. Chen, *et al.*, "STiC — a mixed mode silicon photomultiplier readout ASIC for time-of-flight applications," *Journal of*

Instrumentation **9** (2014) C02003.
`https://doi.org/10.1088/1748-0221/9/02/C02003`.

[38] E. Hans Patrick, *The Mu3e Tile Detector*. PhD thesis, Ruprecht-Karls-Universität Heidelberg, 2015. `https://doi.org/10.11588/heidok.00018763`.

[39] "MIDAS - Maximum Integrated Data Acquisition System." `midas.psi.ch`.

[40] P.-R. Kettle, "PSI-internal LTP Filzbach Meeting," 2010.

[41] P.-R. Kettle *et al.*, "HiMB - Towards a new High-intensity Muon Beam," in *Future Muon Sources Workshop*. University of Huddersfield UK, Jan. 12-13, 2015.

[42] J. Adam, X. Bai, A. M. Baldini, *et al.*, "The MEG detector for $\mu \to e + \gamma$ decay search," *The European Physical Journal C* **73** no. 4, (2013) 2365. `https://doi.org/10.1140/epjc/s10052-013-2365-2`.

[43] MEG. MEG collaboration internal notes.

[44] M. Nishimura, "Performance of MEG II Positron Timing Counter Based on Commissioning Run Result," in *Physics of fundamental Symmetries and Interactions - PSI2016*. Villigen, Switzerland, Oct. 16-20, 2016. `https://indico.psi.ch/contributionDisplay.py?contribId=201&sessionId=25&confId=3914`.

[45] S. Ogawa, "Liquid xenon calorimeter for MEG II experiment with VUV-sensitive MPPCs," *Nuclear Instruments and Methods in Physics Research Section A: Accelerators, Spectrometers, Detectors and Associated Equipment* **845** (2017) 528 – 532. `https://doi.org/10.1016/j.nima.2016.06.085`. Proceedings of the Vienna Conference on Instrumentation 2016.

[46] Y. Fujii, "Development of radiative decay counter to reduce the background in the meg experiment," in *2013 IEEE Nuclear Science Symposium and Medical Imaging Conference (2013 NSS/MIC)*, pp. 1–6. Oct, 2013. `https://doi.org/10.1109/NSSMIC.2013.6829514`.

[47] S. Ritt, "The WaveDAQ system for the MEG II upgrade," 5, 2015. `https://www.psi.ch/drs/DocumentationEN/elba15.pdf`. 13th Pisa Meeting on Advanced Detectors.

[48] S. Ritt, R. Dinapoli, and U. Hartmann, "Application of the DRS chip for fast waveform digitizing," *Nucl. Instrum. Meth.* **A623** (2010) 486–488. `https://doi.org/10.1016/j.nima.2010.03.045`.

[49] S. Ritt, "Midas Slow Control Bus MSCB." `midas.psi.ch/mscb`.

[50] G. Cavoto, "Searching for X(16.7 MeV) at MEG." MEG collaboration meeting 12th July 2016.

[51] U. Rohrer, "PSI Graphic Transport Framework by U. Rohrer, based on a CERN-SLAC-FERMILAB version by K.L. Brown et al.," 2006. `http://aea.web.psi.ch/Urs_Rohrer/MyWeb/trancomp.htm`.

[52] U. Rohrer, "PSI Graphic Turtle Framework by U. Rohrer based on a CERN-SLAC-FERMILAB version by K.L. Brown et al.," 2006. `http://aea.web.psi.ch/Urs_Rohrer/MyWeb/turtcomp.htm`.

[53] S. Agostinelli, J. Allison, K. Amako, *et al.*, "GEANT4: A Simulation toolkit," *Nuclear Instruments and Methods in Physics Research Section A: Accelerators, Spectrometers, Detectors and Associated Equipment* **506** no. 3, (2003) 250 – 303. `https://doi.org/10.1016/S0168-9002(03)01368-8`.

[54] Wolfram Research, Inc., "Mathematica, version 11.1.". Champaign, IL (2017).

[55] H. Grote, *The MAD-X Program (Methodical Accelerator Design) User ' s Reference Manual*, 2017. `http://mad.web.cern.ch/mad/`. Version 5.03.04.

[56] F. Hinterberger, *Physik der Teilchenbeschleuniger und Ionenoptik*. Springer, Berlin, Heidelberg, 2008. `https://doi.org/10.1007/978-3-540-75282-0`.

[57] K. L. Brown, "A First and Second Order Matrix Theory for the Design of Beam Transport Systems and Charged Particle Spectrometers," *Adv. Part. Phys.* **1** (1968) 71–134.

[58] S. Manikonda, *High Order Finite Element Methods to Compute Taylor Transfer Maps*. Michigan State University, 2006.

[59] S. Turner, ed., *CAS - CERN Accelerator School: Second General Accelerator Physics Course*. Geneva, 1987. `http://cds.cern.ch/record/181071/files/fulltext.pdf`.

[60] F. C. Iselin, *The MAD (Methodical Accelerator Design) Program Version 8.13 - Physical Methods Manual*, 1994. `http://mad8.web.cern.ch/mad8/doc/phys_guide.pdf`. CERN SL 92.

[61] E. D. Courant and H. S. Snyder, "Theory of the alternating-gradient synchrotron," *Annals of Physics* **3** no. 1, (1958) 1 – 48. `https://doi.org/10.1016/0003-4916(58)90012-5`.

[62] M. Berz and K. Makino, "Cosy infinity - user's guide and reference manual," 2001. `http://citeseerx.ist.psu.edu/viewdoc/download?doi=10.1.1.201.2818&rep=rep1&type=pdf`. Version 8.1.

[63] Cobham Technical Services, *OPERA-3D User's Guide*, 18 ed. `http://operafea.com/`.

[64] H. Matsuda and H. Wollnik, "Third order transfer matrices for the fringing field of magnetic and electrostatic quadrupole lenses," *Nucl. Instrum. Meth.* **103** (1972) 117–124. `https://doi.org/10.1016/0029-554X(72)90468-5`.

[65] D. Renker, "PiE5." `http://aea.web.psi.ch/beam2lines/beam_pie5.html`. [Online; accessed 21-January-2017].

[66] Z. D. Hodge, *Production, Characterization and Monitoring of muon beams for charged lepton flavor violation experiments*. PhD thesis, ETH Zürich, 2017.

[67] **Mu3e** Collaboration, S. Martin, "The shielded solenoid - Sig Martin for the Mu3e collaboration," Sig Martin report (Mu3e Collaboration Meeting), Paul Scherrer Institut, 2014.

[68] T. E. Oliphant, "Python for Scientific Computing," *Computing in Science & Engineering* (06, 2007) 10–20. `https://doi.org/10.1109/MCSE.2007.58`.

[69] F. Berg, L. Desorgher, A. Fuchs, W. Hajdas, *et al.*, "Target Studies for Surface Muon Production," *Phys. Rev. Accel. Beams* **19** no. 2, (2016) 024701, `arXiv:1511.01288 [physics.ins-det]`. `https://doi.org/10.1103/PhysRevAccelBeams.19.024701`.

[70] C. Elliott, V. Vijayakumar, W. Zink, and R. Hansen, "National instruments labview: A programming environment for laboratory automation and measurement," *JALA: Journal of the Association for Laboratory Automation* **12** no. 1, (2007) 17–24. `https://doi.org/10.1016/j.jala.2006.07.012`.

[71] J. K. Grillenberger, "Status of HIPA Facility at PSI," in *Physics of fundamental Symmetries and Interactions - PSI2016*. Villigen, Switzerland, Oct. 16-20, 2016. `https://indico.psi.ch/contributionDisplay.py?sessionId=10&contribId=252&confId=3914`.

[72] **AlCap** Collaboration, P. Kammel, Y. Kuno, *et al.*, "Progress Report - Study of Muon Capture for Muon to Electron Conversion Experiment." `http://muon.npl.washington.edu/exp/AlCap/progress15.pdf`, 2015.

[73] A. Antognini, "Hyperfine splitting in μp and $\mu^3 He^+$," in *Open Users Meeting BV47*. Villigen, Switzerland, Feb. 9, 2016. `https://indico.psi.ch/getFile.py/access?contribId=12&sessionId=0&resId=0&materialId=slides&confId=4353`.

[74] A. Knecht, "Measurement of the charge radius of radium," in *Open Users Meeting BV47*. Villigen, Switzerland, Feb. 9, 2016. `https://indico.psi.ch/getFile.py/access?contribId=11&sessionId=0&resId=0&materialId=slides&confId=4353`.

[75] P.-R. Kettle, "Private communications.".

[76] E. Ripiccini, "Monte Carlo studies for different passive target solutions." MEG collaboration meeting 16th-17th September 2015, 2015.

[77] Saint-Gobain, *BC-400, BC-404, BC-408, BC-412, BC-416, Premium Plastic Scintillators*, 8, 2016.

[78] Wikipedia, "Polyvinyl toluene." `https://en.wikipedia.org/wiki/Polyvinyl_toluene`. [Online; accessed 12-December-2016].

[79] Wikipedia, "Terphenyl." `https://en.wikipedia.org/wiki/Terphenyl`. [Online; accessed 12-December-2016].

[80] Wikipedia, "Popop." `https://de.wikipedia.org/wiki/POPOP`. [Online; accessed 12-December-2016].

[81] E. Gardés, E. Balanzat, B. Ban-d'Etat, *et al.*, "SPORT: A new sub-nanosecond time-resolved instrument to study swift heavy ion-beam induced luminescence – application to luminescence degradation of a fast plastic scintillator," *Nuclear Instruments and Methods in Physics Research Section B: Beam Interactions with Materials and Atoms* **297** (2013) 39 – 43, `arXiv:1301.5456 [physics.ins-det]`. `https://doi.org/10.1016/j.nimb.2012.12.039`.

[82] C. Zorn, M. Bowen, S. Majewski, *et al.*, *Development of Improved, Radiation-Resistant Plastic and Liquid Scintillators for the SSC*, pp. 537–550. Springer US, Boston, MA, 1989. `https://doi.org/10.1007/978-1-4613-0841-6_50`.

[83] V. Khachatryan, A. M. Sirunyana, A. Tumasyana, *et al.*, "Dose rate effects in the radiation damage of the plastic scintillators of the CMS Hadron Endcap Calorimeter," *JINST* **11** no. 10, (2016) T10004, `arXiv:1608.07267 [physics.ins-det]`. `https://doi.org/10.1088/1748-0221/11/10/T10004`.

[84] L. Torrisi, A. M. Visco, R. Barnà, *et al.*, "Radiation effects induced by MeV electron beams irradiating dense polyethylene (UHMWPE)," *Radiation Effects and Defects in Solids* **159** no. 4, (2004) 259–271. `https://doi.org/10.1080/10420150410001711813`.

[85] A. Dannemann, *Untersuchungen zur Strahlungsresistenz polymerer Materialien für den Einsatz in Experimenten der Hocheneriephysik.* PhD thesis, Hamburg U., 1996. `http://inspirebeta.net/record/417698/files/cer-000222999.pdf`.

[86] W. Busjan, K. Wick, and T. Zoufal, "Shortlived absorption centers in plastic scintillators and their influence on the fluorescence light yield," *Nuclear Instruments and Methods in Physics Research Section B: Beam Interactions with Materials and Atoms* **152** no. 1, (1999) 89 – 104. `https://doi.org/10.1016/S0168-583X(98)00974-4`.

[87] C. Zorn, *Plastic and Liquid Organic Scintillators*, pp. 218–279. WORLD SCIENTIFIC, 2011. `https://doi.org/10.1142/9789814360333_0004`.

[88] C. Zorn, "A pedestrian's guide to radiation damage in plastic scintillators," *Nucl. Phys. Proc. Suppl.* **32** (1993) 377–383. `https://doi.org/10.1016/0920-5632(93)90049-C`.

[89] L. Torrisi, "Radiation damage in polyvinyltoluene (PVT)," *Radiation Physics and Chemistry* **63** (Jan., 2002) 89–92. `https://doi.org/10.1016/S0969-806X(01)00487-X`.

[90] A. D. Bross and A. Pla-Dalmau, "Radiation effects in plastic scintillators and fibers," in *International Conference on Calorimetry in High-energy Physics Batavia, Illinois, October 29-November 1, 1990*, pp. 0443–453. 1991. `http://lss.fnal.gov/cgi-bin/find_paper.pl?pub-91-74`.

[91] Yu. M. Protopopov and V. G. Vasilchenko, "Radiation damage on plastic scintillators and optical fibers," *Instrum. Exp. Tech.* **37** (1994) 53–58.

[92] G. Marini, I. Donatelli, A. Nigro, *et al.*, "Radiation damage to organic scintillation materials," 1985.
https://inis.iaea.org/search/search.aspx?orig{_}q=RN:16074295.

[93] C. Zorn, S. Majewski, R. Wojcik, and K. F. Johnson, "Progress in the design of a radiation hard plastic scintillator," *IEEE Trans. Nucl. Sci.* **38** (1991) 194–199.
https://doi.org/10.1109/23.289296.

[94] M. Hildebrandt, "The drift chamber system of the MEG experiment," *Nuclear Instruments and Methods in Physics Research Section A: Accelerators, Spectrometers, Detectors and Associated Equipment* **623** no. 1, (2010) 111 – 113.
https://doi.org/10.1016/j.nima.2010.02.165. 1st International Conference on Technology and Instrumentation in Particle Physics.

[95] D. E. Groom, N. V. Mokhov, and S. I. Striganov, "Muon stopping power and range tables 10-MeV to 100-TeV," *Atom. Data Nucl. Data Tabl.* **78** (2001) 183–356.
https://doi.org/10.1006/adnd.2001.0861.

[96] A. Jeanine, *New Analysis Method to Confirm the Upper Limit of the Branching Ratio $\mathcal{B}(\mu^+ \rightarrow e^+ + \gamma)$ from the MEG Experiment.* PhD thesis, ETH Zürich, 2012.
https://doi.org/10.3929/ethz-a-007587925.

[97] **MEG** Collaboration, M. Hildebrandt, "3D measurement of (previous) MEG target," Malte Hildebrandt report (MEG Collaboration Meeting 12/17/2013), Paul Scherrer Institut, 2013.

[98] P.-R. Kettle, "Radiation damage studies - a simulation summary," Peter-Raymond Kettle report (HiMB Meeting 27/04/2016), Paul Scherrer Institut, 2016.

[99] M. Van de Voorde and C. Restat, *Selection Guide to Organic Materials for Nuclear Engineering.* CERN Yellow Reports: Monographs. CERN, 1972.
https://doi.org/10.5170/CERN-1972-007.

[100] IDS Imaging Development Systems GmbH, *UI-2220SE-M-GL Rev.3*, 2016.

[101] P. S. Heckbert, "Survey of Texture Mapping," *IEEE Comput. Graph. Appl.* **6** no. 11, (Nov., 1986) 56–67. https://doi.org/10.1109/MCG.1986.276672.

[102] G. Bradski, "The OpenCV Library," *Dr. Dobb's Journal of Software Tools* (2000) –.
http://www.drdobbs.com/open-source/the-opencv-library/184404319.

[103] IDS Imaging Development Systems GmbH, *IDS, UI-2220SE-M-GL, EMVA 1288 Summary Sheet*, 5, 2015.

[104] R. Widenhorn, M. M. Blouke, A. Weber, *et al.*, "Temperature dependence of dark current in a ccd," *Proc.SPIE* **4669** (2002) 4669 – 4669 – 9.
https://doi.org/10.1117/12.463446.

[105] Analog Devices, *2 Terminal IC Temperature Transducer - AD590 Rev. G*, 2013.
`http://www.analog.com/media/en/technical-documentation/data-sheets/`
`AD590.pdf`.

[106] Thorlabs, *Scientific-Grade Digital Camera - 4070M Rev. N*. `https:`
`//www.thorlabs.com/newgrouppage9.cfm?objectgroup_id=7900&pn=4070M-CL`.

[107] T. Prokscha, E. Morenzoni, K. Deiters, *et al.*, "The new high-intensity surface
muon beam for the generation of low-energy muons at PSI," *Physica B: Condensed
Matter* **374–375** (2006) 460 – 463.
`https://doi.org/10.1016/j.physb.2005.11.132`. Proceedings of the Tenth
International Conference on Muon Spin Rotation, Relaxation and Resonance.

[108] Thorlabs, *Mounted Si Photodiode - SM05PD2A Rev. B*, 2012. `https:`
`//www.thorlabs.com/newgrouppage9.cfm?objectgroup_id=1285&pn=SM05PD2A`.

[109] G. Kube and W. Lauth, "Investigation of the light yield of luminescent screens for
high energy and high brilliant electron beams," in *Proc. DIPAC09 (Basel,
Switzerland, 2009)*, pp. 387–389. 2009.

[110] M. A. Lodes, F. S. Kachold, and S. M. Rosiwal, "Mechanical properties of micro-
and nanocrystalline diamond foils," *Philosophical Transactions of the Royal Society
of London A: Mathematical, Physical and Engineering Sciences* **373** no. 2038,
(2015) –. `https://doi.org/10.1098/rsta.2014.0136`.

[111] Eljen Technology, *Plastic Scintillator Polishing Procedure*, May, 2008. `http://www.`
`eljentechnology.com/images/technical_library/Plastic_Polishing.pdf`.

[112] S. Van Der Walt, S. C. Colbert, and G. Varoquaux, "The numpy array: A structure
for efficient numerical computation," *Computing in Science & Engineering* (2011)
22–30, `arXiv:1102.1523 [cs.MS]`. `https://doi.org/10.1109/MCSE.2011.37`.

[113] J. D. Hunter, "Matplotlib: A 2D graphics environment," *Computing In Science &
Engineering* **9** no. 3, (2007) 90–95. `https://doi.org/10.1109/MCSE.2007.55`.

[114] R. von Hahn *et al.*, "The Cryogenic Storage Ring CSR," *Rev. Sci. Instrum.* **87**
no. 6, (2016) 063115, `arXiv:1606.01525 [physics.atom-ph]`.
`https://doi.org/10.1063/1.4953888`.

[115] G. Blatman and B. Sudret, "Sparse polynomial chaos expansions based on an
adaptive Least Angle Regression algorithm," in *19me Congrès Français de
Mécanique - Marseille 24-28 août 2009*. Aug, 2009.

[116] D. Reggiani, K. Deiters, and W. Hajdas, "Secondary Beam Lines and Irradiation
Facility at the PSI Proton Accelerators.". 4th Beam Telescopes and Test Beams
Workshop, 03.02.2016.

List of Figures

List of Tables

Acronyms

ADC	analog-to-digital converter
AIF	annihilation-in-flight
APD	Avalanche Photodiode
BB	Beam Blocker
BGO	Bismuth Germanium Oxide (Bismuth Germanate) $Bi_4Ge_3O_{12}$
BSM	Beyond the Standard Model
BTS	Beam Transport Solenoid
CAD	Computer Aided Design
CCD	Charge-Coupled Device
CDC	Cylindrical Drift Chamber
CERN	Conseil Européen pour la Recherche Nucléaire
CEX	Charge Exchange
cLFV	charged Lepton Flavor Violation
CMBL	Compact Muon Beam Line
COBRA	COnstant Bending RAdius solenoid
C-W	Cockcroft-Walton
DAC	digital-to-analog converter
DCB	Data Concentrator Board
DAQ	Data Acquisition
DOF	depth-of-field
DRS4	Domino Ring Sampler version 4
DS	downstream
FEM	Finite Element Method
FOV	Field-of-view
FPGA	Field Programmable Gate Array
FRET	Förster resonance energy transfer
G4BL	G4Beamline
GUI	Graphical user interface
HiMB	High Intensity Muon Beam
HIPA	High Intensity Proton Accelerator
HV-MAPS	High Voltage Monolithic Active Pixel Sensor
LED	Light Emitting Diode
LEM	Low Energy Muon
LHC	Large Hadron Collider
LTP	Laboratory for Particle Physics
LXe	Liquid Xenon
LY	Light Yield
MC	Monte-Carlo
MIDAS	Maximally Integrated Data Acquisition System

MPPC	Multi-Pixel Photon Counter
MSC	Multiple Scattering
μSR	Muon Spin Resonance
PE	Polyethylene
PET	Polyester
PMNS	Pontecorvo-Maki-Nakagawa-Sakata
PMT	Photomultiplier tube
PS	Polystyrene
PSI	Paul Scherrer Institute
PVT	Polyvinyltoluene
RDC	Radiative Decay Counter
RF	Radio Frequency
RMD	Radiative Muon Decay
SiPM	Silicon Photomultiplier
SINQ	Swiss Spallation Neutron Source
STiC	SiPM Timing Chip
SM	Standard Model
TgE	Target E
TC	Timing Counter
TCB	Trigger Concentrator Board
TOF	Time-Of-Flight
US	upstream
WaveDREAM	Waveform DRS4 based Readout Module